Investigating the Soft X-ray Background of the Milky Way

A thesis submitted for the degree of
Doctor of Philosophy
at the University of Leicester

by

Michelle Supper

X-ray & Observational Astronomy Group
Department of Physics & Astronomy
University of Leicester

June 2011

Investigating the Soft X-ray Background of the Milky Way

Michelle Supper

Abstract

This thesis uses the data from twenty ROSAT and XMM observations to investigate the structures that generate the soft X-ray background of the Milky Way. Ten of these observations lie in the direction of the Loop I Superbubble, specifically, within the North Polar Spur, the Northern Bulge, and immediately south of the Galactic Plane. The others are located in the Anti-centre direction, where the X-ray background is less complex.

Using a novel processing technique, point sources and enhancements were successively removed from the observations until only the Diffuse X-ray Background (DXRB) remained. By modelling the spectra of this clean data, and separately analysing the O VII and O VIII emission lines, the various structures in the DXRB were identified, and their properties determined.

The resulting models strongly indicate the existence of three previously unidentified components: a 14 pc thick, 0.1 keV shell surrounding Loop I, an inhomogeneous 0.25 keV Galactic Halo, and a non-thermal component present in the Galactic Centre direction. In contrast with previous work, no evidence was found for a cool Galactic Halo. The centre of Loop I was placed 290 pc away, 80 pc farther than previously believed. Additionally, an ongoing interaction was discovered between the Local Hot Bubble and Loop I.

This Thesis is Dedicated to the Memory

of my grandparents
Izzy & Ray Rosenthal

and my friend and teacher
Rabbi Dr. Leonard L. Tann

"The memory of the righteous is a blessing"

Declaration

I hereby declare that no part of this thesis has been previously submitted to this or any other University as part of the requirement for a higher degree.

The work described herein was conducted by the undersigned, except for contributions from colleagues as acknowledged in the text.

Michelle Supper

June 2011

Acknowledgements

I have climbed a mountain. This is the summit, my zenith, the closest I have ever been to the stars. In the years it has taken to write this thesis, my mind has stretched out to encompass the Interstellar Medium, and created a three-dimensional image of the structures contained within. With this, I have been able to re-interpret the spectrum of the soft X-ray background, identifying three new sources in the X-ray sky. In the attempt to translate the contents of my brain into English, I have produced this hefty tome, and can only hope that it does justice to the research.

Although, academically, this has been a long and often solitary ordeal, my journey has been made bearable by a team of wonderful, kind people who have worked hard to keep my feet on the ground and my head above the clouds.

The guide on my quest has been my soul-mate, constant companion and, as of June 26th 2005, husband, Dr. Ben Supper. Without him I would have given up long ago. Thank you for having confidence in me, and for rewiring the light at the end of the tunnel.

My Mum and Dad have been my life-support system. Yes, you will have a copy of the thesis, and no, you probably won't understand all of it, but that doesn't matter. I know you'll try your best, you always do, and that's what counts. Your strength and courage over the last few years has been an inspiration, and I hope that the future holds only happiness for you both.

Spiritual enlightenment and guidance has been provided in great abundance by my adoptive parents Rabbi Dr. Leonard zt"l & Irene Tann, and by Rabbi Shmuli & Rivkie Pink. Thank you for keeping my body and soul connected to their true source. After all these years, I can confirm that Rav Eleazar Chisma[1] was right: astronomy and geometry are the after-courses of wisdom.

Many friends have helped along the way, too many to name individually, but special mentions go to Dr. Rafik Taibjee, Dr. Steve Melnikoff, Jo Samuels, Nims Cohen, Michael

[1] Pirkei Avos, Chapter 3, Verse 23

Ross, and of course, to my undergraduate colleague / partner in crime, Dr. Rowan Temple. Thank you for always being there, I could not wish for truer friends.

If one can see further only by standing on the shoulders of giants, then I've been very lucky. Although I'm only 5'3", I have been raised up on high by my teachers and friends at Bury Grammar School, and the Universities of Birmingham and Cambridge. These include my physics teacher Mr. David Lehan, Dr. Somak Raychaudhury, Dr. Ian Stevens, Dr. John Herring, Prof. Mike Cruise, Prof. Douglas Gough, and Prof. Sir Martin Rees. Many thanks also go to my academic confidants at Leicester, Prof. Stan Cowley, Prof. Ken Pounds and most especially, Prof. Derek Raine; your guidance, encouragement and faith in my abilities gave me the determination to complete this thesis. I couldn't have done it without you.

None of this could have happened without training, provided by Dr. Simon Vaughan and Dr. Kim Page (the all-knowing oracle of the XROA department) and funding (for the first three years, at least) from PPARC.

Special thanks must also go to Dr. Jonathan Tedds who, by taking me observing to the Isaac Newton Telescope on La Palma, fulfilled my lifelong ambition to be a professional astronomer. I was born to observe the sky. If you ever need an observing assistant again, you know where to find me.

It is only when you reach the peak that you realise quite how arduous the climb was. Thank you to all of my students, the 2nd and 3rd year undergraduates of Leicester University, who attended my seminars in maths, particle physics, quantum mechanics, electromagnetism, relativity, and condensed matter. Thanks also to the more than one-thousand people who came to my twenty-seven Einstein's Legacy lectures. It was a pleasure to teach you all, and I wish you the best of luck as you make your own ascents of the great mountain of scientific knowledge. I hope I made the way a little easier for you.

Finally, to my thirteen young tutees in maths, physics and logic: Jason, Harrison, Ramiz, Alex, Edward, Isabel, Adam, Gideon, Danielle, Saul, Bethany, Yasmin and Nemisha. It is always an honour for a teacher to educate her pupils, and the destiny of the pupils to educate their teacher. My children, I'm proud of you. The future is yours – reach for the stars.

Michelle Supper

June 2011

Contents

List of Figures

List of Tables

1

Introduction

In this opening chapter, the characteristics of X-radiation, the physical processes by which it is produced, and the techniques used to detect it will be described. The interstellar medium and soft X-ray background of the Milky Way will then be introduced, and finally, the objectives of this research will be outlined.

1.1 The Discovery of X-rays

Wilhelm Konrad Röntgen accidentally discovered X-rays on the 8th of November 1895. Whilst experimenting with a cathode ray tube, he noticed that a barium platinocyanide covered screen lying on a bench nearby had started to glow. This effect could not have been produced by ultra-violet radiation, since none had been produced by the experiment; nor could it have been caused by the cathode rays, because any stray electrons within the tube would have been blocked by both the glass and the surrounding air. Röntgen reasoned that the fluorescence must have arisen through an interaction between the screen and radiation of an unknown nature, which he named 'X-rays'. Following seven weeks of intensive research, he published his groundbreaking findings in what is now considered a classic paper in experimental science (Röntgen 1896), for which he was later awarded the first Nobel Prize for Physics.

After publication, Röntgen's discovery was reported in the *Vienna Presse* (January 5th,

1896*a*), and thence brought to the attention of the general public through the popular media. At first, so many people presumed it to be a hoax that the *London Standard* (January 7th, 1896*b*) felt it necessary to confirm that "... there is no joke or humbug in the matter. It is a serious discovery by a serious German professor."

When the truth was eventually accepted, it caused sensation and scandal. As Schedel (1995) explains, the ability of X-rays to pass through walls deeply concerned the general public, who feared for their privacy. In February 1896, a pre-emptive law was passed banning the use of X-rays in opera glasses in American theatres, and in March of the same year, a company in London started to produce anti-X-ray underwear. Ridiculous claims abounded for the New Rays: even the respected journal *Science* (March 3rd, 1896*c*) reported that medical students were able to retain more information from their lectures when "Röntgen rays were used to reflect anatomic diagrams directly into their brains."

By the turn of the century, the initial flurry of excitement and pseudoscience surrounding the study of X-rays had died away. A more thorough investigation was made of X-radiation, and its real properties were quickly determined. However, despite rapid early progress in Earth-bound laboratories, the attempts of physicists to observe X-rays of extra-terrestrial origin were hampered by the Earth's atmosphere. The ozone layer, a substratum of the stratosphere located approximately 14 km from the Earth's surface and extending upwards for a further 40 km, is opaque to ultra-violet, X- and gamma radiation (Gleason 2006).

It was not until 1949 that a team led by Herbert Friedman et al. (1951) was able to measure, from a position above the ozone layer, the X-ray emission from the solar corona. The detection itself came as a surprise: no-one had predicted that the extremely high temperatures required for X-ray emission would exist within the solar environment. The team's achievement is even more remarkable when one considers their experimental apparatus: a collection of small Geiger counters tucked inside German V2 rockets which had been captured during the Second World War.

X-rays of cosmic origin were finally observed by Riccardo Giacconi et al. (1962) using two uncollimated Geiger counters carried on board an Aerobee rocket. Most of the X-ray flux they detected, at energies of several tens of MeV, originated in a mysterious, diffuse, anisotropic signal of considerable flux that was present across the entire sky. Giacconi's

team deduced that this signal was electromagnetic in nature, rather than particulate, and that it must lie in the soft X-ray band, between 0.1 keV and 10 keV. They also reasoned that since the observation was made at a low point in the solar cycle, when the Sun's activity was at a minimum, solar X-radiation could not account for the signal's observed intensity. Therefore, it had to originate outside the Solar System, forming a diffuse X-ray background of undetermined source.

Of the detected X-ray flux, relatively little came from within own Galaxy. However, further observations carried out by the same team (Giacconi et al. 1964) discovered the brightest source of Galactic X-rays in the night sky. Later named Sco-X1, and classified as a low-mass X-ray binary system, its prodigious X-ray emission is ten thousand times greater than its optical emission, and its energy output in X-rays is one hundred thousand times greater than the total emission of the Sun across all wavelengths.

The discovery of Sco-X1 helped to secure the Nobel Prize for Riccardo Giaconni; he shared the prize in 2002, along with Masatoshi Koshiba and Raymond Davis, Jr., "for pioneering contributions to astrophysics, which have led to the discovery of cosmic X-ray sources, " and his serendipitous discovery of the diffuse X-ray background laid the foundation for this thesis.

1.2 The Basic Properties of X-rays

X-rays lie at the high-energy end of the electromagnetic spectrum, possessing photon energies in the range 0.1 keV – 100 keV, corresponding to a wavelength range of approximately 10 – 0.01 nm. In X-ray astronomy, this range is split arbitrarily into two regimes. 'Soft' X-rays, with which this thesis is primarily concerned, have wavelengths longer than 0.1 nm, equivalent to a photon energy less than $\sim$ 10 keV. 'Hard' X-rays possess wavelengths shorter than 0.1 nm, and photon energy greater than $\sim$ 10 keV.

There are several mechanisms by which X-rays are produced in nature. These may be divided into two groups of processes, thermal and non-thermal, depending on the thermodynamical state of the emitting plasma.

1.2.1 Thermal Processes

Thermal processes arise in relaxed particle systems which have had sufficient time to reach thermal equilibrium. The average temperature of a system at thermal equilibrium may be regarded as uniform and unchanging with time over an extended volume of space. Particles within the system collide frequently, and move at velocities characteristic of their temperature. Consequently, the energy spectrum of such a system may be described using the Maxwell distribution, from which the temperature of the emitting material can be determined directly.

Thermal Bremsstrahlung

Thermal Bremsstrahlung is the primary emission process that occurs in both extended sources and optically thin plasmas, such as supernova remnants and galaxy clusters. Bremsstrahlung radiation is produced when a fast moving electron is attracted to a positively charged nucleus. Although the attraction is often not strong enough to stop the electron, it will slow it down, causing the electron to divert from its original path and to curve around the nucleus. Simultaneously, the electron emits a photon, to account for its reduced energy (Figure 1.1). This photon is the *Bremsstrahlung*, or 'braking radiation', and its wavelength is determined by the amount of energy lost by the progenitor electron as it moved around the nucleus. If the electron is sufficiently decelerated, an X-ray photon may be produced.

Bremsstrahlung photons are produced over a continuous range of energies. There is no upper wavelength boundary but, since an emitted photon may not be more energetic than the progenitor electron, there is a lower limit. Thus, the characteristic Bremsstrahlung spectrum profile is described by a smooth curve that reduces gradually towards zero at high wavelengths, but has a sharp energy cut-off at the wavelength minimum.

Discrete Line Emission

Line emission occurs when a bound electron within an atom is excited to a higher level, or removed altogether, by an input of energy through bombardment from an ion or a

high-energy photon.

If the bound electron is merely excited to a higher energy level, the enhancement is short-lived. The excited state decays spontaneously when the electron quickly falls back to the lower energy level, emitting a photon on the way (Figure 1.1). The energy spectrum of a population of identical atoms undergoing this type of transition consists of a single peak, centred on the characteristic photon energy of the transition.

If, however, the free electron has sufficient energy to penetrate the atom and knock a bound electron from one of the inner electron shells (inner shell ionisation), a vacancy will be created. In order to maintain stability and decrease electrical potential, an electron from a higher shell will drop down to fill the empty space, emitting a photon as it does so. This transition creates a new vacancy, which is subsequently filled by another electron from an even higher shell. The process continues as a cascade, with each transiting electron producing a further photon, ultimately generating an energy spectrum containing a series of peaks, one for each of the electron transitions.

The energy of each emitted photon will be equal to the energy lost by the bound electron as it dropped from the higher energy shell to a lower one. High energy X-ray photons are therefore produced by outer shell electrons falling into the level closest to the nucleus, the K-shell.

Classically, the emission lines produced by this process should resemble delta functions. In practice, however, they broaden as a consequence of the Heisenberg Uncertainty Principle. This insists that there must be uncertainty in the photon energy as a result of the finite lifetime of the excited state, giving the lines a Lorentzian profile. Other factors that can increase the width of an emission line include 'impact pressure broadening' caused when the emission process is interrupted by other particles colliding with the emitting particle, which is also described by a Lorentzian profile, and Doppler broadening, in which different thermal velocities between the emitting atoms cause the photons to appear Doppler shifted in the observer's reference frame, producing a Doppler profile. The ultimate shape of an emission line observed in the spectrum will represent a convolution of the line profiles that produced it. A combination of both Lorentzian and Doppler profiles, for example, would yield a Voigt profile.

Discrete line emission is a powerful tool in X-ray astronomy. Since the positions of the

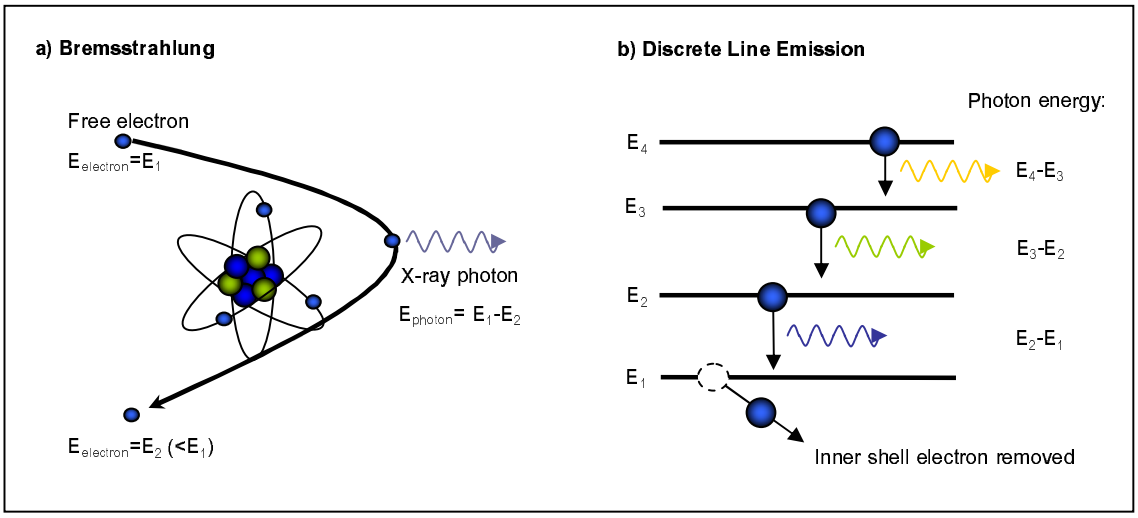

Figure 1.1: Thermal Processes: a) Bremsstrahlung: the free electron curves around a positively charged ion or nucleus, and releases an X-ray photon as it decelerates. b) Discrete line emission: a bound electron is removed from the inner shell of an atom. Each electron then emits a photon as it falls to fill a space in a lower shell.

peaks are determined by the orbital energies of the electrons in each atom, each atomic species produces a unique pattern of emitted lines. Consequently, when emission from a mixture of hot gases is observed, the lines can be used to identify specific transitions within the various atomic species, and hence to determine their relative abundances. Also, since some ionic species exist in significant quantity only within certain environments, these can be used to trace certain astrophysical phenomena and to make precise determinations of plasma temperature.

Bremsstrahlung and discrete line emission both occur in plasmas at all temperatures, however, the ratio of their contributions alters: At high temperatures, the Bremsstrahlung process dominates, but in lower temperature plasmas, discrete line emission is more prominent. Consequently, X-ray spectra from thermal plasmas generally show a series of emission lines standing above a Bremsstrahlung continuum.

1.2.2 Non-Thermal X-ray Production Mechanisms

Non-thermal processes occur in young, energetic gases and plasmas that have not yet reached thermal equilibrium. The constituent particles of these regions move at high velocity, and rarely transfer thermal energy between one another. Such unsettled conditions may be found in the remnants of newly-exploded stars, around cosmic jets, and within the environs of active galactic nuclei. Typically, the energy spectrum of non-thermal radiation appears as a smooth, gently-sloping continuum that can be modelled by a power law. Non-thermal X-rays are most commonly produced through synchrotron radiation and inverse Compton scattering.

Synchrotron Radiation

Magnetic fields exert a force perpendicular to the direction of travel of moving electrons in their vicinity, curving their path, and causing them to accelerate.

In the vacuum of space, fast moving free electrons spiral along strong magnetic field lines at near relativistic velocities. When this occurs, photons are emitted in a tightly-beamed narrow cone in the forward direction of travel, at a tangent to the orbit of the electron (Figure 1.2). These 'synchrotron' photons can be produced over a continuum of wavelengths ranging from radio, through X-ray and gamma-ray bands.

Inverse Compton Scattering

Inverse Compton scattering occurs when free electrons 'collide' with photons. In cases where the electron initially has more energy than the photon, energy appears to be 'transferred' to the photon upon collision. In fact, the low-energy photon excites the electron, which subsequently re-radiates the energy from the photon plus a little of its own, in the form of a higher-energy photon (Figure 1.2). In this way, low-energy photons may generate higher-energy X-ray photons. This effect is particularly important in black hole environments and young supernova remnants where both relativistic particles and seed photons are present.

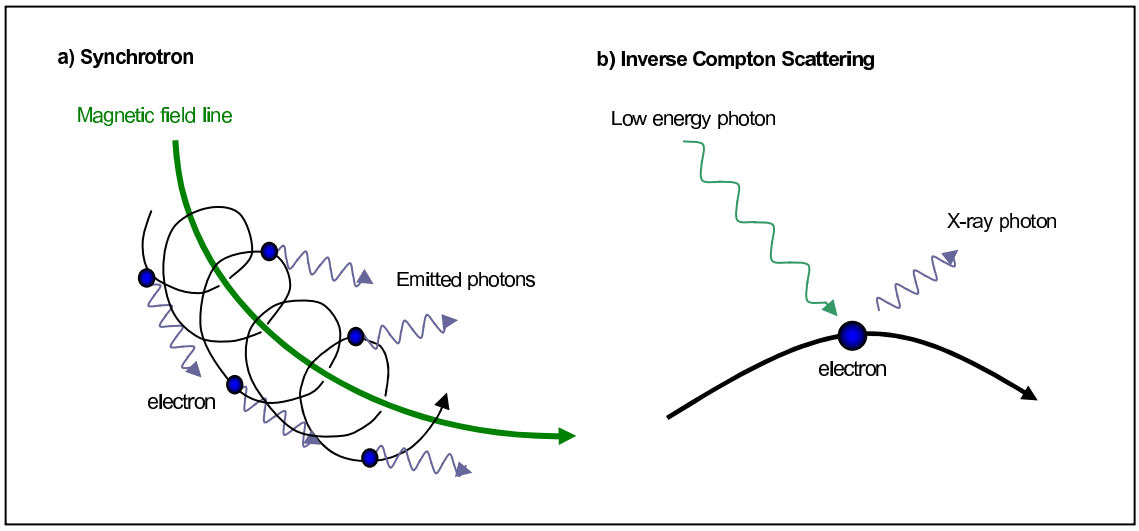

Figure 1.2: Non-Thermal Processes: a) Synchrotron Radiation: a free electron spirals around a magnetic field line, emitting photons at it travels. b) Inverse Compton Scattering: a low-energy photon collides with a free electron. The electron subsequently de-excites, and emits a higher-energy photon.

1.3 Instrumentation: Focusing on the Problem

In the early days of X-ray astronomy, simple X-ray detectors were carried to the outer edges of the Earth's atmosphere using sounding rockets and high-altitude balloons. Although highly informative, the angular resolution of the data acquired in these observations was severely limited and so offered only a tantalizing hint of the richness of the X-ray sky. In recent years, several X-ray observatories have been placed in Earth orbit. The optimal positioning of these space telescopes, together with improvements in X-ray focusing and imaging technology, have allowed a more direct insight into some of the most energetic structures in the Universe.

1.3.1 Proportional Counters

The first X-ray detectors were 'proportional counters'. These were similar in design and principle to the Geiger-Müller (GM) tubes used to detect radioactive particles, but were adapted to accommodate the requirements of X-ray detection as illustrated in Figure 1.3.

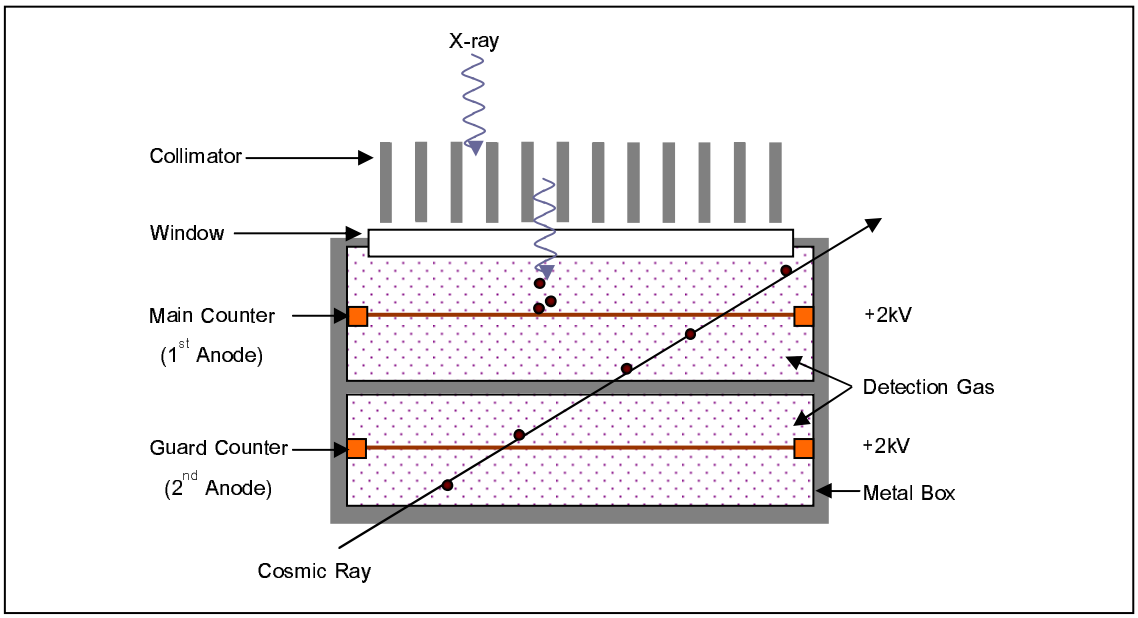

Figure 1.3: The structure of a simple proportional counter.

As in a GM tube, radiation enters through a thin, round window and passes into a mixture of detecting gases. The incident photons ionise the gas, creating a cloud of electron-ion pairs. The newly liberated electrons accelerate toward a positively-charged central wire, the anode. As they approach the anode, they interact with the electric field surrounding it, and trigger further ionisation through 'Townsend Avalanching'. This process greatly increases the number of free electrons, and so magnifies the strength of the initial detection. The pulse of electrons collected by the anode is then conducted to the associated electronics, where it is registered as an *event* or *count*.

Aside from obvious structural enhancements that were needed to make the fragile GM tubes space-worthy, such as replacing the brittle beryllium window with a stronger one made of plastic, two major modifications were required to create an X-ray detector: the avalanching effect had to be reduced, and an extra anode had to be added.

The factor by which the electron population is multiplied by avalanching is partly dependent on the properties of the detecting gas, but relies mainly on the electric field strength, which is itself determined by both the voltage and diameter of the anode. In a GM tube, the operating voltage is very high, causing the multiplication factor to tend toward a maximum value. As a result, all measured pulses from the tube have similar

amplitude. This system is useful when determining the rough intensity of an ionising source but, since it does not differentiate between the individual detections, it has limited diagnostic value.

To create a proportional counter, the multiplication factor had to be set below the maximum level. Thinner wires produce stronger electric fields for a given applied voltage, and so proportional counters were designed to use the thinnest wire available with sufficient mechanical strength (Pounds 2007). The lowest voltage required to give a reasonable signal was then applied, ensuring that the output signal would be approximately proportional to the energy of the incident X-ray photons, and so enabling the energy spectrum of X-ray sources to be measured.

An inescapable constituent of the space environment, cosmic rays are high-energy particles of uncertain origin. Their prodigious energy allows them to pass directly through the metal casing of a proportional counter and into the detecting gas. Once there, they travel straight through, leaving a heavily ionised trail in their wake. The electrons released by the ionisation are detected together with those derived from the detected X-ray source, causing signal contamination. In order to screen the collected data for cosmic rays an extra anode, located below the main detecting chamber in a sealed metal container, was included in proportional counters. Because metal is opaque to X-rays, only the cosmic rays reach the second anode, or 'Guard Counter'. Electron pulses detected only by the first anode are registered as genuine X-ray events, whereas pulses measured simultaneously by both anodes are discounted as cosmic rays.

The earliest proportional counters were able to detect incident X-rays but could not accurately pinpoint their origin. For example, the detector used by Giacconi et al. (1962) to observe the X-ray emission from Sco-X1 had a field of view covering 100°, an area of the sky so large that it encompassed several entire constellations. In subsequent missions, honeycomb filters were installed in front of proportional counters to limit their field of view to a few square degrees. These restricted the X-ray flux to the detectors, and so provided a higher degree of directionality.

Throughout the 1960s, rocket-based observations with proportional counters revealed around fifty X-ray sources, including several objects in the Galactic Plane, the active galaxies M87 and NGC 5128, and quasar 3C 273. The era of rocket-borne X-ray

astronomy culminated in 1970 with the launch of the Uhuru satellite (Giacconi et al. 1971) which, using standard proportional counters in conjunction with a honeycomb collimator, was able to complete the first all-sky X-ray survey.

The Uhuru survey revealed a population of three hundred and thirty-nine sources, including some that were ten times fainter than anything observed by the earlier rocket flights. Although intriguing, the data could show only the relative intensities of the sources and their approximate positions. In order to understand the origin of cosmic X-ray sources, to create images of them, and examine their spectra in detail, it was necessary to develop a method to focus X-rays.

1.3.2 Wolter Mirrors

It is simple to focus visible light: a normal incidence reflecting mirror can be used to create a sharp image of a chosen target. Unfortunately, this is not the case with X-rays. Because the wavelength of X-radiation is similar to the atomic spacing of solid materials, X-ray photons are scattered when they strike a surface at normal incidence, making it very difficult to bring them to a focal point. In 1952, Hans Wolter (1952) discovered a method to focus X-rays based on the principle that X-rays will reflect provided that they are incident at a grazing angle that is almost parallel with their direction of travel. His method was later adopted in the creation of the eponymous 'Wolter type-1' mirror assemblies (Figure 1.4), carried on-board modern X-ray observatories.

A Wolter type-1 mirror is circular in cross-section, but gently curved along its profile so that the incoming photons are incident first on a parabolic surface and then a hyperbolic surface. In order to increase the effective collecting area, Wolter mirrors are nested and aligned concentrically about the optical axis, so that the photons are sent to a single focal point at which an X-ray detector is positioned. This reflecting technique is energy-limited, and is most sensitive at photon energies of 15 keV or less. Consequently, most X-ray imaging telescopes that use this technology have concentrated on the soft X-ray band.

Wolter type-1 mirrors were used on both ROSAT (Röntgensatellit) and XMM-Newton (X-ray Multiple Mirror) observatories to provide an unprecedented view of the X-ray

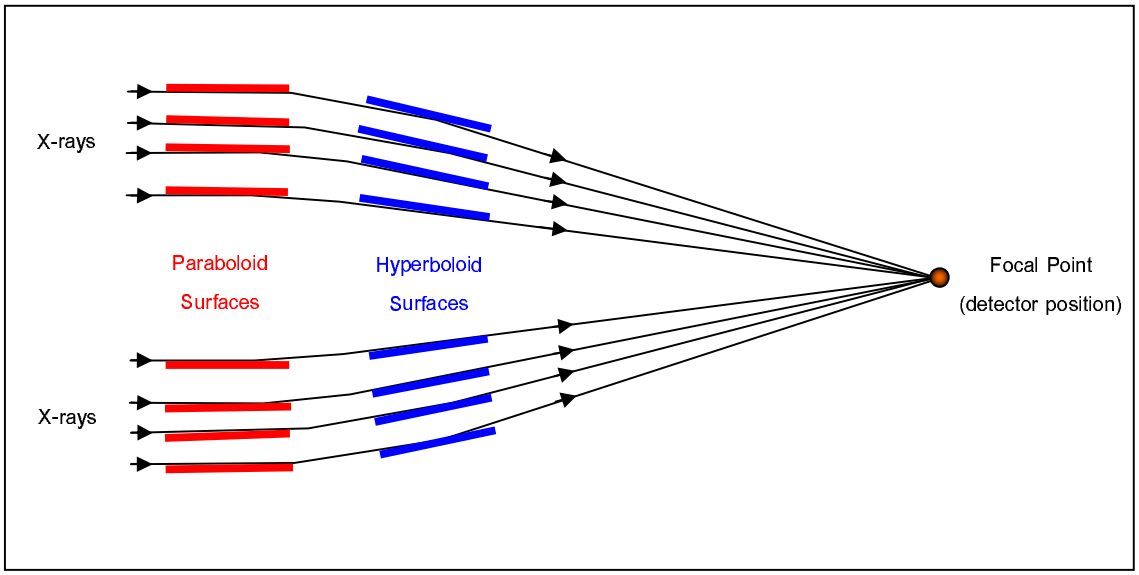

Figure 1.4: The ray paths through a Wolter type-1 mirror assembly: X-ray photons enter in the gap between the concentric mirror shells and strike the paraboloid-hyperboloid mirror surface at a grazing angle. The photons are then guided to a detector, positioned at the confocal point.

sky. Observations made by both of these instruments were used in the course of this research.

1.3.3 ROSAT

The ROSAT observatory (Trümper (1983), Figure 1.5) was launched on June 1st 1990 and decommissioned on February 12th 1999. It was designed to detect low-energy X-rays, specifically between 0.1 and 2.4 keV. Like XMM, ROSAT was equipped with a Wolter type mirror, which allowed X-ray photons to be gathered and focussed onto a detector.

In ROSAT's case, the primary X-ray detector was the Position-Sensitive Proportional Counter (PSPC, Pfeffermann et al. (1987)), a technologically advanced version of the basic proportional counter described above. Instead of a single wire anode, the PSPC used an 'anode grid' comprising two layers of gold-coated tungsten filaments, each 10 micrometres thick, and secured at 1.5 mm intervals on a glass ceramic frame. During operation the wires were kept at an electric potential of 3 kV. Despite this high voltage,

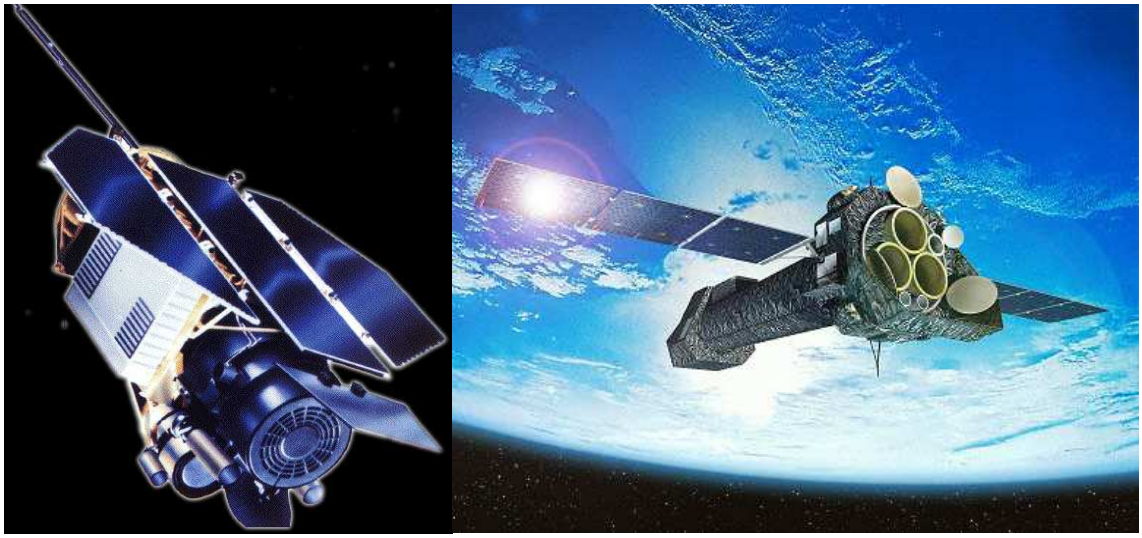

Figure 1.5: Artist's impressions of the ROSAT Space Observatory (left) and the XMM-Newton telescope (right). (Images courtesy of ESA, (VILSPA 2006))

the low ionisation potential of the detecting gas mixture (65% argon, 20% xenon, 15% methane (Aschenbach et al. 1985)) ensured that the charge multiplication factor was kept below its maximum value, and allowed the pulse size of the measured signal to be proportional to that of the incident radiation.

A second anode grid, with a wire separation of 2 mm, was used as a guard counter. By working in anti-coincidence with the main detector, it successfully attained a background rejection efficiency of 99.8% (Briel et al. 1996).

Position sensitivity was achieved using two mutually perpendicular cathode arrays, each made using a large number of parallel 50 micrometres diameter platinum-iridium wires separated by 0.5 mm. The arrays were placed close to the main detector, so that a current would be induced within them whenever an avalanche of electrons impacted the anode. This signal was then used by the on board electronics to estimate the location of the detection: a process that was able to yield a spatial resolution of 30″.

1.3.4 XMM-Newton

Launched on 9th December 1999, the X-ray Multiple Mirror (XMM) telescope (Figure 1.5) is to date the largest scientific observatory developed by the European Space Agency. It is in a highly elliptical orbit about the Earth, and so offers continuous, targeted observation visibility of up to forty hours (144 ks).

XMM carries several instruments, including a 30 cm optical and ultra violet monitoring telescope and the European Photon and Imaging Camera (EPIC). EPIC contains three separate charge coupled device (CCD) X-ray detectors: MOS1, MOS2 (Turner et al. 2001) and pn (Strüder et al. 2001). Each detector lies at the focus of a Wolter type-1 nested mirror module, comprising fifty-eight concentric, confocal reflective shells. The shells are 0.6 m in length, and vary in diameter between 0.3 and 0.7 m. The three mirror modules each provide an effective area of 1550 cm^2 at 1.5 keV: a combined area of 4650 cm^2. (These and other details of the XMM telescopes are sourced from Ehle et al. (2003).)

The complex geometry of the mirrors, and the enormous size of their effective collecting area, allow on-axis point spread functions (PSF) of 6″ at full-width half-maximum (FWHM) to be consistently achieved for all three EPIC instruments, yielding a moderate angular resolution of $\sim$ 15″ at half-energy width. The low PSF value ensures that point sources are clearly resolved by XMM, allowing them to accurately located, isolated, and subsequently studied or removed from a data set.

All of the twenty EPIC observations used in this research were obtained with the cameras operating in 'full frame' mode. This ensured that data was obtained from the full CCD array, so that the entire field of view was covered.

EPIC: The MOS Cameras

The two MOS (metal oxide semiconductor) cameras are capable of detecting X-rays in the energy range 0.1 – 12.0 keV. Each camera contains an array of seven front-illuminated metal oxide CCD chips which cover the 30′ field of view of a mirror module. The square chips each have a 62 mm diameter and a detecting area of 600 by 600 pixels. The central

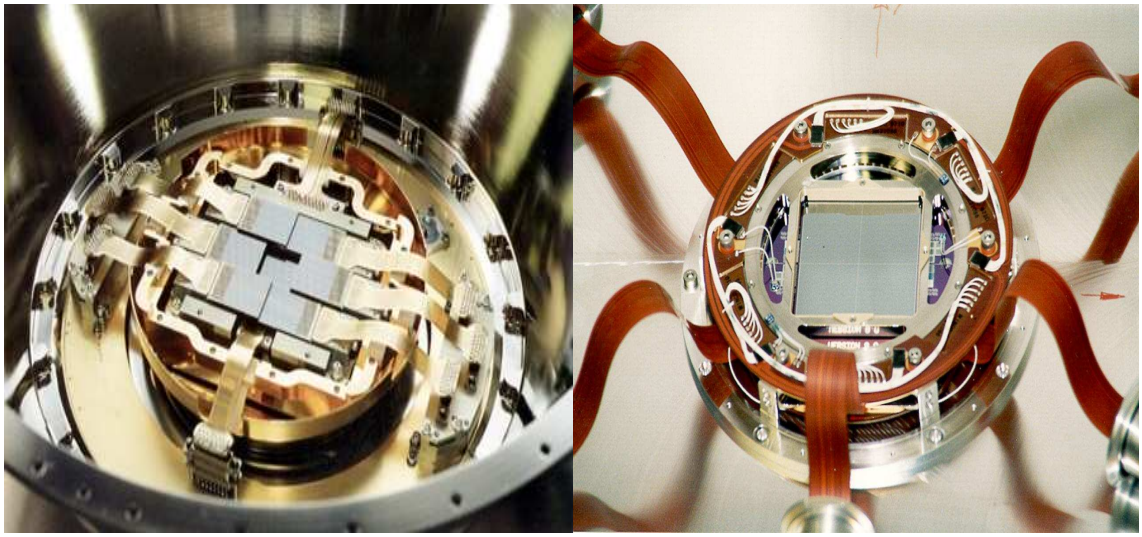

Figure 1.6: The EPIC Cameras: Photographs showing the MOS CCD array (left) and the pn CCD array (right), in their mountings. (Images courtesy of Leicester University, University of Birmingham, CEA Service d'Astrophysique Saclay and ESA, VILSPA (2006)).

chip is positioned at the focal point of the mirror assembly on the optical axis of the telescope. Around it lie the six outer chips, which are stepped toward the central chip by 4.5 mm, following the curvature of the focal plane, and so improving the focus for off-axis sources, as shown in Figure 1.6.

The MOS cameras are particularly sensitive to photon energies in the range 0.4 – 1.0 keV in which many emission lines lie, including the oxygen lines O VII and O VIII.

EPIC: The pn Camera

The pn camera comprises twelve back-illuminated CCDs arranged in a single 60 mm diameter square array (Figure 1.6). The pn cameras are sensitive to photon energies up to 15.0 keV, and tend to have a higher photon throughput than the MOS cameras. Although the use of pn semiconductor technology results in relatively high quantum efficiency around and below 0.5 keV, the MOS cameras have better spectral resolution in this range (Ehle et al. 2003).

1.4 The Interstellar Medium of the Milky Way

The interstellar medium (ISM) is a diverse mixture of ionised plasmas, neutral gas and dust particles that lies between the myriad stars of the Milky Way Galaxy. It amounts to only a few percent of the Galactic mass (about 10^9 $\mathrm{M}_\odot$), and is so tenuous (average density $\sim 10^{-21}$ kg m^{-3}) that on Earth it would be considered a near-perfect vacuum (Tielens 2005). Nevertheless, the structures contained within it are remarkably complex. Neutral, ionised and molecular hydrogen make up about 70% of the mass of the ISM. The remainder is mostly helium, together with approximately solar abundances of heavier elements, such as carbon, nitrogen and oxygen.

The ISM emits and absorbs radiation over several wavelength regimes. The dust present near the Galactic Plane scatters visible light, which hinders optical astronomy, but re-radiates heat, allowing star-forming regions to be located through infra-red observations. Radio astronomy can be used to detect thermal emission, which can trace the concentrations of different chemicals by using the radio photons from a variety of atomic and molecular emission lines, in particular the 21 cm line emitted by neutral hydrogen. It can also detect non-thermal radio synchrotron radiation, which is emitted by charged particles moving at relativistic speeds through magnetic fields.

Karl Jansky (1933) was the first to observe synchrotron radio sources within the Milky Way, but the significance of his discovery was not fully appreciated until the 1950s, more than a decade later. The signal he measured was coming not only from energetic objects near the Galactic Centre, but from the ISM itself.

The field of radio astronomy flourished in the 1960s, a by-product of the major advances in electronics and radar technology that had been achieved during the Second World War. When the radio continuum of the ISM was mapped, it was noticed that ridges of enhanced emission were present, reaching from the Galactic Plane into the higher latitudes. Quigley and Haslam (1965) showed that it was possible to fit arcs of small circles to the three most prominent ridges, the centres of which lay at intermediate latitudes either side of the Galactic Plane. This idea was developed further by Large et al. (1966), who proposed that a series of arcs on either side of the Galactic Plane could be connected into one complete circular formation, which they named Loop I.

Radio measurements by Yates (1968) determined the Galactic co-ordinates of the centre of Loop I to be $329 \pm 1.5°$, $+17.5 \pm 3°$, and found its projected diameter on the sky to be $116 \pm 4°$. Other prominent features that were identified include the Cetus Arc (commonly named Loop 2) and a bright continuum ridge arching up from the Galactic Plane to $\sim 30°$ latitude, which was named the North Polar Spur (NPS).

Several theories were proposed as to the origin of the radio loops and arcs. Rougoor (1966) suggested that they might form a helical structure which crosses the Galactic Plane. Others believed, on the basis of optical polarization measurements (Mathewson 1966), that they were radio tracers of the local Galactic magnetic field, while Bingham (1967) suggested that they were bubbles created in the local magnetic field as a result of its instability to cosmic ray pressure.

The first two ideas, of Rougoor and Mathewson, required the loops to describe a helical structure as they traversed the plane, whereas Bingham's bubble theory required each loop to project from only one side of the plane, and not continue across it. Upon the completion of a series of radio scans of the Galactic Plane, all of these hypotheses were rejected, because the loops appeared to pass straight through the Galactic Plane without forming a helical structure. Fortunately, the data supported a fourth hypothesis (Brown et al. 1960, Berkhuijsen et al. 1971), which proposed that the loops are the remnants supernova explosions: an idea which is now widely accepted.

In spite of their hard work, ingenious experiments and brilliant deduction, the early pioneers of X-ray and radio astronomy had access to only part of the picture. It would take another three decades, until the launch of ROSAT, for the soft X-ray sky to be finally revealed. The ROSAT PSPC had a wide field of view, nearly $2°$ in diameter, and its low spatial resolution prevented it from imaging discrete sources in any detail, but it was optimally designed to produce large-scale surveys in the soft X-ray band, and soon after its launch, the PSPC was used to complete the ROSAT All Sky Survey (RASS) which revealed the presence of structures in the soft X-ray background.

1.5 Thesis Objectives

Any exploration of the soft X-ray structures presents a variety of technical and intellectual difficulties. The flux of the soft X-ray background is relatively weak compared to that of Galactic sources, and is easily drowned out by the internal noise present in most X-ray detectors. It is therefore necessary to use a detector with a large photon throughput and a very high signal-to-noise ratio over a protracted observation time to extract its signal. In addition, because the emissions from several structures are included within each data set, sophisticated spectral analysis and modelling are required to identify the various X-ray sources. It is only in recent years that these requirements have been met. Since the launch and calibration of XMM, high resolution X-ray spectroscopy has become possible, and by using and modifying software developed by Willingale et al. (2003), point sources, cosmic rays and flares can be removed from the raw XMM data, allowing the weak signal of the soft X-ray background to be extracted.

Although it is now apparent that the interstellar medium is the source of the diffuse background X-ray and radio emission, the origin of the emissions and the topology, chemical composition and heating mechanisms of the Local Interstellar Medium (LISM) remain uncertain. The research presented herein investigates the spectral characteristics of the soft X-ray emission observed in twenty locations.

By fitting the X-ray spectra derived from these observations with a combination of plasma and absorption codes, the temperature and chemical composition of the emissive structures will be measured. The best-fit parameters and fluxes of the models will then be used to determine the contribution of each of the emissive structures to the total received oxygen signal. Finally, the parameters will be projected onto a geometric model in order to calculate the physical properties of Loop I and other nearby interstellar structures.

The results of these investigations will be presented in this thesis, together with other new insights into the nature of Loop I and other X-ray emissive structures that produce the soft X-ray background of our Galaxy.

2

The Diffuse X-ray Background

After four decades of investigation, using the most advanced radio and X-ray observatories, many topics within the field remain contentious and uncertain. Competing theories have been proposed in the attempt to explain each aspect of the X-ray background, from its origin and appearance to the individual structures it contains and the interactions between them.

In order that the results presented in this thesis may be taken in context, the literature published in relation to the diffuse X-ray background will be reviewed in this chapter. The major structures present in the interstellar medium will be introduced, and the various theories which relate to them outlined and considered. Before that, however, the primary reason behind the delay in understanding will be described: absorption of the X-ray signal by the neutral atomic hydrogen which permeates the Milky Way.

2.1 Neutral Atomic Hydrogen

Neutral atomic hydrogen (commonly designated HI) is ubiquitous throughout the Milky Way. Although not visible optically, its presence may be inferred through radio mapping of the 21 cm emission line, which was first detected by Ewen & Purcell (1951).

The 21 cm line, with frequency 1420.4058 MHz, is the strongest thermal line in radio

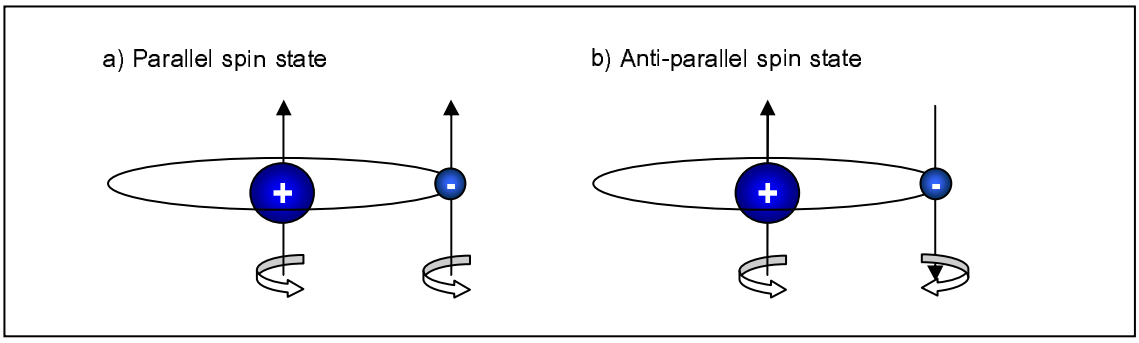

Figure 2.1: The Hyperfine States of Atomic Hydrogen: a) Parallel spins: the higher energy state during which both the electron and proton have the same spin. b) Anti-parallel spins: the lower energy state in which the proton and electron have opposite spins.

astronomy. It is emitted by 'warm'[1] clouds of HI, between 50 and 100 K, and is the only radio transition of ground state neutral hydrogen. Both components of HI, a proton and an electron, have a spin value of $\frac{1}{2}$, meaning that each particle can hold one of two possible quantum states: spin-up or spin-down. In an HI atom, the electron may spin in the same direction as the proton (a parallel-spin state) or in the opposite direction, so that the spins are anti-parallel. These two states are known as the hyperfine energy levels of ground state atomic hydrogen (see Figure 2.1).

An interstellar hydrogen atom is in the higher-energy state when both spins are parallel. Either a spontaneous transition or a random collision with another atom may cause the electron to reverse its spin. For an atom originally in the parallel state, this 'spin-flip' makes the spins anti-parallel: a process which minimises the potential energy of the atom, and makes it more energetically stable. As the electron spin-flips from the higher to the lower energy state, it emits a photon with energy equal to the difference between the energies of the two states, corresponding to a radio wavelength of 21 cm.

The 21 cm line hyperfine transition possesses a spontaneous radiative transition probability of only 2.9×10^{-15} s^{-1} (Tielens 2005), making it highly forbidden. Since a single, isolated atom of HI would be likely to undergo this transition once in ten million years, it would be virtually undetectable under test conditions. Fortunately, the vast population of HI atoms in the Milky Way more than compensates for the low transition probability, and

[1] Warm is a relative term. 100 K is considered hot in radio astronomy, warm in infra-red, and extremely cold in X-ray.

allows the 21 cm emission line to be easily observed and measured by radio telescopes.

2.1.1 The Effects of Absorption

For extraterrestrial soft X-rays, the dominant interaction with matter is photoelectric absorption (McCammon & Sanders 1990), in which atoms absorb X-ray photons. The ability of any given atom to absorb X-rays will steadily decrease as the energy of the incident photons increases. However, this general trend is interrupted by a sharp rise in absorption when the photon energy equals the binding energy of an electron shell (K, L or M for example). This is the minimum energy at which an electron can be removed from the atom, creating a vacancy in a shell, and is referred to as an 'edge' or 'critical excitation' energy.

Characteristic X-ray lines are generated when an 'initial' vacancy in an inner shell, created by X-ray or electron excitation, is filled by transfer of an electron from another shell, leaving a 'final' vacancy in that shell; the energy of the line is equal to the difference in binding energies of the shells with the 'initial' and 'final' vacancies.

The total photoelectric absorption along a line of sight arises as a result of the combined absorption cross-section of all the atomic species in the ISM, the value of which increases in regions with higher densities of atomic material. The photoelectric cross-section is also a function of energy, scaling approximately as $E^{-\frac{8}{3}}$ (Snowden et al. 1997).

Although photoelectric absorption of X-rays is unaffected by the molecular state of a gaseous medium, it is changed by its ionisation state. Ionisation of atomic hydrogen reduces its cross-section to zero, and single ionisation of helium and molecular hydrogen can reduce their absorption cross-sections by a factor of $\sim$2.

For this reason, when the photoabsorption cross-section of an element is calculated, it assumed that the element is in the form of a neutral atomised gas at solar abundance.

If the atoms are clumped into grains, the attenuation of radiation is reduced because atoms within the grain are blanketed. This effect is particularly noticeable in the soft X-ray band (Fireman 1974). The WABS absorption code, which will be used in Chapter 4 to

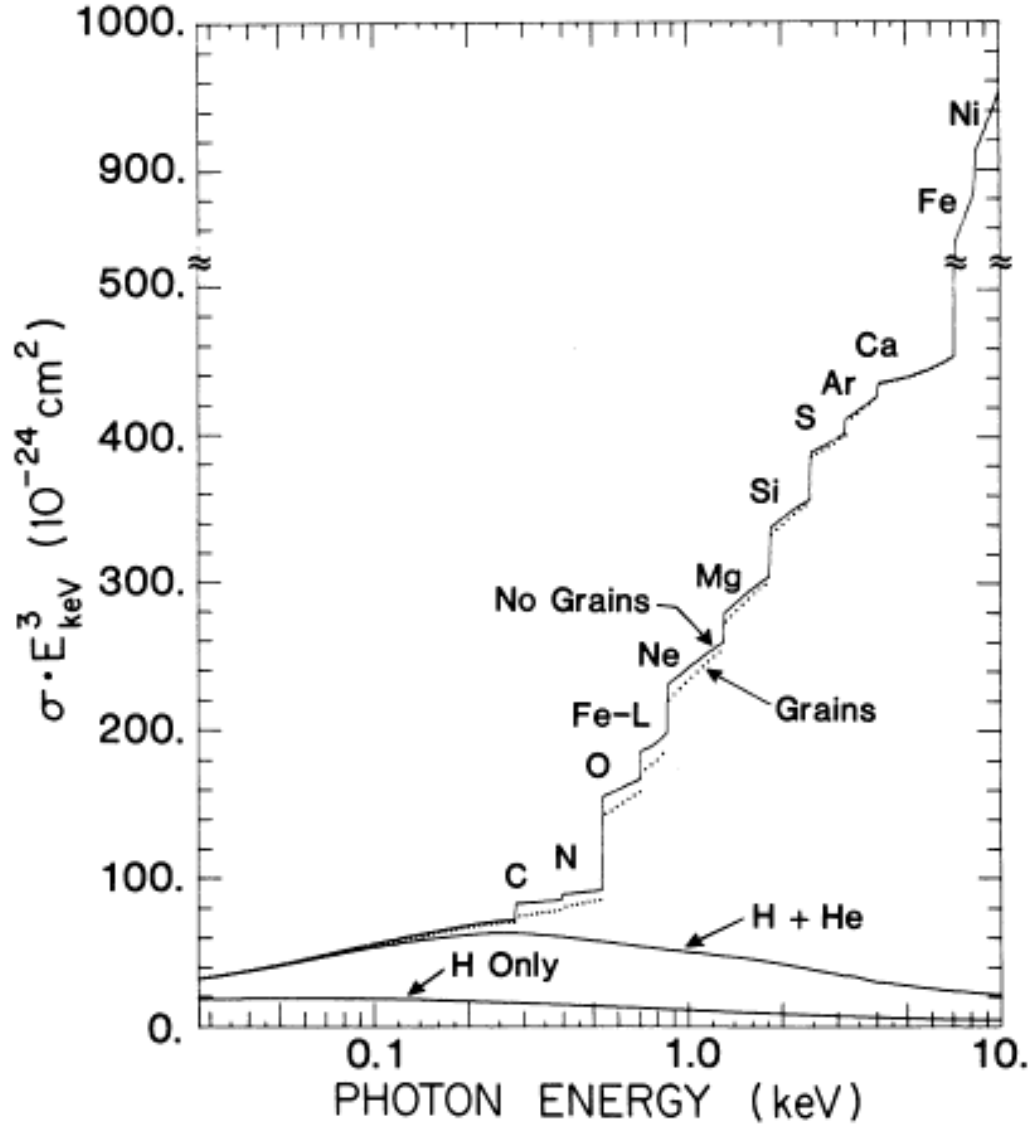

Figure 2.2: Figure taken from Morrison & McCammon (1983) showing the net photo-electic absorption cross-section per hydrogen atom as a function of energy, scaled by $(E/1keV)^3$ for clarity of presentation. The solid line is for solar abundances (as defined in their paper), with all elements in the gas phase and in neutral atomic form. The dotted line shows the effect of condensing the fraction of each element into 0.3 micrometre grains. The contributions of hydrogen, and hydrogen plus helium to the total cross-section are also shown.

fit spectra of the SXRB, does not contain any information about grains. Consequently, the absorption values it produces represent lower limits to the actual amount of absorbing material present.

Both the column density and energy dependency of the photoelectric cross-section impose an artificially close horizon on observations of the SXRB, but this can be used to the astronomer's advantage. By observing at different photon energies, it is possible to probe to different distances in the Galaxy, and so infer information that would not otherwise be apparent. For example, Snowden et al. (1997) calculated that for an average Galactic Disk space density of 0.5 atoms cm^{-3}, unity optical depth in the $\frac{1}{4}$ keV band (0.1 − 0.4 keV), would be attained when the total column density of HI is 1×10^{20} H cm^{-2}, giving a mean free path of 65 pc. Following the discovery by Frisch & York (1983) of an optically thick wall of HI only 50 pc away in the Galactic Centre direction (the Wall, see Section 2.7), Snowden et al. (1997) reasoned that most of the soft $\frac{1}{4}$ keV emission observed in that direction must be of local origin. Sanders (2001) went further, and asserted that the ISM is opaque to $\frac{1}{4}$ keV emission at Galactic latitudes less than 30° from the Plane: hence, the X-ray background at low latitudes must be Galactic in origin, and must originate relatively near to the Sun.

The hydrogen column can also be used to estimate depth in the otherwise two-dimensional X-ray sky. Most of the early studies of the X-ray background were concerned with shadowing experiments (for example Frisch & York (1983), or the definitive catalogue by Snowden et al. (2000)) which were undertaken to determine if known objects −− the Moon, stars and galaxies −− lay in front or behind X-ray emissive regions. These observations were used to deduce the relative positions of X-ray emissive structures in the Galaxy along the line of sight but, due to the uneven distribution of HI, they could not determine the precise distance of X-ray sources from the Earth. The actual column depth required to produce a measured N_H can vary significantly. For example, an N_H of 10^{19} H atoms cm^{-2} could be produced by a column depth of $\sim$ 30 pc in the dense medium near the Galactic Plane, but would require $\sim$ 200 pc near the North Galactic Pole (Cox & Reynolds 1987).

Despite its diagnostic applications, absorption significantly hampers the study of the X-ray background. Since any detected X-ray flux will have been at least partially absorbed by HI, observers never have a complete picture of the emissive structures in the Galaxy,

and have to accept that some features will remain invisible regardless of technological advancement. Also, since soft X-rays are preferentially attenuated, absorption can cause the flux from a distant source to appear artificially hard, which can adversely influence the interpretation of derived spectra. Furthermore, absorption may make the flux from very different regions appear similar; for example, the spectrum of a nearby, weak, hard X-ray source may look identical to a much stronger, but more absorbed, distant source. In such situations, it is very difficult to split the spectrum into the individual source components, and even detailed modelling may not succeed.

2.1.2 Structure in the HI Distribution

Observation of the 21 cm line has unlocked a wealth of information about the interstellar medium. It enabled the gas dynamics of the interstellar medium to be derived, as the full width at half-maximum of the line is equivalent to the velocity (measured relative to the Earth, and along the line of sight) of the emissive cloud responsible for it. The density and temperature distribution of HI were also determined, since the height of the emission line indicates the kinetic temperature of the gas, and its intensity depends on the amount of atomic hydrogen lying along the line of sight. So, for the optically thin clouds of the ISM moving at a given velocity, the brightness temperature integrated over the whole emission line provides a measure of n_H, the column density of the neutral atomic hydrogen at that velocity along the line of sight (Dickey & Lockman 1990, Burke & Graham-Smith 2002). The total number density of neutral hydrogen atoms, measured along an unhindered line of sight from Earth through the Galaxy is called the 'Galactic N_H', or 'Galactic Column'.

The Lockman Hole (Lockman et al. 1986), which lies in the constellation of Ursa Major at (l, b) = (152°,+62°), has the distinction of having the lowest measured N_H ($4.4 \pm 0.5 \times 10^{19}$ cm^{-2}) in the Milky Way. The column density in this direction is so low that soft X-rays can pass through unhindered, allowing flux from the most distant sources to be seen. Another notable location at which one may observe out to a few hundred parsecs is the extravagantly named 'Region of Bizarre Emptiness' which, considering its position near the Galactic Plane at 230° latitude (Cox 1997), contains surprisingly little HI.

The co-ordinates of the highest N_H concentration cannot be confirmed due to the effects

of opacity, since the 21 cm radiation from the emissive HI clouds is attenuated by self-shielding (Cox & Reynolds 1987), but the highest value measured within the Galaxy so far is $\sim 2.6 \times 10^{22}$ cm^{-2}, at a position on the Galactic Plane (Dickey & Lockman 1990). Soft X-rays emitted behind a column of this density would be virtually undetectable from the Earth (Henry et al. 1968).

Several radio surveys of the HI sky have been undertaken (for a review, see Burton (1988)), but to date, only the regions near the Galactic Plane have been mapped to an angular resolution of $\sim 10'$. Even so, structure may be perceived in the distribution of the HI gas. Generally, the neutral hydrogen lies in an approximately uniform disk centred on the Galactic Plane, with the highest concentration of HI present at low latitudes, and progressively lower concentrations located toward the Galactic poles where the Galactic N_H is reduced to $\sim 10^{20}$ cm^{-2} (Dickey & Lockman 1990). On smaller scales, there is substantial variation in N_H at all latitudes, and structure can clearly be observed. The most prominent atomic hydrogen structures are the interstellar clouds, planar sheets, and arcs, which are sometimes arranged in circular shells. Filamentary regions of enhanced N_H, which are often detected as arching ridges of radio emission, have been associated with known structures such as the North Polar Spur and Loop I, which will be discussed in detail below. The prevalence of HI structures within the ISM led Dickey & Lockman (1990) to suggest that the general N_H distribution may be more akin to a filamentary construct, or to a series of gas sheets, than the hazy cloud that is often assumed.

2.2 Shells, Loops and Bubbles

The terms 'loop', 'ridge' and 'arc' were coined by astronomers in order to describe features present in their radio maps. These features are of course the two-dimensional projections of three-dimensional structures; what appears to be a 'loop' on a map is really spherical, and the 'ridges' and 'arcs' are the brightened limbs of these structures: supernova remnants (SNRs) and wind-blown bubbles.

In the simplest case, a SNR is formed when a star reaches the end of its time on the main sequence, and explodes in a supernova event. Huge quantities of energy are released, blowing the star's outer layers away, and creating a dense shell of hot plasma. This

expands rapidly, sweeping up the cool interstellar material ahead of it. Shock fronts form at the leading edge of the shell, transferring the energy of the explosion to the ISM. This not only heats it to several million Kelvin, triggering X-ray and radio continuum emission (Dickey & Lockman 1990), but also serves to slow the expansion of the shell through friction. Often the situation may be more complex, with a shell being formed by the combined effect of multiple supernovae acting in concert (Dickey & Lockman 1990). In either case, with no further energy input the shell will eventually cool to ambient temperature and dissipate back into the ISM, but as long as it persists, it is described as a supernova remnant. Examples of known SNRs include the Lupus Loop (330°,+15°), the Cygnus Loop (71°,−9°) and the Vela-Puppis remnant at (265°,−5°) (Garmire et al. 1992).

Alternatively, a bubble of X-ray emitting plasma, similar to the shell created by a supernova, may be formed by the energy and accumulated momentum of stellar winds (Weaver et al. 1977). Bubbles vary in diameter from $50 - 150$ pc, overlapping the size range of the SNRs, and usually have O-B associations near their centre. The winds linked with these young stellar groups provide the energy required to produce the bubble, some $10 - 100 \times 10^{51}$ ergs (McCray & Kafatos 1987). There are many examples of wind-blown bubbles within the Milky Way, including the Gemini-Monoceros Ring (200°,10°; Nousek et al. (1981)) and the Eridanus Enhancement (200°, −40°; Burrows et al. (1991)). Examples of a SNR and a planetary nebula are shown in Figure 2.3. The planetary nebula is included here to illustrate the appearance of a shocked bubble of plasma; assuming symmetry, material would have been thrown in all directions from the surface of the progenitor star, producing a shocked shell of bright material of approximately even thickness. However, due to the low density of this material, it is can only be clearly seen when viewed at the limb, giving the appearance of a ring. When viewed face-on, through the centre of the structure, this material can only just be discerned.

Over several million years, the shock-fronts of a shell or bubble would continue expand to a radius of around 100 pc (Egger & Aschenbach 1995), making it an ever more significant and extensive part of the X-ray emissive ISM. Doppler measurements show that the expansion velocity of such a bubble would be $\sim$ 25 km s^{-1}, although this value does decrease as the size of the bubble increases. The oldest shells, which have had time to expand to several hundred parsecs, have expansion velocities closer to 3 km s^{-1} (Dickey & Lockman 1990).

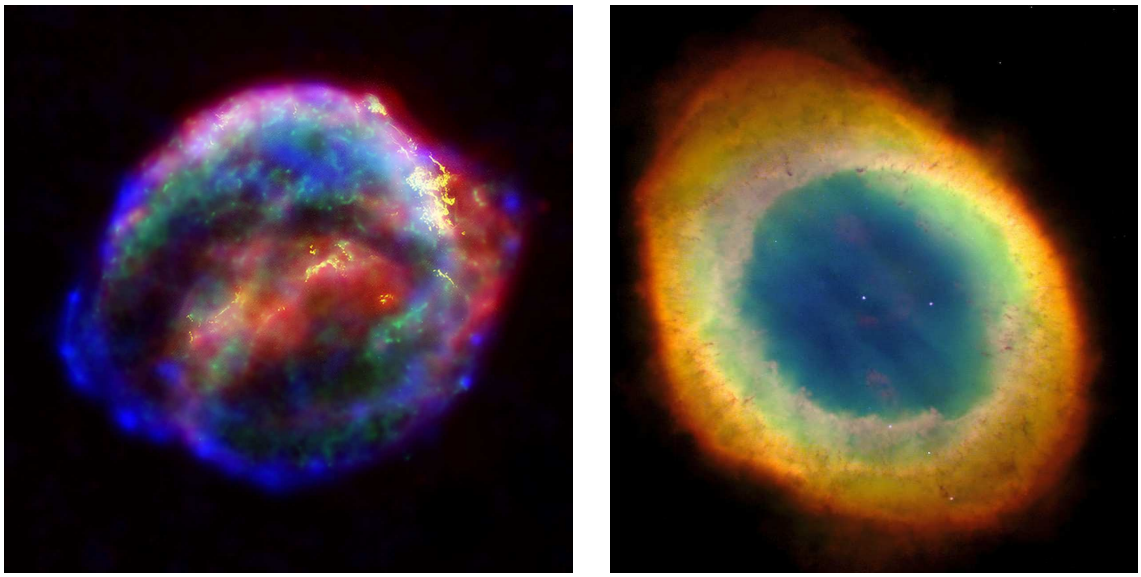

Figure 2.3: A supernova remnant and a planetary nebula, both displaying limb-brightened shells and diffuse, gaseous interiors. Left: A composite image of Kepler's SNR, taken by the Hubble Space Telescope, the Spitzer Space Telescope, and the Chandra X-ray Observatory. Right: The Ring Nebula, a planetary nebula, imaged by the Hubble Space Telescope. A planetary nebula is created when a medium or low mass star exhausts its reserves of hydrogen. When this occurs, the star evolves into a red giant; its inner layers contract under gravity, increasing the density of the core and enabling fusion to continue, while its cooler outer layers expand. Further internal temperature instabilities, arising from the fusion reactions, cause the outer atmosphere to be expelled by hot stellar winds either continuously or in several energetic pulses. This expanding gaseous shell forms the spherical nebula, brightly illuminated by ultraviolet energy from the central star. (Photocredits: STSci)

Occasionally, both mechanisms come into play: a SNR shell may be reheated and inflated by stellar winds, or a wind-blown bubble could be shocked and energized from within by multiple supernova events. In such circumstances a superbubble, larger than the product of any single event, may be produced.

2.3 The Diffuse X-Ray Background

The diffuse X-ray background was discovered serendipitously: evidence for it emerged from the same data that revealed the X-ray source Sco X-1, gathered by Ricardo Giaconni

and others in 1962 using rocket-borne instruments (Section 1.1). Hidden in the low-resolution data, and almost masked by the brighter point sources, lay a few bright Galactic sources superposed upon a featureless, high-energy X-ray background. The detection caused much excitement within the X-ray community. Many hoped that, like the microwave background found later by Penzias and Wilson (1965), it could provide information about the early Universe. Although this was not to be, by revealing the mechanisms through which the ISM is recycled from one generation of stars to the next, the diffuse X-ray background would eventually provide vital clues to the evolution and development of our own Galaxy.

2.3.1 The Extragalactic Background (XRB)

The ROSAT All-Sky Survey (Snowden et al. 1995) has, to date, provided the best image of Giaconni's signal: the 1.5 keV band map clearly shows an isotropic background with discrete Galactic enhancements superposed, together with a distribution of discrete sources in the Galactic Plane and at high Galactic latitudes (Figure 2.4). The background was shown to be isotropic and diffuse to within a 10% tolerance (Sanders et al. 1977). The low end of the high-energy XRB has been detected in spectroscopic studies between $2 - 6$ keV, an energy range at which the Galaxy is almost entirely transparent to X-radiation (McCammon et al. 1983).

Both the wide distribution of the background and its high energy were suggestive of an extragalactic origin, leading Henry et al. (1968) and others to surmise that it was the integrated sum of many unresolved X-ray sources lying at cosmological distances. Many of the distant sources in the 1.5 keV map of the ROSAT All Sky Survey have been resolved, and identified as quasars and other active galactic nuclei. This non-thermal, 'hard' X-ray signal, which originates beyond the limits of the Milky Way, will hereafter be referred to as the Extragalactic Background, or XRB.

When extrapolated to the low energies of the $\frac{1}{4}$ keV band, the expected intensity of the diffuse XRB is significantly lower than that of the total diffuse background in all directions, leaving a soft excess. This was first recognised by Henry et al. (1968), who reasoned that it must be a 'Soft X-Ray Background' (SXRB), independent of the XRB.

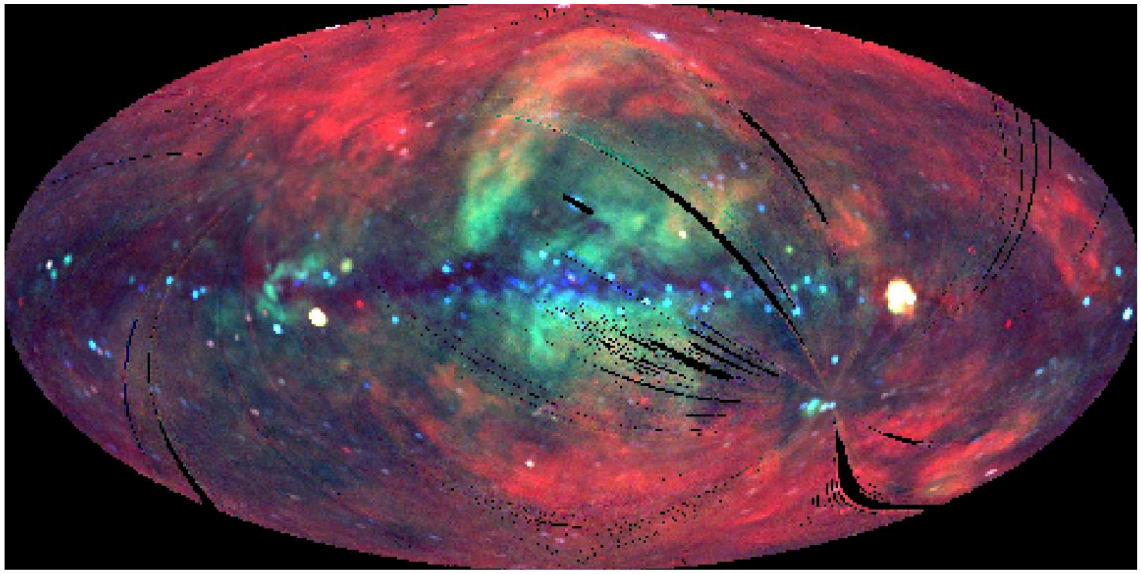

Figure 2.4: The 1.5keV RASS (ROSAT All-Sky Survey) Map by Snowden et al. (1995). The map has been false-coloured with respect to X-ray photon energy. Highest energies are white, purple and blue; lowest are red and black.

2.4 The SXRB and the Local $\frac{1}{4}$ keV Emission

The first observations of the SXRB were made with rocket-borne mechanically-collimated proportional counters, each of which had a very wide field of view, covering $10-50$ square degrees[2]. Because the exposure times were restricted to the few minutes at the peak of the rocket's trajectory, these early missions produced poorly resolved, photon limited data. Despite this, survey maps produced from this data revealed the vast complexity of the SXRB. Contributions from some identifiable objects, such as diffuse supernova remnants and isolated and discrete Galactic Plane sources were plainly apparent (Tanaka & Bleeker 1977), but these were superposed on a mysterious $\frac{1}{4}$ keV X-ray haze of unknown origin which covered the entire sky.

On the basis of rocket data gathered in 1968, Henry et al. (1968) tentatively suggested that the SXRB could be the thermal emission from a previously unseen hot intergalactic gas, at a temperature of $3 - 8 \times 10^8$ K (Henry et al. 1968).

[2]For comparison, the full Moon has an apparent angular diameter of $\frac{1}{2}^\circ$.

To generate the amount of flux seen from the SXRB through thermal emission, extended regions of hot, dissociated gas at a kinetic temperature of $T > 10^6$ K (McCammon & Sanders 1990) are required. The energy needed to create these conditions is generated by stars, and released through localised supernova outbursts, stellar winds and ultra-violet radiation. This energy is then transferred to the ISM by heated particles of dust and gas molecules, which have a mean free path of the order 10^{13} m ($\sim 10^{-3}$ light years.) Because this distance is a little less than the typical extent of interstellar clouds and supernova remnants, it is possible to achieve thermal equilibrium within large volumes of the ISM (Tielens 2005). Consequently, when free electrons collide with the ions in the ISM, they can produce X-radiation by the thermal processes described in Section 1.2.1.

The thermal origin of SXRB flux was eventually put beyond doubt by Burstein et al. (1977) and McCammon et al. (1983), who were able to observe collisionally excited emission lines in its energy spectrum, but the nature of the medium was still uncertain: did the flux arise from a superposition of point sources, or was it truly diffuse?

Levine et al. (1977) argued that the SXRB was diffuse, and calculated that if it were not, then discrete Galactic sources with a space density akin to that of the most common stars would be required to produce it. This premise was supported by Rosner et al. (1981), Helfand & Caillault (1982) and Caillault et al. (1986) who predicted that normal stars of all types should contribute only a small fraction of the observed SXRB flux in the $\frac{1}{4}$ keV band, and no more than 20% of the harder $0.5 - 1$ keV flux. On the strength of their evidence, the diffuse nature of the SXRB was finally accepted (McCammon & Sanders 1990).

2.4.1 Distribution of the $\frac{1}{4}$ keV Emission

Unlike the XRB, the distribution of the $\frac{1}{4}$ keV emission was found to be highly anisotropic, with an X-ray intensity four times greater at the Galactic Poles than at the Plane (Sanders et al. 1977). There was also a distinct negative spatial correlation (hereafter called the 'anti-correlation', see Figure 2.5) between areas of X-ray emission and regions of high absorption which could not be explained by simple photoelectric absorption. This relationship was first recognised by Bowyer et al. (1968), and later confirmed by Marshall & Clark (1984), who used the SAS3 X-ray observatory to map the sky in the C-band

($\sim$ 0.13 $-$ 0.28 keV, Sanders et al. (1977)) at 3° angular resolution, and detected the anti-correlation on all angular scales.

Bunner et al. (1969), Henry et al. (1968) and Bowyer et al. (1968) were among the first to study the soft haze. At first, they believed that it could be an extension of the extragalactic background, or that it could be caused by coronal emission. A series of models were proposed to explain the origin of the supposed extragalactic source. A suggested interaction between cosmic rays and the microwave background, that could produce inverse Compton emission, was quickly rejected because it would produce a higher 100 MeV gamma ray flux than is observed (Kraushaar 2000). Non-thermal X-ray production mechanisms were also ruled out, as the electron flux required for inverse Compton scattering of starlight, would produce too much ionisation (Hayakawa 1973). Synchrotron radiation was also dismissed, because electrons with enough energy to produce soft X-rays through this process would lose half their energy within five thousand years, and with no obvious synchrotron source to replenish the emission, it would have faded away long ago (Williamson et al. 1974).

Eventually, a viable solution was proposed which could both accommodate the assumption that the flux originated beyond the Milky Way, and explain the anti-correlation: the 'absorbed-extragalactic model'.

2.4.2 The Absorbed-Extragalactic Model

The absorbed-extragalactic model was built on the premise that the $\frac{1}{4}$ keV emissions were an extension of the XRB signal to low energies. Absorption of this extragalactic radiation by the intervening Galactic HI was proposed as the primary cause of the anti-correlation (Bowyer et al. (1968), Henry et al. (1968) and others), while the small-scale intensity fluctuations in surface brightness were attributed to variations in the degree of absorption, caused by differing column densities of HI along the line of sight (McCammon & Sanders 1990).

There are several problems with this model, some of which were highlighted by McCammon et al. (1983). Firstly, around $\sim$ 30% of the flux from the direction of the Plane appears to suffer little or no absorption. Indeed, the opacity of the HI to soft X-rays is so

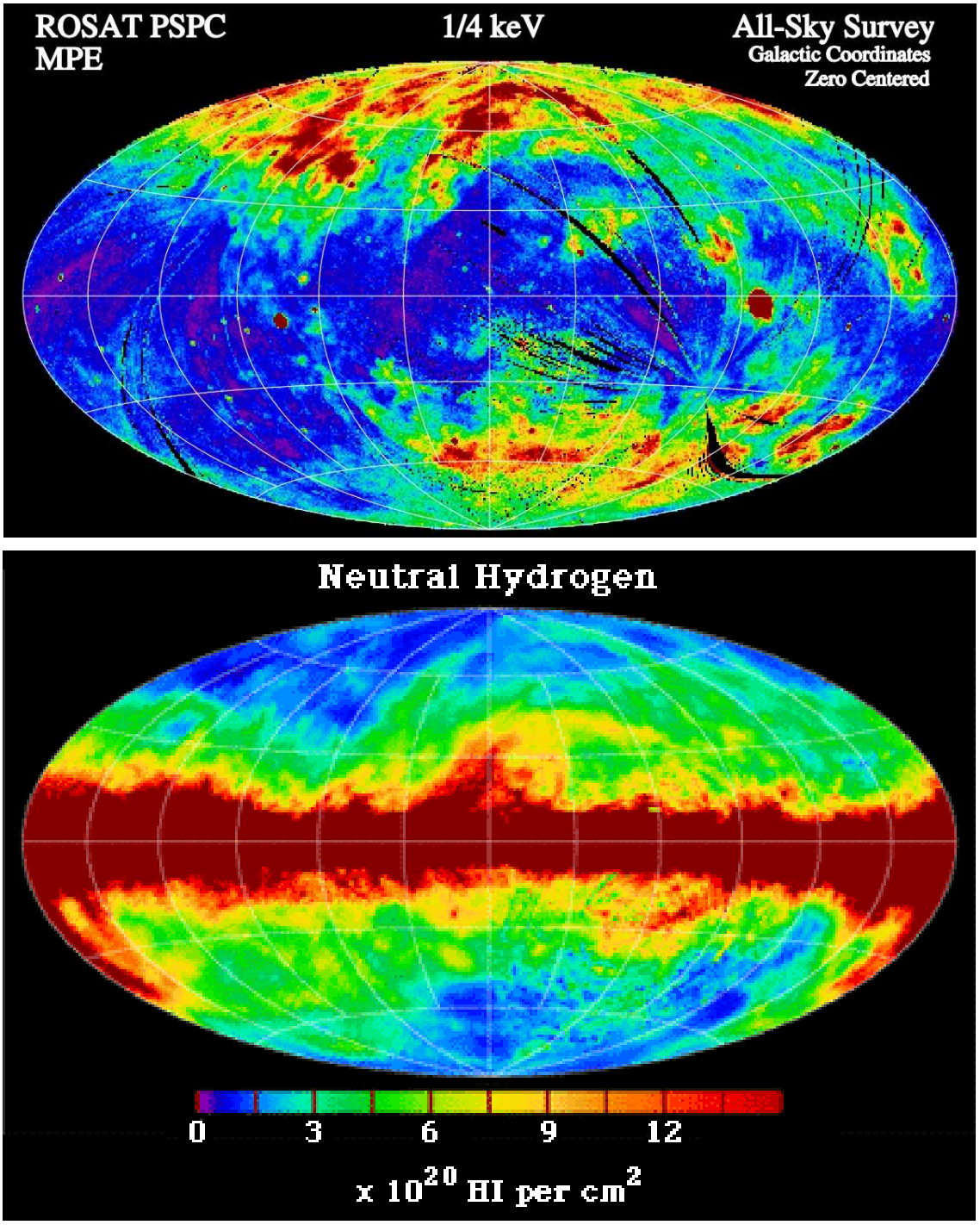

Figure 2.5: The Anti-correlation between the HI distribution and the $\frac{1}{4}$ keV emission. Top: The $\frac{1}{4}$ keV RASS map by Snowden et al. (1995) showing the distribution of the soft X-ray emission in the $0.1 - 0.4$ keV energy band. The map has been false-coloured with respect to X-ray intensity. Lowest intensities are blue; highest are red. Bottom: The distribution of HI, mapped by Dickey & Lockman (1990)

high near the Galactic Plane that some variants of the model, which depended mainly on an extragalactic source, had to invoke an additional local component to provide the flux that is observed there (McCammon & Sanders 1990). Secondly, it was not possible to fit the measured spectra of the $\frac{1}{4}$ keV emissions with simple absorption models, suggesting that it was anisotropic, whereas a distant extragalactic source would be expected to produce uniform emission across the sky. Finally, observations of X-rays from the extragalactic Magellanic Clouds showed no evidence of absorption by Galactic HI (McCammon et al. 1976).

McCammon & Sanders (1990) add that although the extragalactic-absorption model did produce an anti-correlation, it was not the right anti-correlation: the predicted fall-off of soft X-ray intensity with increasing absorption was much steeper than that observed, and it predicted an energy dependence of the fall-off where none was seen. Nor could the model explain the large scatter in the correlation that was observed toward some Galactic absorption features (McCammon & Sanders 1990). In order to overcome these problems, the supporters of extragalactic absorption postulated that the ISM should be 'clumpy'.

If the Galactic HI were evenly distributed, then the absorption optical depth would be the theoretical cross-section multiplied by the observed column density. If, however, the ISM were 'clumped' into unresolved, partially optically-thick clouds ($n_H \sim 2.5 \times 10^{20}$ cm^{-2}, McCammon et al. (1983)), then its ability to absorb diffuse X-ray flux would be reduced (Snowden 2000). This is because the HI clouds would cover very little of the sky, absorbing incident X-rays, but leaving most of the flux unaffected[3].

The effects of clumping were tested by Griesen (1973), who successfully demonstrated that it could, in theory, explain the anti-correlation near the Plane where the HI column density is high. The clumped model was ultimately rejected, however, after follow-up measurements by Dickey et al. (1977) found that it did not work at high latitudes, where even the high resolution Arecibo radio dish failed to detect the small cloudlets required.

[3] Snowden (2000) notes that once such a cloud is optically thick, it would not absorb more X-rays if more material were added to it. However, since this would remove more material from the ISM, it would allow more X-rays to pass between the clouds. Therefore, the effective absorption would become energy independent once the clouds are optically thick.

2.4.3 The Intermixed Model

The second attempt to explain the observed anti-correlation was the 'intermixed'[4] model, initially proposed by Davidsen et al. (1972), which required X-ray emitting plasma and absorbing material to be combined haphazardly within the Galactic Disk. The model was later given a theoretical underpinning by McKee & Ostriker (1977), who stated that the spatial structure of the primordial, diffuse HI in the disk would be strongly modified through interaction with supernovae. They went on to suggest that the energy input of the SNRs would process the ISM into a hot inter-cloud medium, compressing the embedded cool, neutral material into clouds with relatively dense cores and diffuse envelopes.

The intermixed model managed to explain the anti-correlation through a complex arrangement of scale heights and mid-plane densities of HI, but it could not reproduce it at high angular resolution (Snowden et al. 1998). It also required significant clumping within the ISM, and a greater scale height for the emitting X-ray plasma than that of the absorbing gas (Jakobsen & Kahn 1986), neither of which was observed by Burrows (1989) in his measurements of the SXRB.

Although the intermixed model was not perfect, its basic premise, that the $\frac{1}{4}$ keV emissions had a Galactic source, was confirmed in the late 1970s by a series of shadowing experiments. These had been designed to detect blocking of the SXRB by extragalactic objects, but very few instances were found, indicating that most of the measured $\frac{1}{4}$ keV flux ($\sim$ 75% McCammon et al. (1976), $\sim$ 90% Long et al. (1976)) had a local (Galactic) origin.

Even though the intermixed model was not ultimately accepted, its suggestion of a Galactic source for the $\frac{1}{4}$ keV emission laid the foundation for the third, and most successful, attempt to explain the soft X-ray haze: the displacement model.

[4] Sometimes called 'Interspersed'

2.4.4 The Displacement Model

As Cox & Reynolds (1987) noted in their excellent review, *"Although it has always been difficult to detect interstellar matter, the absence of detection was stared at for quite a long time before it inverted, into the detection of an absence."*

The 'inversion' occurred in 1977 when X-ray observations, conducted by Sanders et al., revealed that there was little neutral hydrogen, less than 1×10^{20} atoms cm^{-2}, lying between the Sun and the emissive regions surrounding it. Further analysis of the results showed that despite the anti-correlation, and even in directions of high absorption, the intensity of the soft X-ray flux did not fall below one-third of the maximum values observed in directions of low absorption. This strongly implied that the bulk of the soft flux had a local origin, in front of the neutral material in the Galactic Disk. In a response to these results, Sanders et al. (1977) and Tanaka & Bleeker (1977) developed the displacement model.

The premise of the displacement model is that X-ray emissive plasma is present in regions where neutral material is absent. The anti-correlation was attributed to the displacement of the HI by the presence of hot, emissive plasma, while small-scale variations in the observed X-ray intensity were put down to the varying extents of the absorption and emission volumes along the sight (McCammon & Sanders 1990).

The theoretical details of the displacement model were formulated by Cox & Smith (1974). According to their description, supernova remnants within the Galactic Disk would expand until they intersected with older bubbles. The cavities thus produced would then be re-energized as younger remnants expanded into them, leading to the formation of hot, interconnecting plasma tunnels within a sponge-like ISM, where the cooler, absorbing material formed the matrix. The observed anti-correlation arose naturally from this explanation: because the remnants would be expected to expand more into less dense regions of neutral material, they would produce brighter X-ray regions at higher latitudes (Snowden 2000).

As Snowden (2000) noted in his retrospective on the ISM, the displacement model shed a new light on the isolated, hot plasma structures seen in the maps of the SXRB. Rather than seeing the hot plasma as a ubiquitous substrate in the Galaxy, as in the intermixed

model, displacement allowed it to be seen as a perturbation within a cooler ISM. This, in turn, allowed for a less forced interpretation of the anti-correlation, and removed the need for clumping in the HI distribution which had been required by both the intermixed and extra-galactic absorption models. The success of displacement was such that by the late 1980s, it was the most widely accepted of the three models of the $\frac{1}{4}$ keV flux (McCammon & Sanders 1990).

2.5 The Local Hot Bubble

In 1983, interstellar absorption line studies by Frisch & York (1983) revealed the presence of an irregularly shaped hole in the neutral material surrounding the Sun. The lack of HI in this cavity was also measured by Sanders et al. (1977), who reasoned that it must be filled with soft, X-ray emitting plasma in accordance with the displacement model. Cox & Reynolds (1987) assumed this cavity to be the source of the local $\frac{1}{4}$ keV emissions, and named it the Local Hot Bubble (LHB).

Since the emission from the LHB suffers minimal absorption, Cox & Reynolds (1987) deduced that it must lie inside the 'local' ISM (LISM), which they defined as all neutral material within a column containing the nearest 10^{19} H atoms cm^{-2}. The extent of the LISM varies greatly; from $\sim$ 30 pc in the dense Galactic Plane, to as much as 200 pc within 20° of the North Galactic Pole (Cox & Reynolds 1987). These measurements indicate that the vertical extent of the LHB is similar to the scale height of the HI layer, and so imply that the high latitude HI sky must have been substantially disturbed during the creation of the LHB (Dickey & Lockman 1990).

In some directions, the column density of HI jumps to high levels just beyond the limit of the X-ray emission of the LHB, and appears to form a boundary wall (Frisch & York 1983). At the poles, however, the n_H remains low beyond the measurable extent of the emitting gas, indicating that the bubble may be open-ended. In 1997, Snowden (1986) traced the boundary wall of the LHB by mapping the extent of the emission, and found that it was shaped like a bent hourglass; wasp-waisted in the Plane, and elongated in the Polar Regions.

The unusual shape of the LHB reignited the debate over the correct model for the $\frac{1}{4}$ keV

emissions; as Cox & Reynolds (1987) noted, the strong anti-correlation observed in the flux of the LHB, and hence its observed shape, was consistent with the absorption of a distant source, as previously suggested by the absorbed-extragalactic model. At present, the consensus view is that the LHB emission is local, and limited in actual extent rather than by absorption (Bowyer et al. 1968, McCammon et al. 1983). In fact, because most of the soft emission comes from regions nearer to the Earth than the most local neutral clouds, absorption should have very little, if any, effect on the observed LHB.

The anti-correlation seen in the soft emission is elegantly explained by the displacement model, which stipulates that neutral hydrogen, which is normally present at high latitudes, must have been displaced by the emissive plasma of the LHB. According to the displacement model, the amount of hydrogen displaced will always be proportional to the volume of the hot plasma that impinges upon it. In the case of the LHB, the X-ray emission originates within the cavity, so the observed brightness should be proportional to its extent (assuming constant volume emissivity). Hence, the LHB appears to be dimmer at its narrowest point near the Galactic Plane, but brightest near the North Galactic Pole, where it extends for more than 200 pc (Cox & Reynolds 1987). The model's assumption of uniform conditions throughout the LHB also leads to a prediction of constant hardness in the observed spectrum (Snowden et al. 1997).

Although the displacement model worked well for the $\frac{1}{4}$ keV emission, and led to the identification of the LHB, it assumed that the bulk of the observed SXRB originated within the LHB (Snowden et al. 1998), and consequently neglected the other structures which make significant contributions to the total SXRB flux. These include Loop I, the Galactic Plane and the Galactic Halo, all of which will be described below.

2.5.1 Origin of the Local Hot Bubble

The origin of the LHB has proved to be an even more contentious subject than its morphology. In 1982, Cox & Anderson suggested that the LHB was a remnant bubble produced by one or more supernovae, but they had no direct evidence. A recent supernova would have almost certainly triggered the formation of early-type stars, but no such cluster exists within the LHB.

An alternative theory, put forward by Bochkarev (1987) and Frisch (1996), proposed that the LHB was not a bubble at all, but a region positioned between the Sagittarius and the Perseus spiral arms of the Galaxy. Stellar absorption line studies by Sfeir (1999) and Welsh et al. (1999) appeared to support this claim, by indicating that the LHB had a chimney-like structure with no definite border in the north at high Galactic latitudes, rather than having a complete shell. However, since the inter-arm model could not explain the shadow observed towards the Galactic Centre (Egger & Aschenbach 1995), now known to be produced by a wall of HI lying at the interface between the LHB and Loop 1, it was rejected, leaving supernova outburst as the dominant theory.

Cox & Reynolds (1987) quote spectral measurements of the LHB interior that show its temperature to be in the order of 10^6 K and its electron density to be $\sim 5 \times 10^3$ cm^{-3}, and then go on to suggest two possible mechanisms which could generate these conditions. In their first scenario, the creation of the LHB happened 10^7 years ago when a single supernova event reheated a pre-existing cavity within in the ISM, producing a bubble of diffuse, pressure-confined hot gas surrounded by a dense shell. Since this gas would have a 10^7 year lifetime against radiative losses at current ISM pressures, it could, in theory, produce the cooling remnant observed today. In practice, however, this idea does not work, since the LHB is open ended toward the Galactic Poles; an arrangement that would release the gas into the upper regions of the Galaxy rather than confining it.

In their second scenario, a recent supernova in the Solar Neighbourhood exploded 10^5 years ago reheating the hot gas in a pre-existing cavity. This event would create an active shockwave that would still bound the LHB, and maintain the temperature of its diffuse interior at 10^6 K, hot enough to generate the observed X-ray emission. Although this mechanism seemed more probable than the first, it still lacked one vital piece of information: the identity of the exploding star.

Gehrels & Chen (1993) were the first to propose that Geminga, a millisecond pulsar with high proper motion, could be the remains of the LHB progenitor. The product of a nearby supernova which occurred $3.2 - 3.7 \times 10^5$ years ago (Bignami & Caraveo 1992), Geminga is the right age. If the Geminga was generated by the same event that created the LHB, then the pulsar should have been in the solar neighbourhood at the time of the supernova (Garmire et al. 1992). Unfortunately, the parallactic distance to Geminga was found to be 160 pc (Caraveo et al. 1996), and when its trajectory was extrapolated back,

it was found to be in the Orion Region at the critical moment, well outside the region of the LHB (Berghöfer & Breitschwerdt 2002). At the present time, the identity of the star that produced the LHB remains unknown.

X-ray studies by Welsh et al. (1998) indicated that the LHB cavity is not homogeneously filled with X-ray plasma, and that a non-negligible part of the LHB material must exist in a cooler phase, at around 10^4 K. This implies that the LHB was not formed by one supernova, but by a series of explosions, since the expanding shell of a pressure driven by a single SNR would have been entirely filled with hot plasma. More recent one-dimensional hydrodynamic simulations by Smith & Cox (2001) support the idea of multiple supernova events: they estimated that $2 - 3$ supernovae events within a warm, ionised medium would be required to create the LHB. Such explosions, possibly caused by O-B stars within the Galactic disk, could have provided the low energy input rate and high ambient pressure needed to produce the X-ray spectra observed today. Berghöfer & Breitschwerdt (2002) add that since the energy input of the previous supernovae appears to have largely been used up in the expansion and radiative cooling of the bubble, the emergent X-ray emission presently observed must be largely due to the energy input of the last supernova.

Further evidence of a supernova origin comes from a most unlikely source: analysis of ferro-manganese samples from deep within the ocean crust by Knie et al. (1999) showed an increased flux rate of ^{60}Fe. This rare isotope does not occur naturally on Earth, but could have been transported to the Earth as ejecta from at least one supernova exploding about 30 pc away, within the LHB region. This finding has tremendous implications, not only for the SXRB, but for the development of life as we know it. A supernova explosion within the Solar neighbourhood around five million years ago (as indicated by the depth of the crust sample) would have coincided with the Pliocene Epoch of the Earth's history; flooding the world with ionising radiation as the primitive apes evolved into early humans.

2.6 Loop I

Quigley & Haslam (1965) were the first to realise that groups of prominent radio ridges could be connected by circular arcs, forming complete circles. The largest of these,

Loop I, is centred at l = 329° ± 1.5°, b = +17.5° ± 3° and has a diameter of 116 ± 4° (as measured by Large et al. (1966), Egger & Aschenbach (1995) and de Geus et al. (1989). It is the closest active superbubble to the Sun, with its foremost boundary wall positioned beyond the limit of the LHB (Snowden 2000). With an angular diameter of 110° (McCammon et al. 1983) it is the largest radio feature visible from Earth, covering around a quarter of the all-sky map, and dominating the spatial structure towards the central region of the Galaxy (Cox & Reynolds 1987).

Loop I is clearly observable through the 21 cm radio signal emanating from its HI shell, but its presence can also be detected in the soft X-ray band. A considerable amount of soft X-ray emission can be found at low latitudes either side of the Galactic Plane. Since this emission lies inside the projected boundary of Loop I, it is generally thought to come from the hot, rarefied plasma within the bubble (McCammon et al. 1983, Garmire et al. 1992). Unfortunately, the strongest, hardest flux detected within the boundary of Loop I is coincident with the projected position of the Galactic Centre (l = 355°) (Snowden 2000). It is therefore possible to conclude that a proportion of the X-ray flux measured in this direction originates either within the Galactic Bulge (Snowden et al. 1997), or from some unknown source at the Galactic Centre itself (Snowden 2000). As a result, the quantity of flux assigned to either the Galactic Centre or Loop I during spectral analysis can have a major influence on interpretations of the SXRB.

The softer X-ray emission coming from Loop I is predominantly confined to three bright patches of emission visible on the RASS $\frac{3}{4}$ keV map (Figure 2.7). Two of these X-ray enhanced regions align with the inner edge of the brightest radio ridge, the North Polar Spur, and the third is located just below the Galactic Plane; a position which suggests that it is associated with the two patches in the north. If, indeed, the three patches can be shown to be linked, that would indicate that that Loop I straddles the Galactic Plane, even though radio measurements have shown that the radio ridges do not extend into the southern hemisphere (Berkhuijsen et al. 1971).

The missing radio ridges indicate that outer super-shell of HI surrounding Loop I has been disrupted: damage which may have been caused by an off-centre explosion within the superbubble. In such an event, the shock-front would first have hit the part of the super-shell nearest to it, and only later impact further regions, resulting in an asymmetrical expansion (Egger & Aschenbach 1995). Berghöfer & Breitschwerdt (2002) argued,

however, that the shapes or boundaries of superbubbles would be determined predominantly by the density and pressure of the ambient medium, rather than on the location of individual supernova events with respect to the original centre of the cavity. They reasoned that since shockwaves are weak, they would propagate quickly within the rarefied hot medium of an established bubble, but move more slowly when traversing the higher density material beyond it, since this must be compressed before it can be swept away. In either case, the implication is that Loop I is not perfectly spherical, and may have been flattened or compressed at its southern edge, where a dense region of HI is located. The effects of uneven expansion can also be seen in the LHB, where the combination of weak shock fronts and a dense ambient medium have resulted in its current hourglass shape.

2.6.1 Origin of Loop I

Broadband spectral fitting by Egger (1998) using the ROSAT PSPC revealed that Loop I is considerably hotter than the LHB, with an average temperature of 2.5×10^6 K. It is also much younger than the LHB, although the extent is unclear: Sofue et al. (1974) measured the expansion velocity of the Loop's HI shell as ~ 19 km s^{-1}, indicating an age of 10^6 years, whereas Bunner et al. (1972) suggests an age of only 10^5 years, based on his spectral analysis of the bubble interior. The HI shell itself is almost circular, is ~ 100 pc in radius (Willingale et al. 2003), and has a limb brightened profile.

Both the size and structure of Loop I evince that it was created by a series of supernovae, rather than by stellar winds (Egger & Aschenbach 1995). This 'supernova hypothesis' requires a reasonable probability of supernovae occurring in concert within the Loop I region. Berkhuijsen et al. (1971) estimate that intra-galactic supernovae alone could produce a loop of 65 pc radius in a 7×10^5 year time-frame, with an expansion velocity of 35 km s^{-1}. Thus, ancient supernovae could produce a reasonable analogue of Loop I, providing that the expansion of their ejecta was not so fast that the HI shell was disrupted.

Aside from an enormous SNR, a series of discrete supernovae would have left behind evidence of their activities, in the form of neutron stars and star forming regions. This led Bertiau (1958) to suggest that the initial supernova probably occurred within the Sco-Cen association, a star-forming region circumscribed by Loop I, lying 210 pc from the Sun (Cox & Reynolds 1987). Blaauw (1961), on the other hand, argued that the

destruction of a single star from an O-B association may be responsible for the formation of Loop I.

When the primary star within an O-B association goes nova, the surviving secondary components are released from orbit and thrown into a free trajectory. Three of these vagabonds, known as 'runaway O-B stars', exist within 30 pc of the Sun, one of which, zeta-Ophiuchus, has a high velocity. Tracing back the proper motion of this star revealed that it would have been near to the current centre of Loop I around 3×10^6 years ago, placing it, and its lost primary star, at the right place and time to produce Loop I.

If Blaauw is right, then the primary star of the zeta-Ophiuchus system would have had to release around 100 $\mathrm{M}_\odot$ in a single event in order to produce the Loop and release the runaway star. Such an explosion would be a 'super-supernova', a rare Type III outburst defined by Zwicky (1964).

Although it is possible that Loop I was created in a single cataclysmic outburst, it is far more likely that it was formed through a series of smaller nova events, and then inflated to a large diameter by further supernovae and the stellar winds flowing from the Sco-Cen association (McCammon et al. 1983). Evidence for this can be seen in the bright radio ridge on the north-eastern limb of Loop I, known as the North Polar Spur. The NPS is thought to have formed around 2×10^5 years ago, when a shockwave from a recent supernova within the Sco-Cen association hit the already existing boundary wall of the Loop I superbubble, reheating it to $3 - 4 \times 10^6$ K, and triggering the X-ray and radio emission observed today (Egger & Aschenbach 1995).

2.7 Interaction of the LHB and Loop I

It is tempting when examining static images of the SXRB to presume that it is produced by a permanent, stationary structure, but this is not the case. Decades of observations, with ever increasing spatial resolution and statistical detail, have revealed that the SXRB is produced by a complex and dynamic combination of sources. Supernovae explode, stellar winds blow, and hot plasma bubbles expand, raising the possibility of interaction between the structures of the ISM.

Since the distance to Loop I is similar to the radius of the LHB, it is highly likely that the two structures will interact in the future, and there is considerable evidence that they may already have begun to do so.

In 1990, Snowden et al. found that the plasma in the LHB is warmer towards the Galactic Centre than in the anti-centre direction. This temperature gradient was interpreted as a thermal interaction, caused by a proposed open connection between the two bubbles, which could allow the hotter plasma of Loop I to leak into the LHB.

The possibilities of mechanical interaction were explored by Yoshioka & Ikeuchi (1990) using numerical simulations. By modelling colliding pairs of bubbles, they demonstrated that if one (or both) of the bubbles had reached the radiative stage of evolution prior to collision, then the bubble interiors would not merge. Instead, the expanding shock fronts would sweep up the ISM, forming a sheet of dust and gas $20 - 30$ times denser than the ambient medium between the two expanding shells.

The Wall is one such region: composed mainly of HI, it is found in the northern hemisphere, within 40° of the Plane, in the direction of the Galactic Centre (McCammon et al. 1983, Cox & Reynolds 1987).

In 1995, Egger & Aschenbach proposed that the Wall is an approximately annular volume of dense HI which could have formed through the collision of the LHB and Loop I. This idea was supported by Centurion & Vladilo (1991) who determined, through optical and UV spectral analysis of stars near the centre of Loop I, that the distance to the Wall is 40 ± 25 pc: a value that places it directly between the two bubbles. Further measurements by Snowden et al. (1997), in the direction towards the centre of Loop I, found that the distance to the edge of the LHB is greater than 15 pc, while the nearside of Loop I is less than 65 pc away, thus providing an upper limit for the thickness of the Wall.

The flux of the $\frac{1}{4}$ keV emissions is significantly reduced in the direction of the Wall, an effect which can be attributed to two factors. First the density of the Wall itself, at $\sim 10^{20}$ atoms cm^{-2} (Centurion & Vladilo 1991) is sufficiently optically thick to block most soft X-rays, and second, the decreased emissivity of the shock fronts of the remnants themselves, which have now decelerated and cooled below 10^5 K (Egger & Aschenbach 1995).

2.8 Galactic Plane Radiation

While conducting a radio survey of the NPS ridge, Berkhuijsen et al. (1971) found that otherwise clear signals became confused within 6° of the Galactic Plane. Although unable to identify the source of the interference, they designated it 'Galactic Plane Radiation' (GPR). Following its discovery, the GPR faded into obscurity until Worrall et al. (1982) observed an enhancement in the hard X-ray band, separate to the radio signal, but apparently emanating from the same structures - specifically the Galactic Bulge and the Galactic Ridge; a feature which runs along the centre of the Galactic Plane of scale height 250 pc and radial extent 10 kpc.

Measurements showed that the spectrum of the GPR was softer than the XRB, but harder than that of the LHB (Snowden et al. 1997), with the plasma temperature varying between 3 keV and 14 keV, depending on the direction of observation. Initially, this temperature range suggested to McCammon & Sanders (1990) that if discrete sources were responsible, their number could not be very large, otherwise the variations would be averaged out. Other measurements have indicated, however, that the emission is truly diffuse (Ebisawa et al. 2003). Furthermore, the spectroscopy performed using the ASCA observatory revealed a strong Fe-K emission line present at 6.7 keV, suggesting that the GPR was thermal in origin (Ebisawa et al. 2003).

Garmire & Nousek (1980) suggested that the GPR might be emission from a Galactic Wind that could be emanating from the Galactic Bulge. This idea is supported by Snowden et al. (1997), who went further, suggesting that the emissions may come from a region close to the Galactic Centre itself, a position that falls within the projected interior of Loop 1. They went on to demonstrate mathematically that the observed 0.5 – 2.0 keV enhancement in the southern hemisphere, within 10° of the Plane, would be consistent with an isothermal Galactic Bulge of temperature $10^{6.6}$ K, and a scale height of 1.9 kpc.

The latest research indicates that, at least at high energies (between 6 and 7 keV, more than 80% of the seemingly diffuse X-ray emission of the GPR can be resolved into discrete sources, probably accreting white dwarfs and coronally active stars (Revnivtsev et al. 2009).

2.9 The Galactic Halo and Outflow

Whilst using the Mt. Wilson 100 inch spectrometer, optical astronomers Münch & Zirin (1961) discovered a series of absorption features in the spectra of several high latitude stars, which they were later able to associate with a number of small, absorbing clouds of neutral gas. Under normal circumstances, nearby Galactic gas is virtually stationary with respect to its local frame of reference, moving only at the group velocity imposed by the differential rotation of the Galaxy. These interstellar clouds, however, were moving at up to 50 kms^{-1}, a property which prompted Münch and Zirin to name them the 'high velocity clouds' (HVCs).

Lyman Spitzer, who also worked at Mt. Wilson Observatory, soon learned of the discovery of the HVCs. He surmised that since they were some distance away from the Galactic Plane, they had to be pressurized by some as yet unmapped gaseous region located beyond the disk of the Milky Way. This gas would have to be highly ionised, and therefore very hot (around 3×10^6 K, Spitzer (1956)), or else it would have appeared as metal absorption lines in Münch and Zirin's stellar spectra. Spitzer proposed that, assuming hydrostatic equilibrium, this gas should be positioned several kiloparsecs above and below the disk of the Milky Way; far beyond the domain of Loop I and the LHB. Spitzer dubbed his hypothetical structure the 'Galactic Corona', since at the time, gas at such high temperatures was known to exist only in stellar coronae, and outlined these ideas in Spitzer (1956).

Evidence to support the Galactic Corona was not immediately forthcoming. It was never directly detected in the radio band, because its weak 21 cm flux blended with the signal from the Galactic Disk (Dickey & Lockman 1990), and it remained elusive following the advent of X-ray astronomy. Confusion over its definition did not help matters; the problem was exacerbated in the mid-1980's when the words 'halo' and 'corona' were used interchangeably. Marshall & Clark (1984) defined the 'halo' as the entire volume of diffuse X-ray emissive gas in and around the Milky Way, whereas Garmire et al. (1992) tentatively suggested that a 'halo', with a higher temperature than the LHB, might exist beyond the Galactic disk. Sidher et al. (1996) imagined a disk-like halo comprised of hot gas, energized by the interaction between magnetic fields and cosmic rays escaping from the Galaxy, while a multiphase Galactic corona was proposed in response to early X-ray

spectroscopy by Savage & de Boer (1981), Marshall (1981) and Bregman (1982).

The first positive identification of the Galactic Halo came from ROSAT. In 1995, the RASS $\frac{1}{4}$ keV map revealed excess soft emission coming from material at a scale height greater than 200 pc (Snowden et al. 1995), and in 1997 shadowing experiments were conducted with ROSAT at high Galactic latitudes, where the HI column is sufficiently rarefied to allow distant emissions to be observed (Snowden et al. 1997). Burrows & Mendenhall (1991) used ROSAT data to estimate that in some directions, between one-half and two-thirds of the $\frac{1}{4}$ keV emission originates in the Halo or beyond, although more recent studies (Bellm & Vaillancourt 2005) suggest that the Halo contribution to the total flux may be much smaller, at only $\sim 11\%$.

It is interesting to note that, owing to attenuation by the hydrogen column, the ROSAT shadowing experiments were unable to detect $\frac{1}{4}$ keV Halo emission in and around the Galactic Plane. Wang (1998) adds that even though $\frac{3}{4}$ keV emissions are more resistant to attenuation, any weak Halo flux coming from the Galactic Centre direction would be subsumed within the much stronger signal from Loop I and the Galactic Plane. Nevertheless, the interpretation of X-ray spectra found in Willingale et al. (2003), names the Halo as one of a series of interstellar structures making a contribution to the soft flux originating around the Galactic Plane, within the Loop I boundary.

Analysis of the RASS data by Snowden et al. (1998) showed that the Galactic Halo is brighter in the north Galactic Pole than the south, varying between $0 - 2600 \times 10^{-6}$ counts s^{-1} $arcmin^{-2}$ over the sky. The Halo emission was also found to vary more strongly toward lower latitudes in the south than those in the north, increasing from $500 - 1200 \times 10^{-6}$ counts s^{-1} $arcmin^{-2}$ at the Pole to a few hundred counts s^{-1} $arcmin^{-2}$ near the Plane. Further studies by Snowden (2000) revealed that the Halo is clumpy: an observation that indicated a low scale height, and placed the Halo above the neutral material in the Disk, between a few hundred parsecs to tens of kiloparsecs from the Galactic Plane. Finally, the distribution of the Halo, above and below the Plane, confirmed its association with the Galactic Disk and, by extension, the gravitational potential of the Galaxy.

2.9.1 Modelling the Halo

Snowden et al. (1998) were the first to model the Halo through spectral analysis using data gleaned from the RASS survey. Encountering difficulty when determining the temperature of the Halo, they proposed a two-temperature model. The first component represented the hotter, harder end of the observed soft excess at $\frac{3}{4}$ keV over the extrapolation of the XRB, similar to a hot, uniform, high-scale Corona model proposed earlier by Wang (1998). The second, a cooler, softer component at $\frac{1}{4}$ keV, had a more limited scale height. Snowden (2000) later suggested that this cool component could either be produced in situ by SNRs, or by outflows linked with the Galactic Disk, instances of which could cause the observed $\frac{1}{4}$ keV back-lighting of the Draco Nebula.

Circumstantial evidence for these two components came from the observed difference in angular structure between the variable, clumpy $\frac{1}{4}$ keV emission and the smooth intensity distribution at $\frac{3}{4}$ keV of the XRB flux outside of Loop I (Snowden et al. 1998).

Galactic Haloes have been observed around galaxies other than our own, most notably M101 (see Figure 2.6), the closest face-on analogue of the Milky Way (Bregman & Houck 1997). Kuntz et al. (2000) noted that although we would expect our Galaxy to have a halo similar to that around M101, the two-component models of Kuntz & Snowden (2000) and Wang (1998) predict the same total emission strength that would be expected for the XRB component alone. He concluded, therefore, that either our Galaxy has very little Halo, or that the two-component models over-predict the contribution from the LHB and Loop I.

2.9.2 Origin of the Halo

Most current theories suggest that an outflow of material from lower regions of the Galaxy may be responsible for the creation and maintenance of the Halo.

Both Dickey & Lockman (1990) and Snowden (2000) favour the idea of SNR breakout: in this paradigm the lower Halo, situated 500 pc above the Plane, contains a cool HI disk which regulates the evolution of the SNRs and superbubbles (Norman & Ikeuchi 1989). If the diameter of a superbubble becomes greater than the thickness of the disk, it may rise

Figure 2.6: M101: The closest face-on spiral galaxy, as imaged by the Hubble Space Telescope in visible light (left), and by the Chandra X-ray observatory (right).

out of the Plane and burst; spilling its contents into the halo via a network of 'chimneys' that run though the cooler, confining gas of the ISM. Berghöfer & Breitschwerdt (2002) suggests that since the LHB appears to be open toward the North Galactic Pole, part of its thermal energy may have already been transferred to the Galactic Halo through this process.

If this outflow occurs with sufficient force, then a 'Galactic Fountain' may be set up (Norman & Ikeuchi 1989), which could channel material up from the inner regions of the Galaxy and project it high above the Galactic Disk. Some of this material could then return to the disk under gravity, spreading out as it does so, and producing a diffuse Halo (Shapiro & Field 1976).

2.10 Mapping the SXRB

The earliest all-sky maps of the SXRB were painstakingly compiled, blurry affairs. One of the first, a 0.1 – 10 keV survey completed by McCammon et al. (1983), had a spatial resolution of only 7°, and required seven years of rocket-obtained data to produce. As

McCammon et al. (1983) noted despondently when struggling to interpret the fuzzy image, *"One is easily misled in attempting to draw conclusions from trends observed in a limited area."*

Twelve years later, the ROSAT observatory (Trümper 1983) radically changed our view of the SXRB. ROSAT's main instrument, the PSPC, was initially designed to detect discrete X-ray sources in the 0.1 – 2.4 keV range, but it was quickly realised that it would be ideally suited to studies of the X-ray background. With its large effective area, short focal length, low particle background and unprecedented signal to noise ratio, it was able to survey the entire sky in only 200 days. The collected data was used to produce the ROSAT All Sky Survey (RASS) maps (Snowden et al. 1995), which provided the first clear vision of the structures present within the SXRB of the Milky Way.

In total, Snowden et al. produced three maps over three energy bands: $\frac{1}{4}$ keV (0.1 – 0.4 keV), $\frac{3}{4}$ keV (0.5 – 0.9 keV) & 1.5 keV (0.9 – 2.0 keV) which are presented in Figures 2.4, 2.5, & 2.7 respectively. The maps each have an angular resolution of 2°, and cover 98% of the sky. They are presented in Aitoff equal area projection: a method which minimises distortion in the central portion of the map, and so allows the relative areas of features located there to be displayed correctly, although the map edges are highly distorted.

The 1.5 keV map, covering the high-energy end of the XRB, is dominated by the isotropic haze of the extragalactic X-ray background. A thin, dark line running along the Galactic Plane indicates the presence of absorbing neutral hydrogen. Extended plasma structures, such as the NPS, Loop I interior and the Galactic Centre enhancement can be seen as a confused patch of emission, with no clear separation of components: the positions of these structures are marked in Figure 2.7. Discrete Galactic sources are also apparent, as bright patches particularly within and around the Galactic Plane. Extragalactic sources, such as AGN and galaxy clusters, are faintly visible at higher latitudes, where the Galactic absorption is lower.

Since the Galactic disk is less transparent below 1 keV, the extragalactic background observed in the $\frac{3}{4}$ keV map is smoother than in the 1.5 keV map. Soft emission dominates the $\frac{3}{4}$ keV map, highlighting the Galactic structures; the NPS and Loop I interior appear as a circle, suggesting that they form a single structure (Garmire et al. 1992). Absorption

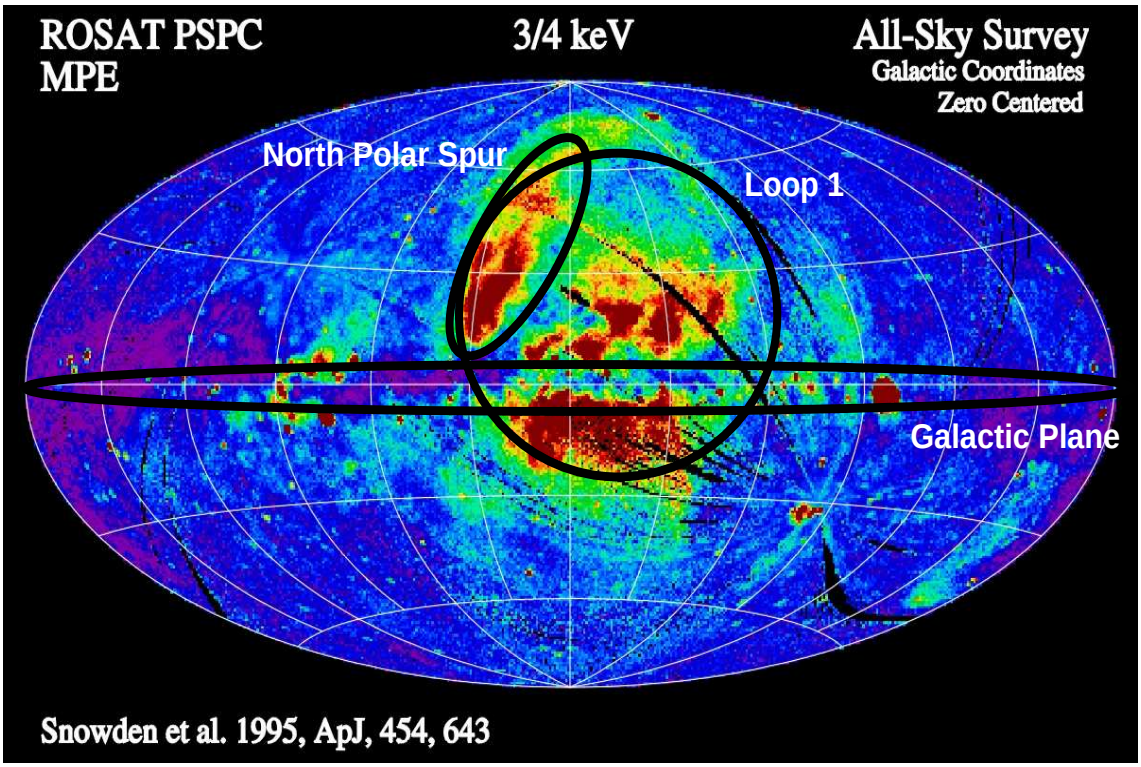

Figure 2.7: The RASS $\frac{3}{4}$ keV map in zero-centred, north-oriented Galactic co-ordinates, displayed using an Aitoff equal-area projection. The North Polar Spur, Loop I and Galactic Plane are shown in projection. The flux of the LHB, XRB and Halo are diffuse, and distributed over the whole sky. The map has been false-coloured with respect to X-ray intensity. The lowest intensities are blue, and the highest are red (Image credit: Snowden et al. (1995)).

is more pronounced in the soft X-ray bands, particularly along the Plane, where the absorption is wide, structured and easily visible.

The $\frac{1}{4}$ keV map shows structure over the whole sky with strong Galactic pole to pole variation (Snowden et al. 1995). It is dominated by the very soft emission of the LHB, showing bright, enhanced regions near the Galactic Poles. The anti-correlation between the HI distribution and the X-ray emission is plainly apparent. Neither the NPS nor Loop I is clearly visible in this map.

On the whole, the RASS maps present an impressive image of the distribution of X-ray emission within the Milky Way but, since they do not possess any spatial depth, they are potentially deceptive. For example, the bright, extended regions in the central region

appear superficially to be separate entities, perhaps arising from a series of discrete sources lying at different distances along the single line of sight, but after the RASS maps were published, it was suggested (by Snowden et al. (1995) and others) that both the NPS and the enhancements on either side of the Plane could be parts of a single emission source, possibly the interior of Loop I. However, prior to the development of high-resolution spectroscopy, this could not be confirmed.

2.11 Summary

The diffuse X-ray background (DXRB) of the Milky Way comprises a complex blend of thermal and non-thermal emission, produced by a wide variety of sources.

The non-thermal component of the DXRB emanates from distant quasars and AGN. This isotropic extragalactic background (XRB) provides most of the continuum energy in the DXRB spectrum in the $2 - 6$ keV range.

The soft X-ray background (SXRB) of the Milky Way constitutes the thermal component of the DXRB, and dominates in the $0.4 - 4.0$ keV band. The spectrum of the SXRB is an amalgamation of the X-ray signals generated by several hot, ionised plasma structures that exist within the ISM, including the Local Hot Bubble (LHB), Loop I, the Galactic Plane and the Galactic Halo.

Both the LHB and Loop I are thought to have been created by supernovae, and subsequently shaped by stellar winds. The LHB has an irregular hourglass profile, and is elongated towards the Galactic Poles. The Solar System is embedded within the LHB, the emission of which appears to be isotropic and unabsorbed. Loop I lies beyond the boundary of the LHB. It is younger and hotter than the LHB, and much larger, having apparently been inflated by stellar winds from the Sco-Cen association, which is 210 pc distant. A thick cloud of displaced HI, the Wall, which lies at the interface between the LHB and Loop I, is thought to indicate an interaction between the two bubbles. The dense Wall is almost opaque to soft X-rays, a property which must be carefully considered when interpreting any spectra of the X-ray background measured in its vicinity.

The Galactic Plane Radiation (GPR) is diffuse, thermal X-ray emission that manifests

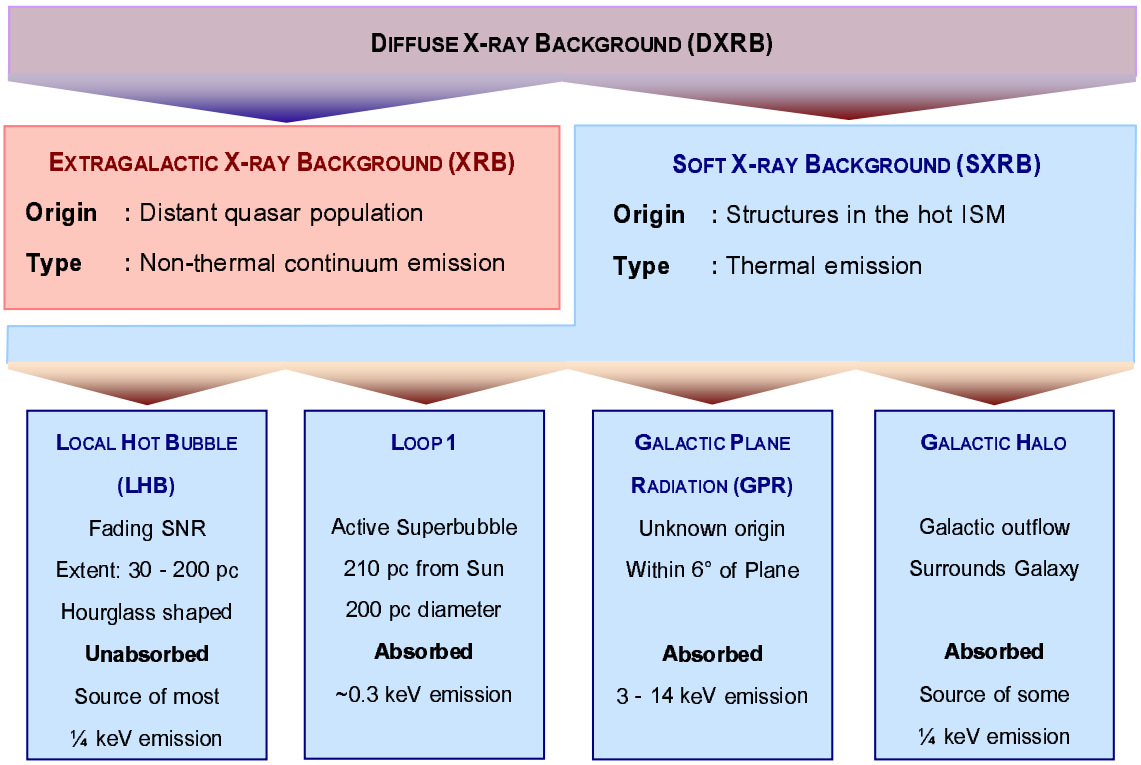

Figure 2.8: The Sources of the DXRB

itself only within 6° of the Plane. It is the least understood component of the SXRB: its source is uncertain, its flux has not been systematically characterised, and its strength as a function of distance from the Plane has not been quantitatively measured. It has, however, been detected in both the radio and soft X-ray bands.

Finally, the Galactic Halo, which lies above the HI disk on either side of the Galactic Plane, makes its contribution to the SXRB. The actual origin of the Halo is still a matter of debate, although both Galactic fountains and SNR outflow have been suggested and modelled with some degree of success.

For any given observation, the structures lying on the line of sight contribute thermal emission lines and continuum energy to the flux of the SXRB. When this flux is combined with that of the XRB, the total spectrum of the DXRB is produced, as summarised in Figure 2.8.

3

Data Reduction

The DXRB a challenging subject: its X-ray flux is weak, diffuse, and produced by a host of interstellar structures. Because its signal is easily overwhelmed by stray photons arising from instrumental contamination, stars and cosmic rays, atypical methods are required to analyse it: for example, most of the measured events, including all those from point sources, must be rejected in the early stages of data reduction rather than preserved. To complicate matters further, data must be sourced from the entire field of view of the X-ray detector, and not from a small selected region.

To meet these requirements, an alternative data reduction process has been formulated to perform instrument calibration and background subtraction. This process, which produces images and spectra of the DXRB from archived XMM observations, is described in this chapter.

3.1 Telescope Limitations

The quality of the data collected by a telescope is determined by the physical limitations of its optics and the technical shortcomings of its detector. Despite the rigorous screening and cleaning processes employed, the final spectra will not be ideal representations of the original X-ray signal. Rather, they are a convolution of the original signal with the responses of the telescope optics and detector to that signal. It is possible to minimise

the deleterious effect of the telescope's response through careful calibration, while other factors, such as the point spread function, are intrinsic to the instrument and cannot be corrected. These artefacts define the limit of accuracy in the reduced data.

3.1.1 Effective Area & Vignetting

The 'effective area' of a detector is the total collecting area of the optical elements and detector system, described as a function of energy. It is affected by several factors, including filter transmission, vignetting effects and the quantum efficiency of the CCD chips.

'Vignetting' reduces the effective area of the telescope mirrors as the off-axis angle increases. In practice, this means that the greater the angle between the telescope's optical axis and the path of an incident photon, the lower the probability of it reaching the focal plane. Vignetting can have serious consequences when observing and detecting point sources, because it reduces the brightness of images of objects detected near the outside chip edges relative to the central region detector. Among the various sources of internal background contamination that are described in the following sections, only soft proton flares are affected by vignetting (Read & Ponman 2003). Contaminating events from electronic artefacts such as bright pixels, power surges, and instrument fluorescence are not spatially vignetted, because they occur at or within the detecting surface, and do not interact with the telescope's optics.

3.1.2 The Point Spread Function

An ideal telescope would be able to focus each incident photon onto a single CCD pixel, producing a perfectly sharp, clear image. In reality, this cannot occur. Instead, the imperfect focusing of the telescope optics causes the energy of each photon to be spread over a number of pixels on the detector. The ability of a telescope to focus photons, its 'resolution', is thus determined by its 'point spread function', or PSF. The PSF is measured in arcseconds, and delimits the size of the features that can be resolved by an instrument. A number of separate objects detected in an area less than the width of the PSF could

not be resolved, and would appear in the image as a single or merged source. In the study of the SXRB, the PSF is not of direct relevance because the signal is diffuse, and by definition, unfocused. It is, however, of vital importance in the detection and removal of point sources.

Like vignetting, the PSF is a function of the off-axis angle within the 30′ field of view of the mirrors. It is also dependent on energy, but fortunately its distribution is narrow and shows little variation over the $0.1 - 4.0$ keV energy range covered in this research. Each of the three EPIC detectors has its own PSF, as shown in Table 3.1.

Table 3.1: The on-axis, in-orbit, 1.5 keV PSFs of the EPIC detectors given for full width at half maximum and half-energy width (Dahlem et al. 1999).

Instrument	pn	MOS1	MOS2
FWHM	$\sim 6.6''$	$4.3''$	$4.4''$
HEW	$15.2''$	$13.8''$	$13.0''$

3.2 The EPIC Filters

The EPIC cameras may be used alone, or in conjunction with one of three aluminium-coated optical blocking filters, named *thick*, *medium*, and *thin*. These are used to minimize contamination by infrared, visible and ultraviolet photons, to which the EPIC CCDs are also sensitive. Unfortunately, the use of a filter has a detrimental effect on the energy response of EPIC, particularly in the $0.1 - 2.0$ keV range, which serves to decrease the effective area of the detector, as illustrated in Figure 3.1.

The optical blocking capacity of the thick filter is approximately one thousand times greater than the medium filter (Dahlem et al. 1999). Although this is strong enough to prevent contamination from point sources with visible magnitudes $1 - 4$ for MOS or $0 - 3$ for pn, it also blocks a significant proportion of the soft X-rays which are critical in the study of the soft X-ray background. Consequently, observations made with the thick filter were not used. The open-filter mode (in which no filter is applied) was also avoided when selecting data for analysis, as it provides no protection from low energy photons, and so guarantees contamination by visible and UV light.

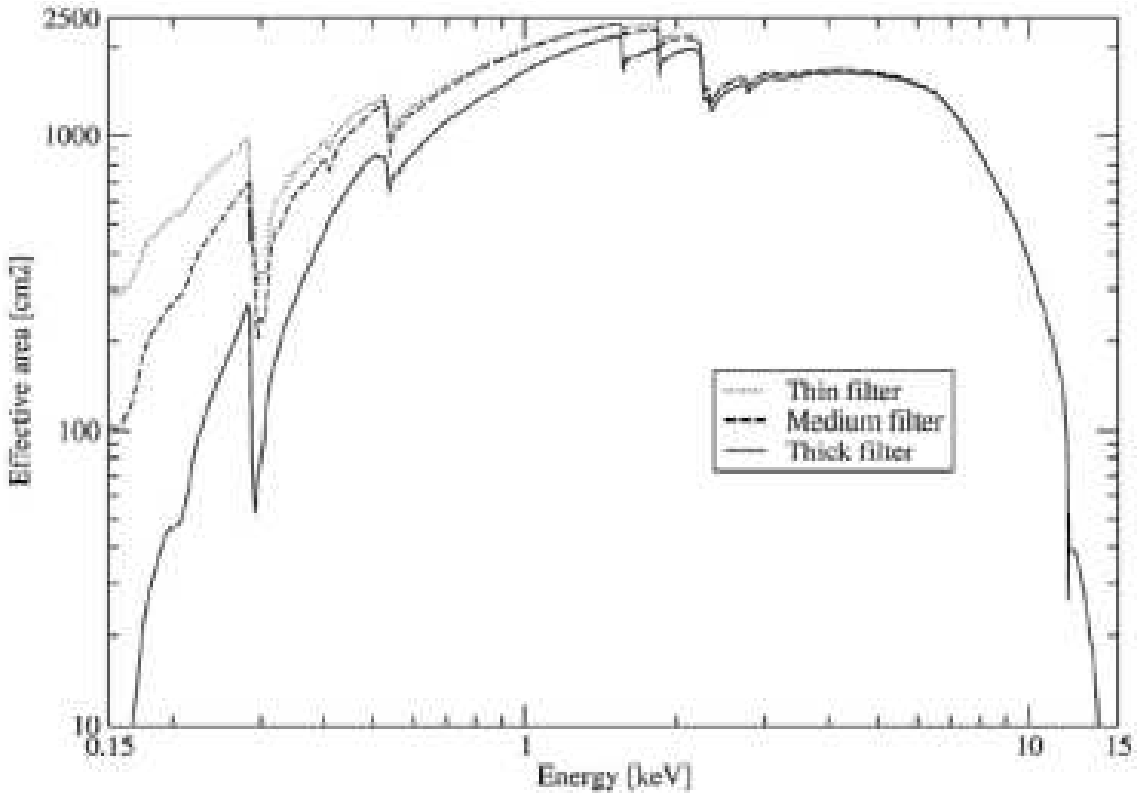

Figure 3.1: The combined effective area of the three X-ray detectors, demonstrating the effect of the thin, medium and thick filters on the energy response of the EPIC. (Image taken from Ehle et al. (2003))

All of the data sets used in this research were obtained using either the thin or medium filters. The thin filter offered some protection from very soft photons, whilst ensuring that the signal from the SXRB could reach the detector. The medium filter is around one hundred times more efficient than the thin filter, and so was able to prevent optical contamination from sources with visible magnitudes of $8 - 10$, but still allowed most of the SXRB signal through.

3.3 SAS, Q and the Data Archive

Observational data from the XMM-Newton Observatory is transmitted directly to the Science Operations Centre (SOC) at the European Space Astronomy Centre in Vilspa.

Once there, it is used to create an Observation Data File (ODF) which contains the image data, science telemetry and operational notes for each instrument, along with a range of auxiliary information such as craft attitude, orbital data, filter descriptions and exposure times.

The ODF is then transferred to the Survey Science Centre (SSC) at the University of Leicester, where it is passed through an automatic analysis pipeline. This outputs a range of data products for each of the EPIC instruments, including optical finding charts, X-ray images, exposure maps and calibrated event lists. Both the ODF and the 'pipeline products' are then stored in the XMM data archive and made available to researchers around the world.

The SSC pipeline consists of a series of Perl (Wall 2007) scripts, each of which utilise the Science Analysis Software tasks: a suite of tools that was designed specifically to process and analyse data obtained from the XMM-Newton Observatory. This software is continually developed and maintained by the SAS Development Team (2006).

Although the SAS tasks can be run independently of the pipeline, they have been used sparingly in the analysis featured in this thesis. Most of the data reduction was performed outside the SAS environment, using a series of scripts written in Q (Willingale 2004) which mimic the SAS tasks and provide some extra functionality.

The Q scripts, used extensively in this research, were originally formulated and described by Willingale et al. (2003), and also used by Hands (2003), to investigate the SXRB near the Galactic Plane and in the central regions of the Milky Way. The motivation behind their alternative approach was that the early versions of SAS, which had been geared toward the study of bright objects, were not able to cope with the low photon count rates associated with the diffuse emission of the SXRB.

Unfortunately, as is often the case in procedural development, several errors were made, both in the methodology and in the coding of the scripts, which pre-exist this project by several years. These were discovered and corrected in the course of this research. This has resulted in a change in interpretation of the spectra, which will be explained at the end of this chapter so that they may be understood in the context of the thesis.

All data and results reported in this thesis have been produced using improved, corrected

versions of the original Q scripts.

3.4 Field Selection and Data

Twenty XMM observations were processed and analysed in order to produce the results presented in this thesis. These were selected on the basis of three criteria. First, that the exposure time was several kiloseconds in length, to ensure that sufficient data had been gathered for detailed analysis. Second, only observations taken with the detectors in full-frame mode in conjunction with either the thin or medium filters were selected, for the reasons described in Section 3.2. Finally, fields with few bright point sources were preferentially selected in order minimise the total contaminated area that would have to be masked when cleaning the data-set. Signal contamination can also be produced by compact diffuse sources, such as nebulae and distant galaxies. This kind of emission is virtually impossible to remove, and so fields containing these features were avoided altogether.

The observations used in this research can be split into two groups, the first of which lies within the projected boundary of the Loop I Superbubble and includes three fields in the Northern Bulge of the Galaxy (X1, X2 and X3), two in the North Polar Spur (N4 and N5) and five below the Galactic Plane in the Southern Bulge (B1, B2, B3, B4 and B5). The positions of these observations were originally proposed by Dr. R. Willingale in the XMM AO-2 programme so that variations in the hard Galactic component of the SXRB could be measured as a function of latitude. The spectra of the SXRB derived from these fields have been examined in great detail, and the outcomes of this investigation into the properties of the SXRB in the Loop I region are presented in Chapter 4 of this thesis.

The second group of observations, the 'Oxygen' fields O1–O10, lie in the anti-centre direction, beyond the limits of Loop I, and have been used in conjunction with the first group of fields to investigate the distribution of O VII and O VIII throughout the Galaxy. The results of this line of research will be discussed in Chapter 5.

Details of all of these observations are presented in Table 3.2, and their pointing locations are shown in Figure 3.2.

Table 3.2: Details of the XMM observations used in this research. The total exposure times and good time intervals for these fields are listed in Table 3.3.

Observation ID	Revolution	Galactic Latitude (b_{II})	Galactic Longitude (l_{II})	Field	Filter	Observation Date
0152630101	673	12.00	345.00	X1	Thin	13/08/2003
0152630201	672	18.00	345.00	X2	Thin	10/08/2003
0152630301	672	24.00	345.00	X3	Thin	11/08/2003
0050940201	413	-2.71	0.46	B1	Medium	12/03/2002
0050940101	413	-3.87	1.05	B2	Medium	11/03/2002
0067340301	229	-5.49	0.39	B3	Medium	09/03/2001
0050940301	323	-8.00	0.56	B4	Medium	13/09/2001
0050940401	414	-12.00	0.00	B5	Medium	14/03/2002
0067340401	224	20.00	25.00	N4	Medium	28/02/2001
0067340501	224	30.00	20.00	N5	Medium	28/02/2001
0079570201	343	-9.50	233.01	O1	Medium	23/10/2001
0092360401	346	-20.80	238.15	O2	Thin	28/10/2001
0103260401	243	0.43	201.22	O3	Medium	06/04/2001
0103262801	702	-3.30	184.37	O4	Medium	09/10/2003
0110661301	128	-37.36	171.11	O5	Thin	20/10/2000
0111100101	399	-17.55	139.50	O6	Thin	11/02/2002
0111100301	149	21.11	202.74	O7	Thin	01/10/2000
0112200201	473	-3.44	126.30	O8	Medium	09/07/2002
0112320301	729	-34.56	159.27	O9	Thin	02/12/2003
0203130201	737	1.12	111.12	O10	Medium	18/12/2003

3.5 Cleaning the Data

The MOS1, MOS2, and pn event lists and exposure maps for the selected fields were downloaded from the XMM Data Archive (XMM Science Operations Centre 2006). Each event list contains the parameters ('flags') associated with the photons recorded by the EPIC. These include the time of each detection, its position on the detector, the pulse height of the signal produced, and also any quantities derived from these values, such as the celestial co-ordinates and photon energy of each event. The exposure map gives the net exposure time per pixel for the observation. It is used to calculate the number of counts per second per pixel in the associated event list, and so allow normalised,

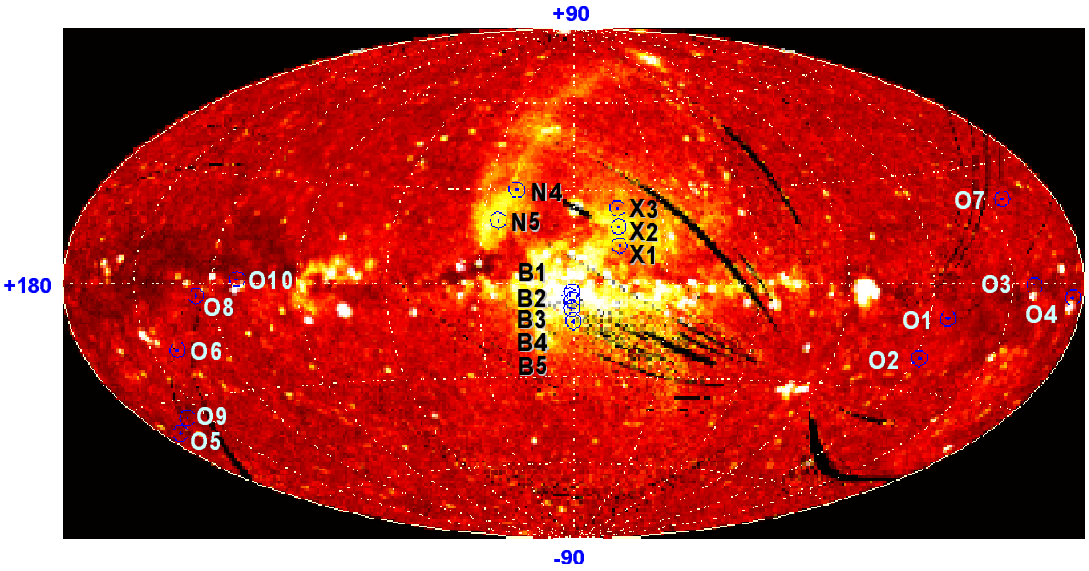

Figure 3.2: The $\frac{3}{4}$ keV RASS map (Snowden et al. 1995), in zero-centred Hammer equal-area projection, showing the positions of the twenty XMM fields used in this research. This is an all-sky map, with the x- and y-axes marked in degrees of Galactic longitude and Galactic latitude.

exposure-corrected images to be created.

As one would expect, an event file contains not only the pure signal from the target of the observation, but also contamination from 'external background' events (cosmic rays and, in this instance, photons from point sources) and 'internal background' events, which originate within the EPIC detector itself. Contributions to the internal background arise from incident charged particles, which interact with the constituent materials of the detector. Electronic noise and damaged regions on the CCD chips also produce spurious events. These background contributions were, as far as possible, identified and removed from the downloaded event lists before spectra were constructed. This was done for each of the EPIC detectors using the steps described below.

3.5.1 Solar Wind Exchange and Long Term Enhancements

While compiling the RASS maps, Snowden et al. (1995) uncovered flares in the X-ray flux, which they named long-term enhancements, or LTEs.

During an LTE, the X-ray photon count rate increases rapidly, and can as much as double over the course of one to two days. In this period, the stable flux of the SXRB is swamped by a blast of soft thermal emission which, after persisting for several days, fades, allowing the background flux to return to its long-term average level. An LTE contaminates both the continuum energy of the SXRB and the intensity of certain emission lines, particularly O VII. Occasionally, the flux contribution of a LTE may reach that of the XRB in the $\frac{1}{4}$ keV band (Sanders 2001), making it a small but significant component of the total SXRB spectrum.

Snowden's LTEs proved to be a major source of contamination during the construction of the RASS maps (Section 2.10). Due to their extended periods of influence, entire observations in the survey were contaminated beyond repair. Fortunately, the survey included many repeated observations, and through direct comparison of these, the enhanced fields could be identified. After painstaking analysis of the survey data, Snowden et al. (1995) were able to claim confidently that they had excluded LTE affected observations from the data included in the final RASS maps. Consequently, the RASS data points used to constrain the low end of the spectra during the fitting process (Section 4.5.1) should have been only minimally affected by LTE activity.

Despite their strong effects, the mechanism through which the LTEs were generated remained uncertain for some time: Snowden et al. (1994) found no correlation between LTEs and the direction of observation, or any other observational parameters. However, after analysing the RASS fields, Snowden et al. (1995) concluded that the X-ray flux of the LTEs must have originated locally: not simply within the LHB, but between the Earth and the Moon. They still could not, however, find a relationship between the intensity or frequency of the LTEs and the lunar orbital parameters, or suggest a mechanism that could generate the LTE flux. Chandra observations of the dark Moon (Wargelin et al. 2004) also showed an excess of O VII and O VIII flux, providing further evidence of a geo-coronal X-ray emission originating in the near-Earth environment, and supporting the proposition of a local LTE source.

The first clue to the origin of the LTEs came from observations of cometary X-ray emission. Through studying comet Hyakutake in 1996, Lisse et al. suggested that the comet's X-ray spectrum might arise as the product of charge exchange between the neutral material released in its tail and the heavy ions present in the solar wind. This idea

was developed by Cox (1998) and Cravens (2000), who suggested that the same process, a Solar Wind Charge Exchange (SWCX), a non-thermal electron capture interaction between the neutrals in the Earth's geocorona and heliosphere, could produce the soft, oxygen-rich flux consistent with that seen in the LTEs, and account for a portion of the SXRB. This was confirmed in 2001, when Robertson et al. (2001) were able to show a correlation between the timings of Snowden's LTEs and the proton flux in the solar wind.

Since the charge exchange must occur within the magnetosheath, at a distance of 2-8 Earth radii (Fujimoto et al. 2007), it follows that the emission spectrum will appear unabsorbed. Moreover, the SWCX flux is virtually indistinguishable from that of the LHB (Snowden et al. 2004); so, while most of the emission from the LHB and Loop I originates from supernova remnants that created them (Dickey & Lockman (1990) & Egger & Aschenbach (1995)), at least part of the flux attributed to the LHB must come from the SWCX.

This assertion alone lead some, including Lallement et al. (2004), to suggest that SWCX might be responsible for a significant fraction of the flux previously attributed to the LHB, thus bringing into question the current model of the local ISM. Fujimoto et al. (2007) considers the contribution of the SWCX flux to be a significant (but less than 50%) contaminating foreground in the SXRB at energies less than 0.1 keV.

Recent interest in the SWCX has lead to a greater understanding of its behaviour and its effect on X-ray spectra.

Two processes are thought to be at work. The first is a geocoronal interaction, which produces sporadic flares in the light curve of the SXRB that vary rapidly in magnitude with time. Fujimoto et al. (2007) recommends light curve filtering, such as that performed during the data reduction process, to eliminate the periods in which this is a major problem. In the second process, charge exchanges occur with interstellar neutrals as they pass through the heliosphere, generating both continuum energy and copious emission lines. These are, however, far more subtle than the flares, because most of their rapid variation is wiped out by the long travel time of solar wind events through interplanetary space.

Fujimoto et al. (2007) argued, on the basis of the short-time scale variations (/sim10 minutes) that they observed in the flares, that their source must have an angular size of

no more than 10 light minutes. The emission region occupied by the source had also to be larger than the field of view of his detector (18'). Hence, they estimated that the source had to lie within a distance of 10^{-3} pc. To produce the emission lines also seen in the spectrum, a significant source of ions would also have to be present within this radius, and as they point out, the only source to meet these criteria is the Sun.

There are two production mechanisms through which the Sun may produce the X-ray emission lines seen in the enhanced flux. The first is scattering of solar X-rays by the Earth's atmosphere, and the second is SWCX. Fujimoto et al. (2007) excluded atmospheric scattering, on the basis that their data showed no correlation between the X-ray intensity of the enhancement and the product of the solar X-ray intensity and the sunlit atmospheric column density. However, they did find a correlation between the proton flux in the upper atmosphere and the flaring periods consistent with SWCX.

The SWCX process gives rise to line emission, in particular C VI, O VII, O VIII, Ne IX, and Mg XI (Krasnopolsky et al. 2004), which by unfortunate coincidence, are the same spectral lines expected from interstellar plasmas at about 0.15 keV. This contamination is therefore indistinguishable from the LHB's signal within the SXRB spectra, and will, to some extent, impact on the analysis performed here.

There is still much debate about the level of contamination. As Fujimoto et al. (2007) notes, we are far from an understanding of the SWCX adequate to determine the true extent of the contribution. According to Koutroumpa et al. (2009) it should contaminate all soft X-ray observations to some extent, although this level would depend strongly on the solar wind flux and abundance variations at the time of observation. Snowden et al. (1995) found that in the $\frac{3}{4}$ keV band, dominated by O VII and O VIII, no emission line flux is required from the LHB, as it could all be generated by the SWCX in most areas, particularly near the plane. Near the Galactic Poles, however, where the ends of the LHB open to the Halo, the SWCX model can not account for all the emission. Koutroumpa et al. (2009) suggest that a mix of SWCX and LHB emission is most likely, but do not estimate proportions.

It is possible that up to half of the unabsorbed flux currently attributed to the LHB is really produced by the SWCX, making the LHB half as bright as previously thought (Cravens 2000). Shelton (2009) calculated that if this were the case, then the electron

density, thermal pressure and emission measure of the LHB would be reduced from the currently accepted value by factors of approximately $\frac{1}{\sqrt{2}}$ and $\frac{1}{2}$ respectively, bringing its properties more in line with adjacent material.

3.5.2 Subtracting the Cosmic-Ray Background

The cosmic rays which interact with XMM tend to be fast-moving, charged particles with energies higher than 100 MeV. When these enter the EPIC, the majority are automatically recognised and rejected, either by the on-board software or by the SSC pipeline, but those that remain are falsely recorded as events. This can produce an apparent count rate of ~ 0.9 counts s^{-1} between $0.2 - 12$ keV for a MOS camera (Lumb 2002) which, although small, is significant because it has a similar magnitude to the measured flux of the SXRB.

X-ray astronomers usually observe 'point sources': stars, quasars, and so on. Having acquired a data-set, they estimate and remove the contribution of the cosmic background, leaving the flux of the desired point source. This is normally achieved by subtracting the measured flux from a 'background' region that contains no obvious point sources from the averaged flux of a small region surrounding the source.

This method could not be used in this research because the weak flux of the SXRB had to be extracted from the complete field of view of all the chips in each detector, preventing the definition of a 'background' region. Fortunately, the construction of the EPIC camera allowed an alternative method to be adopted. The MOS and pn CCD arrays are partially covered by the telescope housing: an arrangement which shields their edges from X-rays during an observation, while exposing the inner regions of the chips to the X-ray sky. Cosmic rays, however, are able to pass straight through the housing, and so cause false detection events to occur with approximately equal probability on all regions of the EPIC CCD chips, including the hidden chip edges.

The first stage of data reduction was, therefore, to separate the data originating from the inner and outer regions of the chips, as illustrated in Figure 3.3. The contribution of the cosmic-ray background was then estimated by measuring the counts in the outer regions and scaling these to the field of view of the detector. This estimated background was then

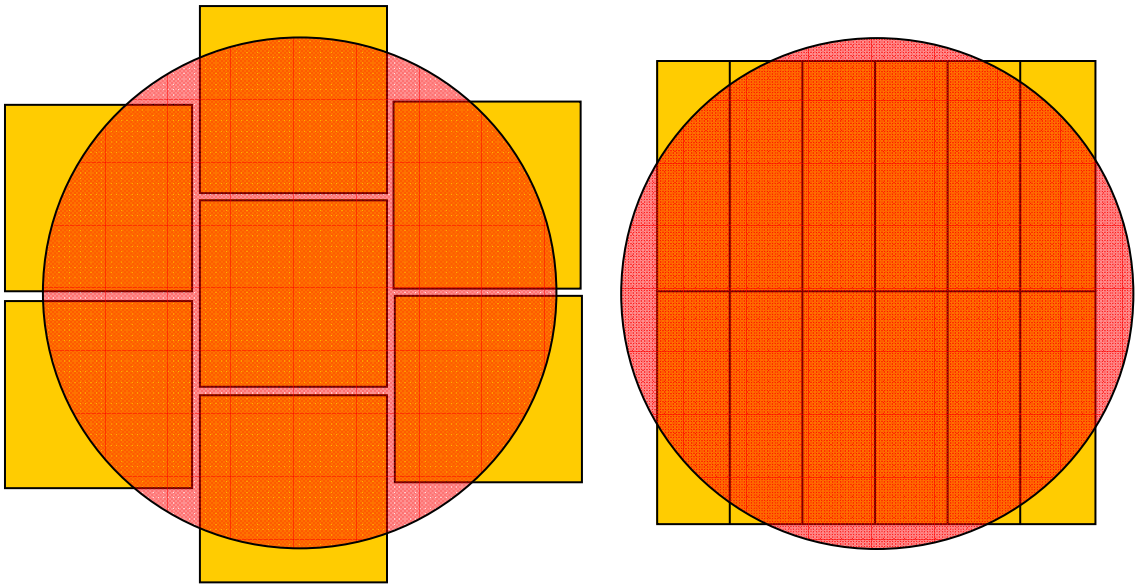

Figure 3.3: The focal plane arrangement of the CCD chips in MOS (left) and pn (right). MOS contains seven chips, each covering $10.9 \times 10.9\,'$, pn has twelve chips of $13.6 \times 4.4\,'$. The red circles, of $30\,'$ diameter, represent the area exposed to the sky. The yellow chip areas lying outside the circles are shielded within the telescope fuselage.

subtracted from the data events gathered from the inner region. It is reasonable to use this method, since the chip edges experience the same instrumental noise and cosmic-ray activity as the inner regions for the duration of the observation, even though they are not directly exposed to space. It is, however, better suited to the MOS detectors since, compared to pn, a larger proportion of their total chip area is shielded.

3.5.3 Filtering the Event List

When a particle (for example, a cosmic ray or photon) is incident on the EPIC, it deposits its charge into a pixel on the CCD surface. Ideally, for each charge cycle of the detector, any given pixel will detect one particle, allowing the particle's energy to be measured accurately. Occasionally, however, a pixel detects more than one particle before the charge is read out. When this occurs, the charges deposited in the pixel add together, and present as a single event with the sum of the particle energies; an effect known as 'photon pile-up'. Pile-up can distort the spectrum, hardening it artificially as piled-up soft events shift into high energies. Pile-up is not a problem for low energy sources, but it

can be a major concern when handling bright point sources and cosmic rays.

When the energy of a single event, or a piled-up event, is under the threshold level, the energy of the incident particle or photon is restricted to a single pixel, and it will register as a Pattern 0 event, as shown in Figure 3.4. However, when the total charge contained within a pixel exceeds the event threshold level of the detector, charge may 'spill over' into neighbouring pixels, producing the patterns numbered 1 through 31.

Since the pattern type is recorded in the event list, it is possible to filter the data by pattern number. Approximately two thirds of the recorded pn events are pattern 0. Spill over is represented by the higher pattern numbers ($\sim 13 - 25$, and 31). Pixels affected in this way are a major problem in spectral analysis, since their presence in the event list can significantly alter the profile of the spectrum. Consequently, when observing bright sources, it is sometimes necessary to mask out all but the single pixel events. In this case, as the emission from the SXRB is so weak, charge saturation of pixels was not a concern, and so severe filtering was not required. Instead, patterns were selected for which the EPIC response files are well calibrated, these being patterns $0 - 12$ for MOS and $0 - 4$ for pn. Events with patterns outside these ranges were masked out.

The event list also incorporates 'flags' that define the quality of data. A quality flag of value 1 or more indicates that an event occurred either at the edge of the CCD, or in close proximity to a broken (bad) pixel. Since some of the charge from these events may have been lost to the bad pixels, broken columns, or undefined regions at the chip edges, they would have altered the final spectrum, and so were masked out. Only reliable data, with a quality flag of zero, were used in the full analysis.

PI refers to 'Pulse-height Invariant' channels which are corrected for gain and charge transfer efficiency, and also combined so that the energy measured on each of the pixels within a pattern is summed into a single event. PI channel information is recorded for each event in the list, and was used to further refine the data set. All events with PI energies less than 0.2 keV and greater than 12 keV were excluded from the final event list, since XMM calibration is unreliable at these energies.

Finally, the event lists were filtered using a spatial flag. Events that were recorded in chip regions which had been exposed for less than 25% of the full on-axis exposure time were masked out. This ensured that data from the highly vignetted regions at the outer edges

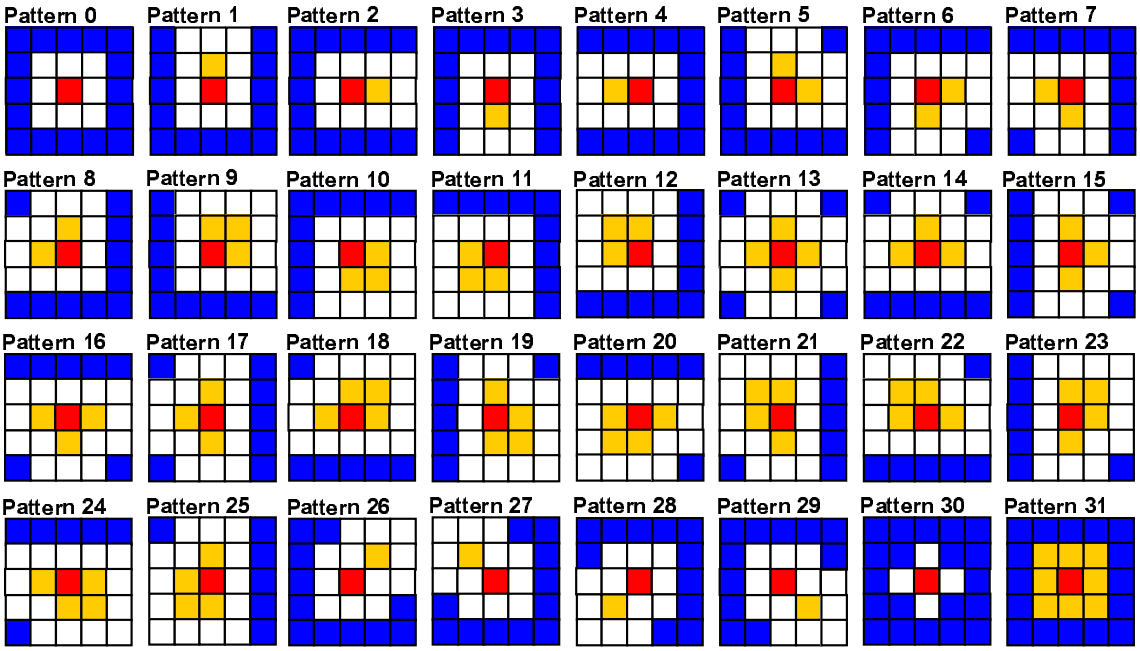

Figure 3.4: The recognised event patterns for the EPIC cameras. Each small square represents a pixel. By definition, a pattern is centred on the pixel with the highest charge, depicted here in red. Adjoining pixels, which accommodate the remaining charge from the event, are coloured yellow. The white squares define the boundary of the pattern, and lie below the threshold level for event detection. The blue squares are indifferent, and can be above threshold.

of the detectors, and the obscured regions on the inner edges of the chips in the MOS arrays, were not included in the final data set.

3.5.4 Light Curves and Flares

Having been 'cleaned', each event list was used to produce a light curve: a graph which shows the variation in count rate as a function of time. The amplitude of the light curve of a steady source such as the SXRB should, in theory, show very little variation, resulting in a flat profile of approximately constant amplitude. In practice, however, it fluctuates owing to yet another contribution to the background: drifting clouds of soft solar protons, encountered by XMM as it orbits the Earth (Read & Ponman 2003).

Soft protons trapped in the Earth's magnetosphere are thought to be accelerated by

'magnetospheric reconnection' events which appear to be unrelated to solar activity (Lumb 2002). As XMM moves through the magnetosphere, these protons are inadvertently scattered by the Wolter mirrors. On passing though the filter they reach the EPIC detectors, where they are registered as 'events'. The contaminating proton events are not identified during pipeline processing, but frequently produce pronounced flares in the light curve. Such flares can be extremely strong, reaching hundreds of counts per second: an intensity far greater than that produced by the soft X-ray background.

The frequency and duration of flares occurring while XMM is within the magnetosphere is highly variable. Ideally, observations intended for background investigations should be performed when XMM is outside the magnetosphere, where the flaring is minimal. This can, in theory, be scheduled and included as part of an observation proposal. However, since the data used in this thesis was taken from the archive (XMM Science Operations Centre 2006) and not specifically proposed, it was necessary to screen the data routinely for flares.

For low brightness sources such as the SXRB, it is necessary to select low intensity ('quiet') time periods from the data set for analysis, to minimize contamination from flares and variable sources. A light curve was created, using the cleaned event list, and including events with energy from 0.2 keV to 12 keV. The light curve was then stringently filtered by masking out regions with count rates just above that of the quiescent level (in each instance, the level was set by eye, as shown in Figure 3.5), effectively removing the proton flares. This process reduces the usable exposure time of the observation, since the data obtained over the duration of the flaring activity is discarded. The remaining period of the exposure time, the 'good time interval' or GTI, is that during which useful data was obtained. The final GTIs calculated for the processed fields are shown in Table 3.3.

3.5.5 Internal Fluorescence

The final contribution to the internal background of the EPIC detectors arises from the interaction between charged particles, with energies of several hundred MeV, and the materials that make up the structure of the XMM telescope. The charged particles excite the electrons of the neutral atoms that make up the EPIC detector and its associ-

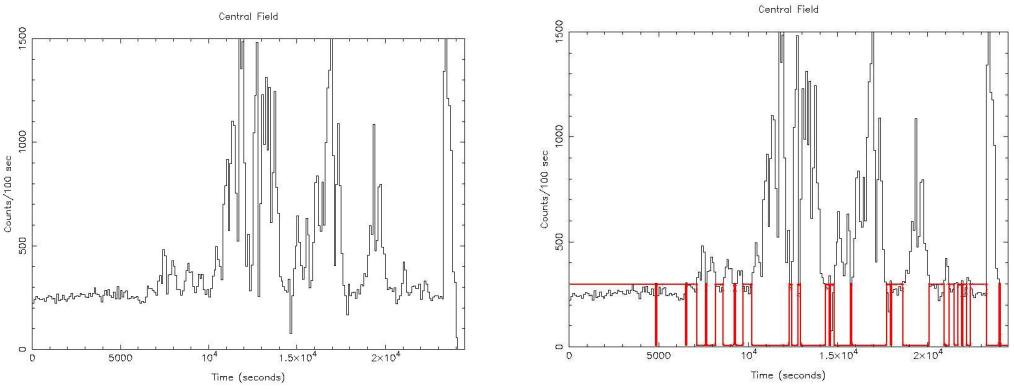

Figure 3.5: The frame on the left shows the unfiltered light curve (counts vs. time) obtained by the MOS cameras in the B1 field. The high peaks in the graphs are flares, which must be removed before the data can be processed. The continuum under the peaks is produced by the weak, constant flux from the DXRB. In the right-hand frame, a time cut (the red line) has been set at 300 counts s^{-1}. All data lying above this line will be excluded from the rest of the reduction process.

ated structures. When the atoms de-excite, they fluoresce, emitting X-ray photons by the same process as that described in Section 1.2.1. These photons are subsequently detected, and appear as discrete emission lines within the spectra produced by EPIC.

Several elements are represented in the internal background spectrum of EPIC, including Cr, Mn, Fe-K, and Au-L in MOS, and Cu-K in pn. The most prominent lines present within EPIC are attributed to the Al-K_α and Si-K_α transitions, which lie at $\sim$ 1.47 keV and $\sim$ 1.68 keV respectively. The relative strength of these emission lines is dependent on the energy spectrum of the incident charged particles.

The fluorescence is not uniformly distributed across the chip arrays. In MOS, the Al-K_α emission is weakest at the edges of the CCDs, in the regions which are overshadowed by surrounding chips. It is also less intense at the outermost edges of both the MOS and pn arrays, because these are partially enclosed by the body of the camera. The Al-K_α emission is brightest at the outside enclosed edges of the outer chips in both arrays, since these are closest to the aluminium camera housing.

The silicon line seen in the MOS spectra arises because its CCD chips overlap in several places. This orientation allows charged particles to impact the back of the CCD chips, and to excite the silicon atoms contained in the substrate found there. The resulting

Table 3.3: Table of Good Exposure Times (MOS1 & MOS2).

Observation ID	Field Name	Full On-axis Exposure Time (s)	Good Exposure Time (s)	Percentage Accepted	Upper Time Cut (counts s^{-1})
0152630101	X1	27349	14400	53	180
0152630201	X2	27346	11100	41	210
0152630301	X3	27343	12800	47	160
0050940201	B1	48055	18000	37	250
0050940101	B2	48055	28500	59	280
0067340301	B3	32892	29800	91	250
0050940301	B4	26943	12500	46	220
0050940401	B5	24666	19600	79	260
0067340401	N4	28984	28300	98	240
0067340501	N5	28988	24900	86	220
0079570201	O1	95124	40900	43	180
0092360401	O2	29542	24700	84	220
0103260401	O3	6022	5840	97	240
0103262801	O4	16137	13000	81	140
0110661301	O5	14381	12900	90	200
0111100101	O6	74453	38200	51	150
0111100301	O7	76097	45900	60	150
0112200201	O8	16846	15000	89	150
0112320301	O9	137340	122500	89	130
0203130201	O10	45142	45200	99	140

Si-K_α emission is therefore strongest at the chip edges which lie beneath adjoining chips. Si-K_α emission does not occur in pn since its CCD array is monolithic and planar, making its silicon substrate inaccessible.

Although it is reasonably stable, and shows only small intensity variations over long time periods (of the order 10% from mean intensities, according to Pizzolato (2001)), fluorescence must still be considered before source detection can be performed, and also when ascertaining and subtracting the internal background from the final spectrum, as will be described in Section 3.9.

Since some of the fluorescence lines match those in the data, they cannot be completely masked out without severely compromising the data set. Instead, the most dominant

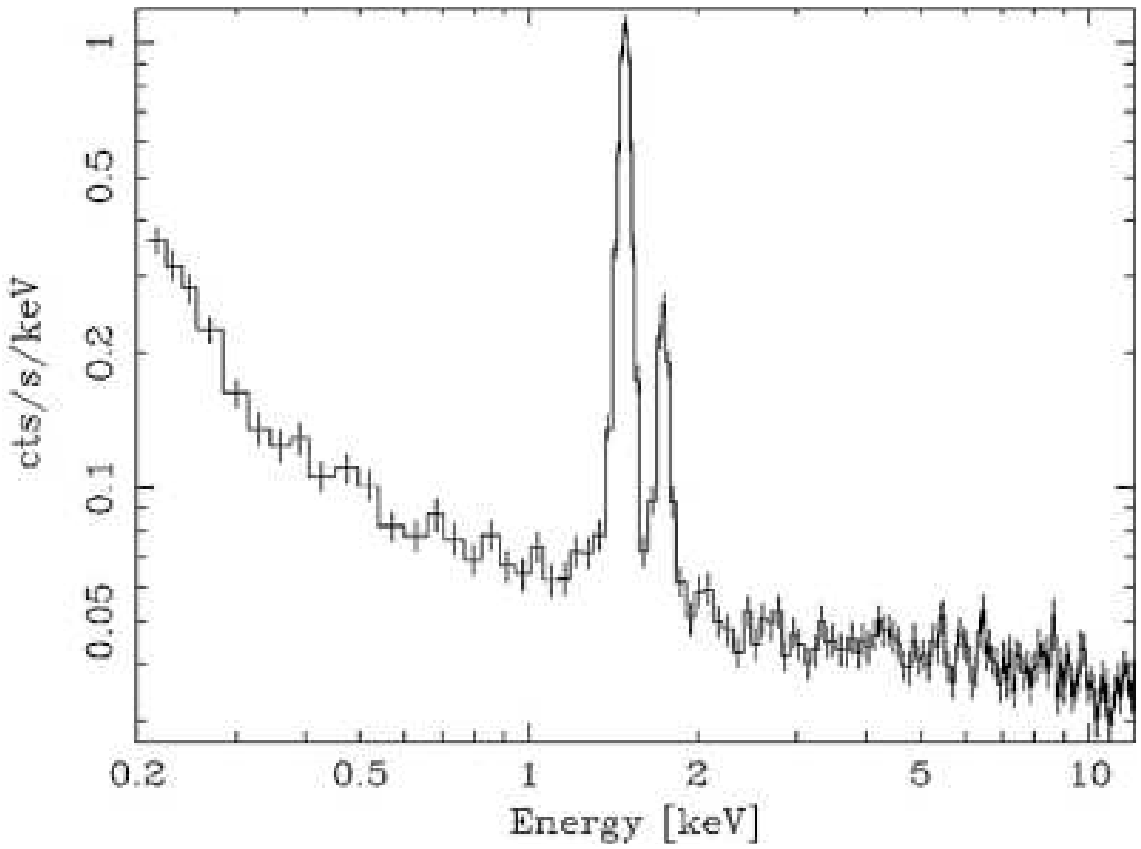

Figure 3.6: The internal background spectrum for the MOS1 detector, obtained with the filter wheel closed. The Al-K_α and Si-K_α fluorescence lines are clearly visible, at 1.47 keV and 1.68 keV respectively. The high continuum below 0.4 keV is caused by electronic noise within the detector. Data below 0.4 keV was rejected on the basis that background subtraction in this region would be unreliable. Image credit Dahlem et al. (1999).

lines (Al-K_α and Si-K_α) were suppressed in the event lists of MOS1, MOS2 and pn, to minimize their effect on the source detection process. This was achieved by masking out events with a PI energy within the energy range of the lines, between 1.4 – 1.575 keV and 1.675 – 1.8 keV respectively. Naturally, photons from sources other than the fluorescence lines were masked by this action, including some of cosmic origin. After the source detection routine had been completed, and the source positions masked out, the events in these ranges were reinstated. This meant that the Al-K_α and Si-K_α lines were included when the final spectra were produced.

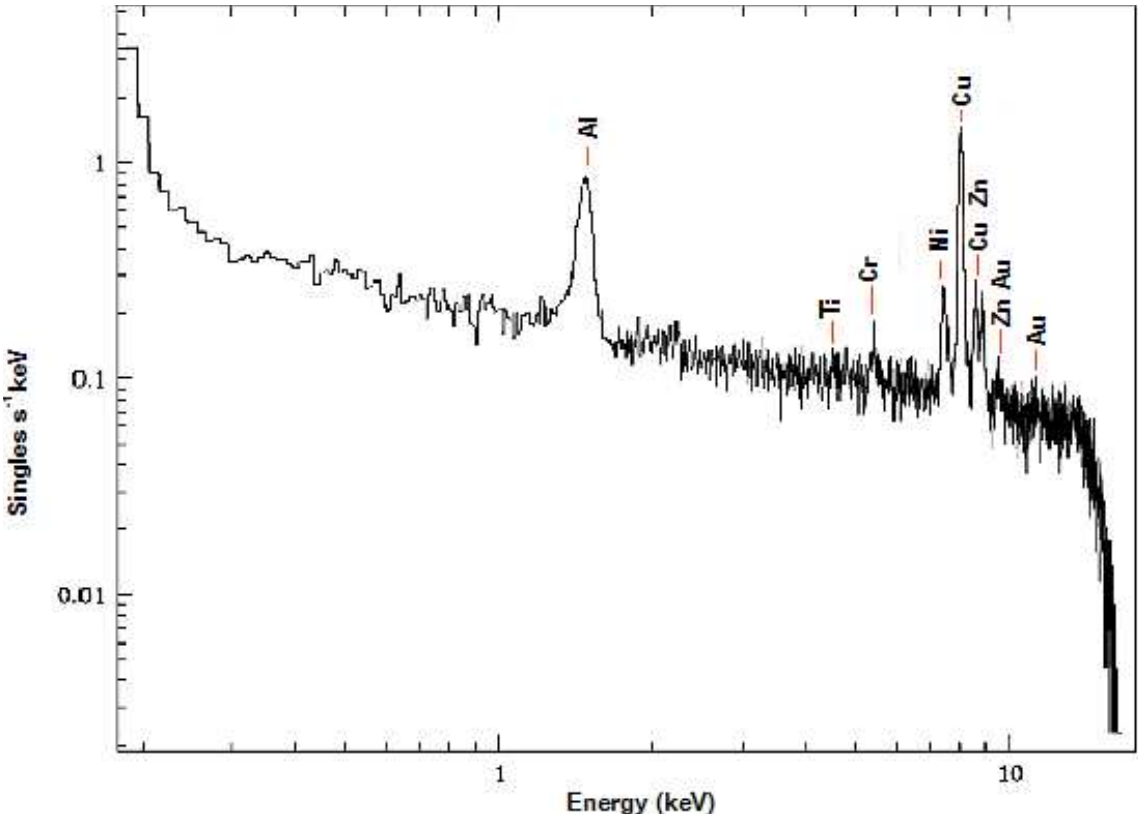

Figure 3.7: The internal background spectrum of the pn camera, taken with the filter wheel closed. The Al-K_α line is clearly visible at $\sim$1.5 keV. The Si-K_α line is not present in the background of the pn camera since its monolithic CCD array prevents charged particle interaction with the silicon substrate. Prominent features in the emission spectrum include Cr-K_α at 5.5 keV, and Ni-K_α, Cu-K_α and Zn-K_α around 8 keV. Like MOS, pn is susceptible to electronic noise, indicated by the rise in the continuum below 0.3 keV. Image credit Dahlem et al. (1999).

3.6 Image Production

After the data had been cleaned as far as possible, images of the chip arrays were produced. The filtered event list from each EPIC detector, containing data from both the inner regions and the chip edges, was convolved with a top hat mask of radius 4 pixels. This created a smoothed image with the data binned into 4 $''$ pixels, a size approximately two-thirds of the instrumental resolution (Figure 3.8). This eased the later stages of source detection by spreading the photons of point sources over several pixels on the CCD array, and so making them more visible to the detection algorithm.

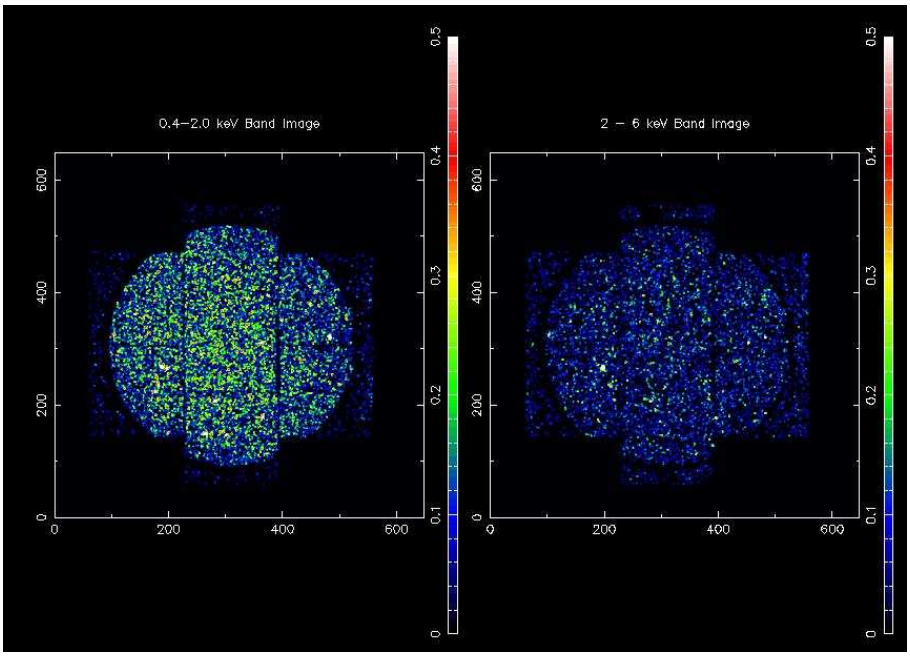

Figure 3.8: A smoothed image of the filtered B1 data set. The inner region and chip edges of the MOS detector are clearly visible.

The data from the two MOS cameras were added together in order to enhance their photon statistics. Although it is possible, using various calibration procedures, to combine the data gathered by all three EPIC detectors into one event list, this was not done. Instead, the pn spectrum was produced separately, allowing the two data sets to be compared and checked for consistency. From this point, the phrase 'MOS data' will refer to the amalgamated MOS1 and MOS2 event list.

The MOS1 and MOS2 exposure maps were then divided by the maximum exposure time experienced by the detector during that observation to normalize them with respect to time, and then combined to create one image. Because the inner regions of the chip arrays were exposed to the sky, these regions were included in the image. The edges, previously used to remove the cosmic ray background, were not needed at this stage, and so were excluded from both the MOS and pn data by masking out chip regions which had been exposed for less than 95% of the exposure time of the observation. Filtering in this way also excluded the highly vignetted regions at the outside edges of the exposed inner regions of the chip arrays. For each field, the 95% exposure boundary was determined by using the on-axis exposure time of the Band 3 (2.0 – 4.5 keV) exposure map which

had been produced by the SAS pipeline and downloaded with the observational data.

3.7 Preliminary Filtering and Smoothing

The normalized and filtered exposure maps from MOS and pn were smoothed through convolution with a circular top hat function of radius 2 pixels. This process removed the enhancements and dark areas produced by chip edges, producing complete, solid images of the chip arrays. These images, and others derived from them, were subsequently used as 'quality masks' for the cleaned EPIC data.

The quality masks were imposed by convolving them with the cleaned images, a process that slightly smoothed the images, while simultaneously removing any remaining edge enhancements. The smoothing process increased the contrast of the image, bringing previously undetected bright emissions from nebulae and galaxy clusters to the fore. To remove these bright pixels, a frequency distribution of the smoothed image showing counts per pixel by frequency was created. The count threshold defining the brightest 5% of the pixels was then calculated. This value was used as a cut-off, and the locations of any pixels with count rates in excess of this threshold value were added to the quality mask. The refined quality mask was then convolved with data, further smoothing the image, and masking out the bright pixels.

3.8 Source Detection and Removal

An image of the filtered data set was then displayed, using colour to represent count intensity, and examined by eye. For each field, an intensity threshold was set at approximately the same magnitude as the average brightness of the chip array, defined such that bright, enhanced regions would lie above this level. The image array was then scanned from left to right, bottom to top in a raster fashion, in order to locate and record the positions of intensity peaks in the data that lay above the threshold level.

The listed peak positions were then subjected to beam analysis: a circular top hat function of radius four pixels (equivalent to 16″) was used to scan the positions of the intensity

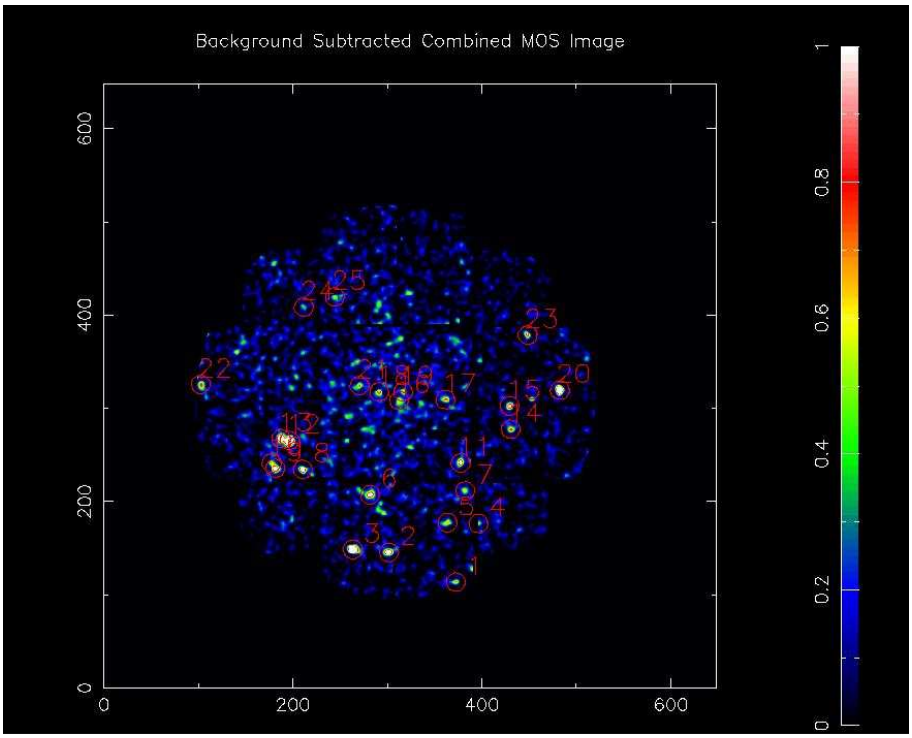

Figure 3.9: Sources detected and flagged in the B1 MOS data.

peaks in both the raw, unsmoothed image and the background map. The background map was also scanned so that the statistical significance of detections in the unsmoothed image could be measured. At each location, the total photon count within the beam area was calculated and tested. If the measurements showed that the photon count was fifteen or more counts higher than the average background level, and that statistically, the detection had a 5σ or greater significance compared to the average background level, then the region was then flagged, and identified as a source (Figure 3.9).

The sources located in this way were used to create another quality mask, in which the flagged source locations were bored out of a blank template, similar in dimensions to the detector area, using a top hat function of radius 8 pixels. The raw data was then blurred using a weighted Gaussian function, and multiplied by the holed quality mask in order to drill out the point sources. This procedure created a 'Swiss Cheese' (Figure 3.10) image, that is, an image of the data set covered in a series of black holes that had once contained point sources. To cover the holes, a square top hat function of width 40 pixels was convolved with the image, producing a final, heavily smoothed image.

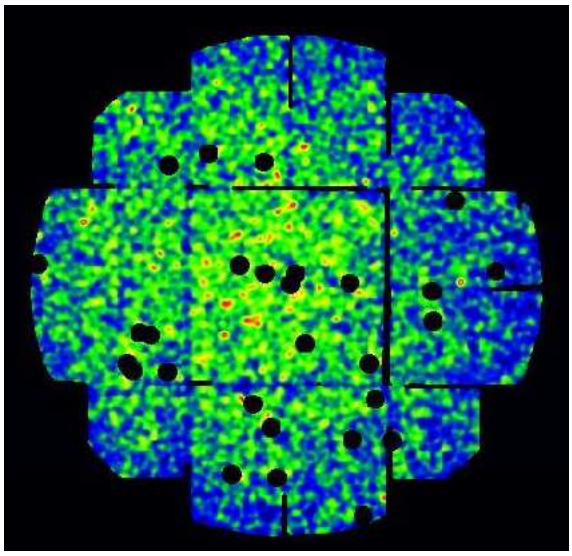

Figure 3.10: The 'Swiss Cheese' image of the B1 field, produced when the flagged sources were removed.

The entire scanning, source detection and removal process was iterated several times for each data set, and the threshold tolerance was lowered at each stage, until no new sources could be detected.

3.9 Estimating the Effect of the Internal Background

The internal background of XMM is an energy spectrum that is present, to some extent, within every data-set obtained with the EPIC. It possesses both a continuum, from electronic noise within EPIC's circuitry, and a series of fluorescence lines generated by the interaction between cosmic rays and the X-ray detectors.

In normal circumstances, the contribution of the internal background would be estimated through comparison with data extracted from a CCD chip that had been unaffected by the target of the observation. Because the flux of the SXRB is present over the entire field of view, this method could not be used in this project. Instead, a technique originally devised by Willingale et al. (2003) was employed in which a generic model of the internal background was scaled to the reduced data.

Willingale et al. (2003) first combined the flux from the masked regions of the MOS CCD chips from several long XMM observations[1], to produce a data-set with an effective total exposure time of 355 kiloseconds.

They then filtered this data-set using the rigorous methods described in the previous sections, and reduced it to produce a close approximation to the internal background spectrum of the MOS detectors. The most prominent fluorescence lines, Al-K_α, Si-K_α, and Au M, were masked out at this stage, because their intensity varies significantly between observations and they have non-uniform emission over the field of view.

Willingale et al. (2003) then fitted the continuum of the background spectrum using a simple polynomial model, and added a series of Gaussian curves to accommodate the weaker, non-varying fluorescence lines, all with energies greater than 5 keV, in order to produce a generic model of the internal background. Both this model and a similar one produced for the pn camera were used in the final stages of data reduction.

Finally, the events contributing to the Al-K_α and Si-K_α emission lines were reinstated, and a spectrum showing count rate versus photon energy was created for each observation from the smoothed image file produced at the end of Section 3.8.

3.9.1 Scaling the Background

In accordance with the method of Willingale et al. (2003), the count rate was measured in the 9.8 – 11.3 keV band both in the exposed regions of the individual observed fields, and in the generic background model. This specific energy band was chosen because it contains no instrumental fluorescence features, and so allowed the spectrum to be normalised against a simple featureless continuum. The ratio between the two count rates was then used as a scaling factor to fit the generic background model to each of the reduced spectra.

[1] Seven in the Galactic Plane, two within the Galactic Ridge, four inside the Loop I boundary, and one deep-survey field. Although a single long-exposure observation could have been used to construct a background spectrum of the whole chip array for each observation, this would have produced poorer statistics, since the single exposure would have been shorter than the cumulative exposure of many long observations.

The scaled generic background spectrum was then subtracted, to remove the internal background of the detector from the data. In effect, this lowered the continua of the final spectra and eliminated the high-energy fluorescence lines which had been included in the generic background model. As the bright aluminium and silicon lines had not been included, they remained in the final spectra and later had to be fitted using Gaussian curves.

This method of background subtraction is based on the implicit assumption that the shape of the internal spectrum will remain constant while its amplitude is modulated by external conditions. While this method is acceptable, and works well to a first approximation, it should be noted that it introduces some uncertainty into the data reduction process. Since the degree of contamination is estimated from a number of different fields, it is not observation specific. Also, the background spectrum created for each detector is valid only for energies greater than 0.4 keV, because the response functions of the EPIC detectors are not well calibrated below this value.

3.10 The Redistribution Matrix Files

The redistribution matrix file (RMF) is designed to redistribute the energy of a modelled spectrum so that it reflects the current energy response and resolution of the detector. To generate individual RMFs with the SAS RMFGEN task would have taken a prohibitively long time. Instead, pre-prepared 'canned' responses were used to calibrate the spectra. These are available online at the XMM-Newton Calibration Portal (VILSPA 2006).

RMFs are not dependent on the filter used in the observation, but are highly sensitive to the energy response of the detector. Selection of suitable RMFs was performed using separate criteria for the MOS and pn detectors.

For pn, the detector response is relatively stable. As a result, the canned RMF is not time dependent, and so only one full-frame 'Y9' RMF was required. This RMF accommodated single and double events (patterns 0 – 4, Figure 3.4), since these had been allowed to remain when the event list was filtered. The 'Y9' version was used because charge transfer effects cause the energy resolution to vary across the pn array. Because this file uses the pixel lines nearest the centre of the array, it provides an average response

representing the whole chip.

Imaging-mode RMFs, accommodating patterns 0 – 12 (Figure 3.4), were selected for the MOS detectors. Unlike pn, the energy response of MOS changes frequently. To compensate for these changes, a series of RMF files have been created by the XMM calibration team, each of which is dependent on a revolution number, that is, the number of times that XMM has orbited the Earth. In most cases, the RMF with the closest revolution number available to that of the observation was used. However, both MOS1 and MOS2 were cooled in revolution 534, in a successful attempt to produce an improved, and more stable, spectral resolution. Consequently, the revolution 534 RMF file was used for all observations taken after this orbit. The canned RMF files available for MOS1 and MOS2 are almost identical. Since data from the MOS cameras was combined, only the RMF for MOS1 was used in the spectral analysis.

3.11 The Auxiliary Response Files

The Auxiliary Response File (ARF) is another calibration file used in conjunction with the RMF which, when applied to a modelled spectrum, allows the filter response of the detector to be taken into account, along with vignetting effects caused by the position of the image. It also corrects for the effective area lost to the chip gaps and bad pixels. ARFs were generated for the reduced spectra using the SAS task ARFGEN: the only time SAS was used directly in the entire data reduction process.

Usually, an ARF would be created for a small region defined around the target of an observation, for example, around a point source. When studying the SXRB, the entire surface of the chip array constitutes the target, and so the ARF files were created to cover this extended region. The auxiliary response is quite stable, because the effects of the filter and vignetting upon the energy response of the detector are virtually constant. Also, since ARFs are not dependent on revolution number, only four standard files were required here to cover all possible eventualities, these being; MOS with the thin filter, pn with the thin filter, MOS with the medium filter and pn with the medium filter. Field X3 was used to produce the ARFs for the thin filter, and B5 was used for the medium, because these were considered 'average' observations: within the projected boundary of

Loop 1, but far enough from the Galactic Plane to avoid unusual astronomical features.

3.12 Calibration of the Spectra

Each background subtracted spectrum was read into Xspec together with the appropriate ARF and RMF files, in order to calibrate the data and to impose the responses of the optics and instrumentation on the applied models. The spectrum files were then binned into groups of at least ten events, to improve the fitting statistics. This step produced the final spectrum, and completed the data reduction process.

3.13 Summary

An overview of the full data reduction process is illustrated in Figure 3.12. The entries in red indicate steps that have been either added to or altered from the original data reduction process. Aside from simple corrections to numerical errors that were present in the code itself, the amendments fall into three categories.

1. **Field Selection:** Data from both MOS cameras is required by the scripts to produce an SXRB spectrum. When acquiring data from the XMM archive, it became apparent that one of the fields (NPS6) used by Willingale et al. (2003) had data from only one MOS detector. Consequently, only data from NPS4 and NPS5 were used in this research and NP6 was omitted. No pn spectra were included in the 2003 paper because the files required to process pn data were developed after its publication. These files are now available, and have been used to process the pn data from the observed fields wherever possible. The ten 'Oxygen' fields lying beyond the Loop 1 boundary were selected by the current author, and have never previously been used in this area of research.

2. **The Good Time Interval:** The GTI is sum (in seconds) of the time periods during the observation when useable data was obtained. It is used in spectral analysis to calibrate the observed events with respect to time, normalising the

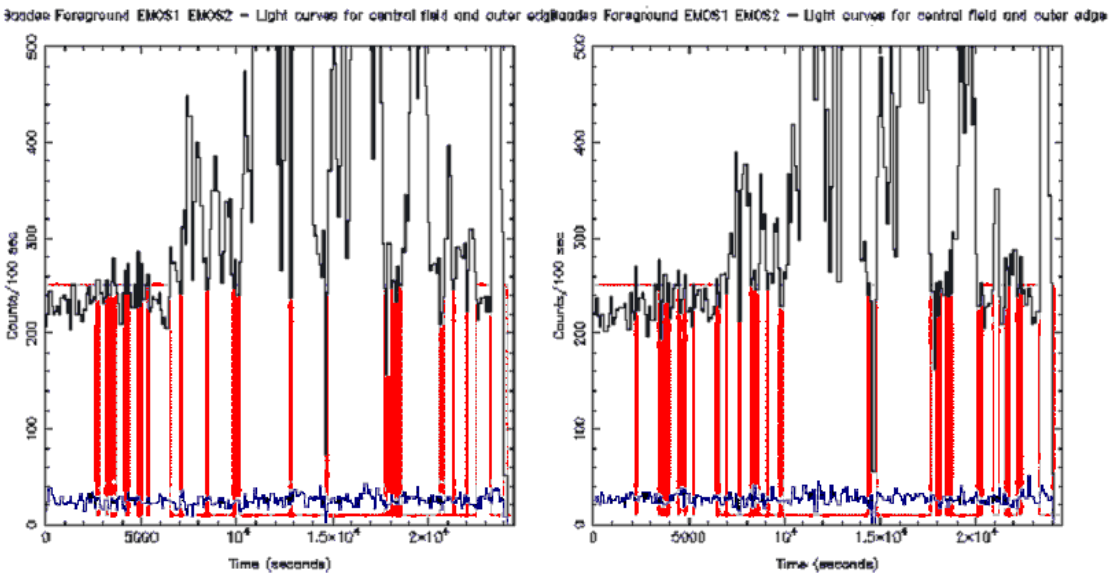

Figure 3.11: After cleaning the data, the light curve is filtered a second time. Here, the cut of the B1 field is reduced from 300 to 250 counts s^{-1}.

photon counts so that a spectrum can be produced showing the count rate as a function of energy. It is therefore imperative that this value is calculated precisely; otherwise the count rates represented by the spectra will not represent the actual signal from the source. In the original scripts, the GTI was calculated following the removal of proton flares from the light curve, because the useful observation time of the observation is reduced when the events related to the flaring are masked out.

However, masking out the point sources described in Section 3.8 further lowers the average photon count rate of the data set, making small peaks in the light curve more prominent. To accommodate this extra reduction, and to remove the smaller peaks, the program was made to produce a second light curve after the source detection algorithm had been completed. New cuts were established to match the lowered quiescent level of the second light curve, and the revised GTI values (see Table 3.3, and Figure 3.11) were used to calibrate the spectra with respect to time.

3. **Calibration:** As described above in Sections 3.11 and 3.10 two auxiliary files, the ARF and the RMF, were read into Xspec along with the reduced dataset. Between them they calibrate any models subsequently applied to the dataset, correcting for

instrumental responses that vary with time, and reducing undesired optical effects, such as vignetting. In this work, appropriate ARFs and RMFs have been used for each of the twenty data sets, ensuring a more accurate measure of the flux in the 0.1 – 4.0 keV range.

1. Data Selection & Acquisition

- **Fields selected.**
- Exposure maps & event lists downloaded.

2. Cleaning the Dataset

- Cosmic background estimated from chip edges and subtracted from dataset.
- Event list filtered by pattern number, 0 – 12 allowed for MOS, 0 – 4 for pn.
- Data with quality flag > 0 rejected.
- Data with PI channel < 0.2keV and > 12keV rejected.
- Light curve produced.
- **Good time interval (GTI) calculated.**
- Proton flares masked out of light curve.
- Internal fluorescence lines suppressed.

3. Image Production

- Image of clean dataset produced.
- Image smoothed by convolution with circular top hat function (radius 4 pixels).
- [Combine MOS event lists]

4. Quality Mask Production

- [Combine MOS exposure maps]
- Exposure map normalised w.r.t. time.
- Highly vignetted regions and chip edges masked out of exposure map.
- Exposure map convolved with circular top hat function (radius 2 pixels), producing a smoothed quality mask.

5. Quality Mask Imposed

- Quality mask convolved with cleaned image.
- Locations of the brightest pixels (top 5%) added to the quality mask.
- Improved quality mask convolved with clean image, to mask out bright pixels.

6. Source Detection & Removal

- Intensity map of dataset displayed.
- Average intensity level determined by eye.
- Image scanned for intensity peaks.
- Peaks subjected to beam analysis.
- Statistically significant peaks flagged as sources and drilled out of a new mask.
- Clean dataset convolved with new mask and then a square top hat function (width 40 pixels) to smooth and remove holes.
- Iterate until no new sources are found.
- **New light curve made, GTI recalculated.**

7. Modelling the Internal Background

- Internal fluorescence lines reinstated.
- Background spectrum created from a composite file containing many data sets.
- Spectrum modelled with a polynomial continuum and Gaussian curves to mask minor emission lines (not Al K_α and Si K_α).
- **Generic internal background scaled to data.**

8. Response Files

- **Canned RMF files downloaded.**
- **ARF files made using ARFGEN SAS task.**

9. Create the Spectrum

- Photon energy vs. count rate spectrum produced from cleaned, smoothed image.
- **Internal background spectrum scaled and subtracted.**
- **Appropriate ARF & RMF files included to calibrate the model to the reduced data and to impose the detector response.**
- Final spectrum binned to improve statistics.

Figure 3.12: An overview of the data reduction process.

4

Fitting the Spectra of the DXRB

The DXRB spectrum is the sum of the emissions from the many X-ray sources lying along the line of sight (Snowden et al. 1990*b*). To deconstruct the DXRB, and to determine the physical properties of the separate emissive structures that produce it, its spectrum must be modelled.

This process involves matching the high-quality X-ray spectra, produced through the data reduction procedure described in Chapter 3, with a series of mathematical plasma *codes*. These are selected and either used as they are or modified by other codes to form model components. These are then combined to produce a *model*. The parameters of the codes are carefully manipulated in order to make the overall model *fit* the reduced spectrum. Finally, when the *best fit* has been achieved, the parameter values can be used to infer the physical properties of the original sources.

This modelling procedure has been undertaken by researchers since the earliest observations of the DXRB. As the quality of the data and the accuracy of the plasma codes have improved, the method has become increasingly powerful. It is only since the launch of XMM-Newton, and the subsequent development of the data reduction process described in Chapter 3, that the resolution of the available spectra has been sufficiently high to permit detailed modelling.

In this chapter, the earlier attempts to model the DXRB will be described, both to show the evolution of the models adopted in this field of research and to justify their unusual

complexity. The models and the separate plasma codes from which they are composed will then be explained, and used to model the spectra created in Chapter 3 from the reduction of twenty XMM observations.

Because the observed spectrum of the SXRB varies across the sky, depending on the structures lying along the line of sight, the twenty fields will be split into two groups. Those positioned in the Anti-centre direction, the ten 'Oxygen Fields', have the simplest spectrum, and will be fitted first. Once the structures present in these fields have been identified and characterised, these results will be used to inform the fitting of the more complicated spectra from the Galactic Centre direction, the 'Loop Fields'. In all cases, the systematic and stepwise development of the models will be shown. Highlights of this work include the identification of a hot Galactic Halo in the Anti-centre, and a new interpretation of the absorbed 0.1 keV signal and hard emissions present in the Galactic Centre direction.

4.1 The Construction of a Model

To construct a model, one begins by fitting a single model component to a spectrum. If it fits well, then the fitted parameters can be analysed. If it does not work at all, it can be swapped for another, but if it partially fits the data, another component may be added to make up for the deficiencies of the first. While it is usually preferable to create a simple model with very few components, such practice is not possible when fitting the SXRB. This is because the characteristics of many individual structures must be considered, rather than the separate aspects of a single object.

All data-sets have finite degrees of freedom (DoF), the number of which is equal to the number of data points plotted in a spectrum, minus the number of parameters allowed to float freely within the model. If a data-set is poor, or the model too complex, the number of DoF may approach the number of free parameters. When the values are equal, many statistically perfect fits are possible, rendering the fit unphysical, and hence meaningless. This problem does not commonly arise when dealing with bright point sources, as these have many data points and a simple model with few free parameters is usually sufficient; however, when fitting the weak but complicated signal from the DXRB,

with comparatively few data points, the risk of over-compensation must be considered. Hence, when fitting the models, various techniques were employed to keep the number of free parameters down to a reasonable level, for example, by simultaneously fitting MOS, pn and ROSAT data sets, and freezing certain parameters to expected values.

4.2 Forty Years of Work

The number of components used to model the DXRB has risen steadily since the late 1960s, in response to the improving quality of the available data. Each time a component was added to the model, an additional aspect of the signal could be disentangled from the whole, enabling the characterization of an additional emissive structure, and prompting a change in interpretation of the DXRB.

The XRB, which had dominated the low-resolution data obtained by Henry et al. (1968), was the first source to be modelled. Henry et al. (and later others, including Garmire et al. (1992) and Willingale et al. (2003)) found that a non-thermal power-law, of photon spectral index 1.4, matched the data reasonably well below 10 keV. McCammon et al. (1983), McCammon & Sanders (1990) and Chen et al. (1997) confirmed the efficacy of this model in their own research. However, when the model was extrapolated to low energies, the match to the data became progressively worse. The power-law could neither fit the thermal emission lines that were present at low energies, nor provide enough flux to accommodate the emission below 2 keV, leaving a 'soft excess' which increased in intensity towards low Galactic latitudes (Snowden et al. 1990*b*, Miyaji et al. 1998).

Following the identification of the LHB, both Marshall & Clark (1984) and Snowden et al. (1990*b*) fitted a two-component model, adding a thermal APEC (Raymond & Smith 1977) to the already established power-law. They also included an absorptive code, representing the Galactic hydrogen column, which acted only on the power-law; reducing its intensity at low energies, and effectively pushing the XRB signal it modelled behind that of the unabsorbed LHB. This two-component model, which included some of the prominent emission lines, produced a reasonable fit to the available data, leading both parties to conclude that "essentially all" of the soft $\frac{1}{4}$ keV flux was generated within the optically

thin plasma of the LHB.

In 1992, Garmire et al. found that to fit high-resolution spectra of the SXRB obtained from the Galactic Centre direction, a further component was needed. In addition to an absorbed power-law and a thermal component, representing the XRB and LHB respectively, an absorbed thermal component was required to fit an apparent energy excess present between 0.3 – 0.5 keV. This third component was later associated with the Loop I superbubble (Section 2.6).

The flux from the Anti-centre, that is, the direction within the Galactic Disk which from Earth is 180° from the Galactic Centre, does not contain the radiation from Loop I. Nevertheless, when fitting the spectra from the Draco Cloud region, far from the Galactic Plane and towards the Anti-centre, Sidher et al. (1996) still required a three-component model to obtain a good fit. In addition to the standard power-law and thermal codes describing the XRB and LHB, their model included an absorbed thermal component to account for an observed soft excess. Because the amount of absorption needed on the third component was equivalent to the full Galactic Column, Sidher et al. (1996) associated it with the Galactic Halo: the structure proposed by Spitzer (1956), and discussed in Section 2.9.

The efficacy of the three-component model in the Anti-centre direction was confirmed by both Chen et al. (1997) and Wang (1998) who determined, through spectroscopy, that the emissive material in the Halo has approximately solar elemental abundances.

Following the creation of the high-resolution RASS maps (Section 2.10), Snowden et al. (1998) used the same three-part model to fit a number of Anti-centre fields. Through detailed analysis they found that the combined signals of the Halo and the XRB provided up to one half of the observed X-ray intensity in some directions, and around a quarter of the observed X-ray photons over the whole sky.

Although the XRB is bright, it is still subject to absorption, and when observing the DXRB around the dusty Galactic Plane in the Anti-centre direction one would expect to see a deep intensity minimum. However, when Snowden et al. (1997) measured this intensity, they found that it dipped only slightly, even close to the Plane. From this, they deduced that there must be another source of emission distributed in such a manner as to compensate for much of the absorption. This source, which came to be known as the

'Galactic Ridge Emission', was studied by Ebisawa et al. (2003), who found that it could be modelled using two components at different temperatures; the first at 0.8 keV, the second a more ionised plasma at 7 keV. Although very little is known about the Ridge Emission, except that is thermal and diffuse, it is 'remarkably similar' (Ebisawa et al. 2003) to, and may be an aspect of, the Galactic Plane Radiation (GPR, see Section 2.8) seen in the vicinity of the Plane in the Galactic Centre direction.

In summary, the general distribution of the SXRB can be fitted using a two-component model, with an angularly-varying thermal component representing the LHB and an isotropic non-thermal component depicting the XRB. Extra components may be added to reflect the contributions of other X-ray sources such as SNRs, the Galactic Centre, Galactic Plane and the Galactic Halo. Often, this produces a very complex spectral model, containing an unusually high number of variables. In many fields of research, this might be perceived as a weakness in the modelling, since the low number of DoF associated with highly variable models can result in the over-fitting of a data-set. When studying the SXRB, however, the number of variables can be justified by the fact that within the model, each plasma component represents the characteristic emission of a completely different structure, and not a detailed aspect of a single object.

4.3 XSPEC

The XSPEC11 (Arnaud 1996) spectral fitting package was used in the work published in Hands (2003), Willingale et al. (2003), and also here, to fit and model the twenty spectra of the SXRB obtained through the reduction process described in Chapter 3. Details of the standard codes, the fitting algorithm and confidence calculations used in this process are presented in the subsections that follow.

4.3.1 The Plasma Codes

Six standard plasma and absorption codes have been used to model the various features present within the SXRB spectra. In brief, the details of these codes, POWER, APEC,

VAPEC, MEKAL, GAUSS and WABS, are as follows[1]:

BKNPOWER

Power law codes come in a number of forms, but two varieties are of particular interest here: single and broken.

The BKNPOWER code, as its name suggests, is a curve described by a broken power law. It has four parameters: a 'break' energy (E_{break}), two power law indices (Γ_1 and Γ_2) which define the gradient either side of the break point, and a normalisation constant K, in photons keV^{-1} cm^{-2} s^{-1} at 1 keV.

It takes the form:

$$A(E) = KE^{-\Gamma_1}, \quad E \leq E_{break}$$
$$A(E) = KE_{break}^{\Gamma_2-\Gamma_1}\left(\frac{E}{1\ keV}\right)^{-\Gamma_2}, \quad E \geq E_{break}$$

Neither the BKNPOWER code, nor the single index version named 'POWER', contains emission line data. They are commonly used to represent the smooth energy continuum produced by non-thermal X-ray sources.

In both Henry et al. (1968) and Willingale et al. (2003) a broken power law was employed to model the XRB, with the absorption frozen at the full Galactic column, calculated using an on-line tool (Angelini 2007). The photon indices were fixed to 2.0 before the break at 0.7 keV, and 1.4 thereafter, in order that the higher value before the break should represent the contribution of the background quasar population, which has now been partly resolved at very faint fluxes in observations by ROSAT and Chandra, while the lower value models the hard, diffuse element of the XRB.

More modern works have employed single power law codes to represent the XRB, with a photon index frozen to 1.4. Hands (2003) used such a model in his doctoral thesis, which

[1] Further information regarding these codes may be found in both the XSPEC manual (K. Arnaud 2007) and in their individual reference publications.

utilized some of the datasets analysed here. In order to provide continuity between these two works, and to minimise the number of parameters in the model, a single power law has been adopted.

APEC & VAPEC

The APEC, or 'Astrophysical Plasma Emission Code' (Smith et al. 2001) is the successor to the Raymond & Smith (1977) thermal plasma model which was commonly used in the past to model the LHB (Marshall & Clark 1984, Snowden et al. 1990*b*). By calculating the emissivities of both the continuum and the emission lines, APEC replicates the total emission spectrum produced by collisionally-ionized diffuse plasma.

The emissivity of a spectral line is defined (Smith et al. 2001) as "the total number of radiative transitions per unit volume, divided by the product of the electron density n_e and the hydrogen (neutrals and protons) density N_H within an astrophysical plasma." Since the number of photons emitted is proportional to the density of the emissive ions, this definition implicitly requires both the elemental abundance and ionization balance for the relevant ion to be specified. Therefore, the APEC contains a catalogue of emission line data for various ionisation states of C, N, O, Ne, Mg, Al, Si, S, Ar, Ca, Fe, and Ni. The abundance of each element within the code is fixed, with He set at cosmic abundance, and the other elements held at solar values, as defined by Anders & Grevesse (1989).

One may fix or fit the temperature of the plasma temperature in keV using the temperature variable within the model. The strength of the emission lines within the code is automatically scaled, with respect to this temperature and to the emission measure of the plasma, and superposed on the continuum. Smith et al. (2001) claim that a typical spectral fit using the APEC will contain in excess of 32,000 unique, sharp emission lines. These lines cannot be seen clearly within a fitted spectrum; instead, the various possible transitions for each ionic state are blended to produce the broader emission peaks commonly observed with the spectra of thermal plasmas.

The normalization of the model is calculated as follows:

$$\frac{10^{-14}}{4\pi[D_A(1+z)]^2}\int n_e n_H \, dV$$

where D_A is the angular size distance to the source (cm), n_e and N_H are the electron and H densities (cm^{-3}), and z is the redshift.

The emission measure of the plasma, which can be calculated from this value using the method described in Appendix C, will be used in Chapter 6 to examine the physical properties of the plasma structures.

The redshift was set to zero in all of the codes, because the signal from the thermal soft X-ray background originates mostly within the confines of the Milky Way.

The VAPEC, or 'Variable Astrophysical Plasma Emission Code' is mathematically identical to the APEC, although the various metal abundances may be set to 1 (solar values, or cosmic for He), or permitted to vary individually within specified limits. In this way, the APEC model can be refined so that specific emission lines may be better accommodated within a fit. The VAPEC variant is particularly useful in younger, more unsettled plasmas, where the ionization balance has been recently disturbed.

MEKAL

The MEKAL code is an extended version of the APEC created by Mewe, Kaastra, and Liedahl, from whom its name is derived. In addition to the extensive APEC line catalogue, MEKAL includes a series of lines from Na, and higher energy transitions from the other elements, particularly those associated with highly-stripped Fe. Like APEC, most of the elemental abundances are set to solar values, He is set to cosmic abundance, and the plasma temperature may be fixed or fitted freely. The normalisation coefficient of the MEKAL code is identical to that used in the APEC, and can be also be used to derive the emission measure of the modelled plasma.

Since MEKAL contains higher energy emission lines than APEC, it is better suited to the high-energy thermal spectra produced in extreme environments, such as stellar coronae. For cooler plasmas, such as those found in SNRs, the APEC is sufficient.

The current reference papers for the MEKAL code are Mewe et al. (1985), Mewe et al. (1986) and Liedahl et al. (1995).

GAUSS

Although not strictly a plasma code, Gaussian curves were included in order to fit the approximately Gaussian internal fluorescence lines created by the interaction of X-ray photons with the aluminium and silicon present within the EPIC detector (see Section 1.3.4). The GAUSS code bundled within the XSPEC package produces a simple Gaussian profile of the form:

$$A(E) = K\frac{1}{\sigma\sqrt{2\pi}}\exp\left[\frac{-(E - E_l)^2}{2\sigma^2}\right]$$

In which E_l is the peak energy of the curve in keV, and its width is σ (also in keV). The curve is normalized by the constant K, which equates to the total number of photons per square centimetre per second required to produce a line of the observed intensity.

WABS

The five codes described above are 'additive'; that is, the curves they produce can be summed algebraically to produce a larger model. The WABS code, by contrast, is 'multiplicative'; it acts on existing additive codes through multiplication, systematically reducing their intensity, and so recreating the effects of absorption.

WABS, the standard absorption code available in XSPEC, is formulated as follows:

$$M(E) = \exp\left[-n_H\sigma(E)\right]$$

where $\sigma(E)$ is the total photoelectric cross-section and N_H is the equivalent hydrogen column to the front of the target object in units of 10^{22} atoms cm^{-2}.

The $\sigma(E)$ values utilized by the code are the so-called 'Wisconsin Cross-sections' calculated by Morrison & McCammon (1983). These are the effective absorption cross-sections per hydrogen atom for the most abundant elements[2] present within the interstellar material, calculated as a function of energy within the $0.3 - 10$ keV range. WABS

[2]Photoelectric absorption cross-sections for the following elements are included in the WABS code: H, He, C, N, O, Ne, Na, Mg, Al, Si, S, Cl, Ar, Ca, Cr, Fe, Ni.

uses the relative abundances of these elements, published by Anders & Ebihara (1982), to automatically calculate the absorption coefficients, and hence it is able to accurately 'absorb' the emission features in other plasma models.

Although WABS adequately represents the absorption of the ISM, the effects of Thomson scattering, where photons are scattered by free charged particles, are not included in the code; nor are the absorptive effects of dust grains, molecules, or localized abundance enhancements.

4.3.2 The Role of Absorption

The neutral hydrogen (see Section 2.1) present within the ISM absorbs energy from incident X-ray photons, reducing the strength of the signal that can be measured. Since the degree of this attenuation is proportional to the depth of the hydrogen column, it can be used as a virtual 'yard-stick': for any line of sight, the emissive source subject to the greatest degree of absorption must also be the most distant.

Absorption affects both the overall intensity of a signal and the shape of its spectrum: soft, low energy X-rays are absorbed more readily than harder ones. This changes the profile of the spectrum by reducing its overall intensity and skewing it towards higher energies. In a model containing many components, this effect causes the less absorbed components to dominate at lower energies.

Together, these effects can be used to differentiate between the signals produced by similar emissive structures lying at different distances along the same line of sight. This is helpful because the spectrum of the SXRB is an amalgamation of emission from various structures, at different distances from the Earth, which are all thermally emissive and have similar chemical compositions and temperatures. Therefore, when modelling the SXRB spectrum the effects of absorption must be included. This point is illustrated in Figure 4.1.

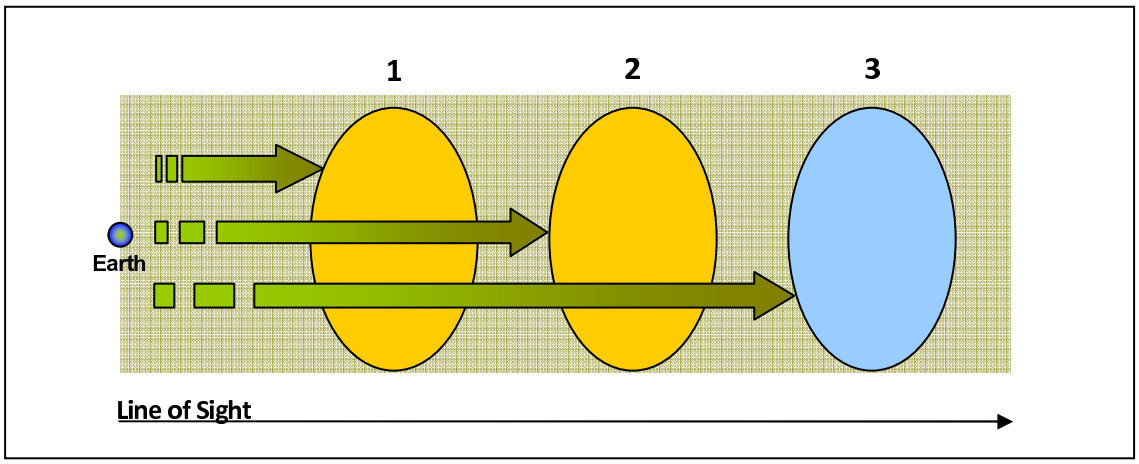

Figure 4.1: Three thermal X-ray sources (1, 2 and 3) lie at successively greater distances from the Earth. 1 and 2 are similar and lie within the Milky Way. Source 3 is significantly different to 1 and 2, and lies beyond the Milky Way. The depth of the absorbing column, indicated by the green arrows, is defined as the distance from the observer (Earth) to the front face of each source. The total flux observed is the sum of contributions from the emissive structures, together with the effects of absorption acting on each one. To fit the spectrum, one would require a model of the form:

$$(\mathrm{WABS1} \times \mathrm{APEC1}) + (\mathrm{WABS2} \times \mathrm{APEC2}) + (\mathrm{WABS3} \times \mathrm{APEC3})$$

where WABS1 $<$ WABS2 $<$ WABS3, and where WABS3 is set to the Galactic N_H. Although similar, the separate contributions of 1 and 2 can, in theory, be identified because they are subject to different amounts of absorption, making the emission from source 1 appear softer and more intense than that of source 2.

4.3.3 Fit Statistics

Once a model has been defined, its variables must be systematically altered in order to match it to the actual observed spectrum. Within XSPEC, this is achieved using a modified Levenberg-Marquardt algorithm: a fitting procedure that searches the local parameter space, incrementally adjusting the model variables in order to improve the fit to the data and so minimize the chi-squared (χ^2) statistic.

The XSPEC manual (K. Arnaud 2007) defines χ^2 value as the squared difference between the incident (C) and the predicted (C_P) count rates in each channel (I) of each data point in the spectrum, divided by the error in that data point (σ(I)), squared and summed over

all of the data points. This is formulated as follows, where C(I) is the number of counts in a channel:

$$\chi^2 = \sum \left[\frac{(C(I) - C_P(I))^2}{(\sigma(I))^2} \right]$$

The error for each channel σ is usually estimated as the square root of measured counts in that channel (K. Arnaud 2007).

The χ^2 statistic indicates the goodness-of-fit of the model to the data for a given number of DoF, which is itself equal to the number of plotted data points used in the χ^2 calculation, minus the number of free parameters.

If the χ^2 statistic exceeds a particular value for a number of DoF, determined through consultation of an appropriate look-up table, then the model can be deemed inadequate. The normalized version of the χ^2 statistic, the 'reduced chi-squared' (designated χ^2_ν) was employed here.

The χ^2_ν is simply the χ^2 value divided by the DoF. Ideally, it should be equal to 1, so that the χ^2 value is equal to the DoF. A χ^2_ν value much greater than one indicates that a model's fit to the data is poor, whereas a value much less than one suggests that the errors on the data have been overestimated.

Historically, the strict interpretation of the χ^2_ν value has been relaxed for SXRB spectra, with published results commonly having χ^2_ν values around 1.3 (Snowden et al. 1994, 1998). Although high, these values are excused on the basis of poor data quality, low survey exposure times, and intrinsic, localized variation of X-ray intensity: all factors which decrease the accuracy of the fits. In addition, the numerous sources contributing to the overall flux of the DXRB produce non-statistical scatter in the data, making modelling more difficult, and often increasing the χ^2_ν beyond formally acceptable levels.

4.3.4 Navigating the Parameter Space

The XSPEC fitting algorithm operates by incrementally altering the values of the free parameters within a multi-dimensional parameter space. In the mind's eye, this space can be pictured as an undulating plane, pockmarked with steep-sided craters. Each crater represents a region in which the set of variable parameters fits the data well, and the χ^2

is relatively low: a 'minimum'. At the bottom of the deepest crater in the plane, where the χ^2 value is at its lowest, and the model's fit to the data is as close as is possible to achieve. This is the best-fit model, and is described by the set of best-fit parameters.

During the fitting procedure, XSPEC explores the parameter space, seeking to minimize the χ^2 statistic. In doing so, it has the unfortunate tendency to get stuck in local minima, stalling the fitting algorithm and preventing the best fit from being achieved. Three actions were undertaken during the new analysis to combat this scenario.

First, hard upper and lower limits were established for each of the variable parameters. This effectively restricted the area of the parameter space, and limited the number of minima present.

Second, sensible initial values, based on the results of the preliminary fits mentioned above, were assigned to the variable parameters. By giving the model a head-start in this manner, the time taken to achieve a good fit was dramatically reduced.

Third, the magnitude of the incremental step taken by each parameter during the fitting process was manually set to be two orders of magnitude lower than the parameter value itself. For example, a parameter with a value of $\sim$1, would be given a step value of 0.01. This ensured that when a local minimum had been detected, the step size was sufficiently large to pull the fit back towards the best fit, but not so great that a potential best-fit minimum could be passed over entirely.

4.3.5 Confidence Intervals

When the best-fit parameters had been determined, the XSPEC 'error' command was used to calculate the 90% confidence interval for each of the values. The error command works by incrementally adjusting the parameter of interest within its allowed hard limits until the overall χ^2 statistic for the fit, minimised by allowing all other non-frozen parameters to vary, is equal to the 'best-fit' value of the fit statistic, plus an indicated deviation; For a confidence interval of 90% on one parameter this amount, the delta chi-squared, is defined as 2.706 (K. Arnaud 2007).

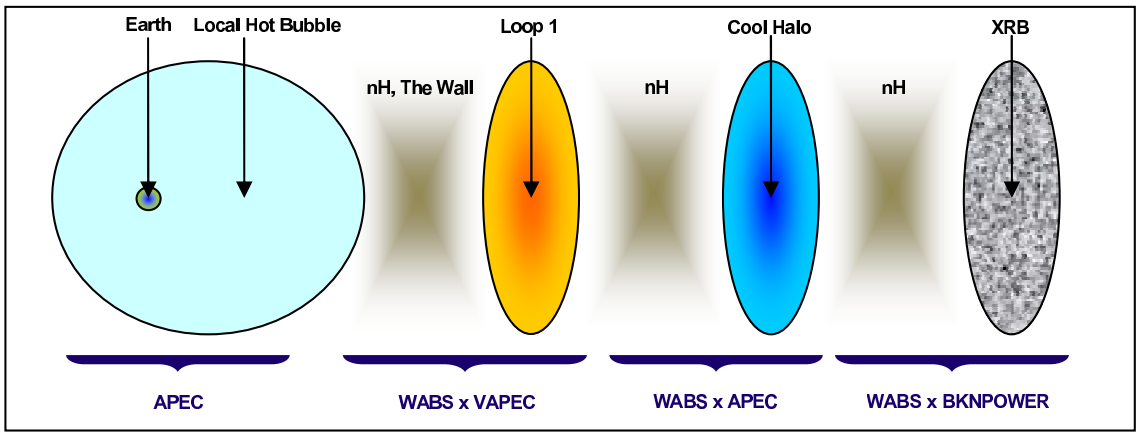

Figure 4.2: The arrangement of emissive structures and associated absorbing columns assumed by Willingale et al. (2003) to lie along the line of sight from the Earth towards the Galactic Centre, together with the model components used to represent them.

4.4 Modelling the DXRB: The Previous Analysis

The first time that the DXRB spectra from the two NPS fields were analysed, by Willingale et al. (2003), it was assumed that the emissions originated from four distinct structures. In order of distance from the Earth, these were the LHB, Loop 1, a cool Galactic Halo, and the XRB. This arrangement is illustrated in Figure 4.2.

On the basis of their interpretation, and in agreement with the findings described in Section 4.2, Willingale et al. (2003) modelled the LHB with an unabsorbed APEC, at a fixed temperature of 0.1 keV.

Loop 1 was represented by an absorbed VAPEC, with a fixed temperature 0.3 keV. Although most of the elements were held at solar abundance, oxygen, neon, iron, and magnesium were allowed to float separately, allowing the prominent O VIII, Fe XVII, Ne IX and Mg XI emission lines to be fitted more accurately. An absorbing component, acting on the VAPEC, was used to represent the Wall as the fraction of the total Galactic hydrogen column density lying between the LHB and Loop 1.

Next, Willingale et al. (2003) used an absorbed APEC to model what they believed to be the emission of a cool ($\sim$ 0.1 keV), isotropic Galactic Halo. As this Halo was assumed

to surround the entire Galaxy but not to lie beyond it, the absorbing column acting on the APEC was set to be close, but not equal, to the full Galactic column density. This served to absorb the bulk of the flux from the APEC, allowing it to dominate only in the $0.4 - 0.6$ keV range in which the O VII line, a characteristic of plasma at 0.1 keV, features prominently.

Willingale et al. (2003) employed a broken power-law to model the XRB, with the absorption frozen at the full Galactic column, calculated using an on-line tool (Angelini 2007). This power-law was given two fixed photon indices, 2.0 before the break at 0.7 keV, and 1.4 thereafter. The higher value before the break modelled the contribution of the background quasar population, which has now been partly resolved at very faint fluxes in observations by ROSAT and Chandra, while the lower value represented the hard, diffuse element of the XRB. The normalisation of the broken power law was frozen to a value equivalent to a flux of 9.0 photons s^{-1} cm^{-2} sr^{-1} keV^{-1} at 1 keV, calculated using the method shown in Appendix C, and based on a measurement made by Lumb, Warwick, Page & Luca (2002).

Finally, two GAUSS components were added to represent the prominent Al K_α and Si K_α fluorescence lines present in the EPIC. These spectral artefacts are, as explained in Section 3.5.5, the result of an interaction between the incident charged particles and the substrate of the EPIC detector, and are not part of the X-ray background. These lines were included in all of the models used in this research.

Hence, the model of Willingale et al. (2003), for observations towards the Galactic Centre can be formulated as follows:

$$\begin{aligned}&\text{APEC} + (\text{WABS} \times \text{VAPEC}) + (\text{WABS} \times \text{APEC}) + (\text{WABS} \times \text{BKNPOWER}) \\ &+ \text{GAUSS1} + \text{GAUSS2}\end{aligned}$$

Which represent the following features:

$$\begin{aligned}&\text{LHB} + (\text{Loop 1}) + (\text{Galactic Halo}) + (\text{XRB}) \\ &+ \text{Al } K_\alpha + \text{Si } K_\alpha\end{aligned}$$

The Willingale et al. (2003) paper did not include analysis of fields located in the Anti-

centre direction.

4.5 The New Analysis

The twenty XMM observations used in this research fall into two main categories: the ten Oxygen fields, which are spread across the sky in the Anti-centre direction, far from the Galactic Centre, and the ten Loop I fields, all of which lie within the projected boundary of the Loop I superbubble (Figure 3.2). The Loop I fields may be split further into two sub-categories, the Northern fields in the northern half of Loop I, comprising the Northern Bulge fields X1, X2 & X3 and the NPS fields N4 & N5, and the Southern fields lying in the southern half of Loop I, below the Galactic Plane; B1, B2, B3, B4 & B5.

While the NPS fields are the subject of the Willingale et al. (2003) paper, and the Southern fields appeared in Hands (2003), this is the first time that the Oxygen fields have been used in the study of the SXRB. As explained in Section 3.4, these were selected on the basis of two criteria: the first, that their co-ordinates must lie in the Anti-centre direction, produced a set of fields which are spread over a large area of the sky. The second, that they should contain minimal contaminating X-ray emission, gave rise to the expectation that the bulk of the flux in the spectra should comprise the isotropic emissions of the XRB and the LHB and, possibly, the Galactic Halo. Several aspects of the analysis are also new, in particular, this is the first time that pn data has been included in SXRB analysis; an improvement which reduces the systematic errors and uncertainty in the fitted models.

Before the spectra were fitted, the measures described in Sections 4.5.1, 4.5.2 & 4.5.3 were undertaken to ease the process.

4.5.1 Constraining the Low Energy Region

Because the XMM background subtraction procedure is known to work particularly well between 0.4 – 4.0 keV, only the events in this range were included, while the rest of the EPIC data was ignored. Although this method is valid, it would exclude a significant proportion of the LHB flux. To remedy this situation, two data points from the RASS

(Section 1.3.3) were included and fitted jointly with the XMM spectra to constrain the model in the $0.1 - 0.4$ keV region. These were obtained by calculating the average photon count rates from the $\frac{1}{4}$ keV PSPC energy band RASS map for each of the twenty field positions using an on-line tool (Sabol 2007).

4.5.2 Reducing the Number of Variables

As demonstrated in Section 4.2, the models used to describe the SXRB contain numerous components, resulting in an unusually high and unwieldy number of parameters, each of which may be fixed to a particular value ('frozen') or allowed to vary ('float') during the fitting process. This situation is further complicated by the fact that for each field, data from MOS, pn and ROSAT spectra were loaded into XSPEC, effectively tripling the number of parameters available at a stroke, as the model could be applied separately to each data set. The challenge, therefore, when using such a model, is to strike a balance which allows the key parameters to vary freely, whilst ensuring that the model is sufficiently constrained so that it eventually converges.

To reduce the number of free parameters, most of them (the normalisations, temperatures, abundances and absorptions) were dynamically tied across the MOS, pn and ROSAT spectra for each field. Only the normalisations and widths of the separate Gaussian components were left untied, because these factors vary as a function of X-ray flux incident upon the individual detectors.

While this helped to ease the instability, a large number of parameters still remained, making it possible to produce many statistically 'good' but unphysical fits. To create sensible fits, the number of parameters was further reduced by freezing some of them to values established in previous research (see Section 4.2). Not only did this reduce the DoF in the fit, but it also allowed stricter limits to be obtained on the remaining free parameters.

4.5.3 The Fitting Procedure

For each field, the MOS, pn and ROSAT data were loaded into XSPEC, together with the appropriate calibration and background files.

The model was input, and in fields where data from both MOS and pn were available, a multiplying constant was included but made to act only on the pn data. This served to make up for uncertainties in the absolute calibration of the individual detectors, allowing them to be fitted in tandem. It also served to designate the MOS data as the dominant data set in the fit; consequently, any calculations requiring the area of the detector's field of view were performed with reference to the MOS cameras.

The models were prepared using the methods described above: by freezing certain values, tying the remaining variables across the three data sets, and establishing their iteration steps and starting values. WABS codes representing the Galactic hydrogen column were frozen to the value appropriate to their observation coordinates. The densities of other absorbing codes within the model were then boundary limited, to prevent their increase above the total Galactic column.

The energies of the Gaussian peaks were manually fixed to 1.49 keV and 1.76 keV, to represent the Al K_α and Si K_α fluorescence lines present in the EPIC data. All chemical abundance ratios were set to solar values, and the fitting routine was run. When this rough fit had been completed, the normalisations of the components were frozen.

Next, the temperatures and normalisations of the plasma codes had to be more accurately defined. In order to give priority to the soft contributors to the local ISM, and so ensure that they were not overpowered by the higher energy components within the models, each plasma code (with its absorption, if not frozen to Galactic N_H) was fitted in turn, in order of increasing energy.

Studies of Loop I by Willingale et al. (2003) and Snowden et al. (1990*b*) revealed that its chemical composition deviates slightly from solar abundance, and is depleted in oxygen, neon, magnesium and iron. Therefore, in fields where the quality was sufficiently high, the fits were further refined by allowing the relative abundance of these elements to vary; however, in order to minimise the number of free parameters, the abundances of neon,

magnesium and iron were tied. Since oxygen is the subject of the next chapter, it was permitted to fit independently. None of the elements was allowed to rise above solar abundance, and in fields where the data was considered too poor to fit the emission lines accurately, the relative abundances were frozen to 1.

Finally, to optimise the parameter values, all of the roughly-fitted variables were thawed and made to fit simultaneously, thus producing the best possible fit of the model to the data.

4.6 Modelling the Oxygen fields

While the properties of both the LHB and the XRB have been studied by several researchers in some detail, the Galactic Halo is relatively unknown. The natural expectation was, however, that if detectable at all, the Halo signal should be more prominent in the Oxygen fields where the X-ray environment is less complex than that in the Galactic centre direction, and where the line of sight to the Halo would be almost unimpeded. With this in mind, the Oxygen fields were chosen as the starting point for the new analysis.

4.6.1 Preliminary Fits

Initially, the following simple model was applied to the ten Oxygen fields:

$$\text{APEC} + (\text{WABS} \times \text{POWER}) + \text{GAUSS1} + \text{GAUSS2}$$

Representing:

$$\text{LHB} + (\text{XRB}) + \text{Al } K_\alpha + \text{Si } K_\alpha$$

Here, the APEC represents the unabsorbed flux from the LHB which, as in Willingale et al. (2003), had a plasma temperature frozen to 0.1 keV, while the normalisation was

allowed to float. The power law, modelling the XRB, was set behind the full Galactic column. In all ten fields, it was given a photon index of 1.4, and a normalisation frozen to a value equivalent to a flux of 9 photons s^{-1} cm^{-2} sr^{-1} keV^{-1} at 1 keV, calculated using the method shown in Appendix C. The same procedure was employed by Hands (2003), who used the same flux values taken from Lumb, Warwick, Page & Luca (2002).

The model worked well at the low energy end of the spectra, but fitted poorly in all fields between $0.6 - 1.0$ keV. In this range, a soft thermal excess flux with weak, unfitted emission lines was clearly visible. The fit was also poor in the high energy end, where the power law component could be seen to sit above the data points.

Although the fitted parameters showed the thermal excess to be widespread, it was weak, and since it had not been accommodated during the fitting process by the unabsorbed APEC modelling the LHB, it had to be differentiated somehow from the LHB signal, either by absorption, by temperature, or both.

From this starting point, the Oxygen fields were refitted five more times (the A and B series of fits), using the simple model plus an absorbed VAPEC component to accommodate the soft excess. In each series, the model was slightly altered, in order to establish the position and temperature of the excess, and hence determine whether or not it was produced by a Galactic Halo. These fit variations are described in the sections that follow and, as the best-fit model shows, the excess is consistent with that expected from a Galactic Halo.

4.6.2 Model A

First, the three-component Model A, illustrated in Figure 4.3, was fitted to the Oxygen fields:

$$\text{APEC} + (\text{WABS} \times \text{VAPEC}) + (\text{WABS} \times \text{POWER}) + \text{GAUSS1} + \text{GAUSS2}$$

Representing:

$$\text{LHB} + (\text{Absorbed Hot Halo}) + (\text{XRB}) + \text{Al } K_\alpha + \text{Si } K_\alpha$$

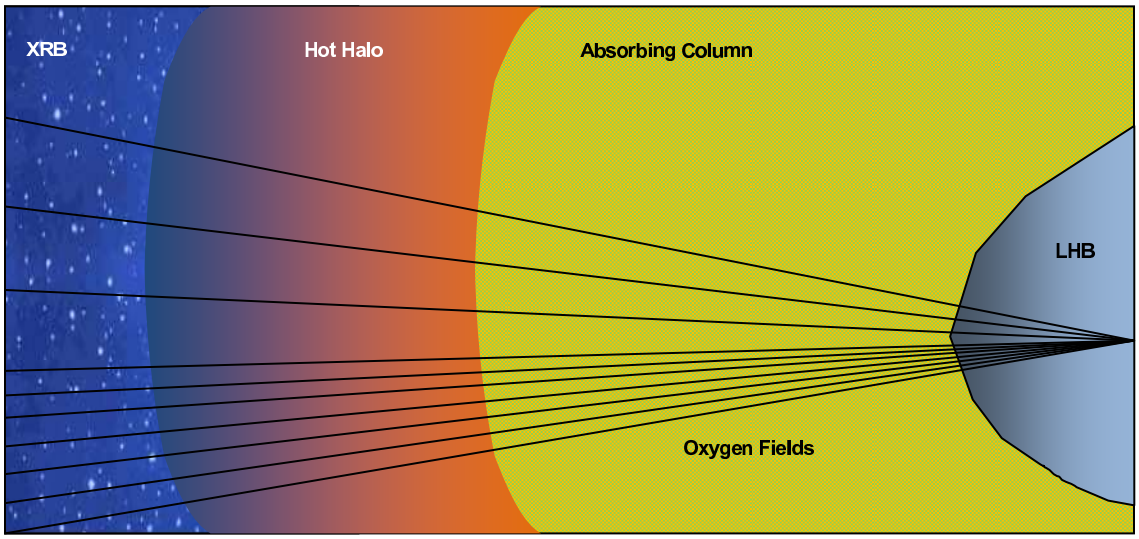

Figure 4.3: Modelling the Oxygen fields: A cartoon illustrating the structures represented by Model A

In Model A, the normalisation of the unabsorbed APEC, representing the LHB, was allowed to float freely, while its temperature was frozen to 0.1 keV. Willingale et al. (2003) reported an absorbed Galactic Halo at 0.1 keV, and so in this model, the absorbed VAPEC used to represent the Halo's flux was set behind the full Galactic column. However, since its signal had not been accommodated in the preliminary fits by the 0.1 keV APEC used to contain the LHB, the temperature and normalisation of the VAPEC were allowed to float. For eight of the ten fields the relative elemental abundances in the VAPEC were frozen to solar values, but in the higher-quality spectra O1 and O2, where the emission lines were clearly discernable, some of the elemental abundances were allowed to fit separately. Neon, magnesium and iron were tied and fitted in tandem; a compromise which allowed the fits to be refined while minimising the number of free parameters. Oxygen was fitted separately, in order to fit the prominent O VII and O VIII lines more accurately.

Model A: Discussion

Since the Oxygen fields are spread out across the whole of the Anti-centre hemisphere, they may contain all manner of diffuse X-ray sources. The fact that Model A produced an

Table 4.1: The A-Series best-fit parameter values for the Oxygen fields. For a key to the table headings, see Appendix B.

Field	O1	O2	O3	O4	O5	O6	O7	O8	O9	O10
Latitude	-9.50	-20.80	0.43	-3.30	-37.36	-17.55	21.11	-3.44	-34.56	1.12
XRB Norm	4.29E-4	4.36E-4	4.54E-4	4.65E-4	4.59E-4	4.29E-4	4.18E-4	4.81E-4	4.09E-4	4.35E-4
LHB Norm	4.59E-4	1.28E-3	1.73E-3	8.46E-4	1.31E-3	1.03E-3	1.45E-3	9.24E-4	8.67E-4	7.57E-4
Halo Norm	2.39E-3	7.01E-4	1.88E-3	2.84E-3	3.22E-4	4.21E-4	3.13E-4	1.60E-3	9.47E-4	5.00E-3
Halo kT	0.18	0.25	0.25	0.25	0.33	0.23	0.24	0.32	0.19	0.29
Relative Abundances:										
O	0.27	0.85	1.00	1.00	1.00	1.00	1.00	1.00	1.00	1.00
Ne/Mg/Fe	0.85	1.00	1.00	1.00	1.00	1.00	1.00	1.00	1.00	1.00
χ^2	387.13	1118.50	548.40	565.70	337.3	250.10	508.40	243.60	824.50	347.20
DoF	225	789	352	568	234	232	232	228	232	232
χ^2_ν	1.72	1.42	1.56	1.00	1.44	1.08	2.19	1.07	3.55	1.50

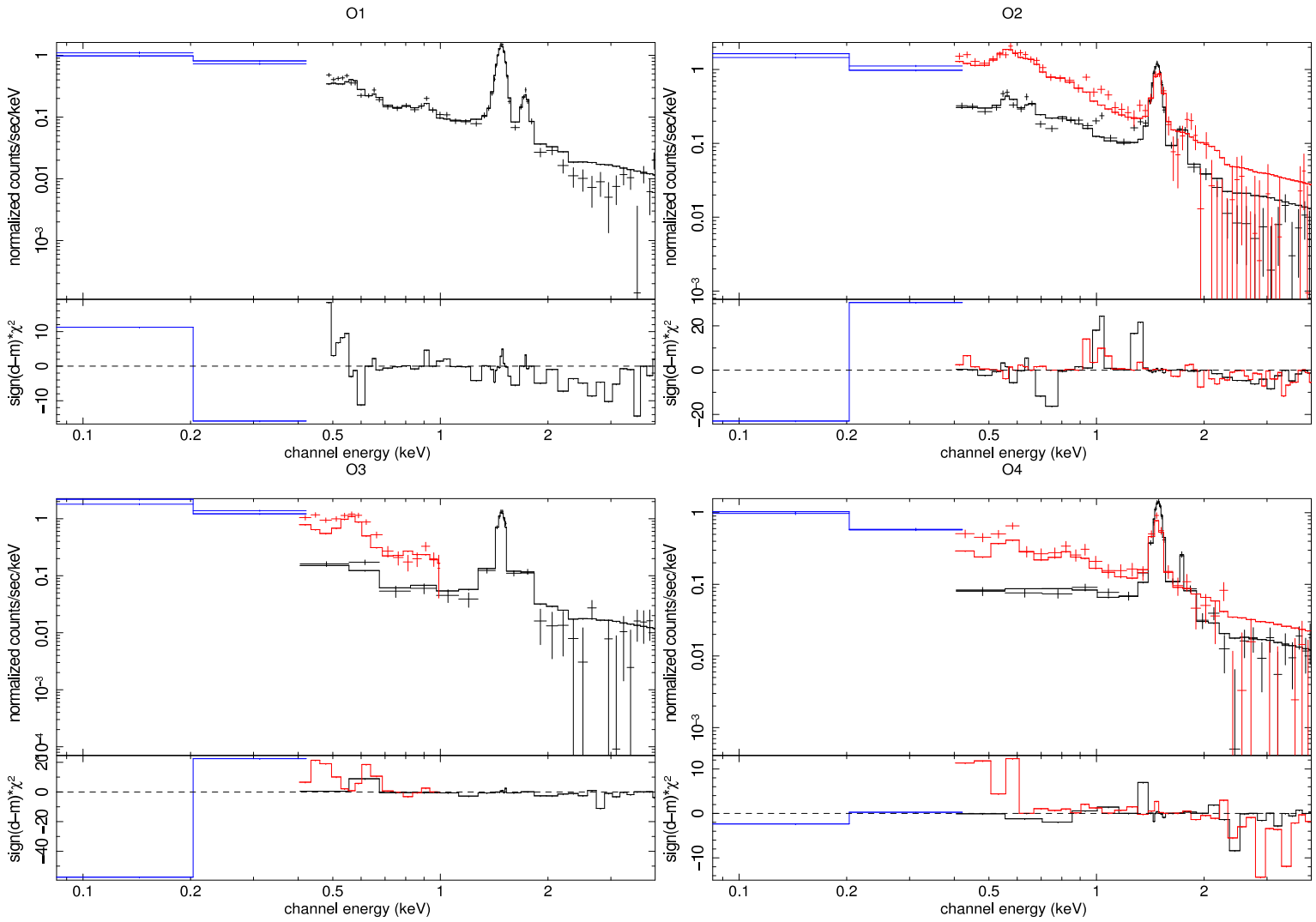

Figure 4.4: Model A: The best-fit spectra for O1, O2, O3 & O4. The traces shown are: ROSAT (blue), MOS (black) and pn (red).

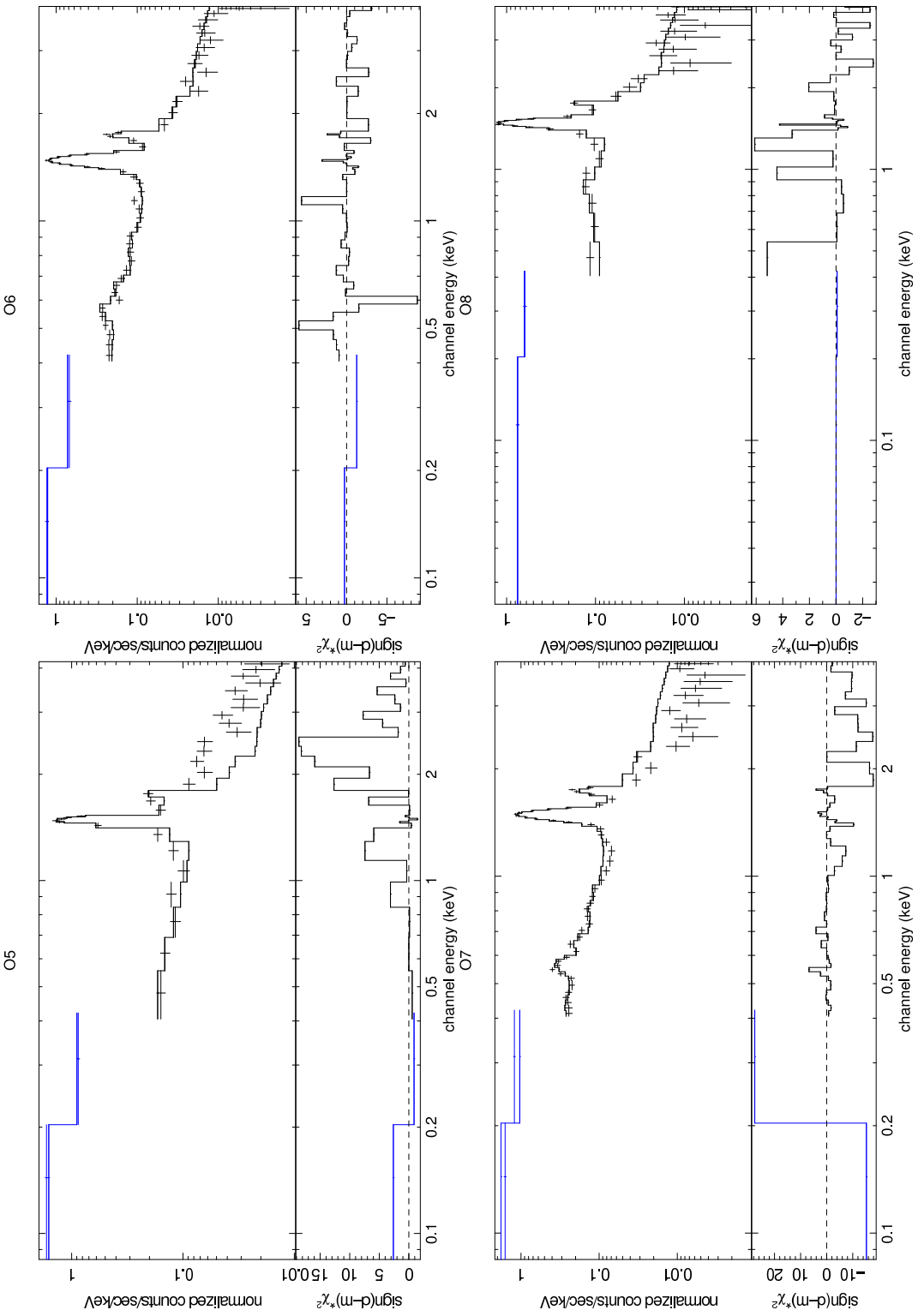

Figure 4.5: Model A: The best-fit spectra for O5, O6, O7 & O8. The traces shown are: ROSAT (blue), MOS (black) and pn (red).

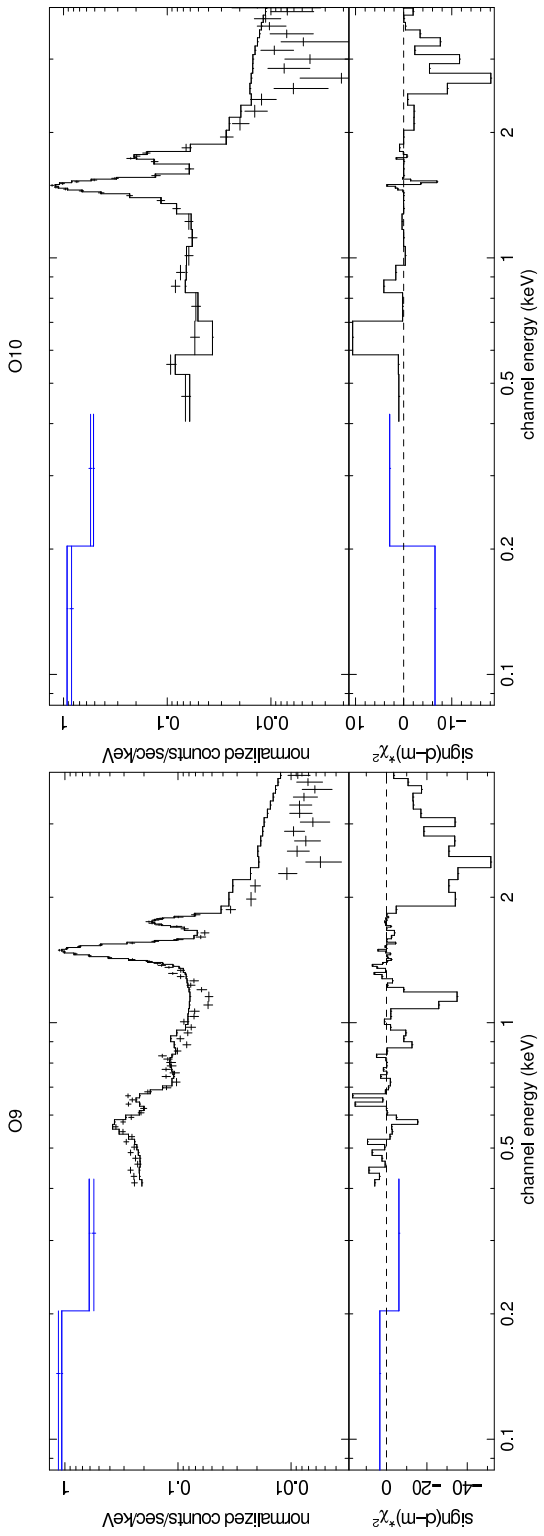

Figure 4.6: Model A: The best-fit spectra for O9 & O10. The traces shown are: ROSAT (blue), MOS (black) and pn (red).

adequate fit in all of the fields indicated that, while not comprehensive, it at least contained the major sources present in the Anti-centre direction. Certainly, the detection of flux from each of the three model components shows that they are common to all of the Oxygen fields.

As the fitted spectra (Figures 4.4, 4.5 & 4.6) illustrate, there is no major disparity between the data and the model. Both the LHB and Halo components appear to fit reasonably well, with the model closely fitting the data points between $0.1 - 1.5$ keV, but once again, the power law representing the XRB proved a poor match to the data. Although the power law is certainly required by the fit, the frozen value of the normalisation is too high, causing the model to sit above the data points in the high energy regime in all of the fields except O5. Because of this discrepancy, the value of the reduced chi squared statistic in many of the fields was so high that it was unusable as a diagnostic. In such circumstances, many statistically identical fits could be produced for the same data set, each with wildly different parameter values. It also hampered the data analysis, as XSPEC can reliably calculate 90% confidence intervals on fitted parameters only when the reduced chi-squared value is lower than $\sim$1.5. All of this raised a question: Why did there appear to be such a difference between the frozen XRB flux value and the data?

The 9 photons s^{-1} cm^{-2} sr^{-1} keV^{-1} at 1 keV flux used in these fits, the same as that used in Hands (2003), is a figure derived originally from work done by Lumb, Warwick, Page & Luca (2002) who, through thin filter observations of the XRB, measured a flux of 8.44 ± 0.24 photons s^{-1} cm^{-2} sr^{-1} keV^{-1} at 1 keV. This value was determined through measurements between $2 - 10$ keV: a much wider range than that used in this research, where only photons from $0.1 - 4.0$ keV are considered.

While it is the accepted view that the XRB is uniformly isotropic, the actual magnitude of the XRB flux intensity is not clear from the literature. For example, Barcons & Fabian (2002) state that "the intensity of 1.7 photons s^{-1} cm^{-2} sr^{-1} keV^{-1} at 1 keV, in the $2 - 10$ keV range, is consistent with current measurements of the XRB." Luca & Molendi (2004) found that the $2 - 8$ keV XRB spectrum, which they modelled with a power-law of photon index 1.41 ± 0.06, had a normalisation of 2.46 ± 0.09 photons s^{-1} cm^{-2} sr^{-1} keV^{-1} at 3 keV, equivalent to $\sim$ 11.6 photons s^{-1} cm^{-2} sr^{-1} keV^{-1} at 1 keV, and finally, Hickox & Markevitch (2006) modelled the XRB with a power law with a photon index of 1.5, and found that, in the

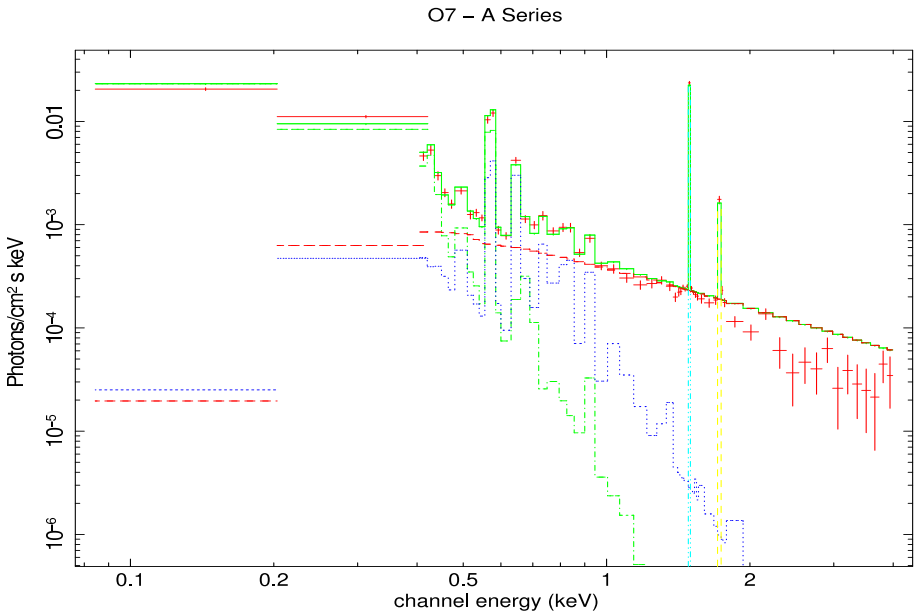

Figure 4.7: Model A: Unfolded Spectrum of Field O7. The red crosses mark the data points. The traces are as follows: Red dashed (XRB power law), green dot-dash (LHB APEC), blue dot (Halo APEC). The cyan and yellow peaks are the two Gaussian curves.

0.5 – 8 keV range, the flux was closer to 2.6 photons s^{-1} cm^{-2} sr^{-1} keV^{-1} at 1 keV.

It is apparent that in the studies mentioned above, the XRB was observed over a large energy range. However, 0.1 – 4.0 keV would constitute only the soft tail of the total XRB flux. Soft photons are affected more by absorption than harder ones, and so when fitting the XRB in the Oxygen fields, with their relatively high levels of absorption, it is not surprising that the data sat below the expected level. Also, as the unfolded spectrum (Figure 4.7) shows, the power law flux, which should underlie the whole spectrum, dominates in the energy range between 2 – 4 keV, but here sits above the data points. The LHB and Halo components fit well, and lie between 0.1 – 1.5 keV. Because the bulk of the XRB flux lies beyond the energy limit of this study, most of the signal has not been included in the reduced spectra. The full Galactic column further reduces the influence of the XRB at low energies, again reducing its presence in the spectra.

However, this raised another question: why did the frozen value of 9 photons s^{-1} cm^{-2} sr^{-1} keV^{-1} at 1 keV work in the similar analysis performed in Willingale et al. (2003) and Hands (2003), but not here? In those works, the authors analysed only fields from the Galactic Centre and Galactic Ridge. In those regions, as will

be seen in the sections that follow, the hard emissions from both the Galactic Plane and Galactic Bulge supplement the flux at high energies, helping to lift the spectra towards the 'expected' flux level of the XRB. These sources are not present in the Anti-centre fields, and as a result, the data sits below the frozen XRB component.

However, neither absorption nor energy ranges can explain why field O5 should be exceptional. Why is the data so much brighter in O5? Closer inspection of the original image from which the O5 spectrum was derived revealed a small but bright X-ray source lying over a chip boundary in the MOS detector. While the source detection algorithm described in the previous chapter is good, it is not perfect, and since it has proved impossible to remove the object completely, part of its flux remains in the data set. It would appear that hard emission from this source has raised the high energy end of the O5 spectrum beyond the level expected from a cleaner X-ray background.

This is not the first occasion on which the XRB has not behaved as expected: Kuntz & Snowden (2008) had a similar experience. After finding that a fixed XRB value did not match their spectra, they allowed the normalisation of the XRB to float, and in so doing, found not only that this greatly improved the fit, but it also had a negligible effect on the fitted values of the softer, more local components. In all subsequent series of fits in this research, the normalisation of the power law will be allowed to float. Consequently, the flux values calculated from the fitted power law normalisations in any of the subsequent fits can be said to constitute only a fraction of the actual XRB flux.

The temperature of the VAPEC component is also interesting. In Willingale et al. (2003), the temperature of the Halo was said to be 0.1 keV, but in this series of fits, the temperature of the VAPEC ranges from $0.18 - 0.33$ keV. This is a wide range, and considerably higher than 0.1 keV, but it does tally well with the Halo temperature proposed by Spitzer (1956). The fields observed by Willingale et al. (2003) were all in the Galactic Centre direction. It is possible that their interpretation of the observed 0.1 keV signal in that direction was mistaken. If this is the case, then the thermal excess modelled here by the absorbed VAPEC is the signal from the Halo, while the 0.1 keV in the Galactic Centre direction signal has some other, as yet unidentified, source.

4.6.3 Model B: Four Variations on a Theme

Model A established that the LHB, a fraction of the XRB, and another thermal component could be detected in the Oxygen fields. To determine whether or not the thermal 0.25 keV signal was from the Halo and not another more local source, the Oxygen fields were refitted using four variations of the following model, forming the B-series of fits. In all four of the four variants, the temperature of the APEC was frozen at 0.1 keV, and the absorption of the power law was set to full Galactic Absorption. The normalisations of both components were allowed to float.

$$\text{APEC} + (\text{WABS} \times \text{VAPEC}) + (\text{WABS} \times \text{POWER}) + \text{GAUSS1} + \text{GAUSS2}$$

Representing:

$$\text{LHB} + (\text{Galactic Halo}) + (\text{XRB}) + \text{Al } K_\alpha + \text{Si } K_\alpha$$

Model B(a)

In this first variation, the temperature of the VAPEC component was allowed to vary, but was not absorbed (the WABS code was set to zero). In this way, it was made to be 'local', positioned directly outside the LHB. A cartoon illustrating the B(a) model is shown in Figure 4.8, and the fitted parameters from this series are shown in Table 4.2.

Model B(a) Discussion

Fitting the thermal component as a local source did not work particularly well, as evidenced by the relatively high reduced chi squared values. Bringing the component into the local area has also adversely affected the measurement of the LHB. This situation occurred because the removal of the absorption from the VAPEC component placed it at the same spatial position as the plasma from the LHB: hence, the two thermal components are forced to fit this portion of flux. In field O1, this effect was so severe that

Table 4.2: The B(a)-Series parameter values for the Oxygen Fields. For a key to the table headings, see Appendix B.

Field	O1	O2	O3	O4	O5	O6	O7	O8	O9	O10
Latitude	-9.50	-20.80	0.43	-3.30	-37.36	-17.55	21.11	-3.44	-34.56	1.12
XRB Norm	3.63E-4	3.78E-4	2.00E-4	3.12E-4	6.75E-4	4.08E-4	2.73E-4	4.69E-4	2.88E-4	3.22E-4
LHB Norm	0	8.76E-4	1.48E-3	7.62E-4	1.25E-3	7.95E-4	1.22E-3	7.98E-4	4.40E-4	6.87E-4
Halo Norm	1.03E-3	5.73E-4	2.48E-3	1.39E-4	8.25E-5	2.90E-4	3.43E-4	2.09E-4	4.99E-4	1.28E-4
Halo kT	0.20	0.26	0.25	0.43	0.33	0.24	0.26	0.40	0.22	0.74
Relative Abundances:										
O	0.66	1.00	1.00	1.00	1.00	1.00	1.00	1.00	1.00	1.00
Ne/Mg/Fe	0.93	1.00	1.00	1.00	1.00	1.00	1.00	1.00	1.00	1.00
χ^2	438.40	1123.70	304.14	581.96	295.33	253.74	341.66	280.22	545.75	368.07
DoF	224	789	232	567	233	231	231	227	231	231
χ^2_ν	1.96	1.42	1.31	1.03	1.27	1.10	1.48	1.23	2.36	1.59

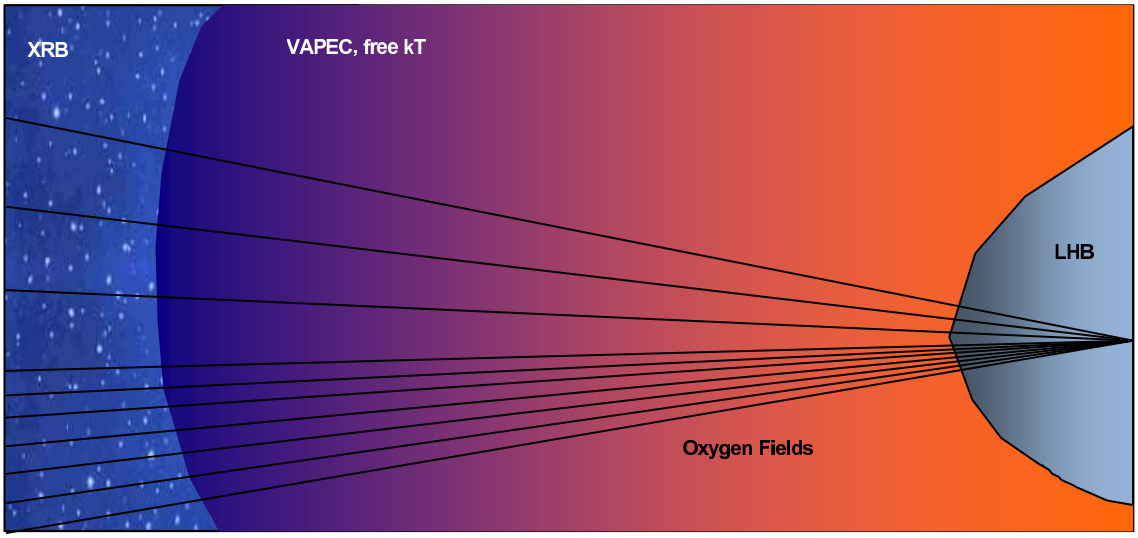

Figure 4.8: Modelling the Oxygen Fields: A cartoon illustrating the structures represented by Model B(a)

the normalisation of the APEC fell away to zero, effectively rejecting the LHB from the model. This instability in the low energy region is also responsible for the large range of temperatures determined for the VAPEC component, varying between 0.20 – 0.74 keV.

Model B(b)

In the second variation, to reduce the confusion in the low energy end of the spectra, the temperature of the VAPEC component was fixed at 0.25 keV. Again, the VAPEC was not absorbed, keeping the component 'local'. A cartoon illustrating the B(b) model is shown in Figure 4.9, and the parameters from this series of fits are shown in Table 4.3.

Model B(b) Discussion

Since both the APEC and VAPEC remain unabsorbed, the conflict between them in the low energy end of the spectra persists. Also, even though the model has been simplified, the fit statistics are generally inferior to those in Series B(a). This is because, by fixing the temperature of the VAPEC, the ability of the two thermal components to accommodate

Table 4.3: The B(b)-Series parameter values for the Oxygen Fields. For a key to the table headings, see Appendix B.

Field	O1	O2	O3	O4	O5	O6	O7	O8	O9	O10
Latitude	-9.50	-20.80	0.43	-3.30	-37.36	-17.55	21.11	-3.44	-34.56	1.12
XRB Norm	3.35E-4	3.87E-4	1.99E-4	3.93E-4	6.92E-4	4.03E-4	2.75E-4	5.36E-4	2.61E-4	3.89E-4
LHB Norm	8.49E-26	8.47E-4	1.49E-3	6.53E-4	1.23E-3	8.15E-4	1.22E-3	6.77E-4	6.47E-4	5.59E-4
Halo Norm	2.39E-3	5.84E-4	2.45E-4	1.99E-4	8.54E-5	2.84E-4	3.46E-4	2.60E-4	4.33E-4	1.72E-4
Halo kT	0.25	0.25	0.25	0.25	0.25	0.25	0.25	0.25	0.25	0.25
Relative Abundances:										
O	0.22	1.00	1.00	1.00	1.00	1.00	1.00	1.00	1.00	1.00
Ne/Mg/Fe	0.12	1.00	1.00	1.00	1.00	1.00	1.00	1.00	1.00	1.00
χ^2	471.17	1126.13	300.43	637.88	298.38	255.66	343.99	354.70	684.59	567.38
DoF	226	790	233	568	234	232	232	228	232	232
χ^2_ν	2.08	1.43	1.29	1.12	1.28	1.10	1.48	1.56	2.95	2.45

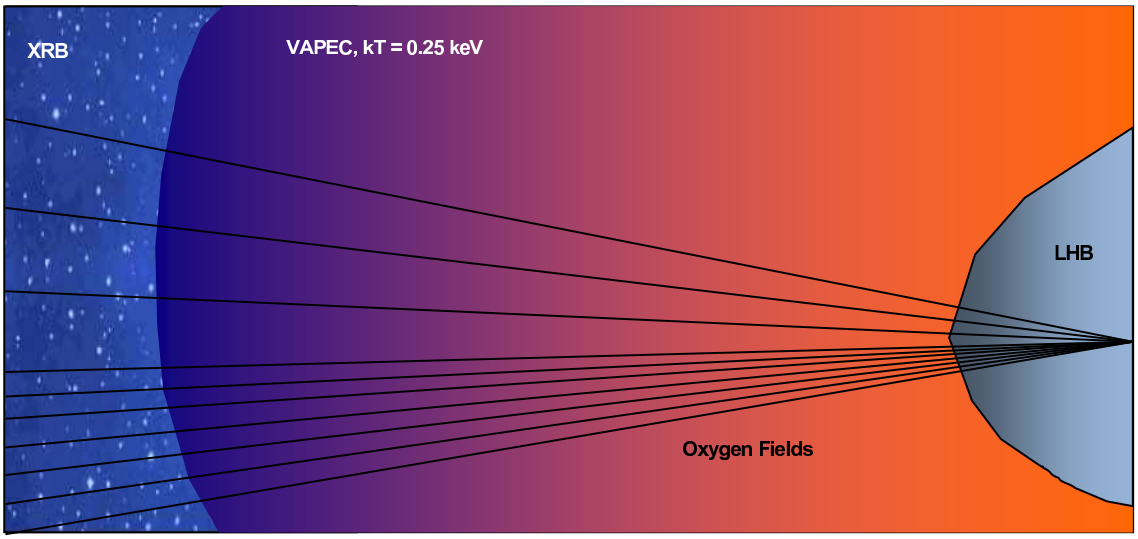

Figure 4.9: Modelling the Oxygen Fields: A cartoon illustrating the structures represented by Model B(b)

the low energy flux is reduced.

Model B(c)

In the third variation, the temperature of the VAPEC component was again fixed at 0.25 keV, but this time the absorption was allowed to vary up to the value of the full Galactic column, making it possible for it to lie in the mid to far distance beyond the LHB. A cartoon illustrating the B(c) model is shown in Figure 4.10, and the parameters from this series of fits are shown in Table 4.4.

Model B(c) Discussion

The fit statistics in the B(c) series are better than both the B(a) and B(b) series. By allowing the VAPEC to settle at a more appropriate, higher absorption level, the conflict between the APEC and the VAPEC components is reduced. Now, they fit slightly different energy ranges, the APEC between 0.1 – 0.4 keV and the VAPEC between 0.4 – 1.0 keV. In half of the ten fields, the absorption on the VAPEC rose all the way to its upper limit,

Table 4.4: The B(c)-Series parameter values for the Oxygen Fields. For a key to the table headings, see Appendix B.

Field	O1	O2	O3	O4	O5	O6	O7	O8	O9	O10
Latitude	-9.50	-20.80	0.43	-3.30	-37.36	-17.55	21.11	-3.44	-34.56	1.12
XRB Norm	3.04E-4	3.58E-4	1.82E-4	3.92E-4	6.81E-4	3.98E-4	2.64E-4	4.32E-4	2.57E-4	2.63E-4
LHB Norm	6.09E-4	1.15E-3	1.71E-3	6.73E-4	1.31E-3	1.03E-3	1.45E-3	9.13E-4	9.06E-4	7.49E-4
Gal Absorption	2.34E-2	3.39E-2	0.596	0.526	0.17	8.1E-2	4.13E-2	0.408	0.108	0.893
Halo Absorption	2.34E-2	1.27E-2	0.143	1.62E-3	0.17	4.16E-2	4.13E-2	0.408	2.42E-2	0.893
Halo Norm	2.34E-2	6.03E-4	4.78E-4	1.99E-4	2.18E-4	3.34E-4	4.41E-4	2.47E-3	4.73E-4	8.96E-3
Halo kT	0.25	0.25	0.25	0.25	0.25	0.25	0.25	0.25	0.25	0.25
Relative Abundances:										
O	0.12	1.00	1.00	1.00	1.00	1.00	1.00	1.00	1.00	1.00
Ne/Mg/Fe	0.10	1.00	1.00	1.00	1.00	1.00	1.00	1.00	1.00	1.00
χ^2	356.40	1108.38	298.87	637.40	297.01	247.34	340.88	255.91	598.95	279.92
DoF	225	789	232	567	233	231	231	227	231	231
χ^2_ν	1.58	1.40	1.29	1.24	1.27	1.07	1.48	1.23	2.59	1.21

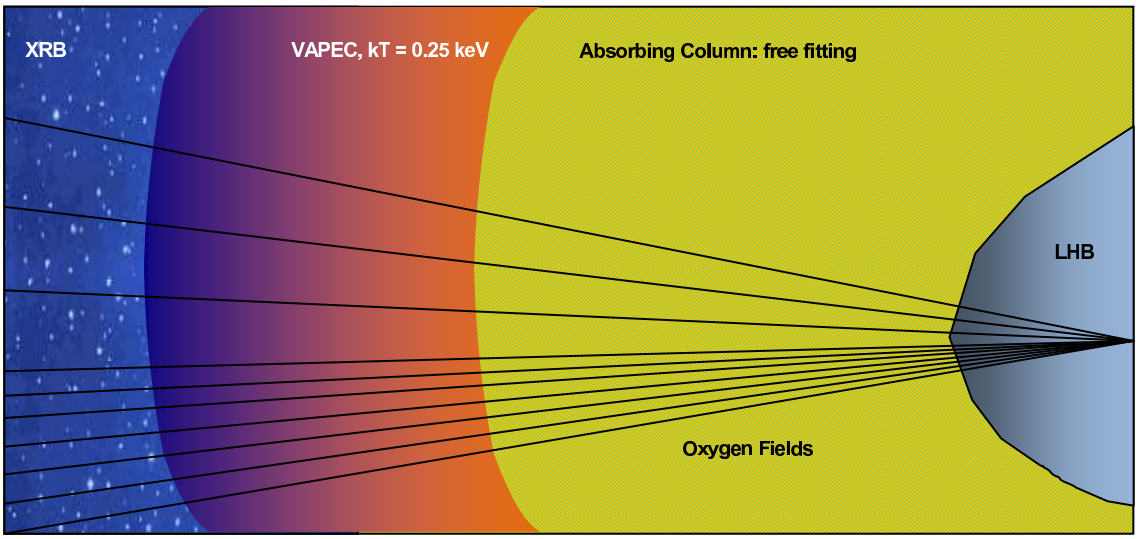

Figure 4.10: Modelling the Oxygen Fields: A cartoon illustrating the structures represented by Model B(c)

the full Galactic Column, putting it at the edge of the Galaxy.

Model B(d)

In the fourth and final variation, the temperature of the VAPEC component was allowed to vary, but the absorption was held to the full Galactic column, placing it in the far distance, in the position expected for the Galactic Halo. The parameters from this series of fits are shown in Table 4.5.

Model B(d) Discussion

The B(d)-series fits are statistically better than the other variants, and so will represent the 'best-fit' parameters to the Oxygen fields in this work, and plots of the fitted spectra are shown in Figures 4.11, 4.12 & 4.13. As the spectra show, the B(d)-series fits were visibly better than those in the A-series. During the fitting process, the power law normalisations fell significantly, so much so that the models matched the data between 2 keV and 4 keV. Since the XRB flux constitutes the continuum of the spectra, improvements in its fit to the

Table 4.5: The B(d) Series parameter values for the Oxygen fields. For a key to the table headings, see Appendix B.

Field	O1	O2	O3	O4	O5	O6	O7	O8	O9	O10
Latitude	-9.50	-20.80	0.43	-3.30	-37.36	-17.55	21.11	-3.44	-34.56	1.12
XRB Norm	3.15E-4	3.63E-4	1.51E-4	2.36E-4	6.75E-4	4.00E-4	2.64E-4	4.79E-4	2.52E-4	2.63E-4
LHB Norm	5.08E-4	1.30E-3	1.64E-3	8.49E-4	1.31E-3	1.04E-3	1.48E-3	9.03E-4	8.60E-4	7.49E-4
Halo Norm	2.70E-3	6.43E-4	3.04E-3	1.81E-3	2.01E-4	4.38E-4	3.94E-4	1.12E-3	3.39E-4	9.07E-3
Halo kT	0.22	0.27	0.21	0.31	0.28	0.23	0.27	0.25	0.25	0.25
Relative Abundances:										
O	0.12	1.00	1.00	1.00	1.00	1.00	1.00	1.00	1.00	1.00
Ne/Mg/Fe	0.23	1.00	1.00	1.00	1.00	1.00	1.00	1.00	1.00	1.00
χ^2	337.60	1102.60	249.18	518.65	295.99	245.90	333.90	291.40	380.50	279.90
DoF	225	789	231	567	233	231	231	228	229	231
χ^2_ν	1.50	1.39	1.08	0.91	1.27	1.06	1.45	1.28	1.66	1.21

data also enabled the APEC and VAPEC components to fit more accurately, constraining them more tightly within the model. Despite this, comparison of the parameter values shows that the B(a)-series parameters have barely moved from their A-series levels.

While the A-series produced fits with reduced chi-squared values up to 3.55, the B(d)-series fits all lie between 0.91 and 1.66. This tremendous improvement in the goodness of the fits, almost wholly brought about by floating the power law, has made it possible to calculate the 90% confidence intervals on the parameters of the B(d)-series which can be found in Appendix B. However, since the power law has floated from its fixed flux value to a non-uniform level, it would seem that the isotropic XRB flux has not been accurately represented within the reduced spectra.

The variation seen in the normalisation of the XRB component is not easy to explain; in most fields, the expected isotropic values were too high for the reduced spectrum. This may have occurred because the energy range used here is too narrow; most of the XRB flux lies above 0.4 keV, the upper limit used in this work. In other fields, the data sat above the expected level, indicating that other hard spectrum components were present in the data in addition to the signal from the XRB. These could include any flares or soft-protons incompletely removed during the screening of low-level particle background components. In any case, since the power law normalisation has not been found to be isotropic across the sky, or at the expected intensity, it can not be said that the XRB flux has been characterised in this fit series or those that follow. Nor can the best-fit values of the power law normalisation be said to represent the whole XRB. Instead, the power law is used in this work to fit those parts of the XRB that are present, along with any other hard components remaining in the data set. By fitting the power law in this way, the contribution of the XRB and the other hard components can be effectively masked, highlighting the SXRB signal with which this work is primarily interested.

By putting the VAPEC behind the full Galactic Column, the conflict between the low energy thermal components has been completely resolved, and now both the APEC and VAPEC can fit separately. The VAPEC is now in the position expected of the Galactic Halo, and by pinning it down in space, the uncertainty in the model has been reduced, making it possible to fit its temperature and normalisation more accurately.

The quality of the B(d)-series fits was also sufficiently high to allow certain parameters

to be 'stepped'; a process by which XSPEC can be used to explore the parameter space, revealing the degree to which a value has been constrained within the fit. The most controversial parameter in the Oxygen fields, the temperature of the Halo, was subjected to this process. The graphs thus produced, shown in Figures 4.14, 4.15 & 4.16, clearly illustrate that the fitted temperature is constrained about $\sim$0.25 keV, not 0.1 keV, and that this is not merely a 'false' local minimum. The parameter space does not indicate any minima around 0.1 keV, the Halo temperature reported by Willingale et al. (2003), further indicating that the thermal signal in the Oxygen fields, and the absorbed 0.1 keV signal observed in the Galactic Centre direction, have different origins.

4.6.4 Oxygen Fields: Final Thoughts

Careful fitting of four variants of Model-B revealed a soft, thermal emission that is present to a varying extent in all of the Oxygen fields. The fact that the emission is so widespread, and that the best fitting model B(d) placed it behind the full Galactic column, strongly indicate that it originates within a distant Galactic Halo. The temperature of this component, which was allowed to fit freely, settled at $\sim$0.25 keV: significantly hotter than the 0.1 keV cool Galactic Halo initially proposed by Willingale et al. (2003), and only a little cooler than the Loop I interior. Nevertheless, this is very much in line with the 'Galactic Corona' hypothesised by Spitzer (1956), and discussed in Section 2.9. If this 0.25 keV signal does originate from the Galactic Halo, then self-evidently, the 0.1 keV signal identified by Willingale et al. (2003) as a cool Galactic Halo in the Galactic Centre direction must originate from some other source. Examples of unfolded spectra from each of the Model-B variants are shown in Figure 4.17.

4.7 Modelling the Loop Fields

While the Oxygen fields are spread across the Anti-centre, the ten Loop fields are concentrated within a relatively small but crowded area of the sky (Figure 3.2), within the projected boundary of the Loop I superbubble, in the Galactic Centre direction. They can be split into two distinct groups: the Northern and Southern fields. The Northern fields can be further subdivided into the 'NPS fields' (N4 & N5), located within the bright

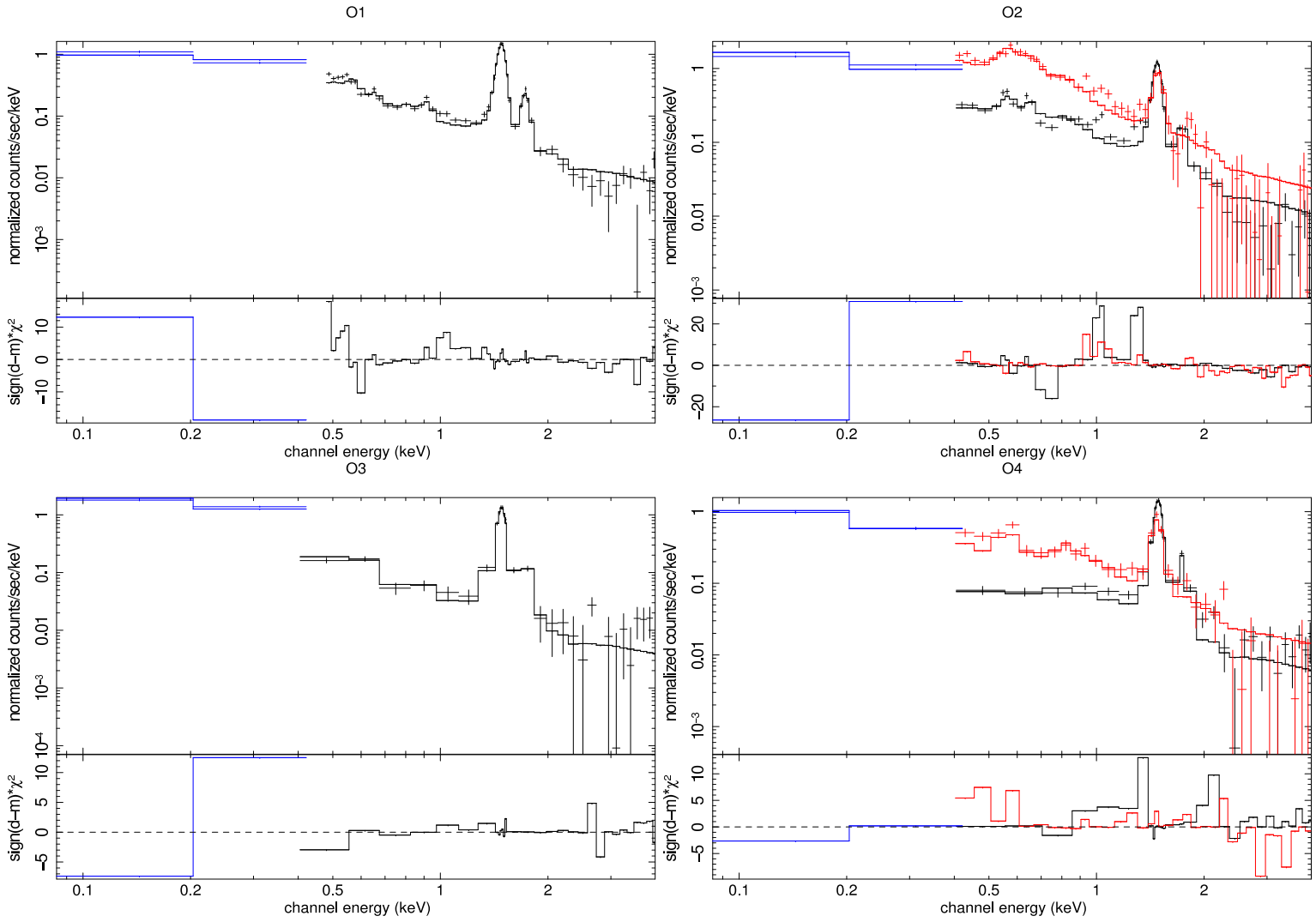

Figure 4.11: Model B(d): The best-fit spectra for O1, O2, O3 & O4. The traces shown are: ROSAT (blue), MOS (black) and pn (red).

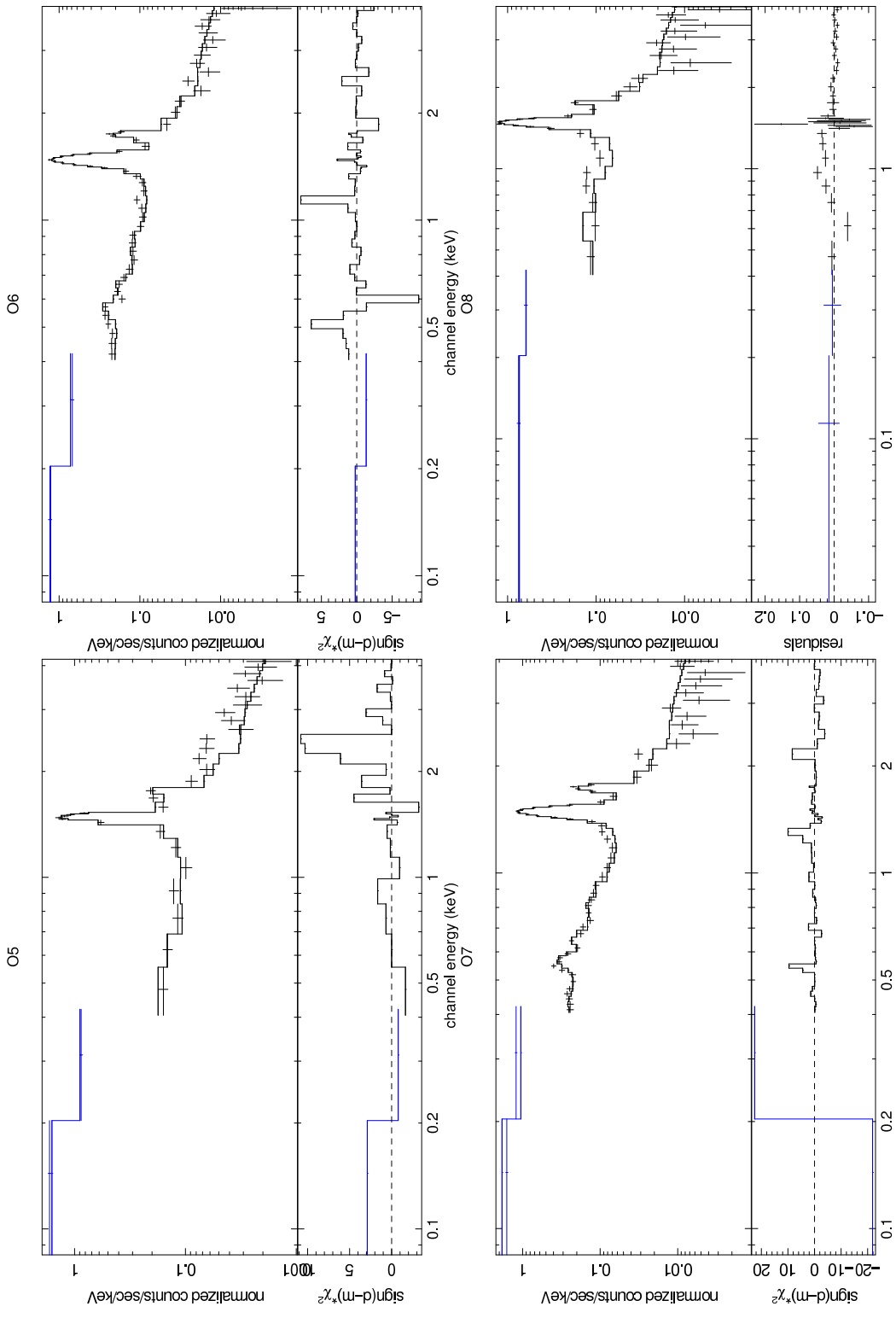

Figure 4.12: Model B(d): The best-fit spectra for O5, O6, O7 & O8. The traces shown are: ROSAT (blue), MOS (black) and pn (red).

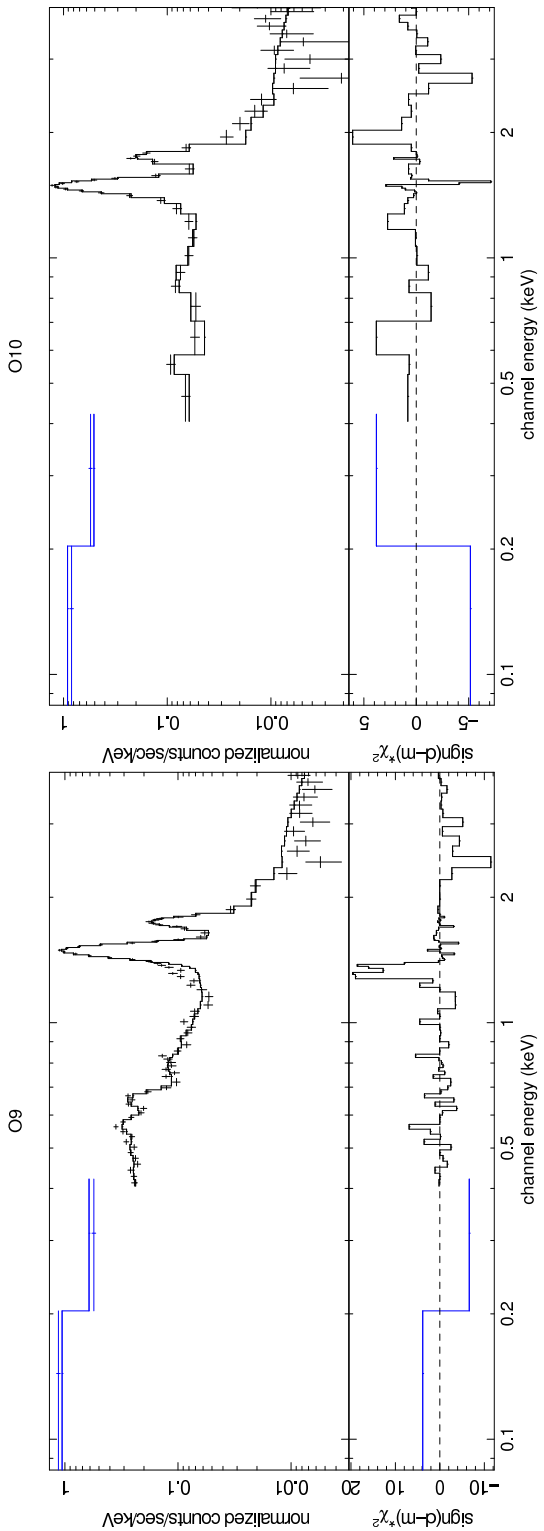

Figure 4.13: Model B(d): The best-fit spectra fit O9 & O10. The traces shown are: ROSAT (blue), MOS (black) and pn (red).

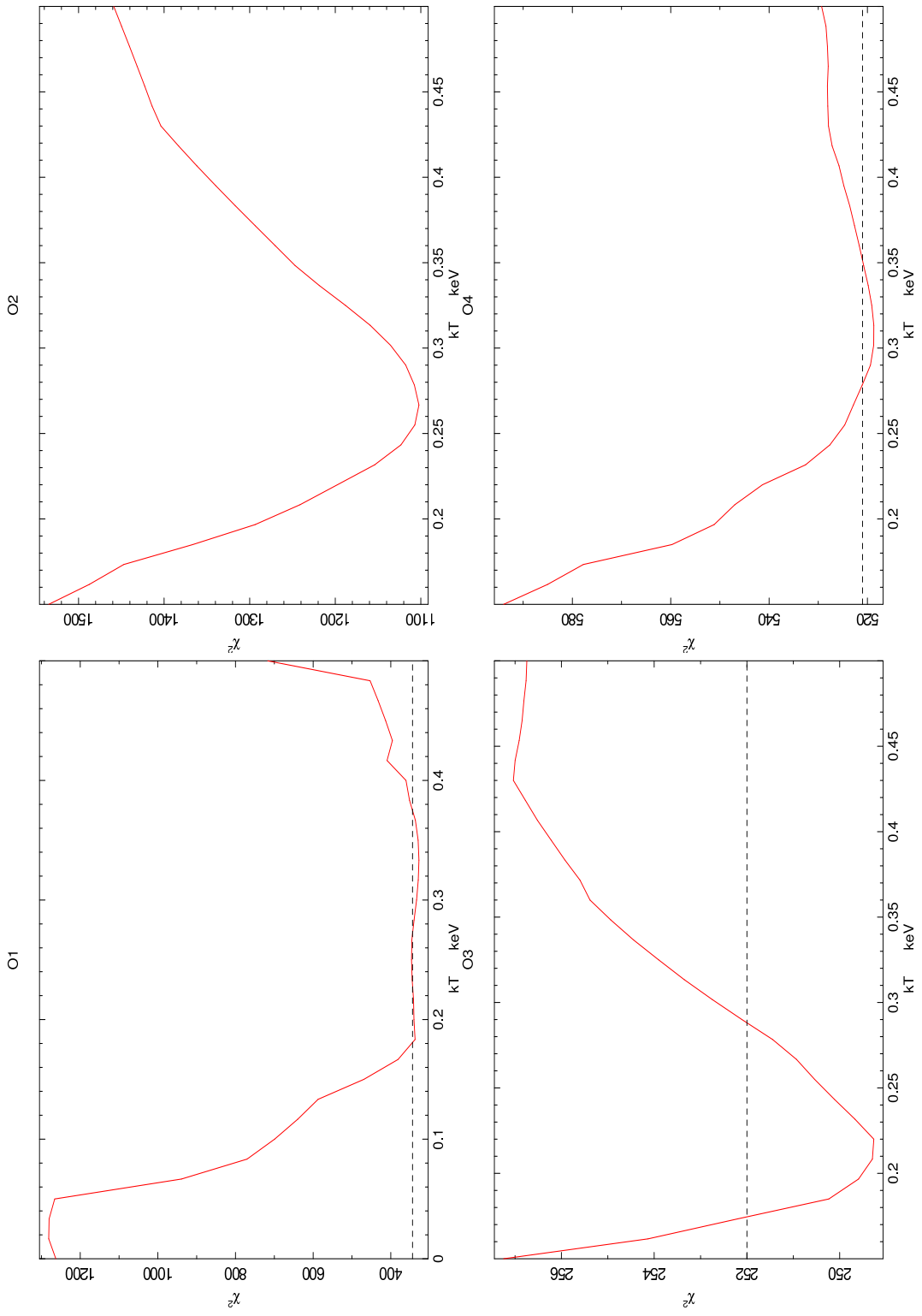

Figure 4.14: Steppars of the Halo kT: O1, O2, O3 & O4.

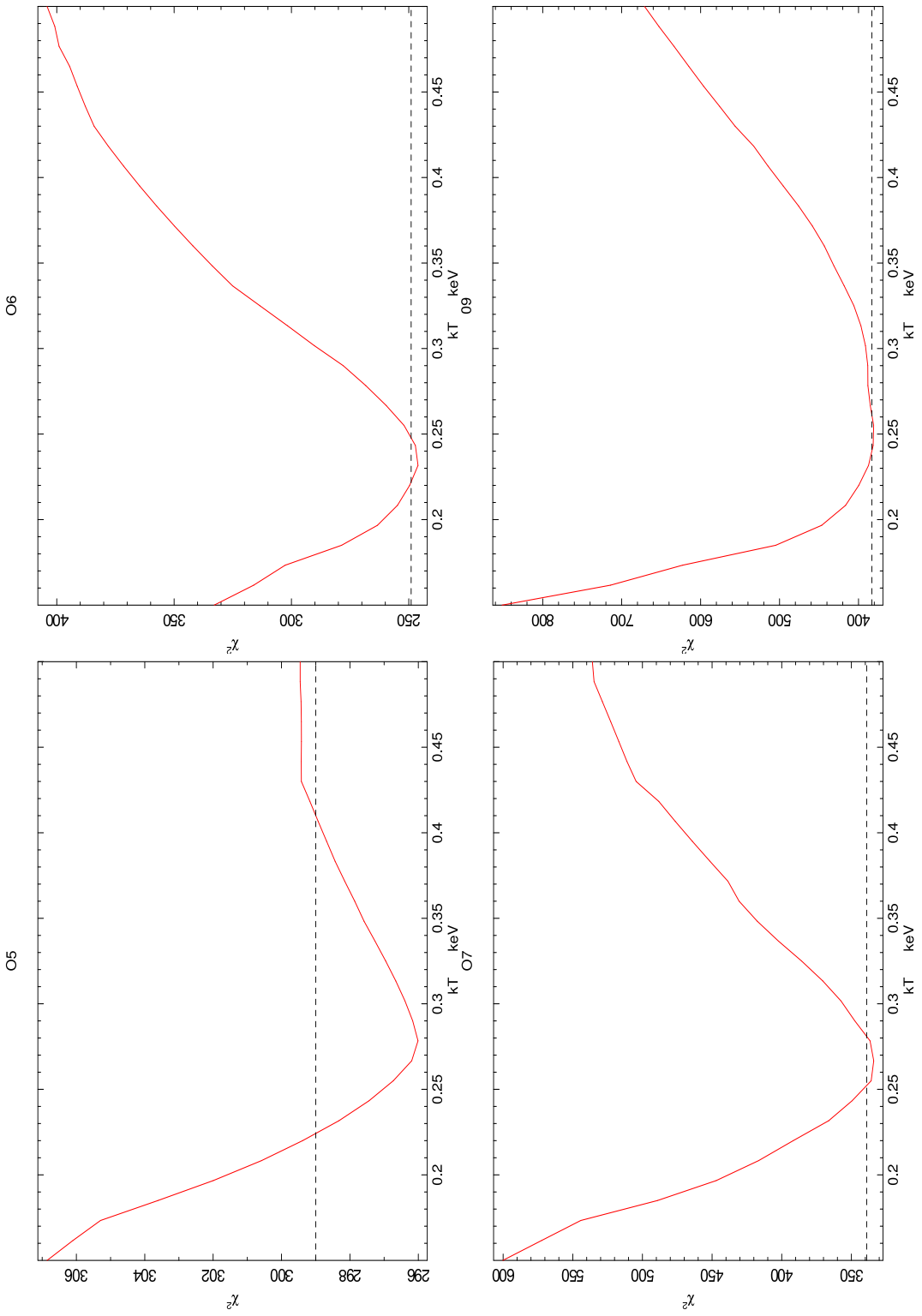

Figure 4.15: Steppars of the Halo kT: O5, O6, O7 & O9.

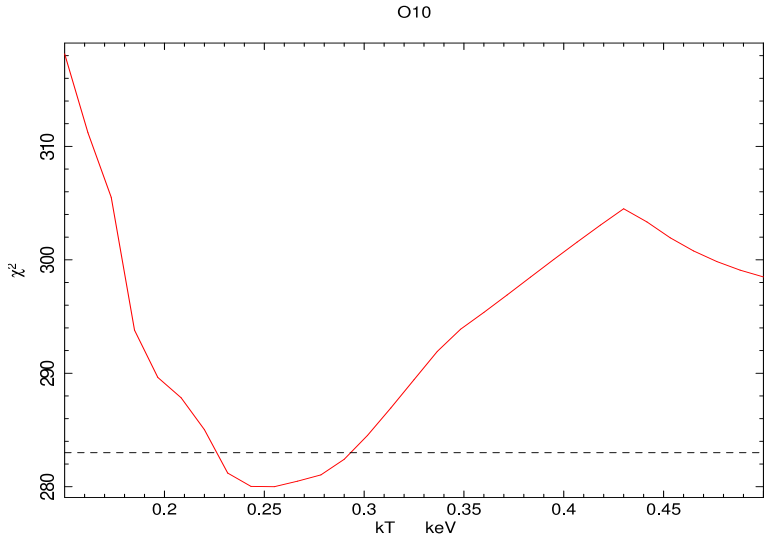

Figure 4.16: Steppar of the Halo kT: O10.

spur of the North Polar Spur on the upper-left edge of the Loop as it appears in the RASS maps, and the 'Bulge fields' (X1, X2 & X3), positioned in the northern bulge of Loop 1. The Southern fields (B1, B2, B3, B4 & B5) lie in the southern bulge of the Loop, within 6° of the Galactic Plane.

As explained in Chapter 3, the data analysis procedure has been refined since its creation in 2003. It is perhaps because of these improvements, and particularly those affecting the energy calibration of the spectra, that the model used by Willingale et al. (2003) proved ineffective in this implementation, even in the Galactic Centre direction. It could not describe the hard emission seen in the Southern Loop fields, and preliminary fits that it produced to the Northern and NPS fields, although formally acceptable, were highly unstable, and statistically insensitive to change. The model used in Willingale et al. (2003) included two APEC plasma codes at 0.1 keV. Although one of these was absorbed and the other was not, the two components were otherwise identical, and so fitted the same lines in the same energy range. Consequently, they traded against one another during the fit, producing many statistically identical fits in which the balance shifted between the normalisations of the two components.

The spectrum of the soft X-ray background is highly complex in the Galactic Centre direction, much more so than in the Anti-centre. Numerous emissive sources are present, each with unique characteristics. To fit these fields accurately, models containing many

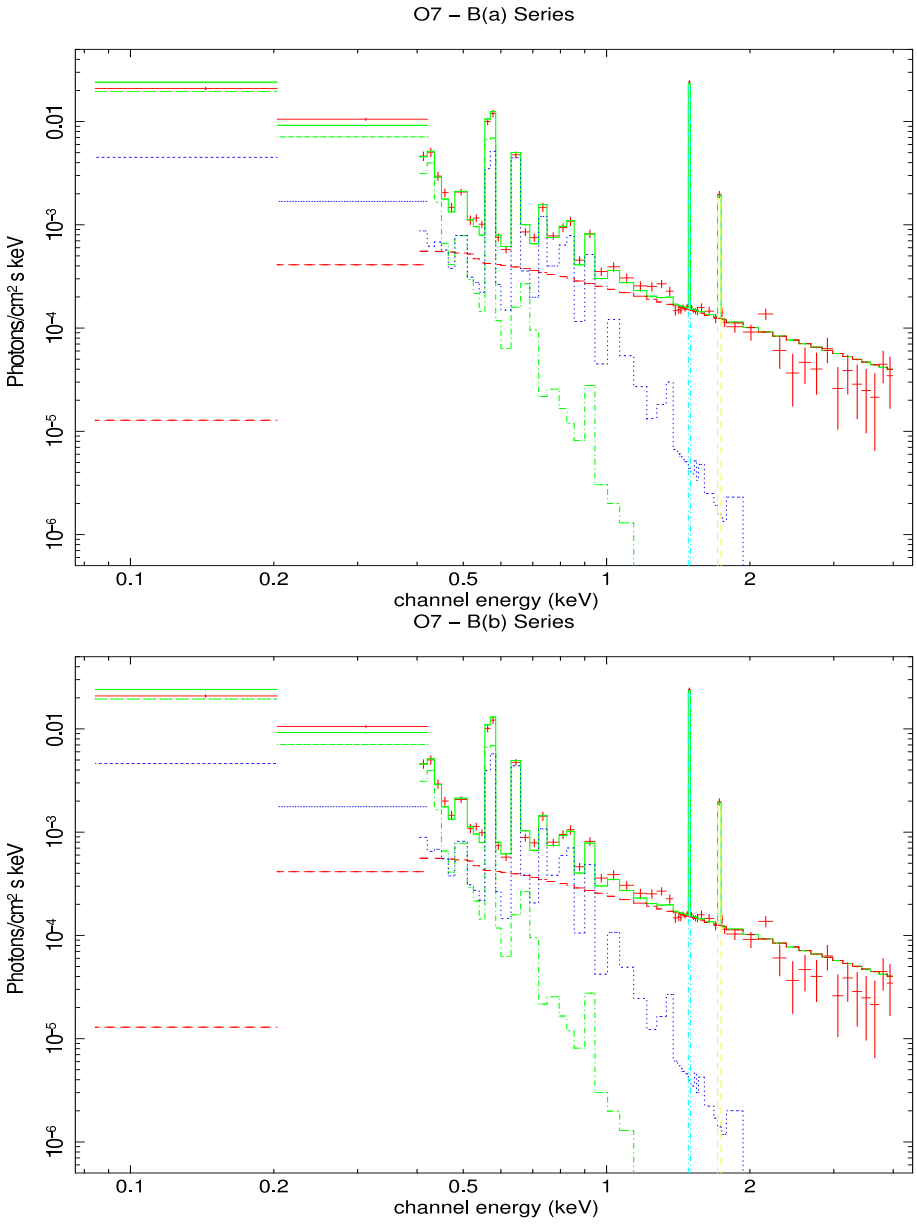

Figure 4.17: Model B: Unfolded Spectra of Field O7. The red crosses mark the data points. The traces are as follows: red dashed (XRB power law), green dot-dash (LHB APEC), blue dot (Halo APEC). The cyan and yellow peaks are the two Gaussian curves.

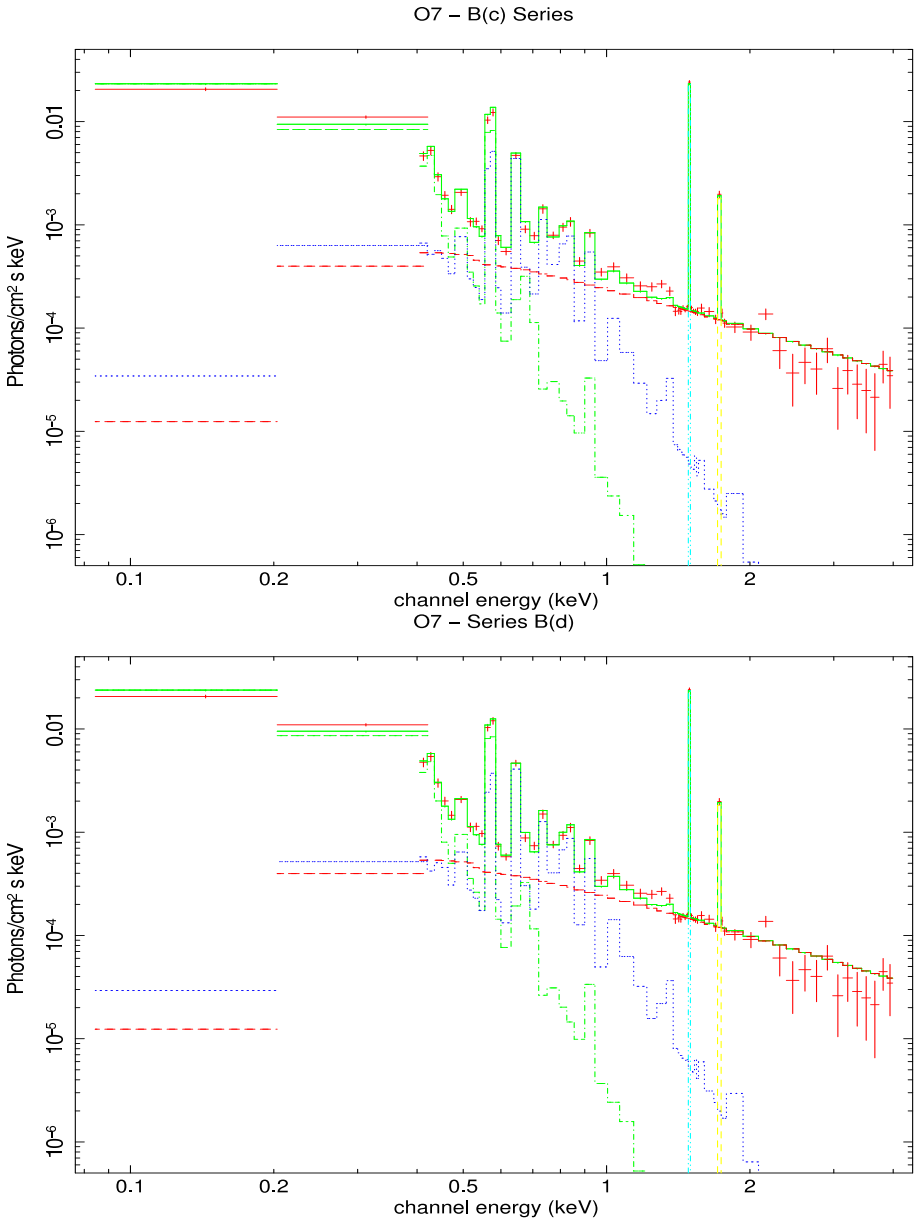

Figure 4.18: Model B: Unfolded Spectra of Field O7. The red crosses mark the data points. The traces are as follows: red dashed (XRB power law), green dot-dash (LHB APEC), blue dot (Halo APEC). The cyan and yellow peaks are the two Gaussian curves.

components and unusually large numbers of parameters are required. Moreover, the absorption of the Wall, the dense layer of dust and neutral gas present at the interface between the LHB and Loop I (see Section 2.7), is approximately equal to that of the full Galactic column. Therefore, one must constantly check the fitted parameters against the known properties of structures lying along the line of sight, and their interactions, in order not to misfit or misinterpret the Loop spectra.

In this section, the development of a new model used to fit the Loop fields will be described, one component and refinement at a time.

4.7.1 Model C

Initially, a simple three-component starting model, Model C, was applied to the ten Loop fields, producing the C-Series of fits:

$$\text{APEC} + (\text{WABS} \times \text{VAPEC}) + (\text{WABS} \times \text{POWER}) + \text{GAUSS1} + \text{GAUSS2}$$

Representing:

$$\text{LHB} + (\text{Loop I}) + (\text{XRB}) + \text{Al } K_{\alpha} + \text{Si } K_{\alpha}$$

From the left, the components represent the Local Hot Bubble, the Loop I superbubble and the XRB (illustrated in Figure 4.19). As before, the GAUSS codes were used to fit the instrumental Al and Si lines present in the spectra.

In common with the fits to the Oxygen fields, the unabsorbed APEC code represents the LHB, and the absorbed power law models the XRB. In all of the fits to the Loop fields, the temperature of the APEC was frozen to 0.1 keV, and the photon index of the power law was frozen to 1.4, with its absorption frozen to the full Galactic column, determined using the on-line tool (Angelini 2007). Following the success of the technique in the Oxygen fields, the normalisations of both the APEC and power law were allowed to float during the fit.

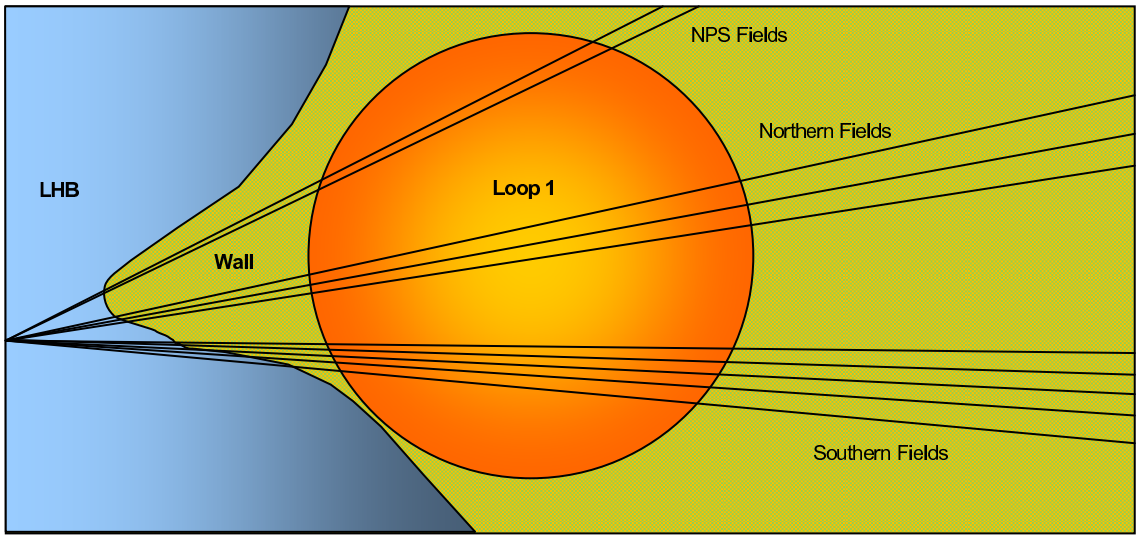

Figure 4.19: Modelling the Loop Fields: A cartoon illustrating the structures represented by Model C

The normalisation of the VAPEC component, which represents the hot plasma of Loop 1, was also allowed to float, while its temperature was frozen to 0.3 keV, as determined by Willingale et al. (2003). The absorption acting on this component, which represents the 'Wall', was capped in the fits so that it could match, but not exceed, the Galactic column in each field. The foreground absorption, listed in the results tables, is the proportion of the total Galactic column present in front of the Loop. On occasions when the foreground absorption is unity, the Wall is particularly dense, and constitutes all of the absorption detectable in that field.

The best-fit parameter values of the C-Series fits are listed in Table 4.6, and plots of the fitted spectra corresponding to those values are shown in Figures 4.20, 4.21 & 4.22.

Model C: Discussion

Unlike the Oxygen field spectra, the fitted spectra from the Loop fields exhibit features which appear to vary strongly in magnitude with respect to the Galactic Plane. Furthermore, as the under-fitted regions and misfits in the spectra show, while Model C represents the main structures present in the fields, other components are still present that are unaccounted for.

Table 4.6: The C-Series best-fit parameter values for the Loop fields. For a key to the table headings, see Appendix B.

Field	N5	N4	X3	X2	X1	B1	B2	B3	B4	B5
Latitude	30.00	20.00	24.00	18.00	12.00	-2.71	-3.87	-5.49	-8.00	-12.00
LHB Norm	8.30E-4	3.40E-4	7.42E-4	5.53E-4	8.11E-4	9.95E-4	1.07E-3	7.07E-4	8.78E-4	9.84E-4
Gal N_H	0.055	0.080	0.122	0.099	0.174	0.455	0.323	0.246	0.166	0.288
Wall N_H	0.017	0.032	0.110	0.037	0.140	0.455	0.294	0.177	0.059	0.026
Fore N_H	0.309	0.403	0.902	0.371	0.805	1.000	0.912	0.720	0.358	0.112
Loop I Norm	3.97E-3	4.96E-3	1.88E-3	3.82E-3	3.34E-3	2.60E-2	1.84E-2	7.38E-3	4.00E-3	4.49E-3
XRB Norm.	2.12E-4	4.12E-4	3.90E-4	3.24E-4	3.61E-4	1.91E-3	1.34E-3	1.05E-3	7.36E-4	3.96E-4
χ^2	1220.0	1316.3	818.7	1305.5	1072.4	2342.0	3989.9	1086.1	1253.5	1890.6
DOF	231	237	621	636	674	812	869	231	634	600
χ^2_ν	5.28	5.55	1.32	2.05	1.59	2.88	4.59	4.70	1.98	3.15

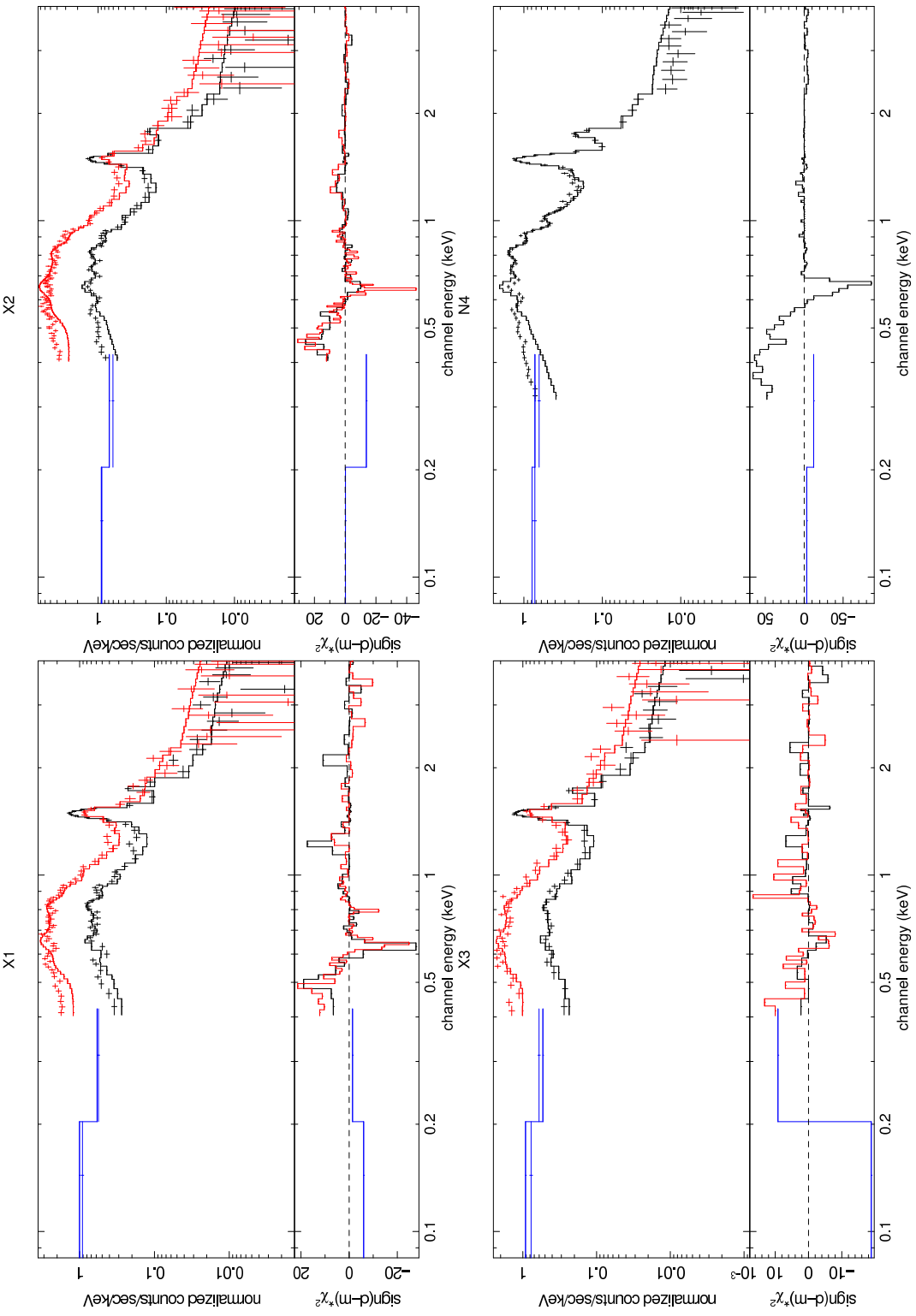

Figure 4.20: Model C: The best-fit spectra for X1, X2, X3 & N4. The traces shown are: ROSAT (blue), MOS (black) and pn (red).

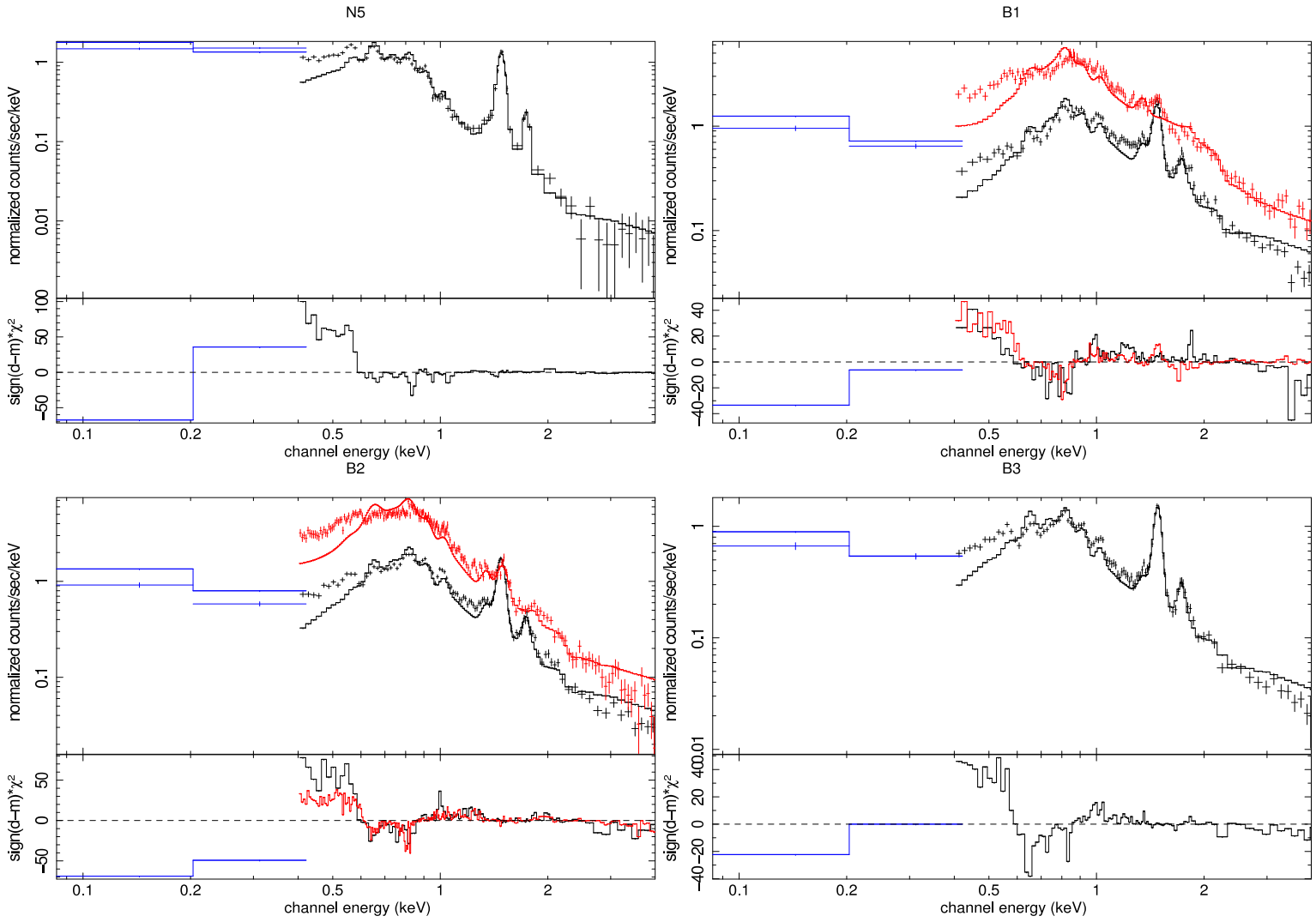

Figure 4.21: The Model C: The best-fit spectra for N5, B1, B2 & B3. The traces shown are: ROSAT (blue), MOS (black) and pn (red).

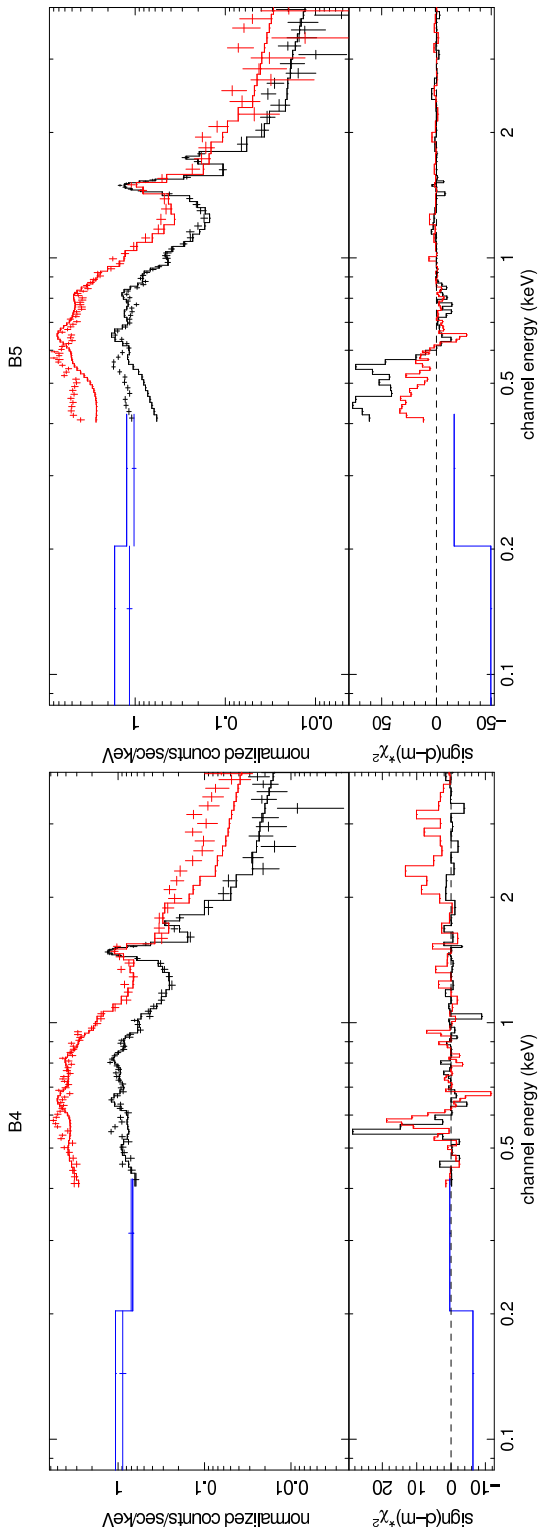

Figure 4.22: Model C: The best-fit spectra for B4 & B5. The traces shown are: ROSAT (blue), MOS (black) and pn (red).

The model fits reasonably well In the Northern fields, roughly matching the data throughout the energy range. It does, however, require more support in the 0.2 – 0.8 keV region, where the model sits below the data, indicating that an extra flux component is needed to make up the deficit. Interestingly, this effect is far more pronounced in the N4 & N5 fields than it is in fields X1, X2 & X3, located within the Northern Bulge.

The fit is not so good in the Southern fields. Although the fit to B5, the Southern field furthest from the Plane, is reasonable and very similar to that in the NPS fields, the situation becomes progressively worse as the fields approach the Plane. In these spectra, the model deviates from the data over a much wider range, between 0.2 – 1.5 keV. As in the Northern fields, the model is too low between 0.2 – 0.8 keV, suggesting that an as yet unidentified structure must be present within all of the Loop fields. Between 0.8 – 1.5 keV, the misfit continues as the continuum of the data rises to an increasing degree from B4 – B1, and the fit to the emission lines worsens, illustrated by the erratic distribution of the residual chi squared values plotted below the spectra.

Clearly, the model required further development, both to raise its level in the low-energy 0.2 – 0.8 keV range, and to address the situation in the Southern fields.

4.7.2 Model D

The 0.1 keV cool Halo, postulated by Willingale et al. (2003) was thought to surround the entire Galaxy, but as the fits to the Oxygen fields showed, this is not the case. Instead, a 0.25 keV Halo was detected. There is no reason why the Halo should be a different temperature in the Galactic Centre to the Anti-centre; however, a 0.1 keV cool Halo was reported, and so, having amended the data reduction process, the model was adjusted and refitted in an attempt to corroborate the earlier results.

The new model, Model D (Figure 4.23), is identical to the previous attempt except for the addition of an absorbed VAPEC to model the cool Halo:

$$\text{APEC} + (\text{WABS} \times \text{VAPEC}) + (\text{WABS} \times \text{VAPEC}) + (\text{WABS} \times \text{POWER}) + \text{GAUSS1} + \text{GAUSS2}$$

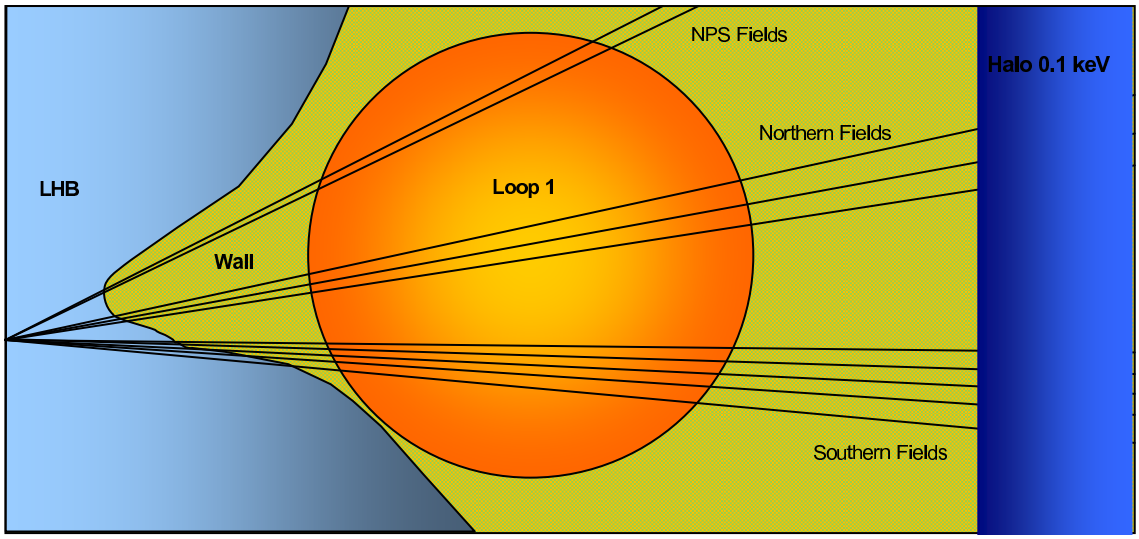

Figure 4.23: Modelling the Loop Fields: A cartoon illustrating the structures represented by Model D

Representing:

$$\text{LHB} + (\text{Loop 1}) + (\text{Halo}) + (\text{XRB}) + \text{Al } K_{\alpha} + \text{Si } K_{\alpha}$$

This is the same combination used by Willingale et al. (2003) to fit the Northern fields. Initially, it was fitted to the Loop fields using the same fixed parameter values presented in Willingale et al. (2003); however, this produced highly unstable fits to the data, in which the LHB and Halo appeared to be interchangeable.

This undesirable situation arose since the model components used to represent the cool Halo and LHB were almost identical: an absorbed and an unabsorbed APEC respectively, both frozen to 0.1 keV. Despite the effects of absorption, these components fitted the same narrow energy range, containing the same emission lines, and so shared the soft flux between them. Because the absorption acting on the cool Halo was allowed to float, the proportion of flux fitted by each component could fluctuate. This arrangement allowed unreasonably high emission measures on the LHB to be entirely compensated by lower normalisation of the cool Halo, and vice versa.

In Model D the temperature of the Halo, represented by the VAPEC, was frozen to 0.15 keV: this is slightly higher than the 0.1 keV used by Willingale et al. (2003), but

sufficiently different from the 0.1 keV APEC modelling the LHB to mitigate the conflict between the two components. The absorption of the Halo was made equal to the full Galactic column, to position it at the edge of the Galaxy, and the model was applied to the Loop fields. The best-fit parameters from this D-Series of fits can be found in Table 4.7, and plots of the fitted spectra corresponding to these values are shown in Figures 4.24, 4.25 & 4.26.

Model D: Discussion

Despite adding the extra component, the fits in the D-series show very little improvement from the C-series. Indeed, the reduced chi squared values are almost identical, and the inadequacies in the fits remain. Although the 0.15 keV VAPEC was frozen at the correct energy to raise the flux of the model between 0.2 – 0.8 keV, the full absorption acting on the component has reduced its intensity at softer energies, preventing it from doing so.

The chi-squared deviations, plotted below the spectra, also show that the inclusion of the 0.15 keV absorbed VAPEC did little to improve the fit in the Southern fields; nevertheless, the fact that its normalisation was greater than zero in four of the five Southern fields shows that it did have a place in the model. It was, however, rejected in the B5 field, with its normalisation falling to zero during the fit. This is curious because the flux from both the Loop and the Galactic Plane are lower in B5 than any other Southern field, and so it should have been easier to discern the signal from the Halo there than in the other B fields.

The implication is clear: if the signal from an absorbed 0.15 keV APEC could be detected in the Loop fields, but not in the Oxygen fields, then it could not originate from an all-encompassing cool Galactic Halo.

The D-series results were also surprising because rather than the steady magnitude expected from an extensive structure, the normalisation of the absorbed VAPEC component could be seen to vary considerably throughout the Loop fields. Moreover, its variation across the sky was not random: when the normalisations of the absorbed VAPEC component (representing Loop I) are compared with those of the cool Halo component in the same fields, the trends in the parameters are very similar, rising and

Table 4.7: The D-Series best-fit parameter values for the Loop fields. For a key to the table headings, see Appendix B.

Field	N5	N4	X3	X2	X1	B1	B2	B3	B4	B5
Latitude	30.00	20.00	24.00	18.00	12.00	-2.71	-3.87	-5.49	-8.00	-12.00
LHB Norm	1.14E-3	4.15E-4	7.37E-4	6.80E-4	8.10E-4	9.73E-4	1.01E-3	6.98E-4	9.36E-4	9.91E-4
Gal N_H	0.055	0.080	0.122	0.099	0.174	0.455	0.323	0.246	0.166	0.288
Wall N_H	0.014	0.034	0.122	0.050	0.174	0.455	0.323	0.246	0.085	0.026
Fore N_H	0.258	0.428	1.000	0.502	1.000	1.000	1.000	1.000	0.511	0.112
Loop I Norm	1.21E-3	4.09E-3	1.69E-3	2.51E-3	3.05E-3	2.08E-2	1.23E-2	5.08E-3	3.20E-3	4.49E-3
Halo Norm	3.94E-3	1.35E-3	4.07E-4	2.38E-3	1.05E-3	7.43E-3	1.14E-2	6.43E-3	2.43E-3	0.00
XRB Norm	2.56E-4	4.23E-4	3.87E-4	3.43E-4	3.54E-4	1.87E-3	1.39E-3	1.03E-3	7.27E-4	3.96E-4
χ^2	890.2	1292.9	812.2	1234.2	1060.9	2274.4	3732.8	992.9	1238.5	1890.6
DOF	230	236	620	635	673	810	868	230	633	599
χ^2_ν	5.28	5.55	1.32	2.05	1.59	2.87	4.59	4.70	1.98	3.15

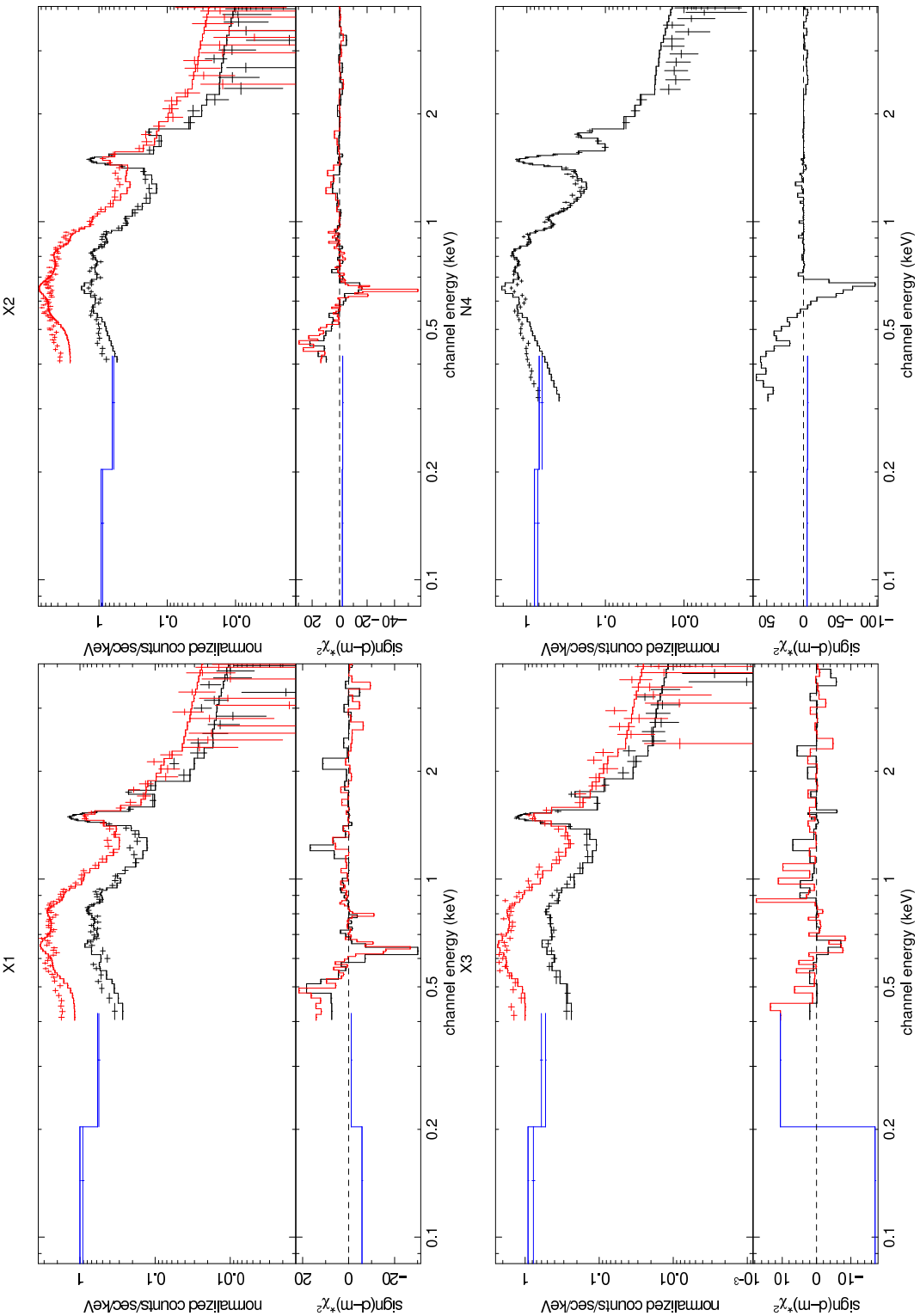

Figure 4.24: Model D: The best-fit spectra for X1, X2, X3 & N4. The traces shown are: ROSAT (blue), MOS (black) and pn (red).

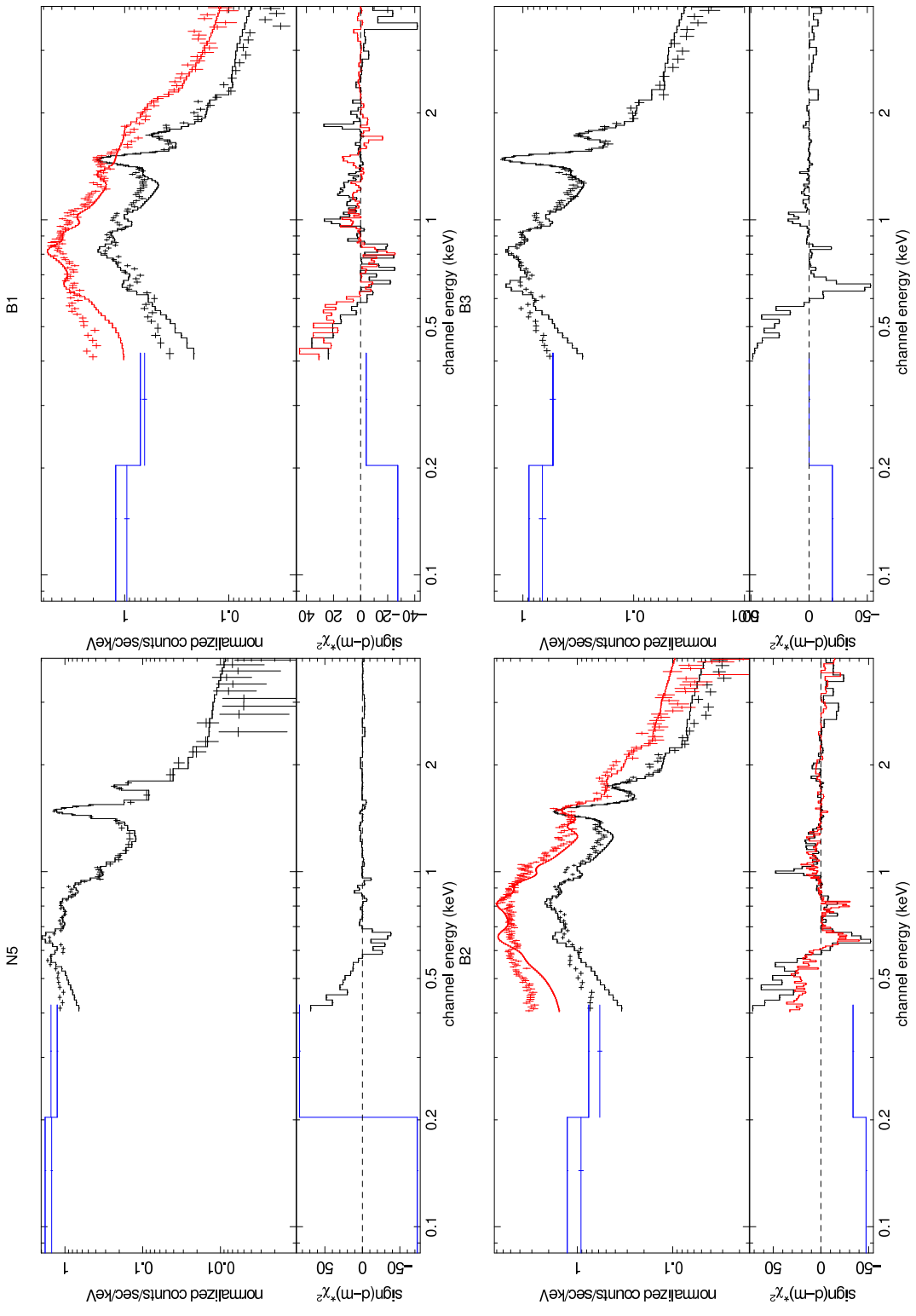

Figure 4.25: The Model D: The best-fit spectra for N5, B1, B2 & B3. The traces shown are: ROSAT (blue), MOS (black) and pn (red).

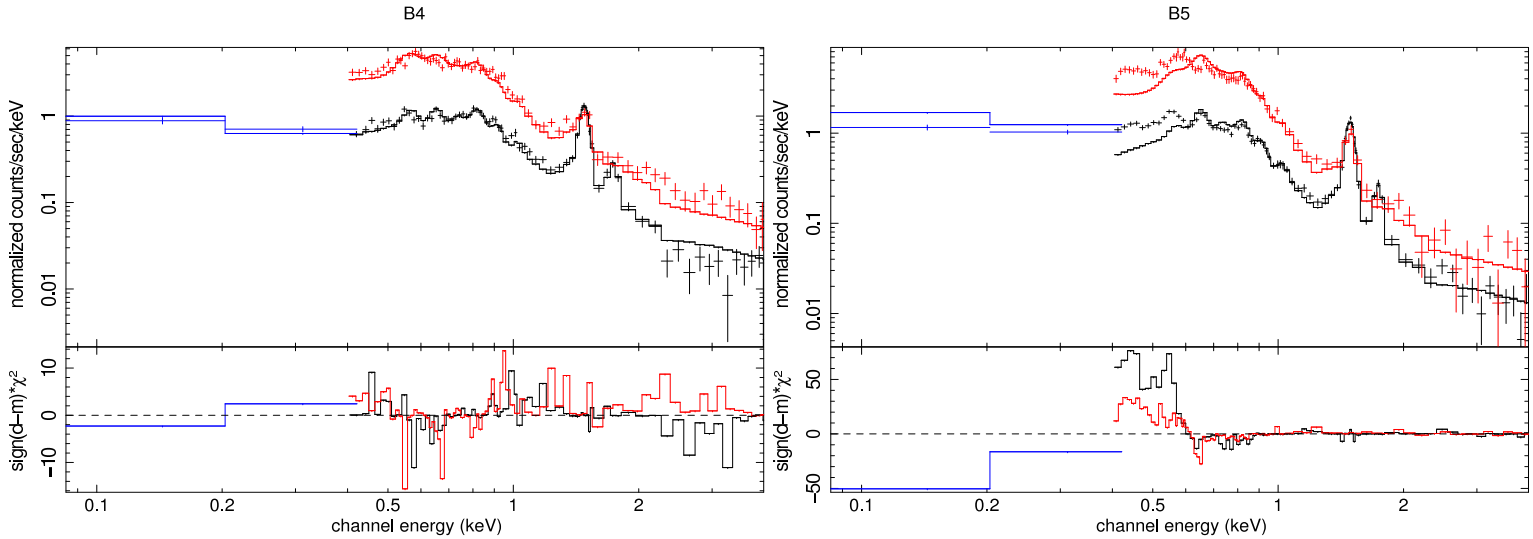

Figure 4.26: Model D: The best-fit spectra for B4 & B5. The traces shown are: ROSAT (blue), MOS (black) and pn (red).

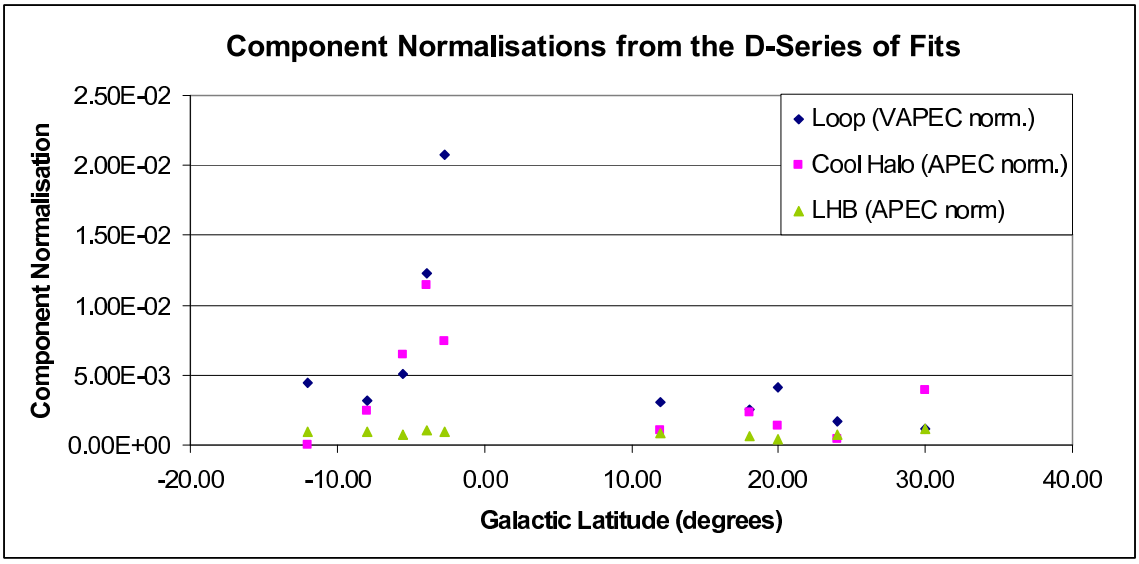

Figure 4.27: Normalisations from the D-series, showing an link between the Loop Interior and the 'Cool Halo.' The normalisation of the LHB (APEC) component is also plotted to show that it does not follow the same trend.

falling together, as shown in Figure 4.27.

4.7.3 A Case of Mistaken Identity

During their analysis of the NPS fields, Willingale et al. (2003) detected an absorbed 0.1 keV signal, which they hypothesised was the signal from a cool Galactic Halo. However, two points have arisen which prompt a reinterpretation of that signal. First, this work has benefited from the inclusion and analysis of the ten Oxygen fields, which revealed the presence of an absorbed 0.25 keV thermal signal. Since this emission could not be attributed to the XRB or the LHB, and because it is present to some extent across the whole of the Anti-centre, its most likely source is the Galactic Halo. Since there is no clear reason why the Halo should be, or should appear to be, cooler in the Galactic Centre, it is likely that the absorbed 0.1 keV signal observed in the Galactic Centre must have some other source.

Second, the absorption of the Wall must be considered. The Wall, the dense layer of absorbing material lying between the LHB and the Loop, is more extensive in the

Northern Bulge and Southern fields than it is in the North Polar Spur, and in most cases, equal to the full Galactic Column. Although the absorbed APEC component observed in the North Polar Spur fields had previously been interpreted as a distant Halo, this is unlikely to be the case: if it were, then prior to detection in the fields closest to the Plane, this signal would have to pass through the full Wall, Loop 1, the Galactic Plane, the full Galactic hydrogen column, and possibly the Galactic Centre itself. Since the Galactic n_H near the Plane is generally greater than 7×10^{20} cm^{-2}, the opacity limit for radiation in the $\frac{1}{4}$ keV energy band (Egger & Aschenbach 1995), it is realistic to assume that such a signal would be completely attenuated long before it reached an X-ray detector.

As Snowden et al. (1990*b*) explains, soft X-rays have a short mean free path, and so any radiation observed in the Galactic Plane must originate relatively nearby in the Disk. It is therefore reasonable to suggest that the radiation represented by the absorbed APEC has a more local origin that was previously thought.

Finally, the connection, mentioned above, between the normalisation of this component and that of the absorbed VAPEC in the Loop 1 fields, strongly indicated that their sources might be linked. There is no known mechanism through which Loop 1, a closed and complete SNR with no sign of major outflow, could interact with a distant Galactic Halo. Evidently, such a Halo could not be the source of the absorbed APEC component. Instead, it must be local, and intrinsically connected with the Loop.

4.7.4 The Anatomy of a SNR

In order to re-interpret the signal from the Loop 1 direction, it is necessary to understand the processes involved in the creation of a superbubble. These are described in great detail in Tielens (2005), from which much of the information in this section has been obtained.

When a high mass star ($M > 8\ M_\odot$) reaches the end of its life, it ejects a large fraction of its mass (between $1 - 5\ M_\odot$) in a supernova event. The explosion, which imparts $\sim 10^{51}$ ergs of kinetic energy into the local region, propels stellar material in all directions, at velocities reaching $\sim 10^4$ km s^{-1}.

The resulting sphere of ejecta (the supernova remnant, or SNR) surges outwards, expanding into the interstellar medium.

From this point, the evolution of the SNR occurs in three distinct stages. In the first, the mass of the stellar ejecta is significantly greater than that of the interstellar material it has displaced, causing the shock-front at the leading edge of the remnant to expand rapidly under its own momentum.

During this process a reverse shock, arising from the impact of the explosion on the pre-existing ISM, passes back through the remnant, thermalizing its interior and creating a bubble of hot, rarefied gas. The shocked stellar material at the edges of the remnant creates a relatively thin, but dense, shell around this hot interior. Provided that the shockwave produced by the supernova is 'strong', that is, the density behind the shock is at least four times greater than that ahead of it, the thickness of this shell will be approximately one twelfth of the total radius of the remnant[3].

The second developmental stage is attained when the mass of the material swept up by the remnant exceeds that of the ejecta. The growth of the remnant continues, although friction slows its leading-edge to $\sim$ 250 km s^{-1}. At this stage, the plasma temperature of the remnant is around 10^6 K, ideal for X-ray emission. Since the high ionisation of the plasma causes its cooling to be inefficient, the total energy of the remnant is conserved as its volume increases, allowing its expansion to continue adiabatically.

In the third stage, the growth of the remnant ceases and it becomes isothermal. In the absence of any further energy input, the internal pressure of the bubble will equalise with the surrounding environment. The remnant will gradually lose its identity, and merge back into the ISM.

When this information is applied to the SXRB, one can get a better insight into the SNRs that dominate our sky. The LHB appears to be at the end of stage two, and beginning stage three of its development. It is virtually isothermal: its temperature is tightly constrained, and stable around 0.1 keV. Also, its irregular shape indicates that rather than dominating the local region, other structures may have begun to impinge upon it, deforming its outer layers. Moreover, its faint, apparently open polar regions suggest that it has already begun

[3] Equation 12.70, page 441 in Tielens (2005)

to fade into obscurity.

In contrast, Loop I seems to have reached stage two. Although Loop I is thought to have been created by more than one explosion, the basic evolutionary model still holds, since these supernovae all occurred within the same remnant boundary.

Newer shock-fronts would have experienced little resistance to their expansion from the already established bubble interior, it having been recently cleared of debris. Upon contact with the new shock-front, the old shell would have been re-energised and inflated. However, since material is added to the shell by this process, the thickness of the shell would be maintained at around one twelfth of the total radius of the remnant.

Beyond the limits of this shell, the HI from the ISM displaced by the encroaching remnant can be said to have formed a further shell: an envelope of cool, absorbing gas. This material would be energised by thermal energy transferred from the hot shock-front, causing it to the emit 21 cm line radio emission detected by Berkhuijsen et al. (1971) and others.

Hence, Loop I can be described as a multilayered structure comprising a hot interior, a cool shell, and a cold HI envelope.

4.7.5 Re-interpreting and Modelling the Cool Component

When the theoretical structure of a SNR (Section 4.7.4) was taken into account, it seemed logical to reinterpret the signal modelled by the absorbed APEC component as an X-ray emissive cool shell surrounding the hot Loop I interior, rather than a 'cool Galactic Halo'. In terms of the 'anatomy', this is the shell that lies between the hot, rarefied interior and the cool neutral hydrogen surrounding the bubble.

To model a shell, the absorption on the APEC component was reduced from almost the full Galactic column (as used in Willingale et al. (2003)), and made to equal the absorption on the VAPEC, effectively placing it behind the Wall, at the same distance from the Earth as Loop I.

This change in interpretation, from a cool Galactic Halo to a local supershell, is quite a

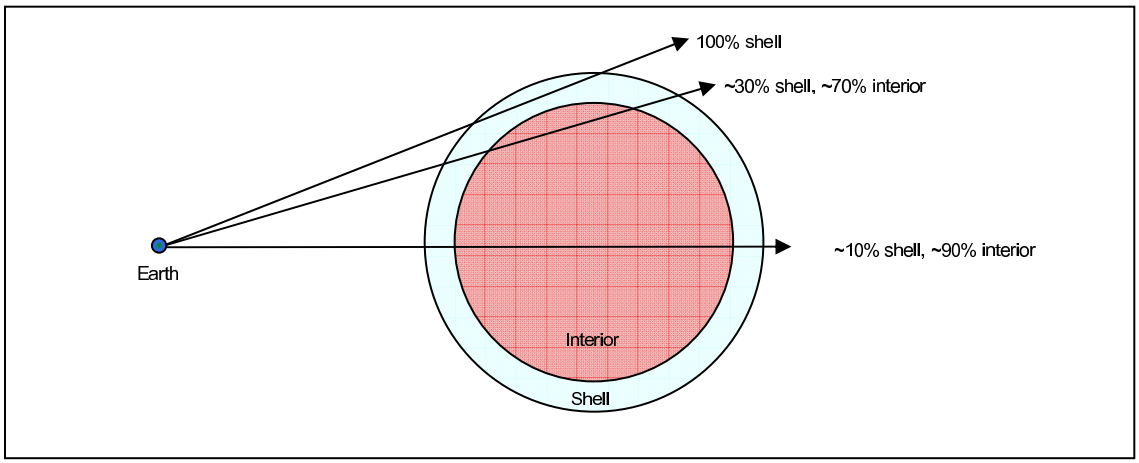

Figure 4.28: Cartoon (not to scale) showing the effect of viewing angle on the received flux from Loop I.

leap, but it can be tested, and concurs with the models advanced by other researchers. The idea will be developed further through detailed spectroscopy in Chapter 5, and with geometric modelling in Chapter 6. However, in this interpretation of the fitted spectra, it will suffice to consider the structure of the shell itself. Assuming that Loop I is spherical, the proposed shell would lie concentrically around its interior, as shown in Figure 4.28.

When analysing the spectra from the Galactic Centre direction, contributions from both the Loop's interior and the cool shell can be expected; however, the quantity of flux coming from each structure will vary depending on the viewing angle. Although the density of the shell is expected to be higher, its interior should be more prominent when looking towards the Loop's centre, since the column depth of the interior is much greater than that through the shell. Conversely, when looking close to the limbs of the Loop, one would expect the shell to produce a greater share of the flux. In the extreme case, if one observes directly through the shell, missing the interior layer completely, then only the signal from the shell should be discernable.

4.7.6 Model E

To implement the new interpretation, the absorption on the 0.1 keV absorbed APEC component used in Model D was tied to that of the Wall. This brought it forward to the

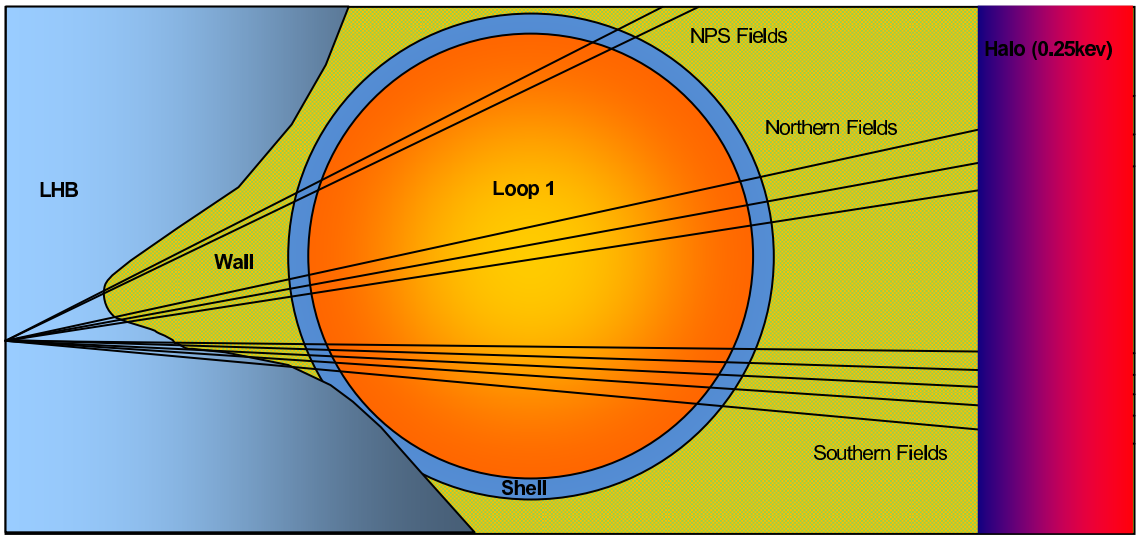

Figure 4.29: Modelling the Loop Fields: A cartoon illustrating the structures represented by Model E

same distance as the 0.3 keV absorbed VAPEC, allowing the 0.3 keV VAPEC to represent the hot interior of the Loop, while the 0.1 keV modelled its cool outer shell, as shown in Figure 4.29.

Having reassigned the absorbed APEC, a new component had to be included to represent the Halo. To this end a 0.25 keV VAPEC, set behind the full Galactic column, was included to be consistent with the results from the Oxygen fields. Hence, the new formulation, Model E, can be written as follows:

$$\text{APEC} + (\text{WABS} \times \text{VAPEC}) + (\text{WABS} \times \text{APEC}) + (\text{WABS} \times \text{VAPEC}) + (\text{WABS} \times \text{POWER}) + \text{GAUSS1} + \text{GAUSS2}$$

Representing:

$$\text{LHB} + (\text{Loop 1}) + (\text{Shell}) + (\text{Halo}) + (\text{XRB}) + \text{Al } K_\alpha + \text{Si } K_\alpha$$

Model E was applied to all ten of the Loop fields. In this iteration, the chemical abundances in the VAPEC components were fixed to solar values. The best-fit parameter values of

the E-Series fits are listed in Table 4.8, and plots of the fitted spectra corresponding to these values are shown in Figures 4.30, 4.31 & 4.32.

Model E: Discussion

Since the 0.25 keV VAPEC component was rejected in all but one of the fields, it was apparent that the Halo is not generally visible in the Loop I direction. It would appear that both absorption and the SXRB flux are too high near the Galactic Centre, blocking out and swamping the Halo signal in this direction. Tellingly, the Halo only registered in field B5, positioned right at the edge of the projected boundary of the proposed shell, and even this was at a very low level, with a normalisation of $7.07 \times 10^{-4} \mathrm{cm}^{-6}$ pc.

However, the shell model worked well, making the fits both visibly and statistically better, and lifting the flux of the model between $0.2 - 0.8$ keV. Improving the fit to the continuum and the Halo has also highlighted two new features of the spectra. First, the misfit to the emission lines has become more obvious, with particularly bad chi squared deviations around the O VII and O VIII lines. Second, a hard, thermal excess has been exposed in the Southern Fields which increases towards the Galactic Plane.

4.7.7 The Galactic Plane

The increasing hardness towards the Galactic Centre is clearly visible in profiles of the unfitted reduced spectra (Figure 4.33). The DXRB signal can be seen to increase in brightness in the vicinity of the Galactic Plane: the energy continuum rises significantly, reducing the prominence of the large Al-K_α and Si-K_α fluorescence lines, present at $\sim$ 1.49 keV and $\sim$ 1.76 keV respectively, and the O VII, O VIII, Fe and Si emission lines from the SXRB present between $0.4 - 1.4$ keV. The emission lines in this range are fitted primarily by the absorbed VAPEC component, and so can be mostly attributed to the plasma within Loop I. Since continuum energy in the vicinity of the Plane rises disproportionately with respect to the strength of these lines, the hard excess must be of separate origin, and not produced by the Loop itself.

At the same time, the flux of the spectrum shifts towards higher energies. On the left-

Table 4.8: The E-Series best-fit parameter values for the Loop fields. For a key to the table headings, see Appendix B.

Field	N5	N4	X3	X2	X1	B1	B2	B3	B4	B5
Latitude	30.00	20.00	24.00	18.00	12.00	-2.71	-3.87	-5.49	-8.00	-12.00
LHB Norm	2.72E-4	4.96E-4	7.10E-4	6.67E-4	7.53E-4	8.12E-4	7.39E-4	5.89E-4	7.88E-4	7.26E-4
Gal N_H	0.055	0.080	0.122	0.099	0.174	0.455	0.323	0.246	0.166	0.288
Wall N_H	0.031	0.080	0.122	0.099	0.174	0.455	0.323	0.246	0.166	0.085
Fore N_H	0.564	1.000	1.000	1.000	1.000	1.000	1.000	1.000	1.000	0.373
Loop I Norm	3.60E-3	5.41E-3	1.93E-3	4.58E-3	3.64E-3	2.42E-2	1.86E-2	8.83E-3	5.83E-3	4.72E-3
Shell Norm	9.65E-3	1.14E-2	2.03E-3	1.00E-2	6.76E-3	1.42E-1	8.62E-2	3.54E-2	1.87E-2	1.83E-2
Halo Norm	0.00	0.00	0.00	0.00	0.00	0.00	0.00	0.00	0.00	7.07E-4
XRB Norm	2.21E-4	3.82E-4	3.86E-4	2.90E-4	3.57E-4	1.89E-3	1.39E-3	1.01E-3	6.77E-4	4.07E-4
χ^2	364.8	611.6	770.3	809.1	883.5	1866.1	2307.1	517.2	868.0	701.2
DOF	229	235	619	634	672	809	867	229	632	598
χ^2_ν	1.59	2.60	1.24	1.28	1.31	2.31	2.66	2.26	1.37	1.17

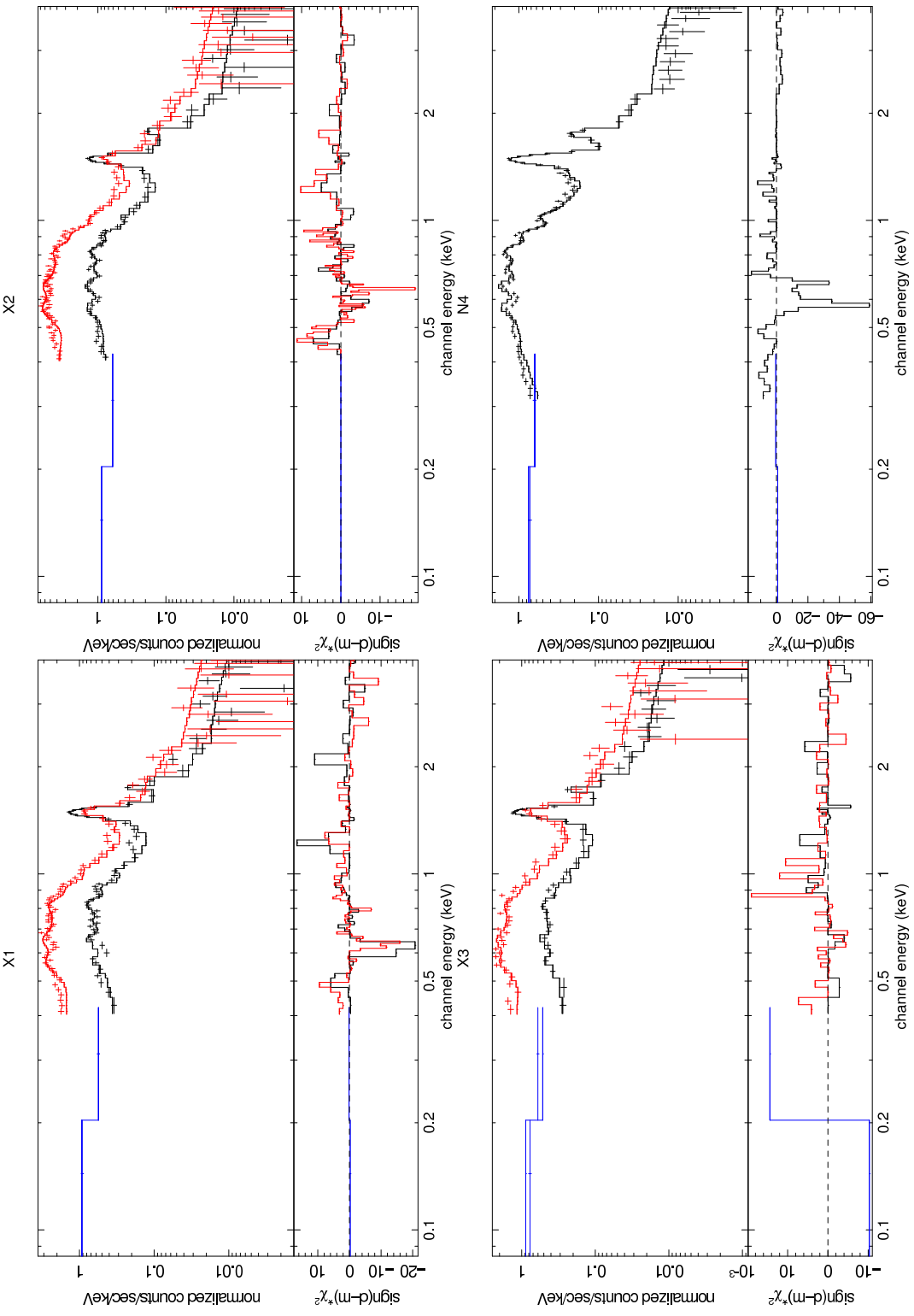

Figure 4.30: Model E: The best-fit spectra for X1, X2, X3 & N4. The traces shown are: ROSAT (blue), MOS (black) and pn (red).

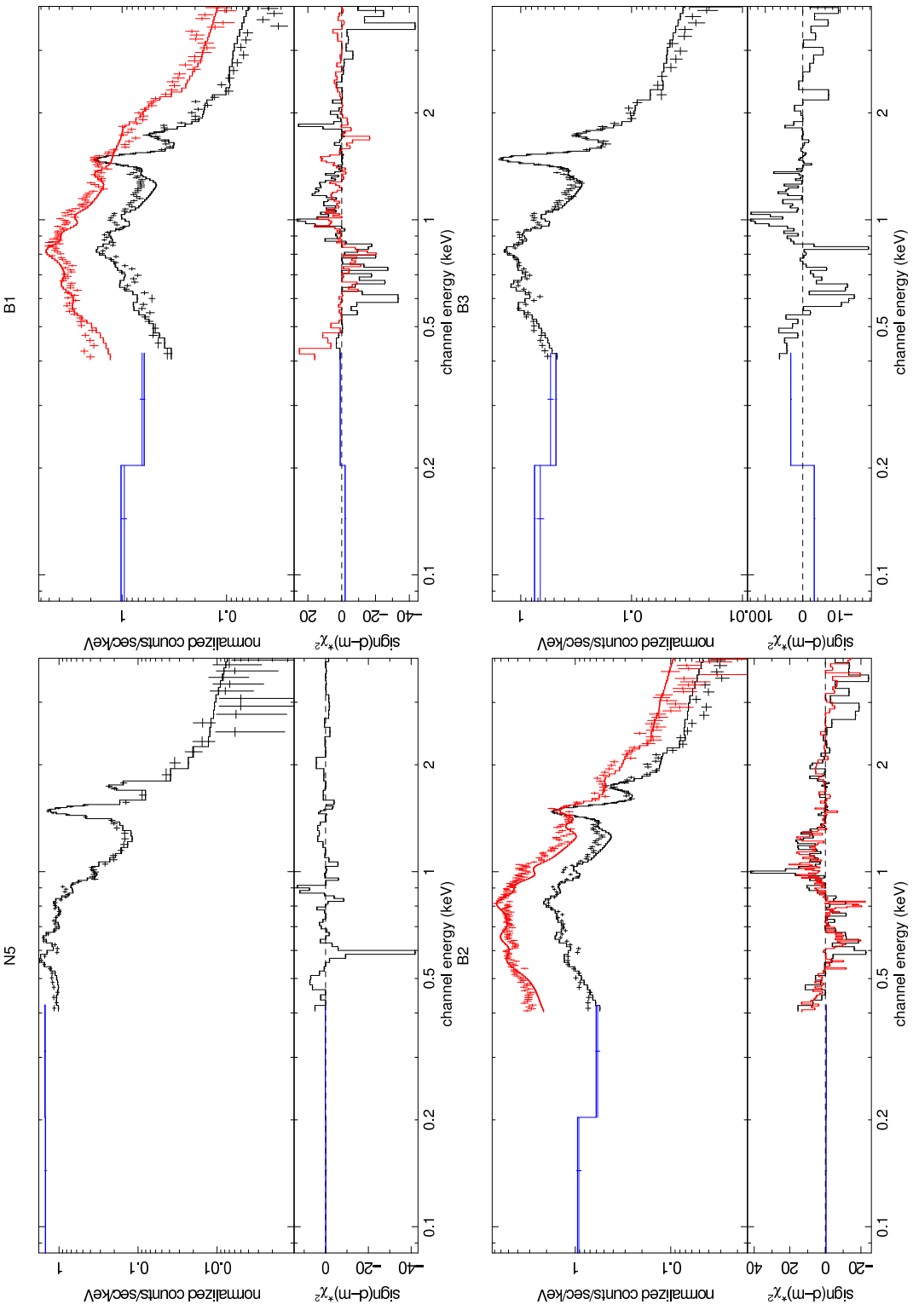

Figure 4.31: Model E: The best-fit spectra for N5, B1, B2 & B3. The traces shown are: ROSAT (blue), MOS (black) and pn (red).

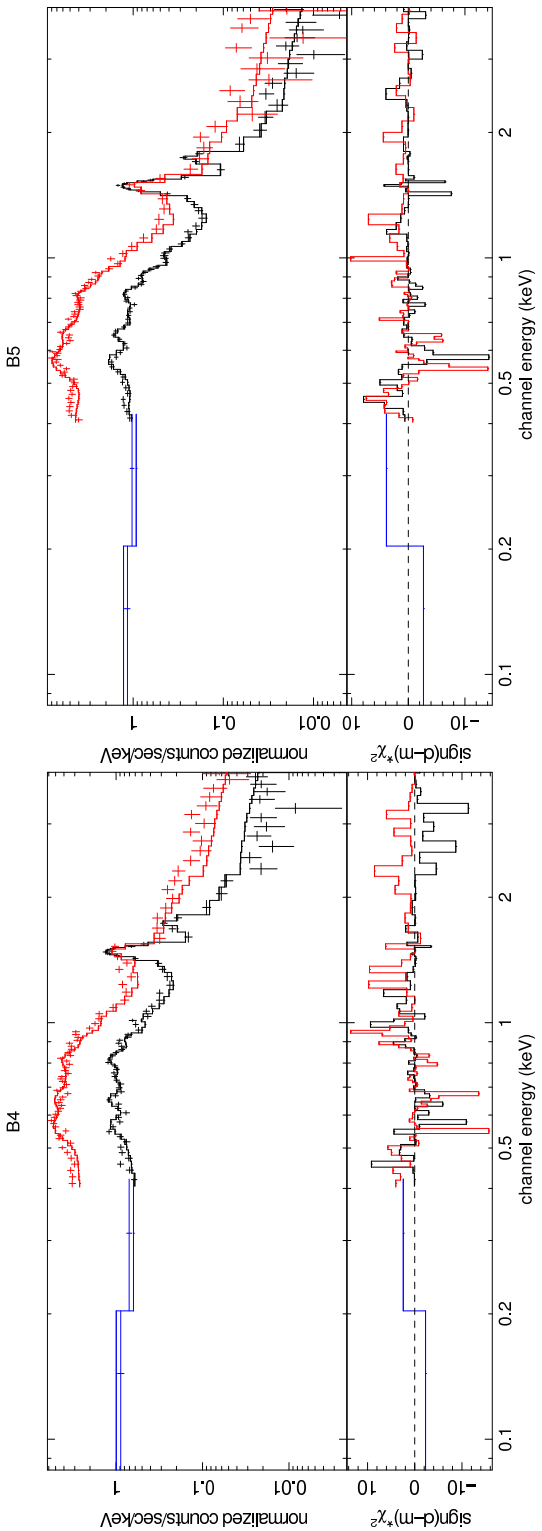

Figure 4.32: Model E: The best-fit spectra for: B4 & B5. The traces shown are: ROSAT (blue), MOS (black) and pn (red).

hand side of the graph, the blue (B4) and green (B5) data dominates, followed by magenta (B3), orange (B2) and red (B1). Clearly, the soft radiation from the LHB and Loop I make up the bulk of the flux in the B4 and B5 fields, which are furthest from the Plane. The colour sequence inverts around 0.8 keV, showing that the spectra from the fields closer to the Plane (B1, B2 & B3) contain a flux contribution from an additional, harder source. From this point until $\sim$ 1.5 keV, the continua of the B1, B2 & B3 fields rise, and silicon and sulphur lines, unseen in the Northern fields, become apparent, revealing that the extra source is hotter than the Loop, and thermal in origin.

The source of the hard emission has been a topic of debate for some time. Hayakawa et al. (1977) thought that the enhancement was entirely due to processes within Loop I, Garmire & Nugent (1981) suggested that it was a Galactic Wind produced in the Galactic Centre, and Egger & Aschenbach (1995) proposed that both sources might be responsible. Snowden et al. (1997) partially resolved the matter, by using the latitude dependence of the excess and the absorption trough in the Galactic Plane to argue that the Galactic Bulge was responsible. However, since the spectral influence of this source is manifest only in the fields within 6° of the Plane, it can be confidently identified as the Galactic Plane Radiation, the GPR, first observed by Berkhuijsen et al. (1971), and discussed in Section 2.8.

4.7.8 Model F

Model E's fit to the Southern fields was poor because it could not accommodate the hard excess originating from the GPR. In this series of fits, an absorbed MEKAL component was added to the model to represent the excess flux attributed to the GPR, since it is better suited than VAPEC to younger, more energetic plasmas. The new model, Model F, was then applied only to the Southern fields, where the GPR is present.

Although the source of the GPR is currently unknown, for the purposes of the model, it was assumed to be of non-local origin, and possibly associated with the Galactic Centre. This placed its source at a great distance from the Sun, certainly behind Loop I; and because it is associated with the Plane, it had to be behind a dense hydrogen column. Absorption equivalent to the full Galactic column was therefore imposed, creating the model, which is illustrated in Figure 4.34:

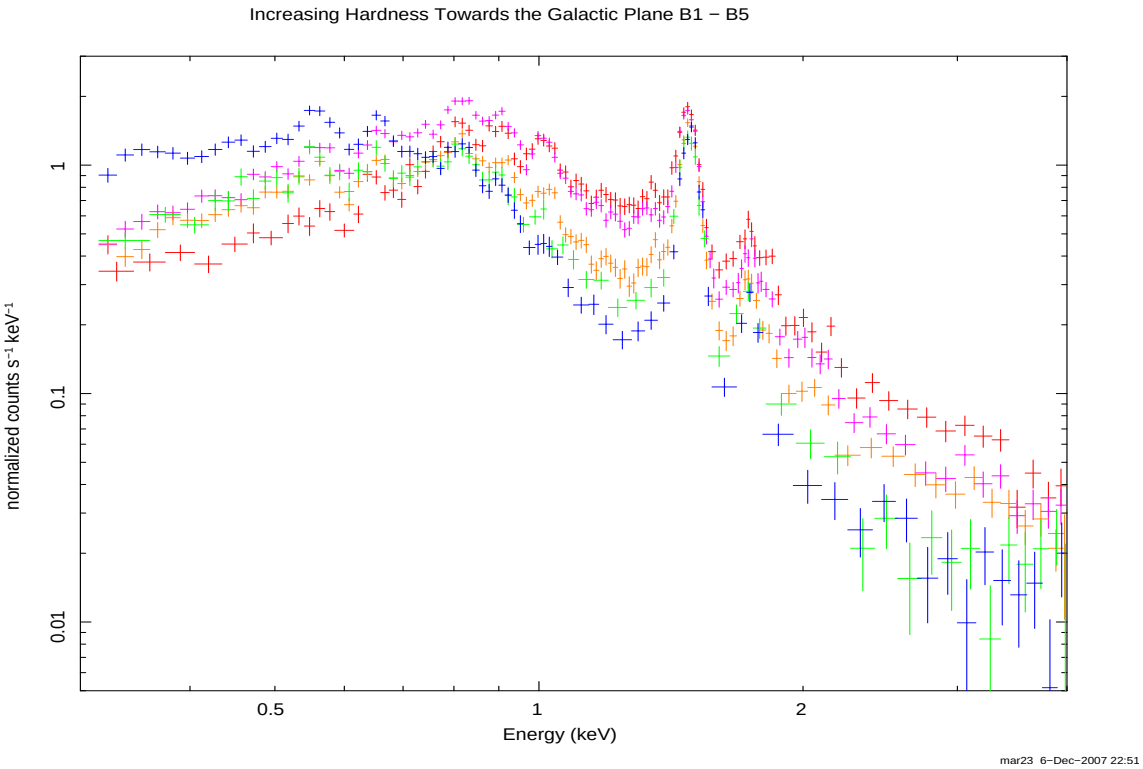

Figure 4.33: The reduced MOS data from the Southern fields, superposed to show the increasing hardness towards the Galactic Plane. For clarity, the data has been colour-coded: The data from the field closest to the Plane, B1, is shown in red. In order of increasing distance from the Plane, the remaining traces are from B2 (magenta), B3 (orange), B4 (green) and B5 (blue).

$$\text{APEC} + (\text{WABS} \times \text{VAPEC}) + (\text{WABS} \times \text{APEC}) + (\text{WABS} \times \text{MEKAL}) + (\text{WABS} \times \text{POWER}) + \text{GAUSS1} + \text{GAUSS2}$$

Representing:

$$\text{LHB} + (\text{Loop 1}) + (\text{Shell}) + (\text{GPR}) + (\text{XRB}) + \text{Al K}_\alpha + \text{Si K}_\alpha$$

Preliminary fits in which the temperature of the MEKAL was allowed to float found that it fitted well at $\sim$1 keV. Due to the complexity of the signal near the Plane, and to minimise the number of parameters in the fit, the model was then fitted with all temperatures

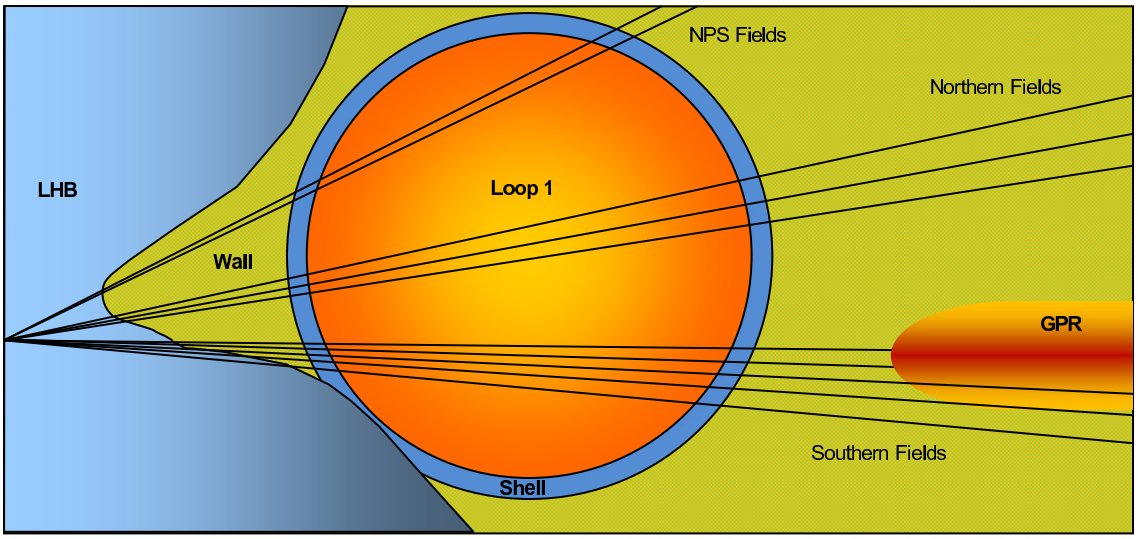

Figure 4.34: Modelling the Loop Fields: A cartoon illustrating the structures represented by Model F. The XRB is contained in the model, but not shown here.

frozen: the MEKAL at 1 keV, the LHB at 0.1 keV, the shell at 0.1 keV, the Loop's interior at 0.3 keV, and the Halo at 0.25 keV. All abundances were fixed to solar values. The best-fit parameter values of this F-Series of fits are listed in Table 4.9, and plots of the fitted spectra corresponding to these values are shown in Figures 4.35 & 4.36.

Model F: Discussion

Including the absorbed MEKAL has a tremendous effect on the statistics, lowering the reduced chi squared to acceptable values, between 1.1 – 1.5. In addition, the flux from this extra component supports the model at high energies, with the result that the Halo component disappears completely: it was entirely rejected by the model, with its normalisation falling to zero in all five fields. The continuum fit between 1 – 3 keV was also greatly improved, highlighting the emission lines which remain unfitted within Loop's signal.

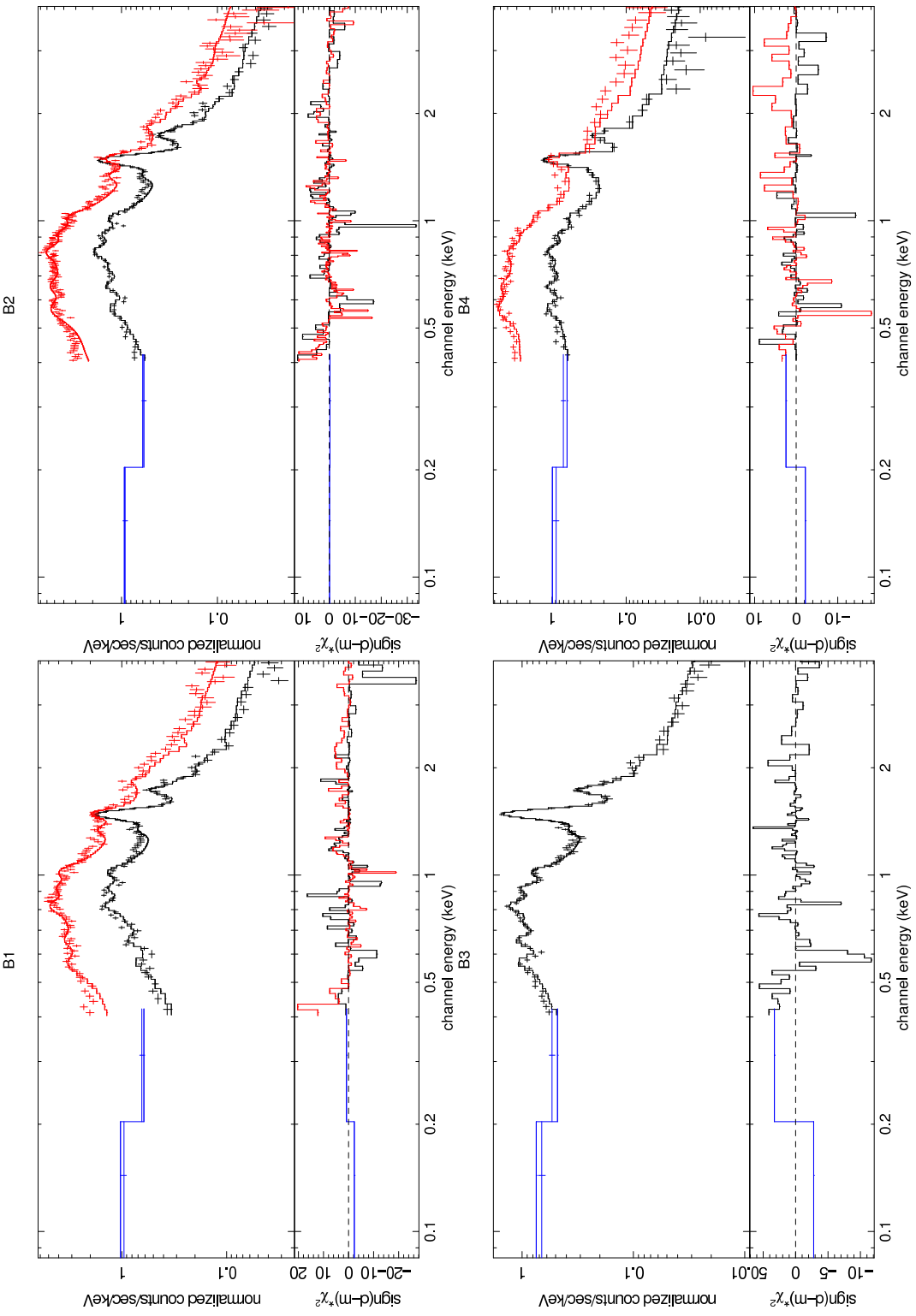

Figure 4.35: Model F: The best-fit spectra for B1, B2, B3 & B4. The traces shown are: ROSAT (blue), MOS (black) and pn (red).

Table 4.9: The F-Series best-fit parameter values for the Loop fields. For a key to the table headings, see Appendix B.

Field	B1	B2	B3	B4	B5
Latitude	-2.71	-3.87	-5.49	-8.00	-12.00
LHB Norm	8.17E-4	7.29E-4	5.85E-4	7.86E-4	8.67E-4
Gal N_H	0.455	0.323	0.246	0.166	0.288
Wall N_H	0.455	0.323	0.246	0.166	0.077
Fore N_H	1.000	1.000	1.000	1.000	0.336
Loop 1 Norm	1.74E-2	1.55E-2	7.66E-3	5.33E-3	4.66E-3
Shell Norm	1.56E-1	9.86E-2	4.03E-2	2.03E-2	1.71E-2
Halo Norm	0.00	0.00	0.00	0.00	0.00
Mekal Norm	3.57E-3	2.18E-3	8.73E-4	4.44e-4	2.36e-4
Mekal kT	1.06	1.03	1.00	1.00	1.00
XRB Norm.	1.57-3	1.02E-3	8.45E-4	5.65E-4	3.62E-4
χ^2	1117.8	1327.1	311.3	799.5	684.4
DOF	807	865	228	631	598
χ^2_ν	1.39	1.53	1.37	1.27	1.14

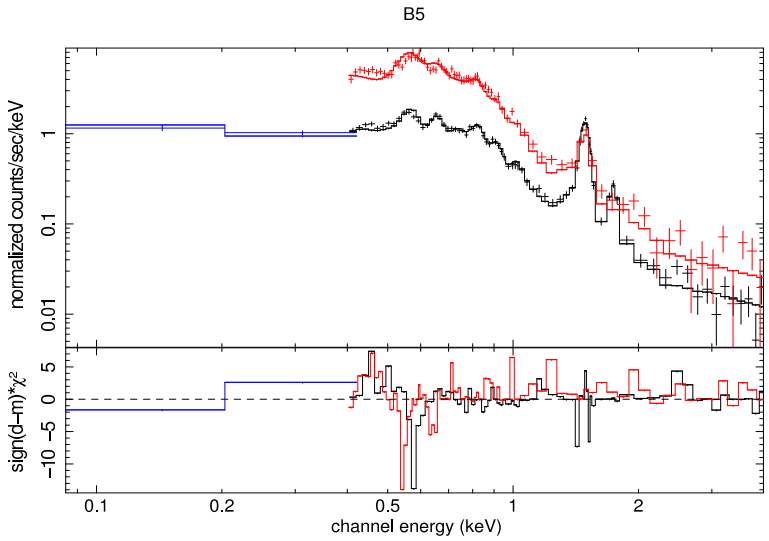

Figure 4.36: Model F: The best-fit spectrum for B5. The traces shown are: ROSAT (blue), MOS (black) and pn (red).

4.7.9 Model G

In an attempt to refine the fit from Model F, the data were refitted, this time allowing the relative abundances Ne, Mg, Fe and O to fit freely within the Loop interior. To reduce the number of free parameters, the abundances of Ne, Mg and Fe were tied, but as in the Oxygen fields, the O was allowed to fit freely. All other chemicals abundances were kept frozen to solar values, and the absorbed MEKAL component was used only in the Southern fields.

The best-fit parameter values of this G-Series fits are listed in Table 4.10, and plots of the fitted spectra corresponding to these values are shown in Figures 4.37, 4.38, 4.39 & 4.40.

Model G: Discussion

Free fitting the emission lines worked well, reducing the fit statistics in all of the fields. Also, as in the F series, the Halo component was rejected during the fit, confirming that even when the chemicals in the Loop were significantly lower than solar abundance, the Halo was still not required to make up the flux levels. It is also reassuring that the signal from the cool shell, set at the same absorption as the Loop interior, was strongly detected across the face of the Loop.

At first glance, the statistics are apparently excellent and the fits look good. However, a closer look reveals a significant problem: the normalisations of all of the components rise steadily within 6° of the Galactic Plane. This effect is evident in Figure 4.41, which show the distributions of the normalisations with latitude in the Loop fields.

Although the raised values may be partly explained by a local increase in plasma density near the Plane (the normalisation is proportional to the square of the plasma's electron density), it seems unlikely that such different structures, each with their own characteristics, would all be affected so consistently. Certainly, distant sources such as the XRB should be unaffected by the local environment: since it is unrelated to the Milky Way, its brightness should not increase near the Galactic Plane. If anything, one would expect the apparent flux of the XRB to decrease near the Plane, where the higher density of dust and gas produces greater absorption.

Table 4.10: The G-Series best-fit parameter values for the Loop fields. For a key to the table headings, see Appendix B.

Field	N5	N4	X3	X2	X1	B1	B2	B3	B4	B5
Latitude	30.00	20.00	24.00	18.00	12.00	-2.71	-3.87	-5.49	-8.00	-12.00
LHB Norm	3.66E-4	4.37E-4	7.03E-4	6.47E-4	7.44E-4	8.13E-4	7.15E-4	5.81E-4	7.73E-4	7.04E-4
Gal N_H	0.055	0.080	0.122	0.099	0.174	0.455	0.323	0.246	0.166	0.288
Wall N_H	0.032	0.076	0.122	0.099	0.174	0.448	0.306	0.246	0.166	0.063
Fore N_H	0.585	0.948	1.000	1.000	1.000	0.985	0.947	1.000	1.000	0.274
Loop I Norm	9.59E-3	1.61E-2	4.32E-3	1.25E-2	1.13E-2	8.33E-2	5.75E-2	2.83E-2	1.73E-2	1.21E-2
Abundances:										
O	0.351	0.244	0.348	0.303	0.222	0.184	0.207	0.234	0.258	0.340
Ne/Mg /Fe	0.360	0.347	0.472	0.366	0.334	0.178	0.246	0.267	0.319	0.351
Shell Norm	6.94E-3	6.85E-3	1.65E-3	7.43E-3	5.17E-3	1.08E-1	6.38E-2	3.08E-2	1.58E-2	1.10E-2
Halo Norm	0.00	0.00	0.00	0.00	0.00	0.00	0.00	0.00	0.00	0.00
Mekal Norm	0.00	0.00	0.00	0.00	0.00	2.38E-3	1.42E-3	5.03E-4	1.93E-4	7.15E-5
Mekal kT	0.00	0.00	0.00	0.00	0.00	1.000	1.000	1.000	1.000	1.000
XRB Norm.	2.88E-4	2.88E-4	3.49E-4	2.11E-4	2.78E-4	1.52E-3	9.88E-4	8.11E-4	5.41E-4	3.50E-4
χ^2	297.6	293.3	744.4	680.9	734.9	1006.1	1134.3	245.5	735.7	612.9
DOF	228	234	618	633	671	807	866	227	629	596
χ^2_ν	1.10	1.08	1.20	1.25	1.31	1.25	1.31	1.08	1.17	1.03

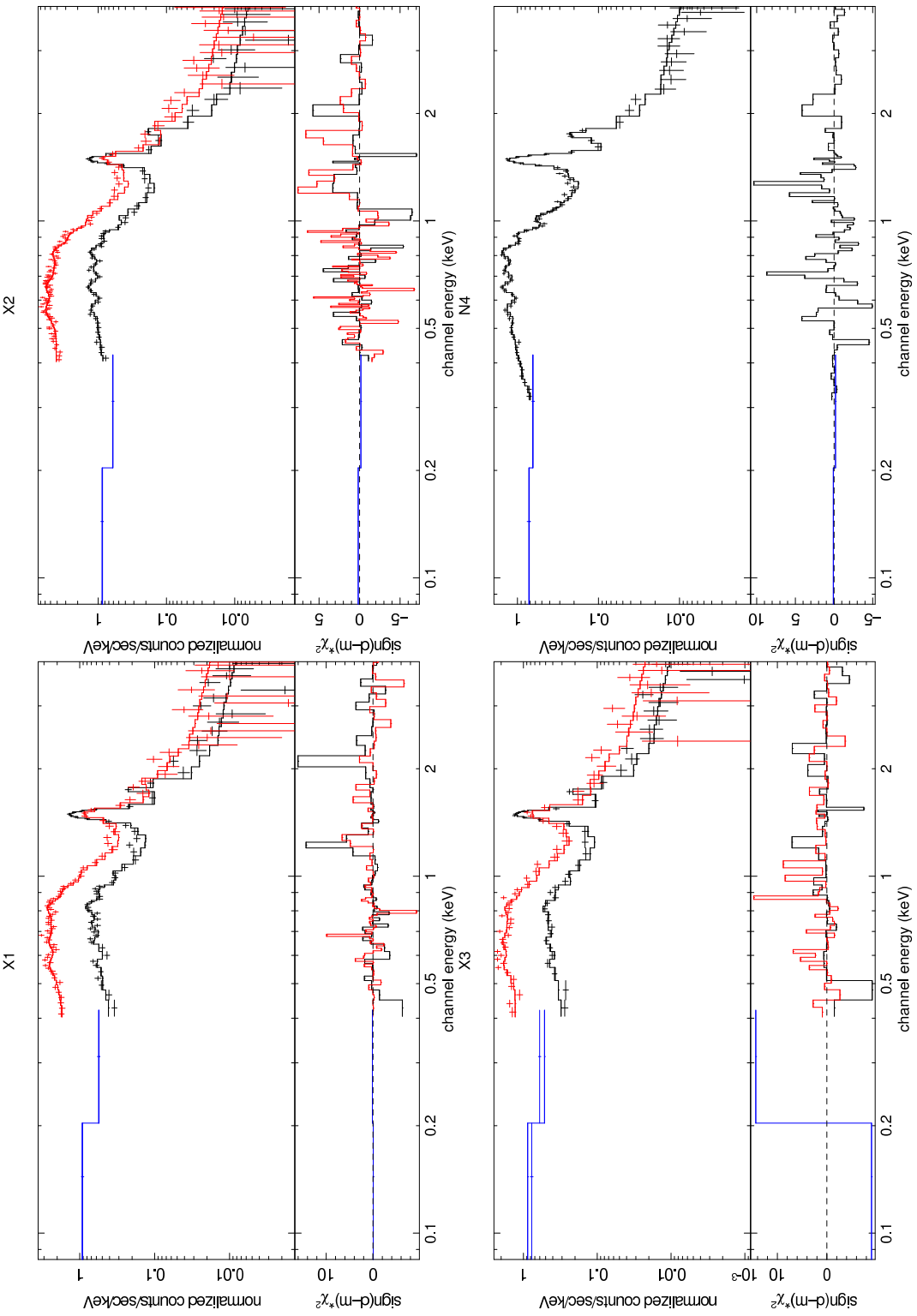

Figure 4.37: Model G: The best-fit spectra for X1, X2, X3 & N4. The traces shown are: ROSAT (blue), MOS (black) and pn (red).

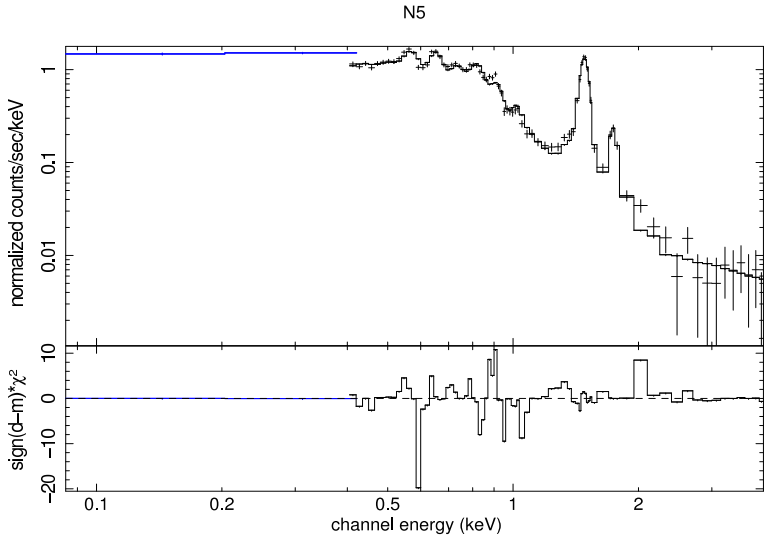

Figure 4.38: Model G: The best-fit spectrum for N5. The traces shown are: ROSAT (blue), MOS (black) and pn (red).

The source of the Plane enhancement is unclear. Although the GPR, modelled by the MEKAL component, is known to be a thermal source (see Section 2.8), the normalisations of all the components, including the non-thermal XRB, can be seen to rise near the Plane. At first glance, it would appear that the model has not fully accommodated the flux from the GPR, and so the normalisations of the other components have increased to compensate; however, such an effect should not have affected the XRB in the manner observed. Instead, there appears to be another non-thermal source adding to the continuum energy close to the Plane, the flux of which is being mistakenly accommodated by the normalisations of all of the other components.

4.7.10 Model H

In the earlier series of fits, poorly fitted parts of spectra were clear to see, as the model fell short of the data in those specific energy regions. The influence of energy enhancement in the Southern fields is not so obvious, because Model G did fit the data, albeit incorrectly, with the enhancement accommodated within the other components. To extract the enhancement's signal, the normalisations of the other components had to be frozen to realistic values, so that it could be fitted separately. Because this practice heavily biases the fitting process and hampers a detailed analysis of the SXRB near the

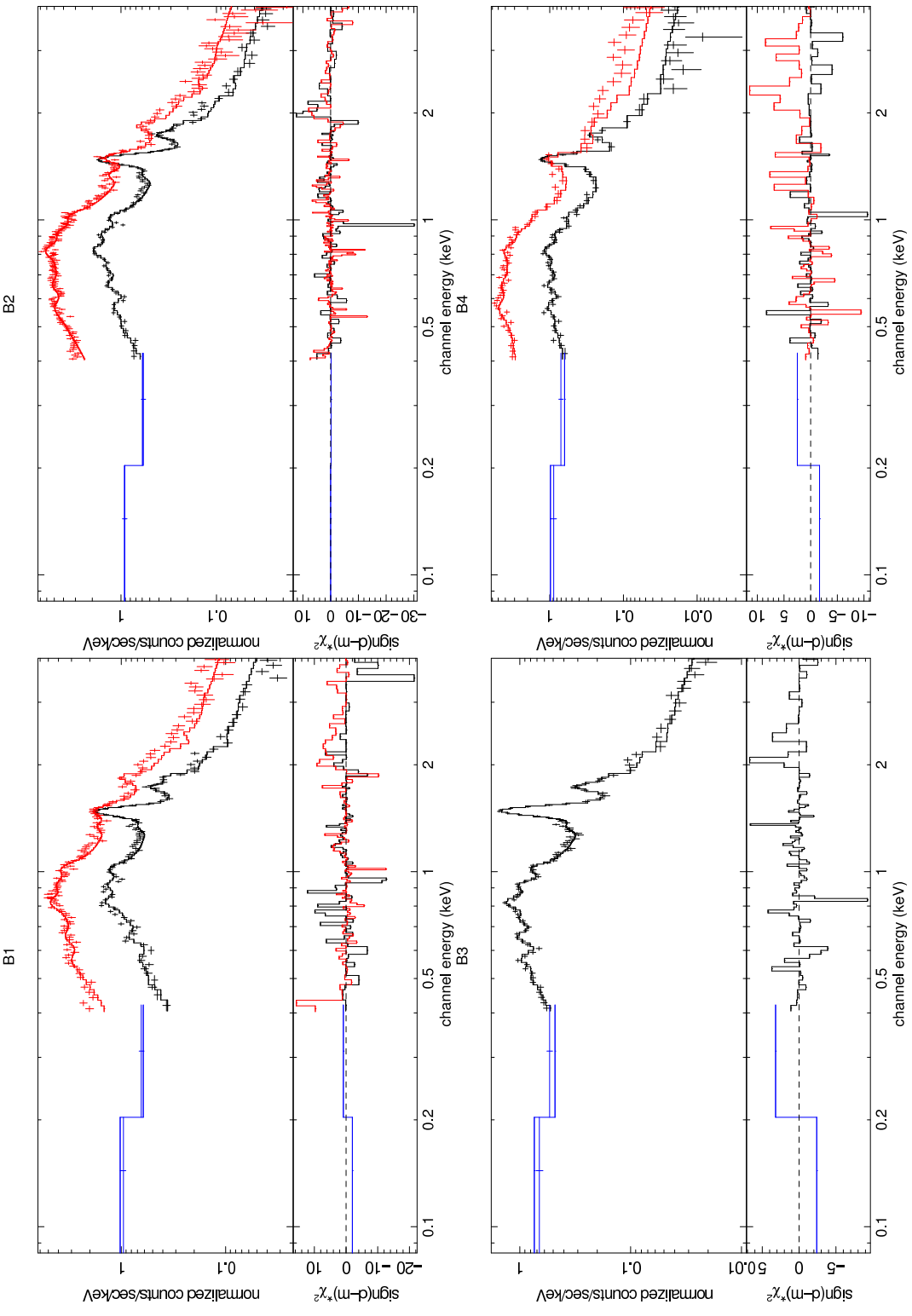

Figure 4.39: Model G: The best-fit spectra for B1, B2, B3 & B4. The traces shown are: ROSAT (blue), MOS (black) and pn (red).

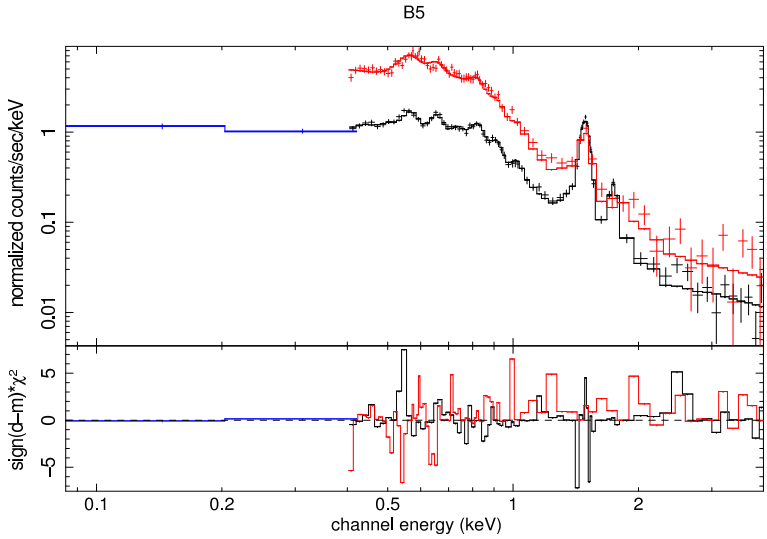

Figure 4.40: Model G: The best-fit spectra for B5. The traces shown are: ROSAT (blue), MOS (black) and pn (red).

Plane, it was used only in the Southern fields. The following model was applied:

$$\text{APEC} + (\text{WABS} \times \text{VAPEC}) + (\text{WABS} \times \text{APEC}) + (\text{WABS} \times \text{MEKAL}) + (\text{WABS} \times \text{POWER}) + (\text{WABS} \times \text{POWER}) + \text{GAUSS1} + \text{GAUSS2}$$

Representing:

$$\text{LHB} + (\text{Loop 1}) + (\text{Shell}) + (\text{GPR(thermal)}) + (\text{GPR(non-thermal)}) + (\text{XRB}) + \text{Al K}_\alpha + \text{Si K}_\alpha$$

This model includes two components designed to accommodate the Plane Enhancement: a MEKAL at 1 keV to fit the signal from the thermal GPR, and an absorbed power law, with a photon index of 2.5 to accommodate the non-thermal excess seen in the G-Series. Both the MEKAL and the power law were set behind the full Galactic column. While fitting, the normalisations of the LHB, Loop, Shell and XRB were frozen to their average values as determined in the G-Series fits to the Northern fields. Although this method allowed the extra components to fit freely, it also implicitly assumed that the properties

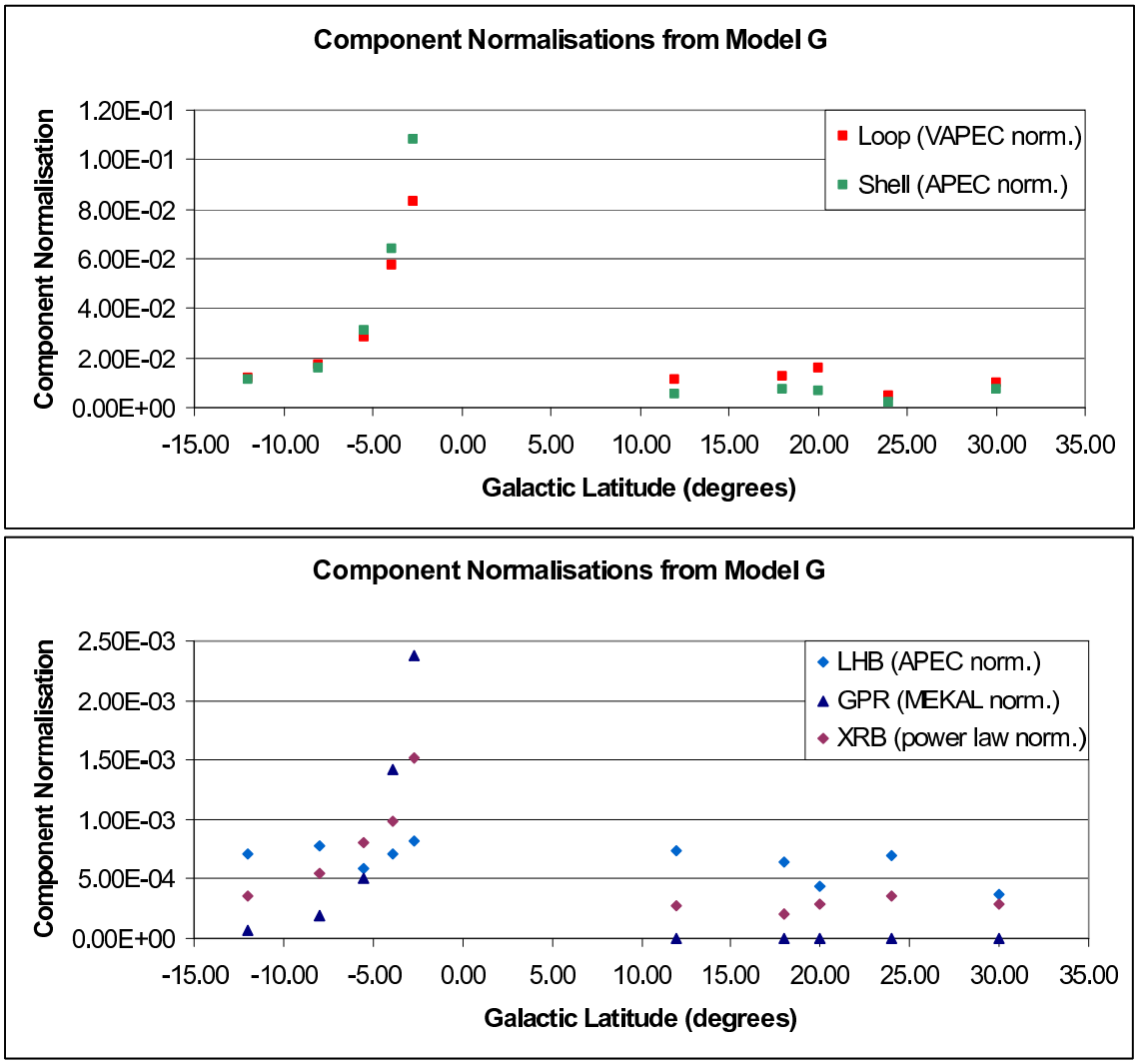

Figure 4.41: Component normalisations from Model G vs. Galactic latitude, showing the anomalous enhancement as the Plane is approached.

Table 4.11: The H-Series best-fit parameter values for the Loop fields. For a key to the table headings, see Appendix B.

Field	B1	B2	B3	B4	B5
Latitude	-2.71	-3.87	-5.49	-8.00	-12.00
LHB Norm	8.32E-4	6.43E-4	5.56E-4	7.35E-4	3.07E-4
Gal N_H	0.455	0.323	0.246	0.166	0.288
Wall N_H	0.201	0.094	0.115	0.099	0.037
Fore N_H	0.442	0.290	0.467	0.596	0.128
Loop I Norm	1.08E-2	1.08E-2	1.08E-2	1.08E-2	1.08E-2
Abundances:					
O	0.383	0.335	0.282	0.280	0.371
Ne / Mg / Fe	0.621	0.600	0.408	0.378	0.343
Shell Norm	5.61E-3	5.61E-3	5.61E-3	5.61E-3	5.61E-3
Mekal Norm	3.19E-3	2.24E-3	5.95E-4	1.80E-4	6.08E-5
Mekal kT	1.00	1.00	1.00	1.00	1.00
XRB Norm.	2.83E-4	2.83E-4	2.83E-4	2.83E-4	2.83E-4
GPR Norm	4.29E-3	2.71E-3	1.83E-3	9.59E-4	3.60E-4
GPR Photon Index	2.5	2.5	2.5	2.5	2.5
χ^2	943.7	1071.2	284.2	739.9	682.4
DOF	809	867	231	632	598
χ^2_ν	1.17	1.24	1.23	1.17	1.14

of both the SXRB and the XRB were similar above and below the Galactic Plane; a factor which may affect the interpretation of the SXRB in Chapter 6.

The best-fit parameter values of the H-Series fits are listed in Table 4.11, and plots of the fitted spectra corresponding to these values are shown in Figures 4.42 and 4.43.

Model H: Discussion

Although the normalisations of the LHB, Loop, Shell, and XRB are frozen to the average values found in the Northern fields, it has still been possible to produce excellent fits in the Southern fields. The absorbed MEKAL and power law have been able to fit the enhancement present near the Plane: the thermal signal from the GPR is covered by the MEKAL, while the power law fits the non-thermal excess responsible for the

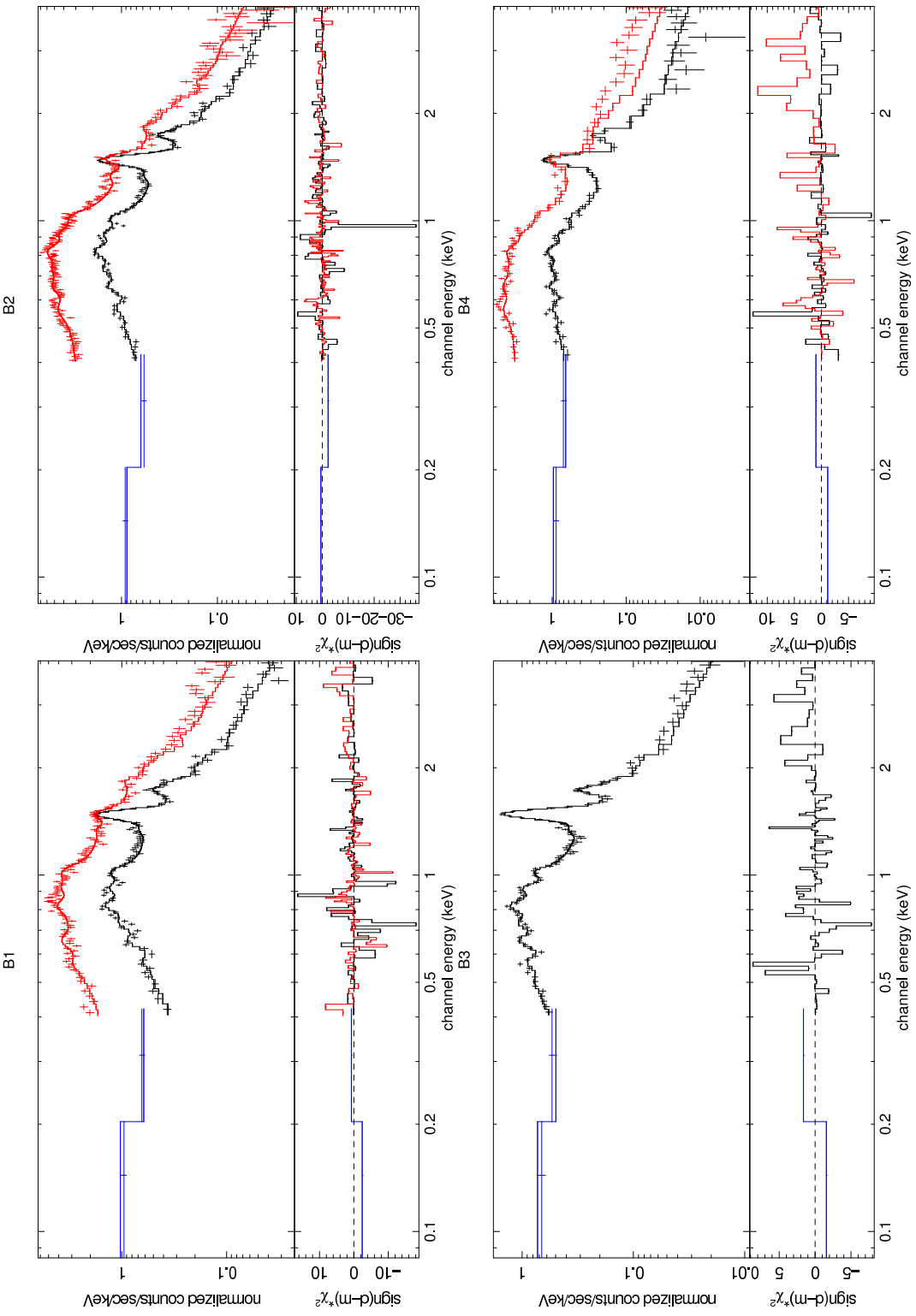

Figure 4.42: Model H: The best-fit spectra for B1, B2, B3 & B4. The traces shown are: ROSAT (blue), MOS (black) and pn (red).

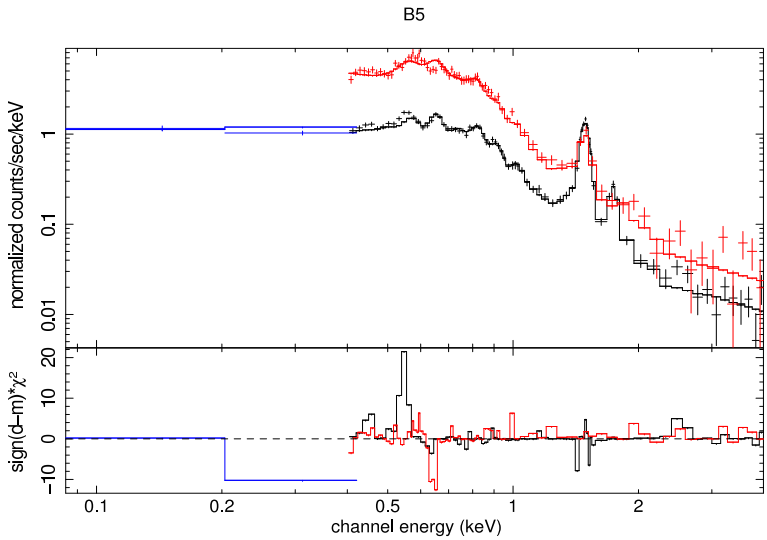

Figure 4.43: Model H: The best-fit spectrum for B5. The traces shown are: ROSAT (blue), MOS (black) and pn (red).

continuum enhancement seen in Figure 4.41. The source of this non-thermal excess is unclear, although the fact that it has been observed only close to the Galactic Plane in the Galactic Centre direction indicates that it may be associated with the Galactic Centre itself.

As the stepwise development of the model has shown, all of the components present in the model are required, and so the low reduced chi squared values obtained cannot be ascribed simply to an over complexity in the model. Indeed, since many of the parameters have been frozen to predetermined values, the model applied to the Southern fields has fewer free parameters than that applied to the Northern fields.

4.8 The Final Models

Through the iterations described above, the best fit models to the twenty fields have been determined.

In the Oxygen fields, the simple three-component Model B(d), representing the LHB, the Galactic Halo, and the XRB, provided the best fit:

$$\text{APEC} + (\text{WABS} \times \text{VAPEC}) + (\text{WABS} \times \text{POWER}) + \text{GAUSS1} + \text{GAUSS2}$$

Representing:

$$\text{LHB} + (\text{Halo}) + (\text{XRB}) + \text{Al } K_\alpha + \text{Si } K_\alpha$$

While the LHB behaved as expected, the Halo was found to have a plasma temperature of $\sim$0.25 keV, significantly higher than the 0.1 keV predicted by Willingale et al. (2003). In addition, while a fixed flux value was tried for the XRB, this did not work well. Instead, its normalisation was allowed to float, providing a 'best-fit' value which was in most cases significantly lower that the 9.0 photons s^{-1} cm^{-2} sr^{-1} keV^{-1} at 1 keV used by Hands (2003), indicating that only a fraction of the total XRB flux was really contained within the reduced spectra.

The Halo, identified in the Loop I region by Willingale et al. (2003), was not found to be discernible in any of the Loop I fields. Through consideration of the structure of SNRs, the possibility of the presence of a cool shell around Loop I was proposed, and then confirmed through fitting. Ultimately, the best fit to the Northern fields was obtained using Model G:

$$\text{APEC} + (\text{WABS} \times \text{VAPEC}) + (\text{WABS} \times \text{APEC}) + (\text{WABS} \times \text{POWER}) + \text{GAUSS1} + \text{GAUSS2}$$

Representing:

$$\text{LHB} + (\text{Loop I}) + (\text{Shell}) + (\text{XRB}) + \text{Al } K_\alpha + \text{Si } K_\alpha$$

which represents the LHB, Loop interior, Shell, and the XRB. In the Southern fields, however, two additional components, a MEKAL and a power law, were included to accommodate the thermal GPR and the non-thermal enhancement seen near the Galactic Plane, yielding Model H:

APEC + (WABS $\times$ VAPEC) + (WABS $\times$ APEC) + (WABS $\times$ MEKAL) + (WABS $\times$ POWER)
+ (WABS $\times$ POWER) + GAUSS1 + GAUSS2

Representing:

LHB + (Loop 1) + (Shell) + (GPR(thermal)) + (GPR(non-thermal))
+ (XRB) + Al K_α + Si K_α

The best-fit unfolded spectra from the Loop fields, showing the contribution of each component to the total flux, are shown in Figures 4.44, 4.45, 4.46, 4.47, 4.48 & 4.49.

In order to extract the signals from the Galactic Plane, it was necessary to freeze the normalisations of the four components represented in Model G to the average values found in the Northern fields prior to fitting. While this simplified the fitting procedure, and allowed the GPR to be characterised, it also introduced the assumption that the properties of the Loop are approximately symmetrical above and below the Plane; an assumption that will be tested in Chapter 6, where the physical properties of the SXRB structures will be examined.

The final best-fit parameter values for the Loop and Oxygen Fields, with their 90% confidence intervals, are listed in Appendix B.

4.9 Summary

The reduced spectra of the DXRB from twenty positions in the Milky Way have been fitted with XSPEC models. The results of this process, the best-fit parameters from Models B(d) in the Oxygen fields, G in the Northern fields and H in the Southern fields, have confirmed some established ideas, such as the ubiquity of the LHB. They have also provided new insights into the soft X-ray background, particularly the reinterpretation of the cool Halo of Willingale et al. (2003), which has allowed the identification of a cool shell around Loop 1. Fitting spectra from the Anti-centre also revealed the true signal

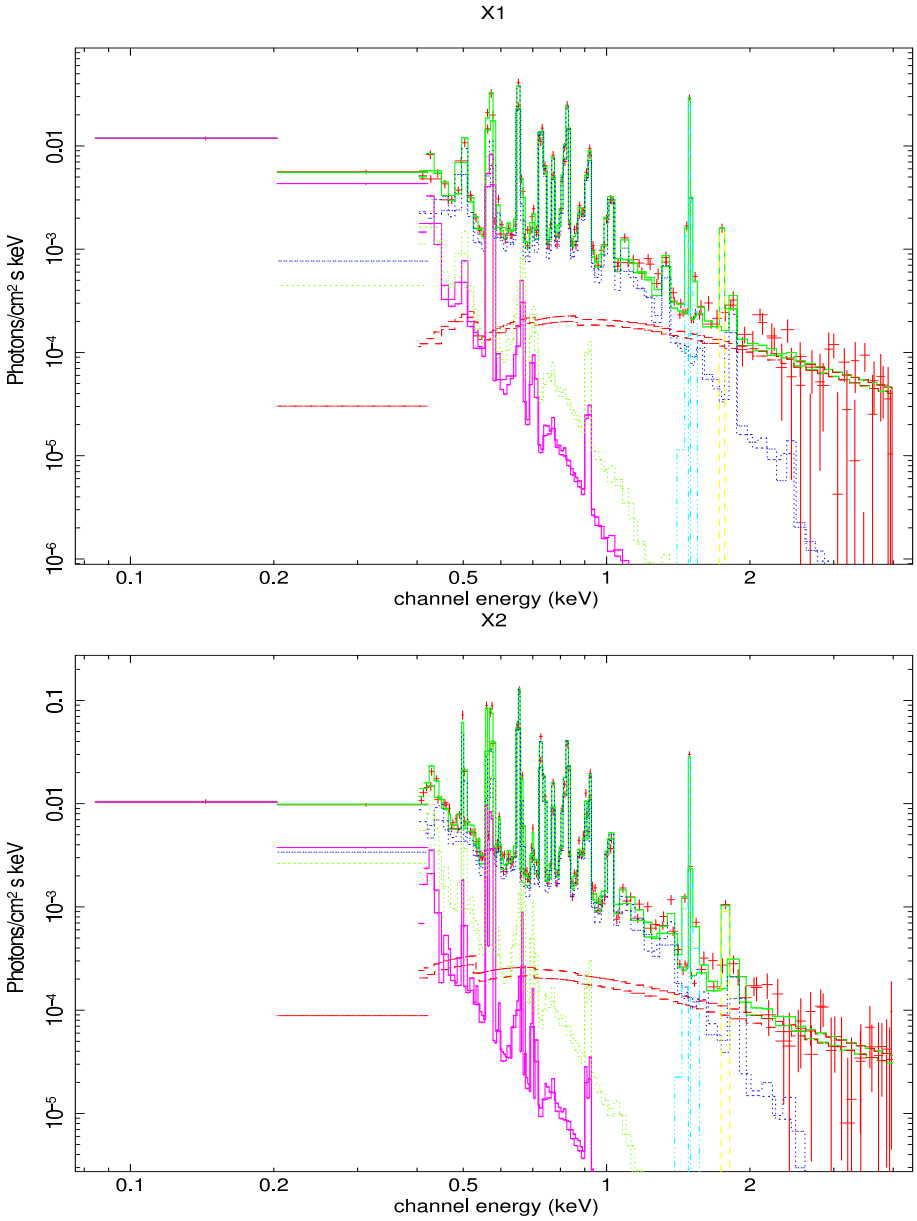

Figure 4.44: Unfolded spectra of fields X1 & X2. The red crosses mark the data points. The traces are as follows: Pink solid (LHB APEC), green dotted (shell APEC), dark blue dotted (Loop interior VAPEC), red dashed (XRB power law). The cyan and yellow peaks are the two Gaussian curves.

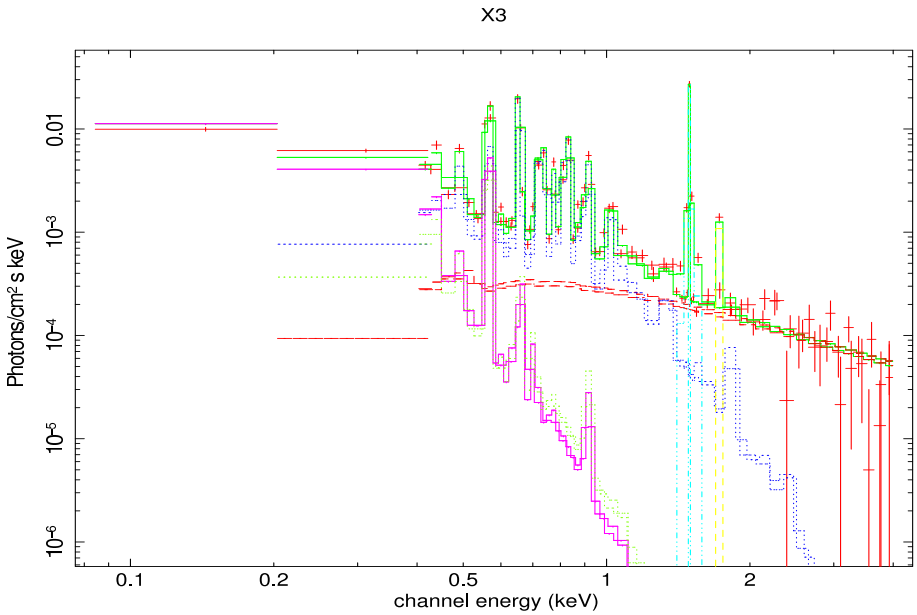

Figure 4.45: Unfolded spectrum of field X3. The red crosses mark the data points. The traces are as follows: Pink solid (LHB APEC), green dotted (shell APEC), dark blue dotted (Loop interior VAPEC), red dashed (XRB power law). The cyan and yellow peaks are the two Gaussian curves.

from the Halo, a warm 0.25 keV flux from chemically depleted plasma similar to the Loop I interior.

While the signal from the extragalactic background (the XRB, Section 2.3.1) is partly discernable in all twenty fields, it has been possible to free fit it only in the Oxygen and Northern fields. In the Southern fields, the normalisation of the XRB had to be frozen to an expected value to prevent it from rising in the proximity of the Galactic Plane. When allowed to fit freely, the normalisation of the power law used to model the XRB was seen to vary between 1.51×10^{-4} and 6.75×10^{-4} photons keV^{-1} cm^{-2} s^{-1}. While this amount of flux is relatively insignificant when compared with that produced by the SXRB, it is still vital to the fitted spectra, because it provides the high energy continuum that underlies the contribution of the various thermal sources.

Prior to fitting, the flux of the XRB had been expected to be isotropic. When fitted in the fields N4 and N5 by Willingale et al. (2003), and at other points along the Galactic Ridge by Hands (2003), the normalisation of the XRB was frozen in each field to a value equivalent to a flux of 9 photons s^{-1} cm^{-2} sr^{-1} keV, after Lumb, Warwick, Page &

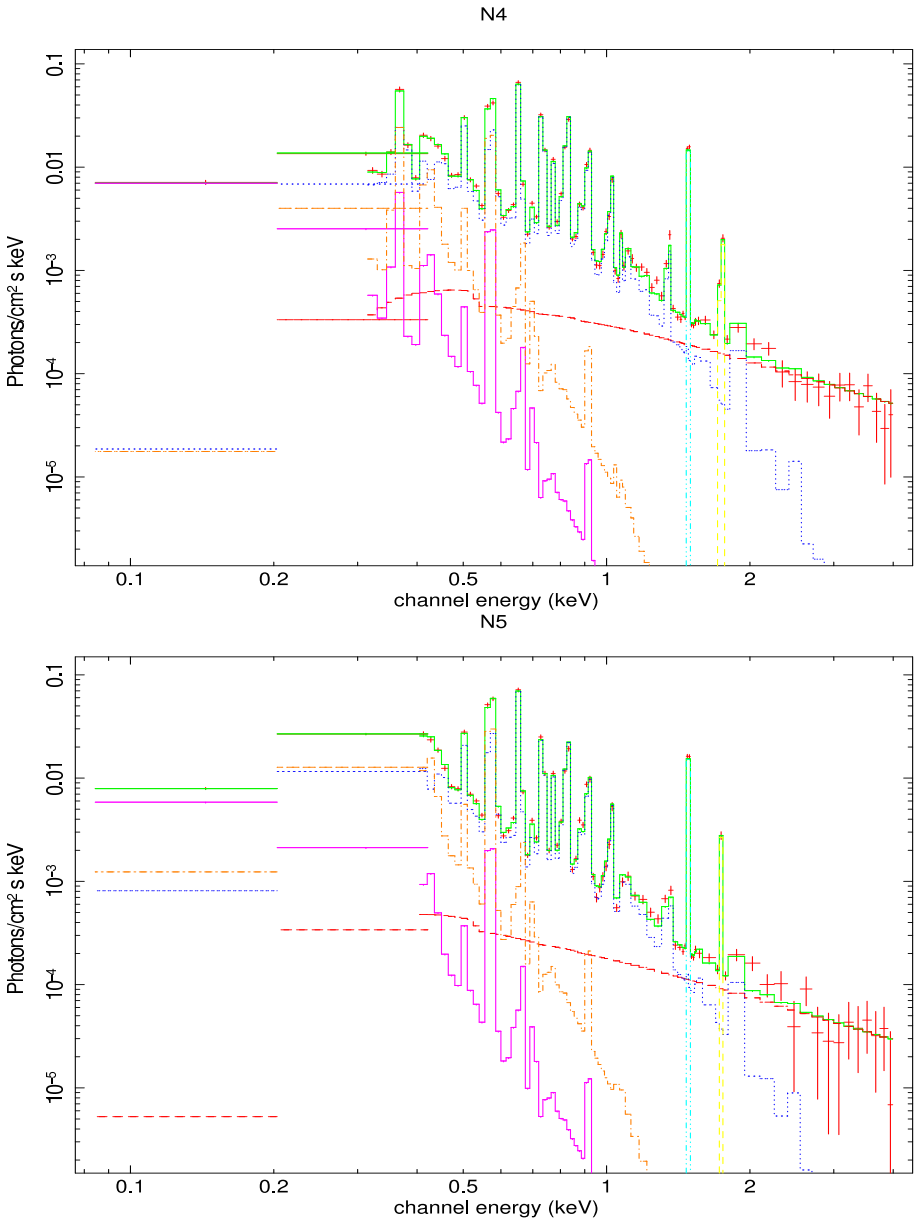

Figure 4.46: Unfolded spectra of fields N4 & N5. The red crosses mark the data points. The traces are as follows: Pink solid (LHB APEC), orange dot dash (shell APEC), dark blue dotted (Loop interior VAPEC), red dashed (XRB power law). The cyan and yellow peaks are the two Gaussian curves.

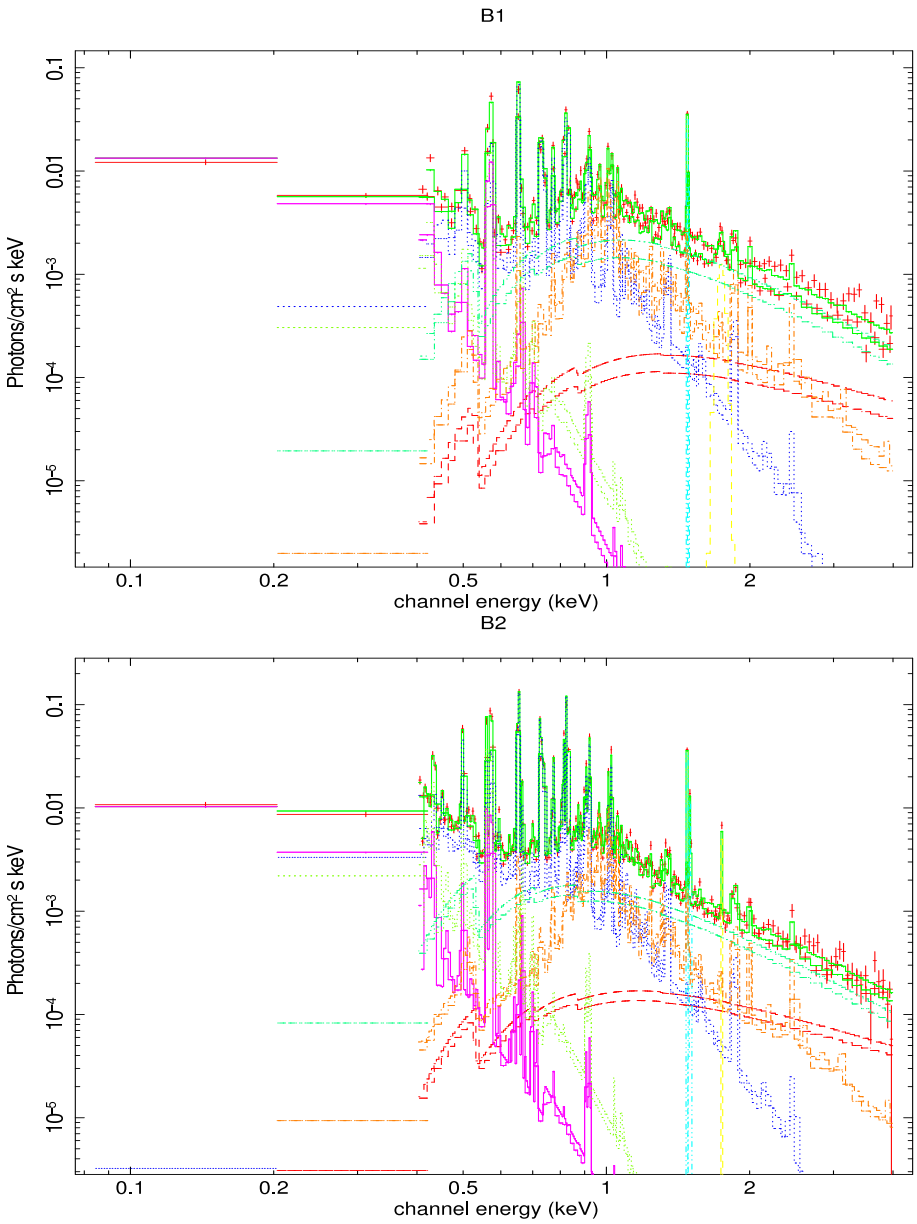

Figure 4.47: Unfolded spectra of fields B1 & B2. The red crosses mark the data points. The traces are as follows: Pink solid (LHB APEC), green dotted (shell APEC), dark blue dotted (Loop interior VAPEC), orange dot dash (MEKAL GPR), red dashed (XRB power law), cyan dashed (extra power law). The cyan and yellow peaks are the two Gaussian curves.

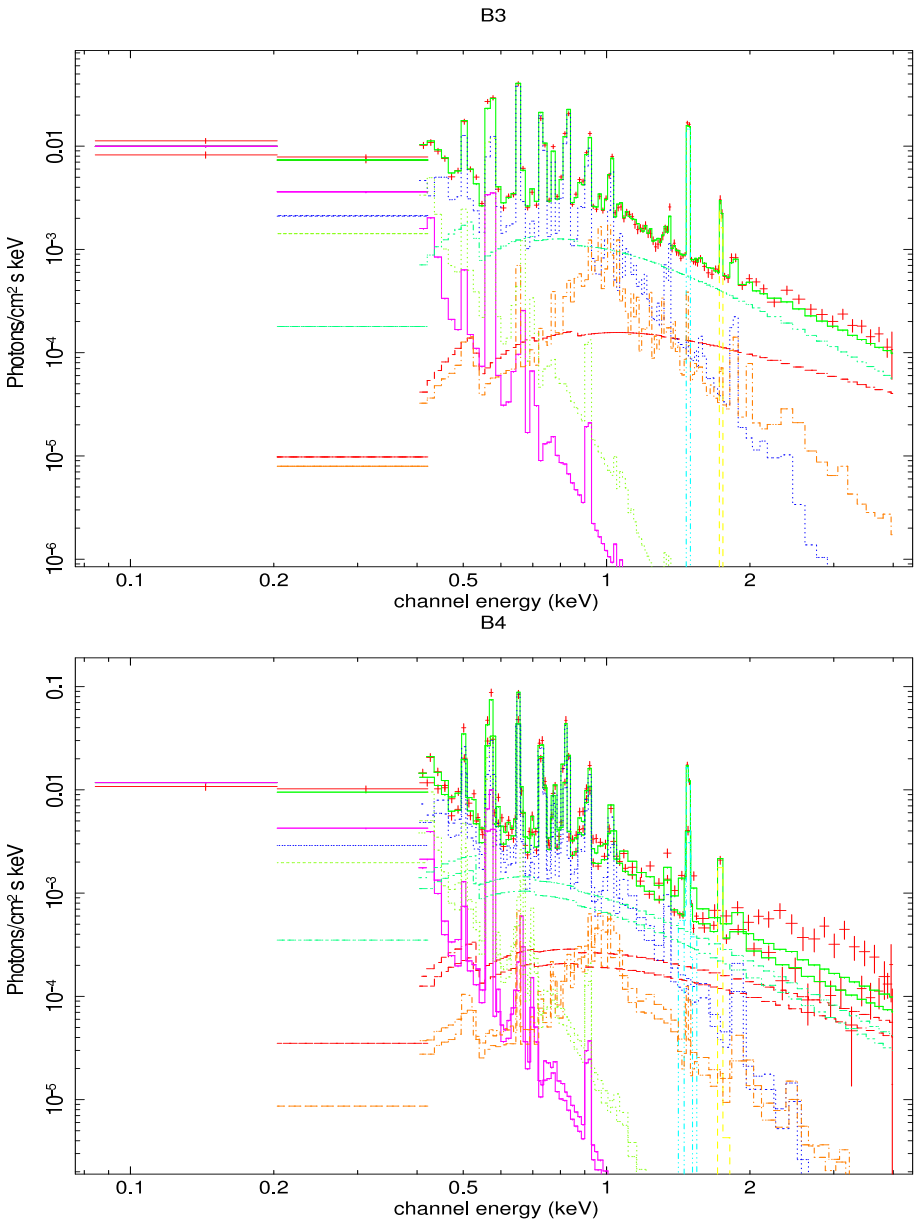

Figure 4.48: Unfolded spectra of fields B3 & B4. The red crosses mark the data points. The traces are as follows: Pink solid (LHB APEC), green dotted (shell APEC), dark blue dotted (Loop interior VAPEC), orange dot dash (MEKAL GPR), red dashed (XRB power law), cyan dashed (extra power law). The cyan and yellow peaks are the two Gaussian curves.

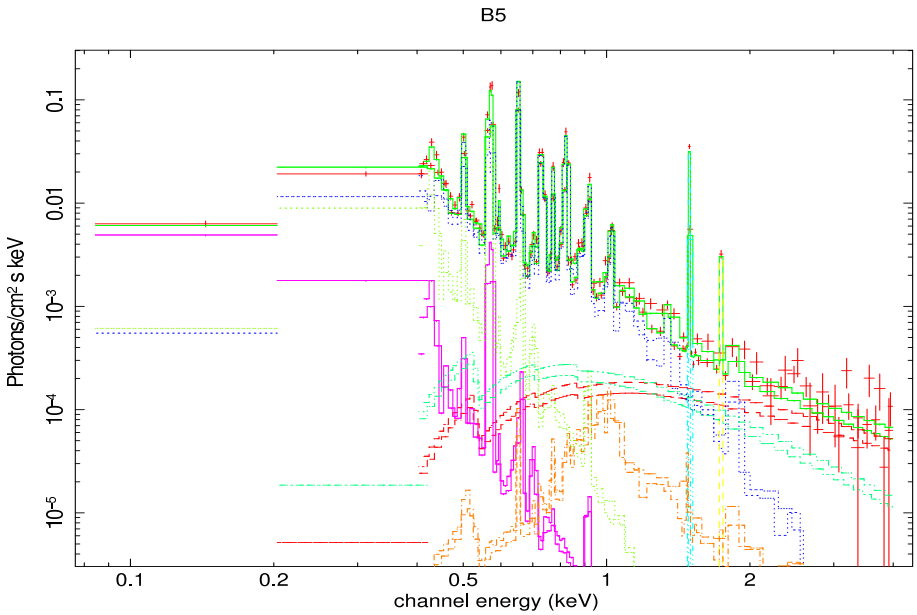

Figure 4.49: Unfolded spectrum of field B5. The red crosses mark the data points. The traces are as follows: Pink solid (LHB APEC), green dotted (shell APEC), dark blue dotted (Loop interior VAPEC), orange dot dash (MEKAL GPR), red dashed (XRB power law), cyan dashed (extra power law). The cyan and yellow peaks are the two Gaussian curves.

Luca (2002). While fitting the Oxygen fields (Section 4.6.2), however, it rapidly became apparent that this value was inappropriate for use in this study, as it caused the model to sit above the data. In the Anti-centre direction, the flux levels from the SXRB are much lower than in the Galactic Centre, and the hard end of the spectrum is not confused by emission from the GPR. However, in these fields, the detected flux from the XRB was found to be much lower than in the Galactic Centre direction, indicating that the whole of the XRB flux had not been included within the reduced spectra.

Also, when allowed to fit freely in the N4 and N5 fields, using the same energy range and fitting procedure as Willingale et al. (2003), the best-fit flux of the XRB was found to be about 30% lower, at 6.00 photons s^{-1} cm^{-2} sr^{-1} keV and 5.81 photons s^{-1} cm^{-2} sr^{-1} keV respectively. While this discrepancy can partly be attributed to the adjustments made to the data reduction process, the reassignment of the absorbed 0.1 keV component may also be responsible. By reducing the absorption acting on this component, its contribution to the flux in these fields was increased, reducing the flux fraction left to be fitted by the XRB.

Table 4.12: Best-fit Flux Values of the XRB with 90% confidence intervals. Units are photons s^{-1} cm^{-2} sr^{-1} keV.

Field	XRB Flux	+ / −
O1	6.61	0.71 / 0.38
O2	7.49	0.29 / 0.00
O3	2.99	0.00 / 0.85
O4	4.57	0.97 / 0.95
O5	13.24	1.04 / 1.08
O6	8.39	0.27 / 0.00
O7	5.69	0.19 / 0.02
O8	9.55	0.00 / 0.02
O9	5.54	0.15 / 0.00
O10	5.44	0.39 / 0.00
X1	5.48	0.67 / 0.67
X2	4.13	0.53 / 0.76
X3	6.82	0.66 / 0.63
N4	6.00	0.56 / 0.69
N5	5.81	0.14 / 3.00

Hence, while an XRB contribution has been extracted from the total flux in all of the fields, it is unlikely that its total flux has been observed, and so it would not be prudent to draw conclusions regarding its total flux intensity. Instead, it can be said that because its contribution within this lower energy range has been fitted by the absorbed power-law, it has made it easier to extract, fit and characterise the signal from the softer components of the SXRB. The magnitude of the flux contributions of the XRB found in each field are listed in Table 4.12

The LHB, fitted at 0.1 keV, appears to be brighter in Northern Bulge fields compared with those in the NPS fields; a feature which may indicate an interaction with Loop I in this region. The LHB is also more prominent in the Anti-centre direction, where it is far more extensive.

Loop I has been modelled using two components: a VAPEC for the hot, rarefied interior, and an APEC representing a cool shell around the Loop. By subjecting both of these components to the same level of absorption, they have effectively been held together at the same distance from the Earth, and positioned outside the boundary of the LHB,

behind the absorbing Wall.

As in Willingale et al. (2003), the temperature of the Loop's interior was frozen to 0.3 keV to simplify the fitting process. The normalisation of the VAPEC modelling the Loop's interior was found to be $\sim$ 4 times higher in the NPS than in the Northern Bulge fields, indicating that the plasma near the limb of the bubble is being heated, and perhaps compressed, as it impacts the outer shell. As in Willingale et al. (2003), the interior was found to be chemically depleted in oxygen, magnesium, neon and iron.

The cool shell around Loop 1, identified in this research, has been modelled using a thermal APEC frozen at 0.1 keV. The origin of this flux has been reinterpreted, from being a cool Galactic Halo (as in Willingale et al. (2003)) to a local supershell, for three reasons: first, it was not observed in the Anti-centre direction, a prerequisite for an all-encompassing Halo. Second, the high absorption in the Wall precluded the possibility that the 0.1 keV signal could originate behind Loop 1, a hypothesis tested by fitting the model with the Halo at 0.15 keV, and again at 0.25 keV. Third, the shell's emission measure appears to be related to that of the Loop's interior. The physical properties of the shell, and the other structures in the SXRB, will be analysed further in Chapter 6.

In the Southern fields, two additional sources, a thermal source and a non-thermal source, have been observed within 6° of the Galactic Plane. These have been fitted with a MEKAL at 1 keV and a power law with a photon index of 2.5 respectively. Both of these were set behind the full Galactic column. While the thermal source can be tentatively identified as the Galactic Plane Radiation, the non-thermal source has not been identified previously in literature, but could possibly originate at the Galactic Centre.

Finally, the emission from the Galactic Halo was detected in all ten Oxygen fields. Through fitting four variations of Model B, it has been shown that the Halo fits best at full Galactic Absorption, ruling out the possibility that it is a local source. The Halo plasma was found to resemble that of the Loop interior, with a $0.21 - 0.31$ keV temperature range, and a hint of chemical depletion. The similarity of the Halo plasma to that in the Loop 1 interior, which itself is the product of many supernovae (Egger 1998), is intriguing, and strongly supports the theory that the Halo was generated through the outflow of material from SNRs, the so-called 'fountain' hypothesis of Halo creation.

5

Oxygen in the Milky Way

The ISM contains many different elements and ionic species which, having absorbed high-energy photons by the processes described in Section 1.2.1, de-excite to produce emission lines. The number density of energised ions determines the observed intensity of these lines, but their frequency and energy are dictated by the species from which they originate. Consequently, the lines can be used as a chemical 'fingerprint', their detection unambiguously revealing the presence of specific ions within the ISM. Spectral analysis can also provide an estimate of the temperature of the emissive plasma, since characteristic lines are created by electron transitions which occur only within a narrow energy range. In this chapter, attention will be focussed on the oxygen lines present in the SXRB spectra.

The prominent O VII and O VIII lines play an important part in the thermal balance of the ISM. However, the point of origin of the observed lines is the subject of much debate. Whilst Willingale et al. (2003) supposed a distant cool Galactic Halo to be the primary source of O VII emission in the SXRB, others such as Snowden et al. (1995) and Sanders (2001) have proposed that 'Long Term Enhancements' (LTEs) in the local flux, produced by interaction between the Earth's magnetic field and the solar wind, may generate the clouds of oxygen ions responsible for the lines. On balance, it is likely that both of these, possibly in conjunction with other sources, contribute to the oxygen signal.

Here, the fitted parameters described in the previous chapter will be 'dissected': the total flux of the fitted models will be separated into the contributions from the emissive

plasma codes. These will then be split further, to isolate the O VII and O VIII line fluxes from the continuum. Using the results of this analysis, the sources of the oxygen emission shall be identified, and the veracity of the shell model will be tested.

5.1 Emission in the ISM

The material of the ISM is heated and energised through a variety of extreme phenomena, including star formation, stellar wind activity and supernova events. The vast extent and low density of the ISM allows most of this thermal energy to persist for millennia, but some energy is lost through absorption by neutral atoms (Section 2.1) and via particle interaction.

Three varieties of particle interaction are possible. The first, a 'free-bound' interaction, occurs when a free electron recombines radiatively with an ion. This process effectively removes the kinetic energy of the electron from the total thermal energy of the plasma. Although the influence of this interaction can be seen in the LHB which, having been reheated by the last supernova to explode in its vicinity (Berghöfer & Breitschwerdt 2002) is now in a state of long-term recombination, it generally has a negligible cooling effect on the ISM.

In the second, an electron decelerates in the electric field of a proton, and dumps its excess energy in the form of Bremsstrahlung radiation (Section 1.2.1). Since both particles are unbound, this is commonly known as a 'free-free' interaction. While this process cools the ISM more efficiently than the 'free-bound', it has little influence beyond pure hydrogen environments (Tielens 2005).

The dominant cooling mechanism for optically-thin ionized gas is widely recognised to be excitation by incident photons of the low-lying electronic states of trace species (Tielens 2005). This particle interaction is named 'bound-bound', because an initially bound electron is raised to a higher, yet still bound, energy state within the same ion. In average-density plasma, such as that artificially generated on Earth, a bound-bound interaction would be promptly followed by de-excitation through collision with a free electron. This does not happen readily in the ISM as the electron density is so low. Instead, the ions de-excite spontaneously, releasing photons of energy equal to that of

the electron's transition. It is these photons, observed as emission lines, which carry away thermal energy from the plasma and, of all the lines present in the ISM, O VII is the most effective coolant (Berghöfer & Breitschwerdt (2002) & Snowden et al. (2004)).

The emission lines also act to regulate the temperature of the ISM. Because atoms may be raised to many different ionisation states, it is possible for all of these to exist simultaneously within an atomic population. It is, however, more probable that the majority of the ions will be in one particular ionisation state, with an energy equivalent to the plasma temperature. When these ions de-excite, they produce emission lines characteristic of the plasma temperature. The cooling effect produced by this process is inefficient, and unlikely to reduce the plasma temperature by the amount required to shift the ionic balance of the plasma, and so allow a lower ionisation state. However, its impact is usually sufficient to prevent slight temperature increases in localised regions of the ISM, which would otherwise enable higher ionisation states to be attained. In this way, the emission lines act as a thermostat in the interstellar plasma, making thermal equilibrium possible.

5.2 Plasma Codes, Emission Lines, Photons and Flux

Thermal plasma codes, such as APEC and MEKAL, include line catalogues which represent the line photons, produced by electron transitions that occur between the sub-levels of different ions, in the form of sharp emission peaks. When convolved with the energy response of a detector, the peaks broaden and blend together, mimicking the emission lines that dominate the energy spectrum of the SXRB. The MEKAL code, for example, blends seven electron transition peaks to produce the O VIII emission line, and seventeen to generate O VII.

In a thermal plasma code, the strength of each electron transition's contribution to an emission line is determined by the temperature and ion density of the emitting plasma; consequently, both the individual and relative strengths of the two oxygen lines vary from field to field. This relationship has long been exploited by spectroscopists in order to measure the properties of diffuse plasmas. Indeed, the very existence of interstellar plasma at $1 - 4 \times 10^6$ K was first revealed by Inoue et al. (1979) through the detection

of the O VII and O VIII emission lines that are the subject of this chapter.

In practice, when an X-ray photon is incident on a detector, it is registered and stored in the events file of the observation. Because the rate at which the events are registered is related to the number of photons incident in a given time, it can be considered to be the 'photon count rate' of the observed source.

After the events file has been screened and processed, it is used to produce an energy spectrum, which is then fitted with a series of plasma codes. The flux of the fitted spectrum may be then estimated by integrating the model over the required energy interval with respect to the number of normalised events: in essence, by finding the area under the curve.

To split the model flux into its various components, the MOS data from the B4 data-set was read into Xspec and modelled using a simple VAPEC code with a normalisation frozen to 1, and a plasma temperature of 0.1 keV. All chemical abundances in the code were then frozen to zero, effectively removing the emission lines from the model curve, and leaving only the continuum energy.

Because the profile of the VAPEC curve was not fitted, it did not match the data; instead, it showed the shape of the code after it had been folded through the energy response of the telescope. This revealed the emission features produced by instrumental contamination, in particular, an oxygen edge centred at 0.5 keV, arising from the filter used in front of the MOS detector. The presence of this artefact highlighted the importance of using the appropriate ARF and RMF files during the fitting process: the different filters (thin, medium, and thick) used in conjunction with the EPIC detector (Section 1.3.4) each contain different trace elements which, when energised, produce photons that contaminate the observed data. By using the appropriate calibration files, these features can be accounted for in the modelled spectrum.

The oxygen abundance of the VAPEC code was then reset to 1, and the model's curve redrawn to show the O VII and O VIII lines superposed on the continuum, each centred around $\sim$0.55 keV and $\sim$0.7 keV respectively. Using the IPLOT package (K. Arnaud 2007), the energy intervals occupied by the oxygen lines were measured, yielding the limits $0.46 - 0.62$ keV and $0.62 - 0.72$ keV for O VII and O VIII respectively. These values represent the best compromise: emission peaks with close transition energies may blend

to produce one emission feature, and unfortunately this is the case for the O VII and O VIII lines, which overlap slightly at their bases. The midpoint between the lines lies at ∼0.62 keV, and so this limit was set to ensure that when their flux was measured, events in the blended region would not be counted twice. For the purposes of this chapter, these two energy ranges will be assumed to contain all of the O VII and O VIII signal in the modelled spectra.

5.3 The Effect of Temperature on the Oxygen Lines

Two thermal codes were used to model the reduced SXRB spectra: APEC (Section 4.3.1) and MEKAL (Section 4.3.1). Both of these codes include O VII and O VIII peak data, but the individual and relative strengths of the lines they produce are dependent on the temperature of the emissive plasma. To examine this effect, the flux of the lines in each of the models was measured over a range of temperatures. The VAPEC and VMEKAL code variants were used for this purpose because they allow the chemical abundances to be adjusted, unlike the standard APEC and MEKAL implementations, in which all abundances have set values.

A VAPEC code was read into Xspec. It was given a normalisation of 1, a plasma temperature of 0.080 keV, and all chemical abundances were set to solar (1). The total flux of the model was then measured using the Xspec 'flux' command, in the 0.46 – 0.62 keV and 0.62 – 0.72 keV energy ranges defined above.

The oxygen abundance was then set to 0, removing the oxygen lines from the spectrum, and the flux was re-measured in the two energy ranges, yielding the flux of the model continuum which underpins the lines (Figure 5.1). These values were then subtracted from the total fluxes to give the continuum-subtracted fluxes of the O VII and O VIII lines.

This process was repeated for a range of plasma temperatures, after which the entire procedure was performed using the VMEKAL code. The flux measurements obtained are presented in Figures 5.2 and 5.3.

From the graphs, it can be clearly seen that O VII dominates at lower plasma temperatures, rising sharply in magnitude until it reaches a maximum at 0.175 keV. After this, the

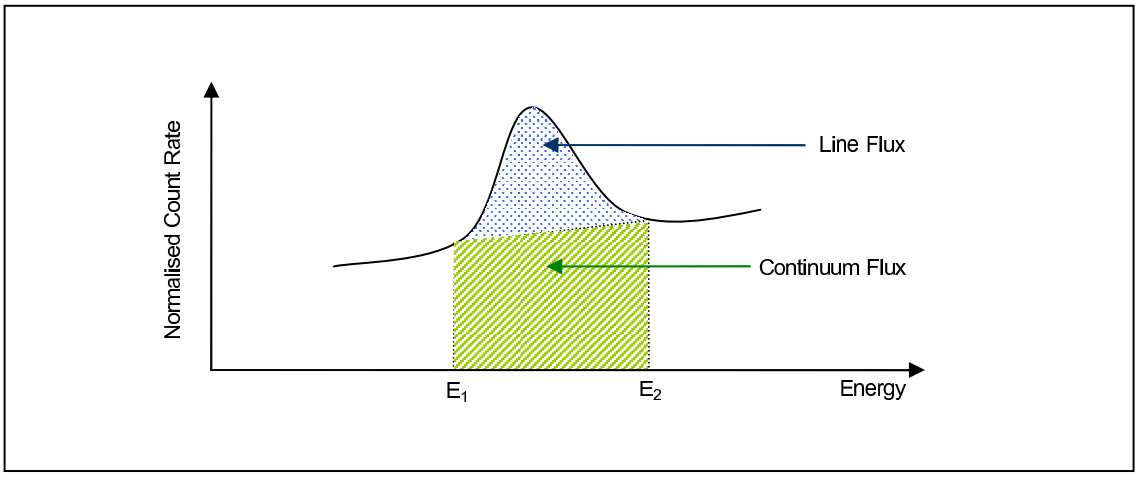

Figure 5.1: The continuum and line fluxes in an emission line region.

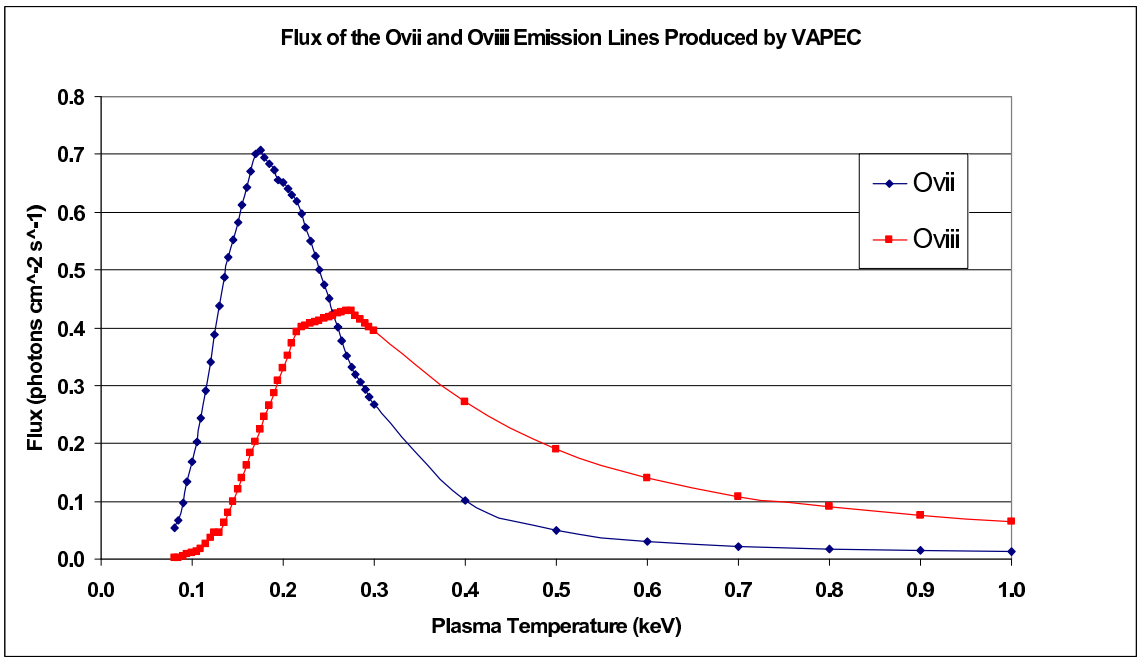

Figure 5.2: The continuum-subtracted flux of the oxygen lines produced by the VAPEC code, at solar abundance and normalisation of 1, as a function of plasma temperature.

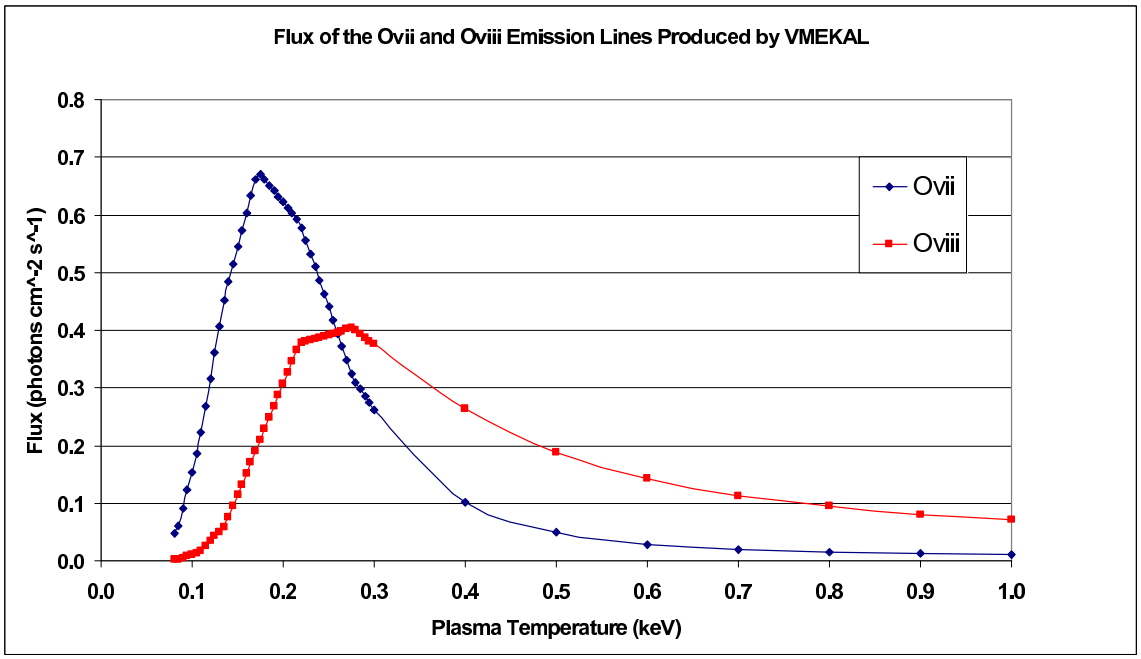

Figure 5.3: The continuum-subtracted flux of the oxygen lines produced by a VMEKAL code, at solar abundance and an normalisation of 1, as a function of plasma temperature.

magnitude of the O VII line decreases rapidly, falling away to zero a little beyond 1 keV.

Since O VIII represents one further ionization of oxygen from O VII, it requires more energy, and is therefore generated in greater proportion at higher temperatures. It peaks in magnitude around 0.27 keV, similar to the measured temperature of the Loop I interior but, because the rate at which its flux increases with temperature is slower than that of O VII, O VIII reaches only 57% of the maximum peak magnitude of O VII. However, the O VIII flux also falls at a slower rate than O VII, allowing it to remain relatively high long after its maximum has been attained. This effect is apparent in the graphs: at ~0.26 keV, the O VII and O VIII lines produced by the plasma codes are of approximately equal magnitude. Below this temperature, the O VII line is more prominent than O VIII, but above it, the situation is reversed.

O VII has long been considered a tracer of 0.1 keV plasma but, although it is certainly present at this temperature, the O VII flux is far from its maximum value. The significance of 0.1 keV to the O VII flux can be appreciated if one calculates the ratio of O VII / O VIII flux over the temperature range. This relationship is shown in Figures 5.4 and 5.5.

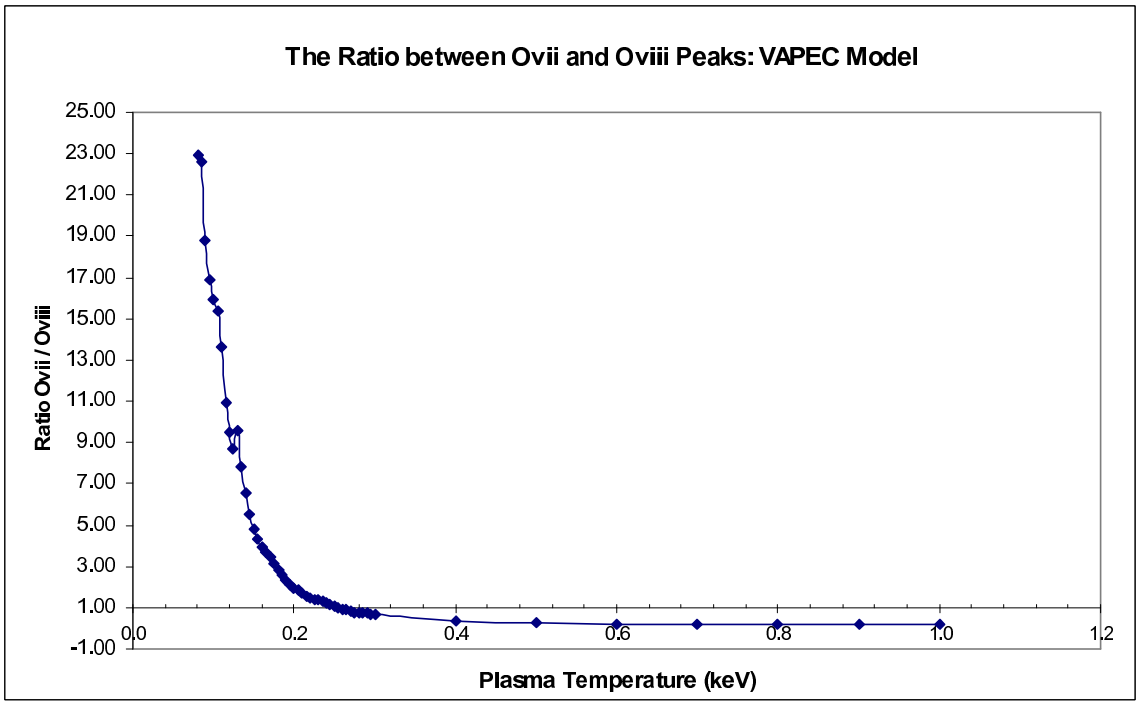

Figure 5.4: The ratio of oxygen line intensities in the VAPEC code.

Figures 5.4 & 5.5 reveal by what magnitude the O VII flux is larger than the O VIII flux over a range of plasma temperatures. At lower temperatures, ∼0.1 keV, the magnitude of the O VII line is ∼22 times that of the O VIII line. As this is by far the largest value that the ratio can hold in this temperature range, the presence of the O VII line, in the absence of O VIII, has become associated with 0.1 keV plasma. At higher temperatures, the ratio of the relative sizes of the lines is less extreme, reducing the significance of the O VII line.

5.4 Splitting the Fluxes

In Chapter 4, the reduced spectra were fitted with plasma models comprising a number of components, which represented the structures of the ISM. Each component contained a plasma code and, where required, an absorbing code. During the fitting process, Xspec calculates the flux of the continuum and the emission lines of the codes separately. The individual fluxes of the different components are then summed to give the total flux of the model, and hence, to create the final fitted spectrum.

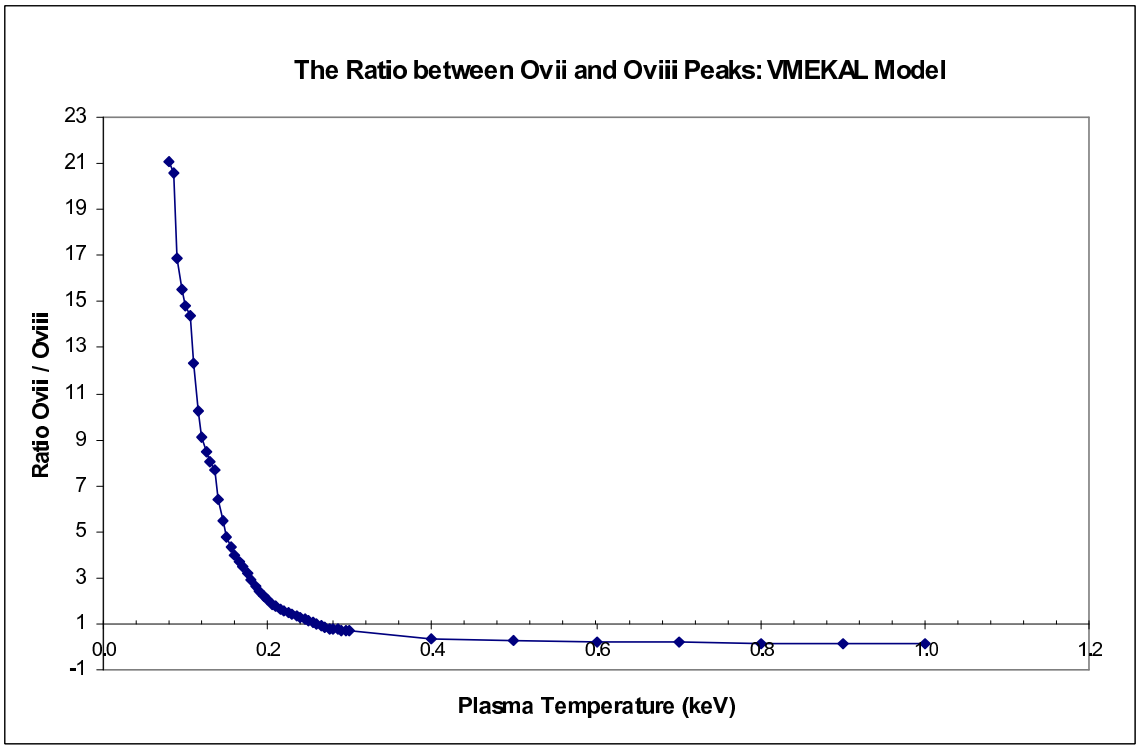

Figure 5.5: The ratio of oxygen line intensities in the VMEKAL code.

Since a modelled spectrum is formed from separate parts, it can be deconstructed, and returned to those original flux components. Although this process is both possible and useful, it is not generally performed, and so a two-stage process had to be developed especially for this research. Essentially based on the principle of 'measurement by difference', the first stage determined the contribution of the emission line and continuum flux of each component to the total flux of the spectrum. In the second, the flux values were manipulated to remove the effects of absorption, and so determine the absolute (at source) flux of the interstellar structures represented by the plasma codes. These two stages, and their results, are discussed in the sections that follow.

5.4.1 Stage 1: The Apparent Flux of the Model Components

The model used to fit the SXRB fields contains up to six different components. To determine the apparent flux of an unabsorbed component within the model, say 'component A', in the energy range containing the O VII line, a procedure similar to that described in

Section 5.3 was performed: one of the spectra fitted in Chapter 4 was read into Xspec, and the 'flux' command was used to calculate the total flux within the required energy interval. The normalisation of component A was then set to zero, removing it from the model. The flux was then recalculated, and the normalisation of the component restored. The difference between the two values is the flux contribution of the component's emission line and continuum, and is numerically equal to the total apparent flux of the component within the energy interval.

To separate the line and continuum flux, the complete model was replaced by component A. The fitted parameter values from the modelled spectrum were then input, making component A exactly as it would be within the complete model. The oxygen abundance of component A was then reset to zero, and the flux recalculated, giving the apparent continuum flux. This value was then subtracted from the total apparent flux of the component to obtain the apparent line flux of the component.

For an absorbed component, say, WABS $\times$ VAPEC, the component was input as a new model, and assigned parameter values equal to those in the fitted model. The total flux in the energy interval was then calculated, giving the absorbed apparent flux of both the line and continuum. Further values were then obtained in anticipation of the second stage of the analysis: the absorption was set to zero, and the flux recalculated, to give the unabsorbed absolute flux of the line and continuum of the component. This done, the WABS value was reinstated, and the oxygen abundance set to zero. The flux was then recalculated, producing the absorbed continuum flux of the component. Finally, with both the absorption and oxygen abundance held at zero, the flux was calculated once more to give the unabsorbed continuum flux of the component.

5.4.2 Percentage Contributions from the Plasma Components

The percentage flux contributions to the total apparent flux[1] made by the continuum and emission lines of each component were calculated for all twenty observed fields. These values are presented as pie charts, shown in Figures 5.6, 5.7, 5.8 & 5.9.

[1] The percentage flux contribution of the component is simply its apparent flux, divided by the total flux, multiplied by one hundred.

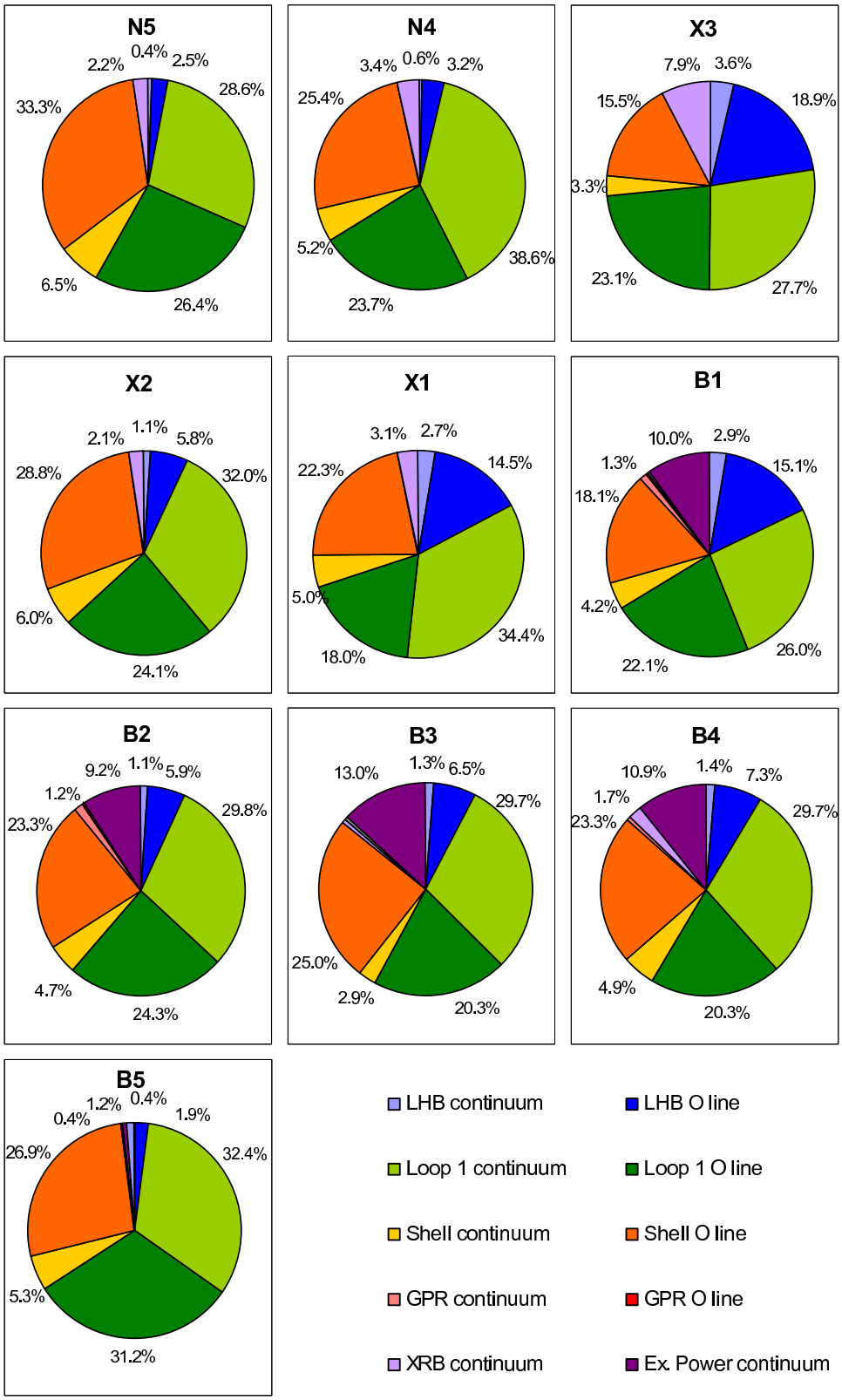

Figure 5.6: Pie charts showing the contributions made by the emissive structures to the modelled O VII (0.46 – 0.62 keV) flux in the Loop 1 fields.

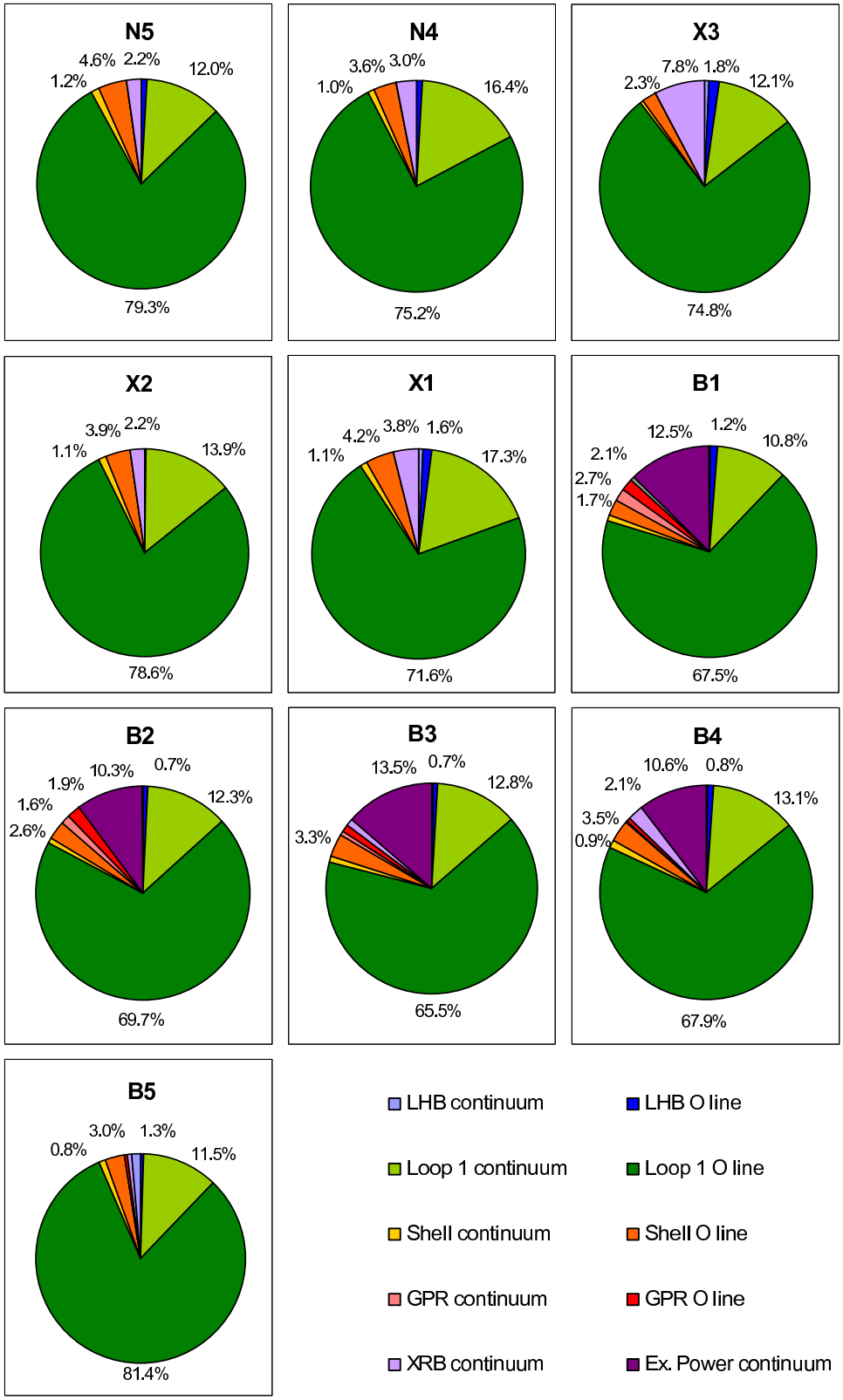

Figure 5.7: Pie charts showing the contributions made by the emissive structures to the modelled O VIII (0.62 – 0.72 keV) flux in the Loop 1 fields.

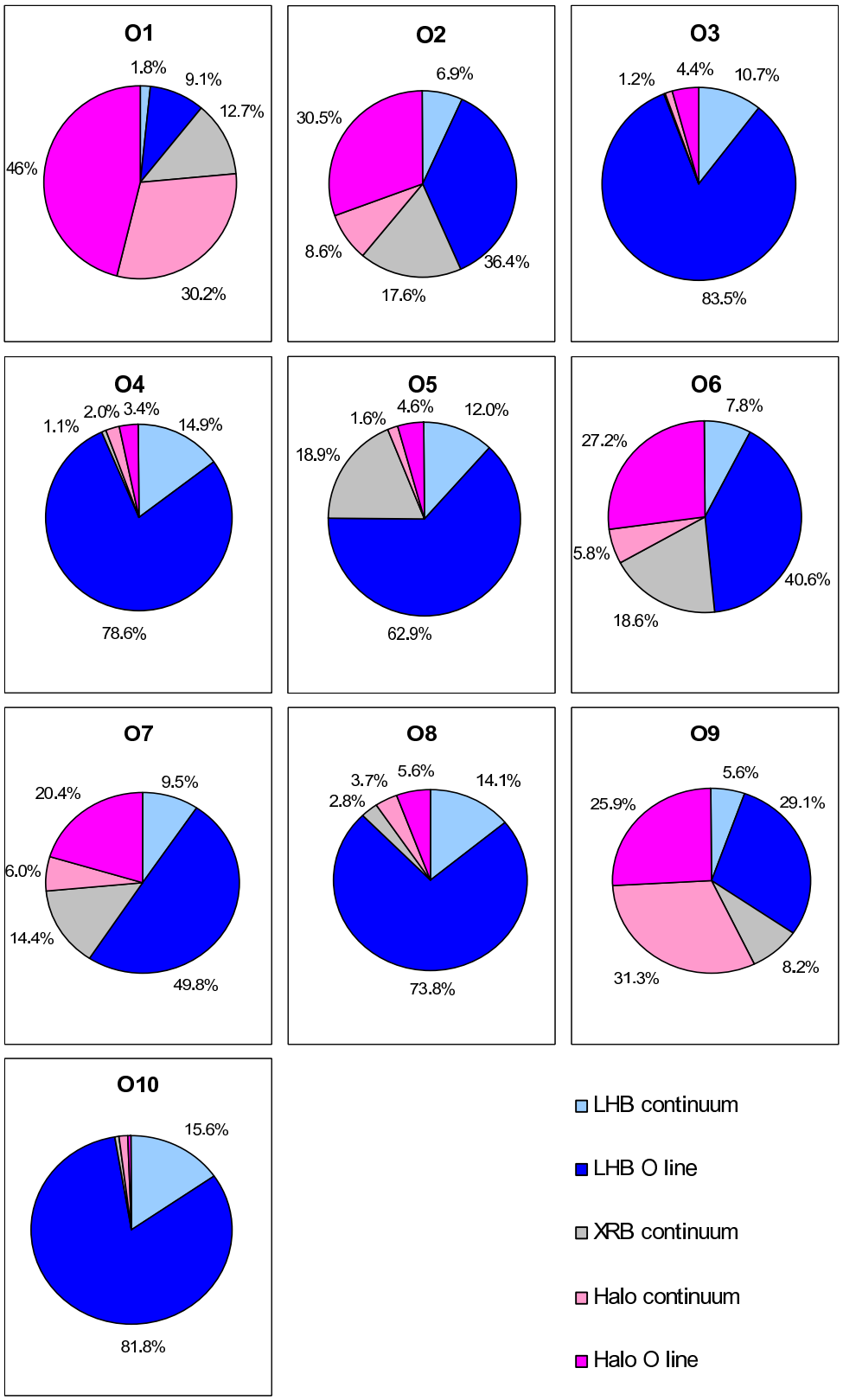

Figure 5.8: Pie charts showing the contributions made by the emissive structures to the modelled O VII (0.46 – 0.62 keV) flux in the oxygen fields.

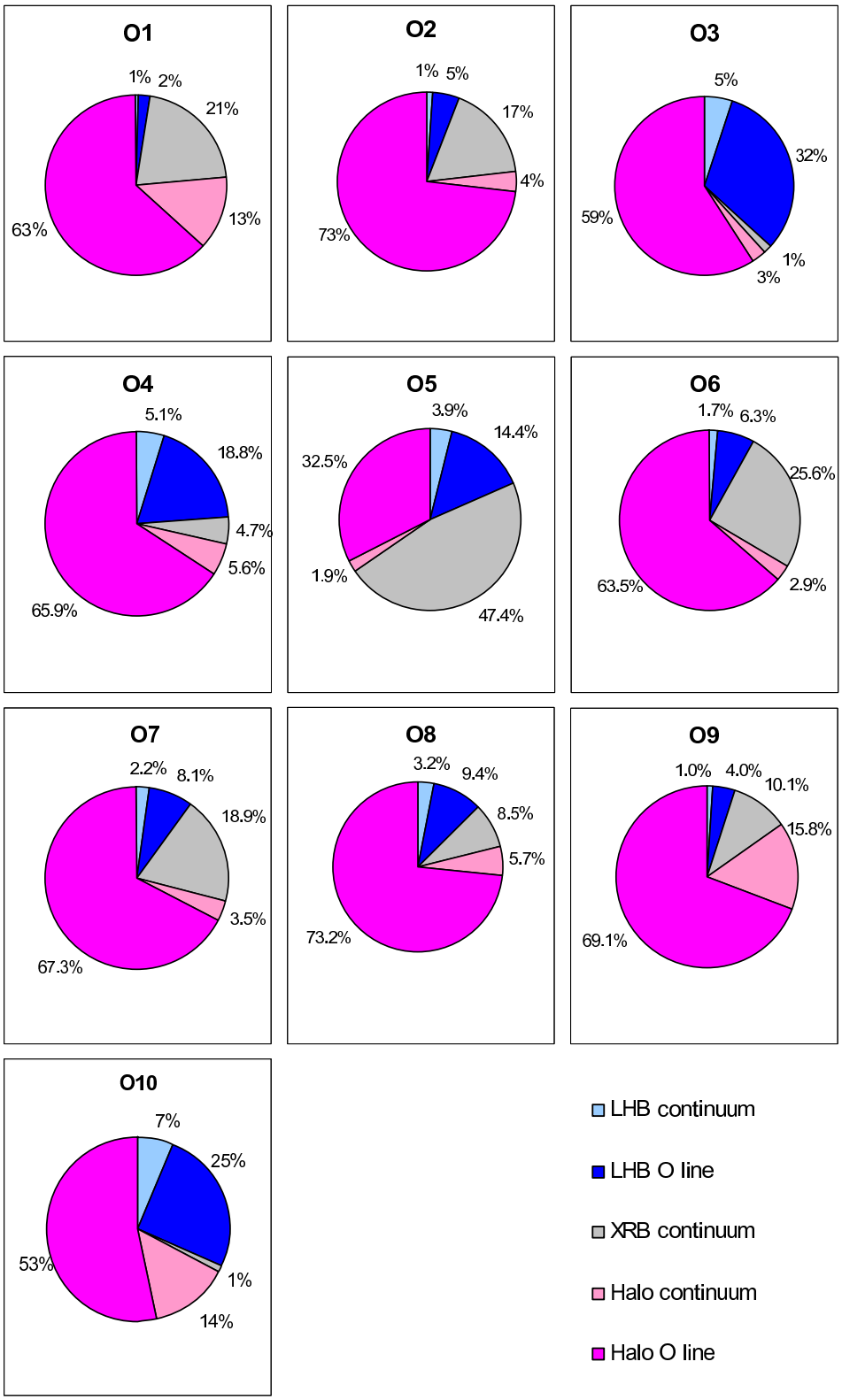

Figure 5.9: Pie charts showing the contributions made by the emissive structures to the modelled O VIII (0.62 – 0.72 keV) flux in the Oxygen fields.

O VII in the Loop I Fields

The charts showing the percentage O VII flux contributions in the Loop I fields (Figure 5.6) form three distinct groups: the Southern, the Northern Bulge, and the NPS fields.

Unsurprisingly, the breakdowns of the O VII flux in the five Southern fields (B1–B5) are almost identical, despite their close proximity to the Galactic Plane; as explained in Section 5.3, the normalisations of several components were frozen to the average fitted values derived from the Northern fields.

The hot, non-thermal GPR (modelled by an absorbed MEKAL) makes little impact on the Southern fields, producing no more than 1% of the total O VII flux even in fields closest to the Plane, B1 and B2, and so for clarity, it is not shown. The percentage contribution of the XRB is also small in this energy range, yielding only $\sim$3% in the Northern fields. It is almost undetectable in the South, where it is overwhelmed near the Galactic Plane by the complexity and intensity of the SXRB in this region.

The Loop's interior contributes the majority (between 50% and 60%) of the received flux in the Southern fields, and of this share, almost half can be attributed directly to the O VII line. The second highest contribution, around 30% of the total, originates in the shell around Loop I, and $\sim$8% comes from the LHB, mostly from the line itself, with very little input from the continuum. The remainder is provided by the continuum of the extra power law, included in the model to accommodate the enhancement near the Galactic Plane.

The cool shell makes its greatest percentage contribution in the Northern Polar Spur fields (N4 and N5), a trend that supports the hypothesis that a shell surrounds the hot interior of the Loop.

The composition of the flux in the two NPS fields is almost identical, with a third of the total produced by the cool shell, about 60% by the interior of Loop I, and the remainder coming from the LHB. It is significant that while the proportion of flux from the shell is high, that from the interior of the Loop is still greater. The NPS fields were originally selected by Willingale et al. (2003) because they were thought to lie on the edge of Loop I but, if this were the case, then the shell would provide more flux than the interior. This

prompts a question: just what does the bright arc of the NPS emission represent? It is probable that rather than being on the limit of the Loop I Superbubble, the NPS is an interface region, lying between the hot interior of the Loop and the cool outer shell. This idea will be developed in the next chapter.

O VIII in the Loop I Fields

Like the O VII flux in the Loop I fields, the percentage breakdowns of O VIII flux in Loop I are similar to one another (Figure 5.7). The cooler structures produce far more O VII than O VIII, and as a result, the shell produces only $\sim$5% of the total O VIII flux, while the more diffuse LHB makes a negligible contribution. The hot (2 keV) GPR generates only $\sim$3% of the O VIII flux in B1–B3 fields, while the extra power law makes up $\sim$10% as the Plane is approached. The remaining 80 – 90% is generated by the 0.3 keV plasma in the Loop I interior, with the O VIII line contributing many times more flux than the continuum beneath it.

O VII in the Oxygen Fields

Because the ten Oxygen fields are spread widely over the sky, they were expected to exhibit far more variation than the closely grouped Loop I fields. However, when their flux breakdowns were determined, several trends became apparent.

Overall, the dominant colour in Figure 5.8 is dark blue, representing the O VII line photons from the LHB; indeed, in the O3 and O10 fields, virtually the whole of the O VII flux comes from this source. With the exception of fields O1 and O9, the results show that the LHB, not the Halo, is the main source of the observed O VII in the SXRB spectra.

The second highest contributor to the O VII flux is the Galactic Halo; however, the wide variation in the strength of the Halo contribution, from 0 – 86% of the total flux, shows that the sky coverage of the Halo is patchy, and indicates that it is a relatively young structure which has not yet had time to settle into a homogeneous state.

Finally, the O VII contribution from the XRB component is far more pronounced in the

Oxygen fields than in the Loop I fields. This is because the situation in the anti-centre direction is far simpler than the Galactic Centre direction, and in the absence of the sources in the Galactic Centre, Loop I, and all of the absorbing dust associated with the Wall and Plane, the XRB can be seen more easily. Also, because the flux in the Oxygen fields is lower than in the Loop I fields, the small contribution from the XRB represents a much higher fraction of the total flux.

O VIII in the Oxygen Fields

In Figure 5.9, with the exception of O5, the largest segments are pink, representing the percentage contribution of the O VIII line from the Galactic Halo. This is not surprising: of the three emissive structures observed in the Oxygen fields, the LHB, the Halo and the XRB, only the Halo is at the optimum temperature to produce O VIII flux. Like the percentage contribution of O VII made by the Halo in the Oxygen fields, the O VIII flux covers a large range, between 35% and 78%. The second largest share is produced by the LHB, while the XRB continuum makes up the rest of the flux, underpinning the oxygen lines.

5.4.3 Stage 2: The Absolute Flux of the Oxygen Lines

In order to compare the oxygen content of the separate interstellar structures, the absolute fluxes of the oxygen lines are required. These values indicate both the density of oxygen ions in the emissive plasma, and the brightness of the emission lines at source, that is, the flux which would be observable in the total absence of the absorbing column.

For unabsorbed components, such as the APEC used to measure the LHB, the flux-splitting procedure (described in Section 5.4) yields both the apparent and the absolute value of the line flux. However, for absorbed codes such as WABS $\times$ VAPEC, this is not sufficient. To acquire the absolute line fluxes for these components, the influence of the WABS code must be removed.

Unfortunately, this cannot be done by simply switching off the absorption and finding the flux of the remaining plasma code: because the WABS code increases as a function

of energy, its strength varies across the narrow energy interval occupied by the oxygen lines. It was therefore necessary to develop a new method to calculate the absolute line fluxes, designed both to isolate the absorption on the emission line and, simultaneously, to account for the absorption on the continuum.

Calculating the Absolute Flux

For a component of the form WABS $\times$ FLUX(L+C) where WABS is the absorption, and FLUX is a thermal plasma code comprising line flux L and continuum flux C, the following values, obtained during the flux splitting procedure, are used:

Quantity	Meaning
A = WABS $\times$ FLUX(L+C)	Apparent flux of the code: line and continuum.
B = WABS $\times$ FLUX(C)	Apparent flux of the code: continuum only.
C = FLUX(L+C)	Unabsorbed flux of the code: line and continuum.
D = FLUX(C)	Unabsorbed flux of the code: continuum only.

Using these flux values, the absorption factor **W** on the line may be calculated as follows:

$$\begin{aligned}\frac{\mathbf{A}-\mathbf{B}}{\mathbf{C}-\mathbf{D}} &= \frac{\text{WABS}\times\text{FLUX(L)} + \text{WABS}\times\text{FLUX(C)} - \text{WABS}\times\text{FLUX(C)}}{(\text{FLUX(L)} + \text{FLUX(C)} - \text{FLUX(C)})} \\ &= \frac{\text{WABS}\times\text{FLUX(L)}}{\text{FLUX(L)}} \\ &= \mathbf{W}\end{aligned}$$

This absorption factor can then used to find the absolute flux of the line photons (FLUX(L)):

$$\begin{aligned}\frac{\mathbf{A}-\mathbf{B}}{\mathbf{W}} &= \frac{[\text{WABS}\times\text{FLUX(L)} + \text{WABS}\times\text{FLUX(C)} - \text{WABS}\times\text{FLUX(C)}]}{\mathbf{W}} \\ &= \text{FLUX(L)}\end{aligned}$$

The absolute line fluxes obtained through this method are presented in Figures 5.10, 5.11, 5.12 and 5.13. These figures show the most significant sources of flux in the observed

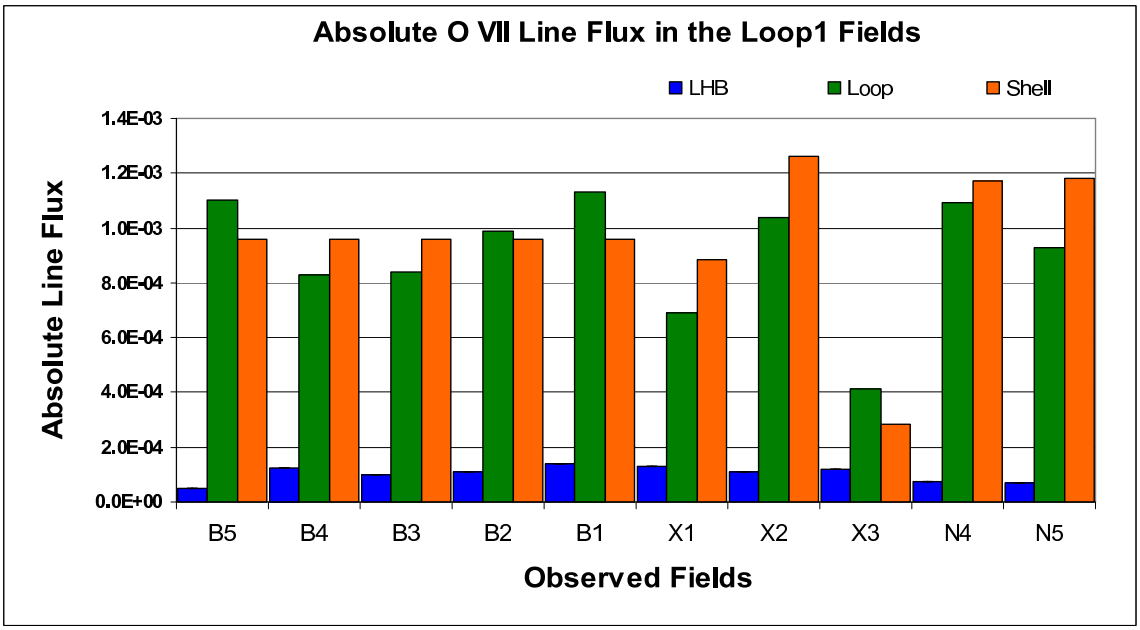

Figure 5.10: The absolute flux of the O VII line in the Loop 1 fields.

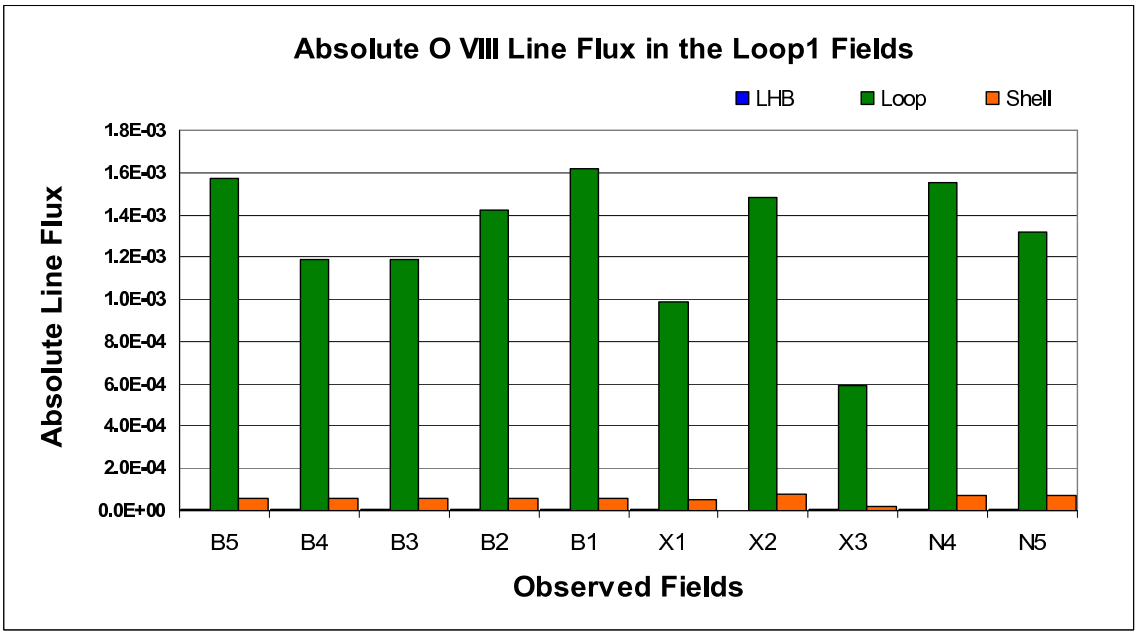

Figure 5.11: The absolute flux of the O VIII line in the Loop 1 fields.

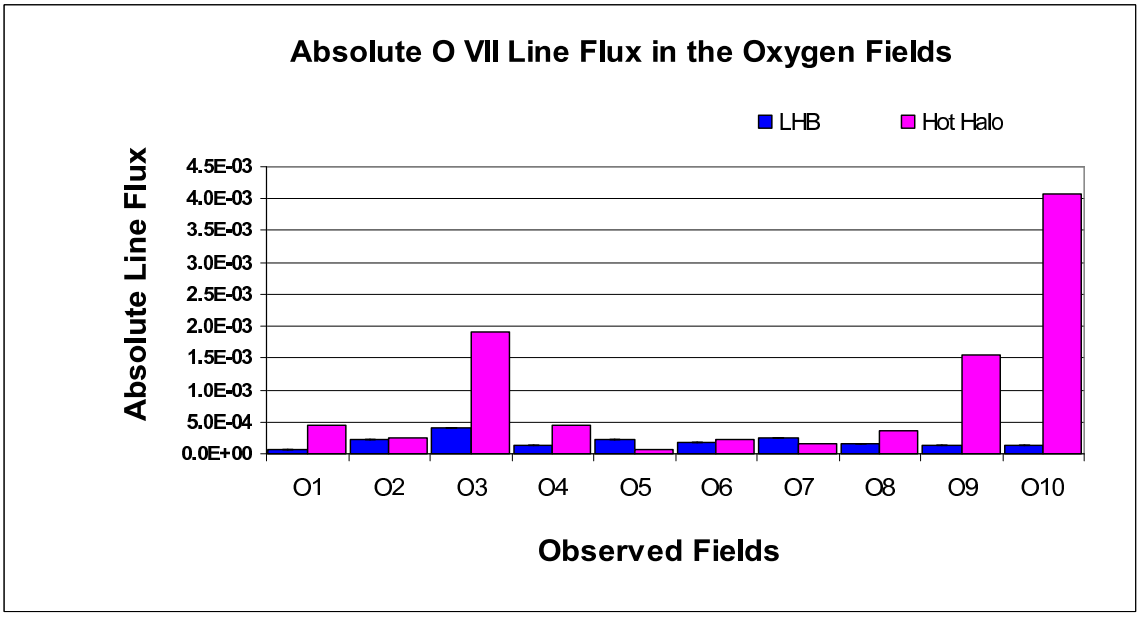

Figure 5.12: The absolute flux of the O VII line in the Oxygen fields.

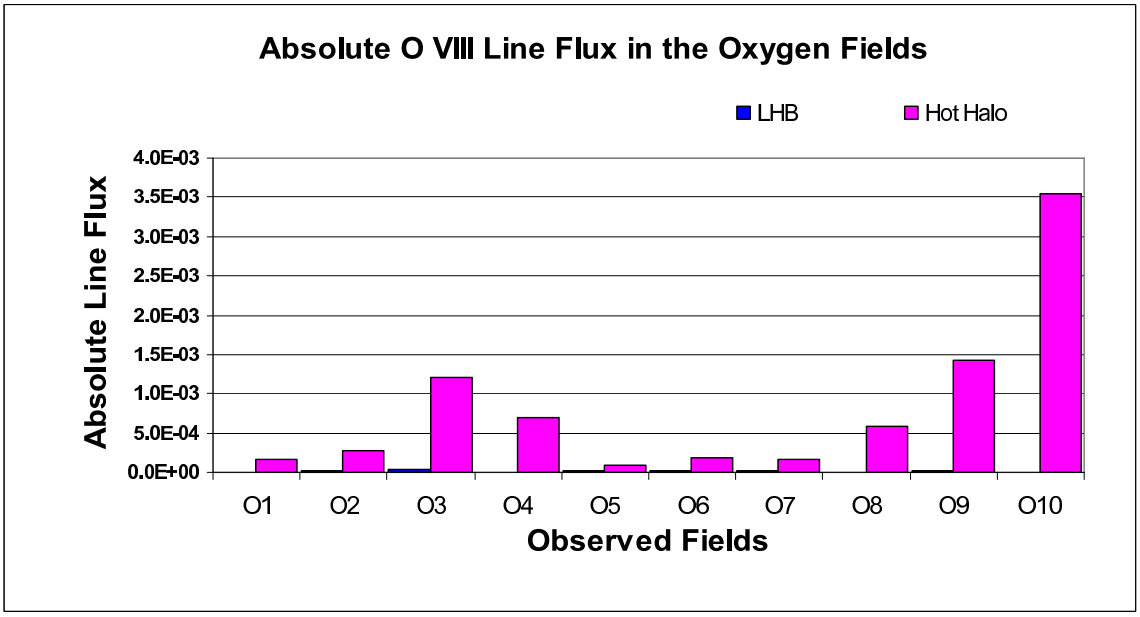

Figure 5.13: The absolute flux of the O VIII line in the Oxygen fields.

fields. Sources such as the GPR and XRB are not shown, since they produce only a small fraction of the total flux. The absorbed MEKAL component, included in the fields nearest the Galactic plane, contributes relatively little flux to the overall model, and even then, is only marginally significant in fields B1 and B2.

The Absolute Line Fluxes

The LHB makes a small but significant contribution to the O VII line flux, with a magnitude that varies by a factor of ten across the twenty fields, ranging from 5.0×10^{-5} photons cm^{-2} s^{-1} to 4.2×10^{-4} photons cm^{-2} s^{-1}. On average, the absolute O VII line flux from the LHB is $\sim$2 times greater in the Oxygen fields compared to those in Loop I. This may be due to the greater extent of the LHB in the anti-centre direction.

The range of the O VII line fluxes from the Halo is much larger than those from the LHB, rising from 6.8×10^{-5} photons cm^{-2} s^{-1} to 4.1×10^{-3} photons cm^{-2} s^{-1}: a factor of 60. This wide range reveals that the concentration of oxygen ions varies throughout the plasma, and indicates that the material in the Halo is still young, clumpy and inhomogeneous, and may have originated from a number of different sources. If these sources were individual supernovae, then this would lend strong support to the fountain hypothesis discussed in Section **??**.

Having removed the effects of absorption, the Halo proved to be a surprisingly strong source of O VII emission, producing more flux than the LHB in eight of the ten Oxygen fields. This is not the case when the absorption is included because the Halo lies behind the entire depth of the Galactic Column, which greatly reduces its apparent flux, as shown in the pie charts (Figures 5.6, 5.7, 5.8 & 5.9) above. The Halo is also the main source of O VIII line flux in the Oxygen fields. Like O VII, the O VIII flux varies over a considerable range as a result of non-uniformity in the Halo plasma.

It is difficult to draw inferences from the distribution of the flux in the Loop fields, since the normalisations of many of the plasma components were frozen in the Southern fields; nevertheless, some observations can be made. In the Loop I fields, the strongest sources of O VII flux are the cool shell and the Loop interior, which make similar flux contributions to each field. The LHB, however, makes a comparatively small contribution. The shell's

O VII contribution is particularly noticeable in the N4 and N5 fields.

The O VIII line flux is mostly generated within the Loop's interior, which at 0.3 keV, is at the ideal temperature to produce this signal (see Figure 5.2).

The O VII line flux of the shell is surprisingly similar to the NPS and Southern fields, indicating again that these fields are not actually positioned on the limb of the bubble. As suspected from the evidence of the photon count rates, the NPS fields appear to be positioned near the shell, or possibly at the boundary between the shell and the interior. Also, as expected, the Northern Bulge fields contain less O VII line flux than the NPS fields, and encouragingly, the B4 and B5 fields, which are also near the edge of the shell, have almost the same O VII line flux as seen in the NPS fields. The same distribution can be seen in the O VIII line fluxes, lending further support to the shell model of Loop I.

5.5 Discussion

5.5.1 The Cool Shell

In Willingale et al. (2003), the cool, absorbed 0.1 keV component observed in the Loop I direction was interpreted as a cool Galactic Halo. Most of the strong O VII signal detected in this direction was attributed to this structure, which had been modelled as diffuse and isotropic, with an arbitrary scale height of 1 kpc. One of the predicted outcomes of their model was that the Halo's O VII flux should be distributed evenly across the sky, with an intensity comparable to that seen in the Galactic Centre direction. If this were the case, then the apparent O VII flux produced by the cool Halo in the anti-centre direction (where the absorption is relatively low) should have been at least as strong as that observed in the dusty Galactic Centre regions they observed. However, an examination of the results presented above shows that this is not the case.

The total observed flux of the O VII line is much greater in the Loop I region than in the anti-centre direction. Since this measurement is largely independent of the separate parts of the model, it is not biased by the different interpretations of the cool component; nevertheless, the disparity between the fluxes within and outside the Loop has a clear

implication for the model. It confirms that the primary origin of O VII photons in the Galactic Centre direction is not a cool, distant Halo, but more local source, probably a structure associated with Loop 1: the cool super-shell, proposed in Chapter 4.

The 'shell' arrangement also makes it easier to visualize the emissive structures that create the SXRB. The 'cool Halo' interpretation of the 0.1 keV emission is problematic, because it requires the Halo to be visible in the Loop 1 region. In practice, and as demonstrated in Chapter 4, any such emission is swamped by the much brighter, harder radiation from the Galactic Centre, and absorbed by the full Galactic column, rendering it undetectable in the Galactic Centre direction. Also in Chapter 4, it was shown that these issues can be resolved by placing the cool component in the foreground, where it is subjected only to the Wall absorption.

The shell can be tested against three criteria. The first is that most of the O VII flux in the Loop 1 fields should originate from the shell component, and the second, that the contribution of this flux should increase as the limbs of the bubble are approached. Finally, more O VII should be seen in the Loop 1 region than in the rest of the sky. As the results of the analysis show, all three of these criteria have been satisfied, supporting the shell model. The physical properties of this shell, and the other emissive structures, will be calculated in the next chapter.

5.5.2 The Hot Halo

In Chapter 4, the cool Halo component used by Willingale et al. (2003) was reinterpreted as a cool shell, and replaced by a Hot Halo component, similar to that proposed by Spitzer (1956) (see Section 2.9). The Halo, which was identified in the spectra of all ten Oxygen fields, was fitted using an absorbed VAPEC. The results of this process revealed a similarity between the plasma of the Halo and the interior of Loop 1: both were chemically depleted, and shared similar temperatures ($\sim 0.25 - 0.3$ keV, Section 4.5.3). The flux splitting procedure, undertaken in Section 5.4, went further, revealing a strong O VIII flux from the Halo. The level of this flux varies, but is generally slightly lower than that from the Loop 1 interior; nevertheless, it reinforces the link between SNR material and the plasma of the Halo and supports the outflow, or Galactic Fountain (Section **??**), model for the creation of the Halo.

In the fountain scenario, superbubbles that have reached a critical size expand and rise out of the Plane. Upon reaching the less dense region above the neutral hydrogen disk, their shells breach, allowing the hot interior plasma to flow outwards. Some of this material recombines and falls back down under gravity towards the Galactic disk in the form of high velocity clouds (Woerden et al. 2004), while the remainder contributes to the hot Galactic Halo.

5.6 Summary

The SXRB spectrum contains many emission lines, which arise through the de-excitation of ions present in the ISM. The photons that create the lines also play an important role in the thermal balance of the ISM, enabling large regions of plasma to attain thermal equilibrium by carrying away energy from localised hotspots. The O VII and O VIII lines which lie in the soft energy band are especially significant, primarily because they are associated with 0.1 keV and 0.3 keV plasma from which the local ISM is constructed, and also because O VII is the most efficient coolant of the ISM plasma.

In this chapter, the regions of the fitted spectra containing the oxygen lines (0.46 – 0.62 keV for O VII and 0.62 – 0.72 keV for O VIII) were analysed in some detail, by splitting the flux of the model to reveal the apparent and absolute oxygen flux of the various emissive structures lying along the line of sight. To achieve this, a new technique was developed to split the flux of the best-fit models into their component parts, from which the absolute and apparent fluxes of each structure were determined for each field.

The results of this process reveal that the O VII flux observed in the Loop I fields comes mainly from the cool shell and the interior of the Loop, and only $\sim$10% comes from the LHB. In the Oxygen fields, where the flux is far lower than in the Loop I fields, most of the flux originates in the LHB, in addition to a variable contribution from the Galactic Halo.

The breakdown of the O VIII fluxes is far simpler than that of the O VII. $\sim$90% of the O VIII flux in the Loop I fields comes from the interior of Loop I, with the remainder produced by the cool shell. In the Oxygen fields, some flux comes from the LHB, but much of the observed flux, $\sim$ 45%, originates in the Halo.

By manipulating the flux components, it was possible to remove the effects of absorption, and so calculate the absolute (at source) flux of the emissive structures. The absolute flux of the LHB was found to be almost constant across all fields, although it was slightly brighter in the Oxygen fields, probably because of the greater extent of the LHB in that direction.

The Halo is brighter in O VII than O VIII, but patchy, and so suggestive of a young structure. Taken together with the results obtained in Chapter 4, which showed that the temperature and chemical abundances in the Halo and Loop interior are very similar, this lends strong support to the fountain hypothesis, in which the Halo is thought to have been formed by SNRs which have risen out of the Galactic Plane and burst, expelling their hot interior plasma.

Finally, the levels of O VII line flux are similar in the fields closest to the shell, in B4, B5 and the NPS fields, and higher than the level seen in the Northern Bulge fields at the centre of the Loop, supporting the hypothesis that a shell surrounds Loop 1.

6

Modelling the LISM

In Chapter 4, the SXRB spectra were fitted with plasma codes which revealed variations in temperature, emission measure, and chemical abundances in the various interstellar structures. This work was continued in Chapter 5, where the best-fit model parameters were used to determine the contribution of each structure to the observed O VII and O VIII flux. Here, the analysis of the Loop I fields will be taken into the third dimension, through the creation of a geometric model of the structures in the LISM. This will allow the physical dimensions of the various structures to be measured which will, in conjunction with the fitted parameters, enable the density and pressure of the ISM plasma to be calculated.

6.1 Adding the Third Dimension to the RASS Maps

In order to include depth in the analysis, the best-fit parameter values from the modelled spectra were 'projected' onto a geometric construct designed to mimic the shape and size of the structures of the LISM: a process that enabled the spatial properties of individual structures to be calculated, and highlighted the interactions between them.

To do this, a framework describing the extent and relative position of the two nearest superbubbles, Loop I and the LHB, had to be constructed; a process that required knowledge of the physical dimensions of the structures. However, two aspects of the

available X-ray data made these difficult to determine. When viewed from within, the outer limits of the LHB are obscured and invisible. Also, while the hot interior of Loop I is plainly observable in the soft X-ray band, its cooler outer circumference is not clearly defined. As a result, the super-shell described in Chapters 4 and 5 does not feature prominently in the RASS maps.

Fortunately, several researchers (Snowden et al. (1995), Berkhuijsen et al. (1971) and others) have been able to discern the extent of the major features in the X-ray sky through a variety of techniques including radio astronomy, parallax measurements, and extreme ultra-violet observations. Their work has been synthesised here in order to produce the required model.

6.2 Part 1: The Boundary of the LHB

In 1999, Hutchinson compiled a catalogue of more than two thousand X-ray active late-type stars for which Hipparcos parallax measurements, and hence distances, were known. He estimated the depth of the neutral hydrogen column to each of these stars through measurement of absorption features present within their X-ray and extreme UV spectra, and combined this data with other published measurements of stellar N_H to improve the sky coverage of their catalogue. With this extended data-set, Hutchinson produced a rough map showing the distribution of neutral hydrogen within 500 pc of the Sun and, in so doing, confirmed the presence of a local void: the LHB.

Through consideration of the probable distance to the LHB boundary and the depth of the hydrogen column, Hutchinson estimated that the density of the plasma within the LHB was very low, ≤ 0.02 cm^{-3}, with an electron density of only $n_e = 0.0062 \pm 0.0015$ cm^{-3}, and observed that this plasma was partially bounded by a denser, cooler ambient gas. He then proceeded to model the LHB as an anisotropic cavity, with an extent matching the observed depth out to a column density of $n_H = 10^{20}$ cm^{-2}, his predicted opacity of the bounding wall. When this fit had been optimized, it was smoothed using a set of spherical harmonic functions, and used to generate the contiguous all-sky map (Figure 6.1), which shows the distance to the boundary wall at an angular resolution of $\sim 3^\circ$. Hutchinson stated that the minimum distance to the Wall (located behind the central blue feature on

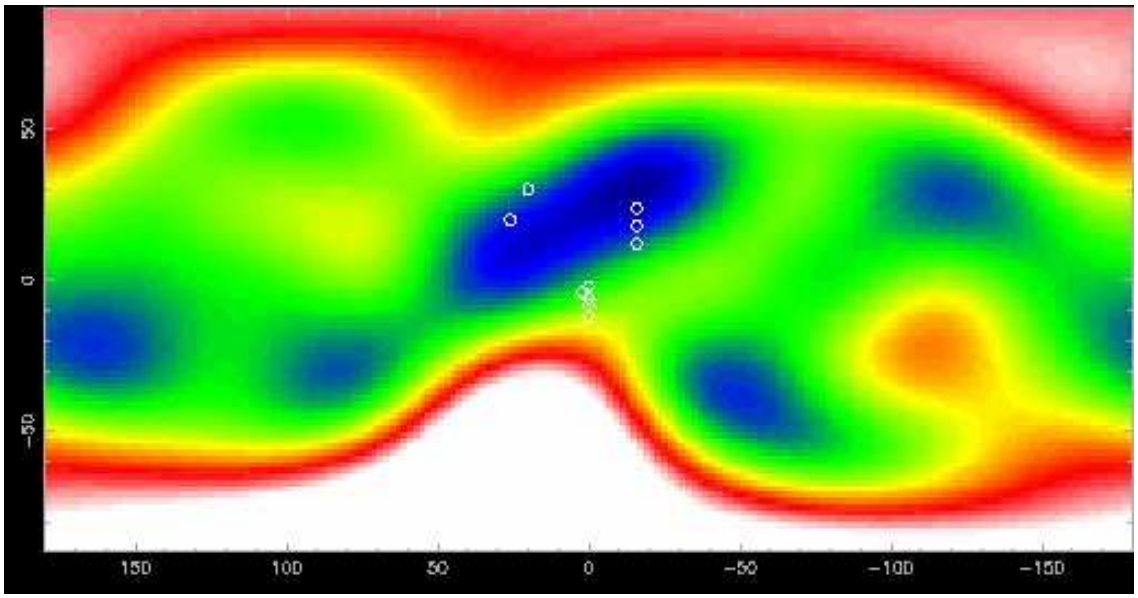

Figure 6.1: A smoothed, all-sky contour map in equirectangular projection, showing the distance from the Sun to the boundary wall of the LHB, produced using the Hutchinson (1999) model. The x and y axes are marked in degrees of Galactic longitude and latitude, and the positions of the Loop I fields are indicated by small circles. Distance is represented by a linear colour scale, blue being the closest at around 20 parsecs, with distance to the LHB boundary increasing in reverse spectrum order through red, a distance of some 250 parsecs. The white regions indicate where the required boundary density has not been attained, that is, the open ends of the LHB.

the map) was $\sim$ 35 pc, at a position around 30° north of the Galactic Centre, although this appears to be in error. Using the same model, the current author has found the minimum distance to the Wall to be $\sim$ 21 pc, just above the position of the Northern Bulge fields, as shown in Figure 6.2. Hutchinson also found no evidence of a bounding wall or a step in the gas density near the Galactic Poles, indicating that the LHB is open-ended.

This 'Hutchinson model' was used in this research to calculate the distance to the boundary wall of the LHB (designated dw) for each of the Loop I fields (Figure 6.2).

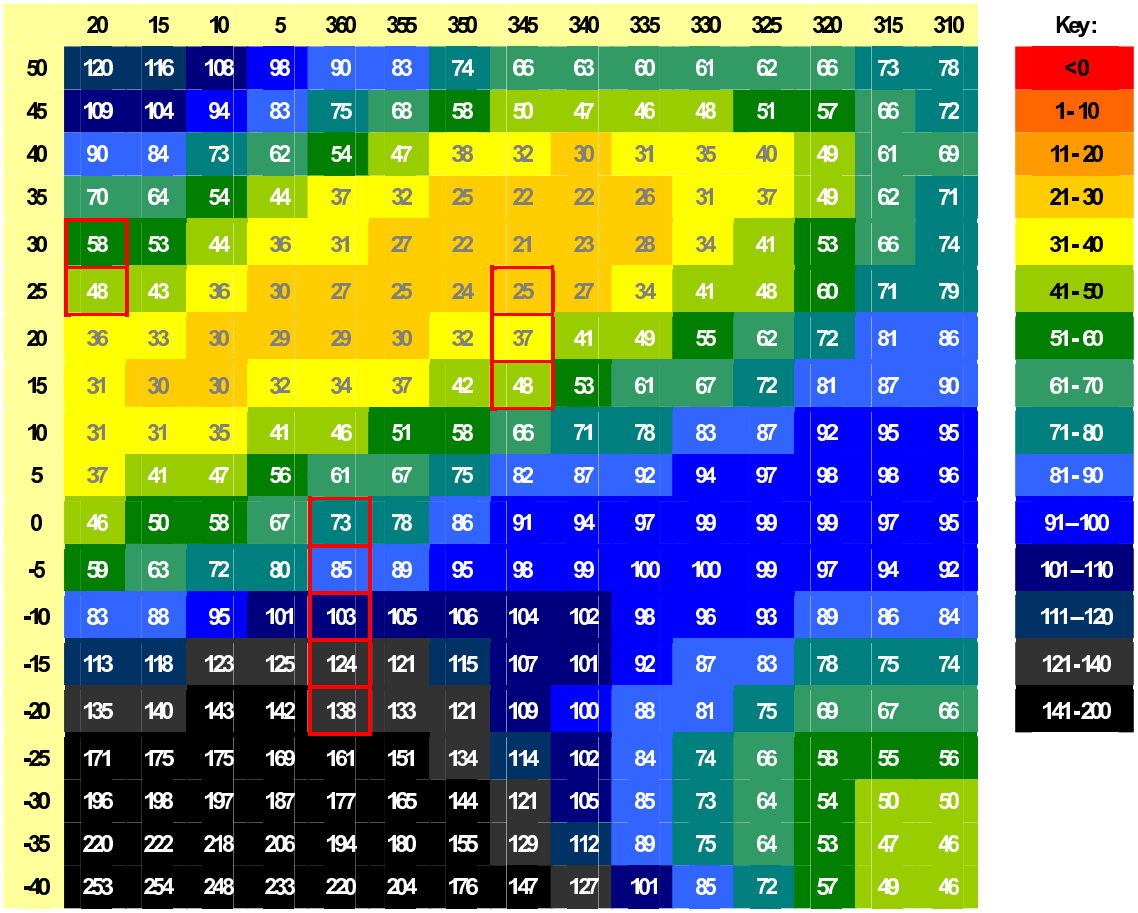

Figure 6.2: The distance in parsecs to the boundary of the LHB, calculated using the Hutchinson model, to an array of Galactic co-ordinates in the Loop I region. The locations of the Loop I fields are outlined in red.

6.3 Part 2: Loop I

The starting point for the research presented in this thesis was the work published in both Hands (2003) and Willingale et al. (2003). To produce their results, Willingale et al. modelled Loop I as a sphere of angular radius 42°, which is considerably smaller than the extent of Loop I estimated by Berkhuijsen et al. (1971), who had suggested a value of $58^{\pm}4°$. The discrepancy is understandable, however, when one considers that the measurement made by Berkhuijsen et al. (1971) was based on radio observations of the Loop's cool outer layers, while the estimate in Willingale et al. (2003) was made in relation to the appearance of the Loop in the $\frac{3}{4}$ keV RASS map, and so based only on its

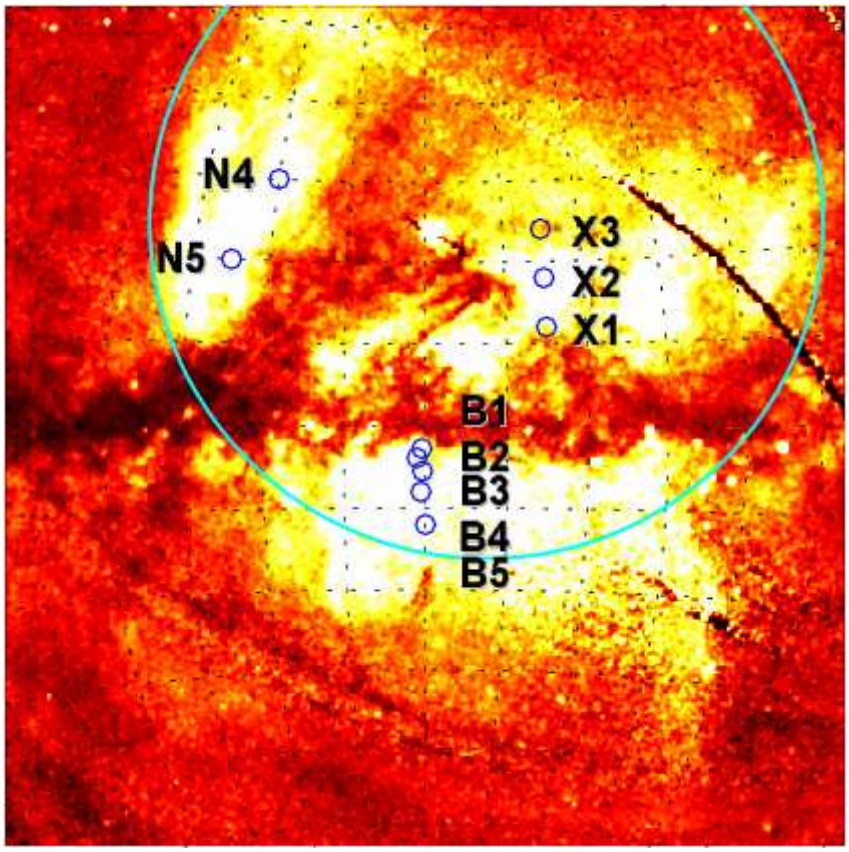

Figure 6.3: The projected boundary of the original Loop I, used in Willingale et al. (2003), together with the locations of the ten Loop I fields, superposed on the RASS $\frac{3}{4}$ keV map.

hotter, X-ray emissive interior.

The modelled sphere was centred, in Galactic co-ordinates, at $(-8^\circ, 15^\circ)$; a position chosen so that its projected boundary would enclose as much of the observed bright, soft emission in the Loop I region as possible (Figure 6.3).

Finally, the sphere had to be placed at some distance from the Sun. Since one cannot infer exact distance measurements in the X-ray band, Willingale et al. (2003) looked to the radio research of Bingham (1967).

During a supernova event, the magnetic field of the exploding star is entangled with the ejecta, and so becomes part of the SNR. Although this magnetic field will cause all electromagnetic radiation travelling in its vicinity to polarise to varying degrees, the effect

is strongest when radiation is emitted in close proximity to the outer shell of the SNR, where the magnetic field strength is most concentrated.

In his study of the magnetic fields in the Galactic spurs, Bingham (1967) measured the degree of polarization present in the 1407 MHz (radio) emissions from the radio ridge of the North Polar Spur (NPS), and compared this with optical polarization data, obtained by Behr (1959), of stars present in the same region. He found that the polarising effect of the magnetic field was apparent in the spectra of all the stars lying between 90 pc and 120 pc from the Sun, but that stars closer than 70 pc showed little evidence of the Spur's influence. On this basis, Bingham estimated that the NPS must be 100 ± 20 pc from the Sun.

In addition to the large margin for error assigned to his distance measurement, Bingham made clear in his paper that his value was probably, on two counts, an underestimate of the true distance. In the first instance, he did not have data for stars lying further than 120 pc from the Sun. Since he could not measure the polarisation of stellar spectra beyond this point, it set an upper limit on his distance estimate. Second, as Behr noted in 1959, there is a rapid increase in polarization with distance in the range $50 - 120$ pc. Behr attributed this increase to the rise in the density of polarizing dust in proximity to the NPS. However, since this dust also absorbs radiation, it is possible that the apparent brightness of the stars nearest to the NPS would have been too low to have been included in his study, biasing the sample toward foreground stars. Consequently, on the basis of polarization measurements alone, the NPS would appear to be closer than it is in reality.

However, when using Bingham's measurement to place the bubble, Willingale et al. (2003) used the low value of 100 pc, and positioned the modelled sphere such that its north-west limb would lie at this distance from the Sun. They also attempted to ensure that the nearest point of the sphere would lie more than 35 pc away; the minimum distance to the boundary of the LHB found by Hutchinson (1999).

6.4 Checking the Model

Both the boundary and sphere models were used here in order to develop the work described in Willingale et al. (2003), and to continue the analysis of the results presented

in Chapter 4. Unfortunately, closer inspection of the models revealed two problems.

The first of these was discovered when the distance to the front face of the sphere (designated dlo) was calculated for an array of co-ordinates in and around the Loop I region, using the method described in Appendix D. When seen from Earth, the modelled sphere should present a hemispherical profile, bulging out towards the observer, resembling a beach-ball held at arm's length. However, when the values were plotted in a grid, and colour-coded to highlight the curved surface of the model, a 'Mexican hat' profile was revealed; bulging slightly in the middle of the Loop, and receding sharply with increasing distance from the centre, only to rise up again towards the edges. Moreover, the program used to create the sphere generated negative values of dlo for lines of sight that did not intersect Loop I, corresponding to a position behind the observer. Profiles of the shape produced by this program are shown in Figures 6.4 and 6.5.

The code was subsequently altered to produce a model of the intended, spherical form, and made to return 0 for lines of sight that did not pass through the sphere. This new model was then rechecked, to ensure compatibility with Hutchinson's model of the LHB.

6.5 An Unlikely Interaction

The Wall is a dense region of dust and HI gas lying between the LHB and Loop I which is thought to have been created through compression of the primordial ISM by the expanding bubbles (as discussed in Section 2.7). Although there is some evidence that the two bubbles are interacting (Egger & Aschenbach 1995), and that the bottom (southern) limb of Loop I may be slightly flattened as a result, it is unlikely that the Wall impinges significantly upon the interior of Loop I. This is because hot material should displace cooler material, and not vice versa. This principle is central to the displacement model (Section 2.4.4), in which the hot plasma shells of SNRs and wind-blown bubbles displace the cool, neutral material of the ISM as they expand, and is the basis for the existence of the Wall itself.

The effect of displacement is plainly visible in the Ring Nebula, a planetary nebula with a hot rarefied centre, surrounded by (but not mixing with) a cooler outer layer (Figure 2.3). Although the nebula appears to have a 'ring-like' structure, it is really spherical; the orange

	20	15	10	5	360	355	350	345	340	335	330	325	320	315	310	305	300
50	156	129	117	110	107	105	105	106	110	116	127	138	152	146	139	131	122
45	118	107	101	97	94	93	92	94	96	100	106	116	138	153	145	136	127
40	104	97	92	88	86	85	85	85	88	91	96	103	115	146	150	141	131
35	97	90	86	83	81	80	79	81	82	85	89	96	105	122	155	145	133
30	92	86	82	79	77	76	76	77	79	81	85	91	99	113	158	147	135
25	89	83	79	76	75	74	74	75	76	79	83	88	96	109	141	148	136
20	88	82	78	75	74	73	73	73	75	78	81	87	94	107	137	149	136
15	88	82	78	75	73	72	72	73	75	77	81	86	94	108	140	148	135
10	89	83	78	76	74	73	73	73	75	78	82	88	96	110	158	146	132
5	91	85	80	77	75	74	74	75	77	79	84	90	99	116	155	143	129
0	95	88	83	79	77	76	76	77	79	82	87	94	105	129	151	138	125
-5	103	93	87	83	81	80	79	81	83	86	92	101	115	157	145	133	120
-10	114	101	94	89	86	85	85	86	89	93	100	111	138	150	158	137	114
-15	147	115	105	98	95	93	93	94	97	103	113	135	152	142	140	120	107
-20	150	156	126	114	108	106	105	107	113	123	158	151	143	134	137	111	99
-25						134	134	142	157	153	148	141	133	124	114	102	90
-30						148	148	147	145	140	136	129	122	113	103	93	81
-35						134	135	134	131	127	123	117	110	102	92	82	71
-40						120	120	119	117	113	109	104	97	89	81	71	61
-45						105	104	104	101	98	95	89	83	76	68	59	50
-50						88	87	88	86	83	79	75	69	63	55	47	39
-55						72	72	71	69	67	63	59	54	48	42	35	27
-60						54	54	54	52	50	47	43	39	34	28	22	15
-65						36	36	36	35	33	30	27	23	19	14	9	4
-70						18	18	18	17	15	13	11	8	4	0	-4	-8
-75						-7	-3	0	-1	-2	-4	-6	-8	-11	-14	-17	-20
-80						-18	-18	-18	-19	-20	-21	-22	-24	-25	-27	-30	-32
-85						-36	-36	-36	-37	-27	-38	-38	-39	-40	-41	-42	-43
-90						-54	-54	-54	-54	-54	-54	-54	-54	-54	-54	-54	-54

Figure 6.4: A two-dimensional representation of the front surface of the distorted model used in Willingale et al. (2003). The diagram shows the distance to the front face of the sphere (dw) in parsecs for an array of Galactic co-ordinates in the Loop I region. The distances have been coloured coded to highlight the warped shape of the model's profile.

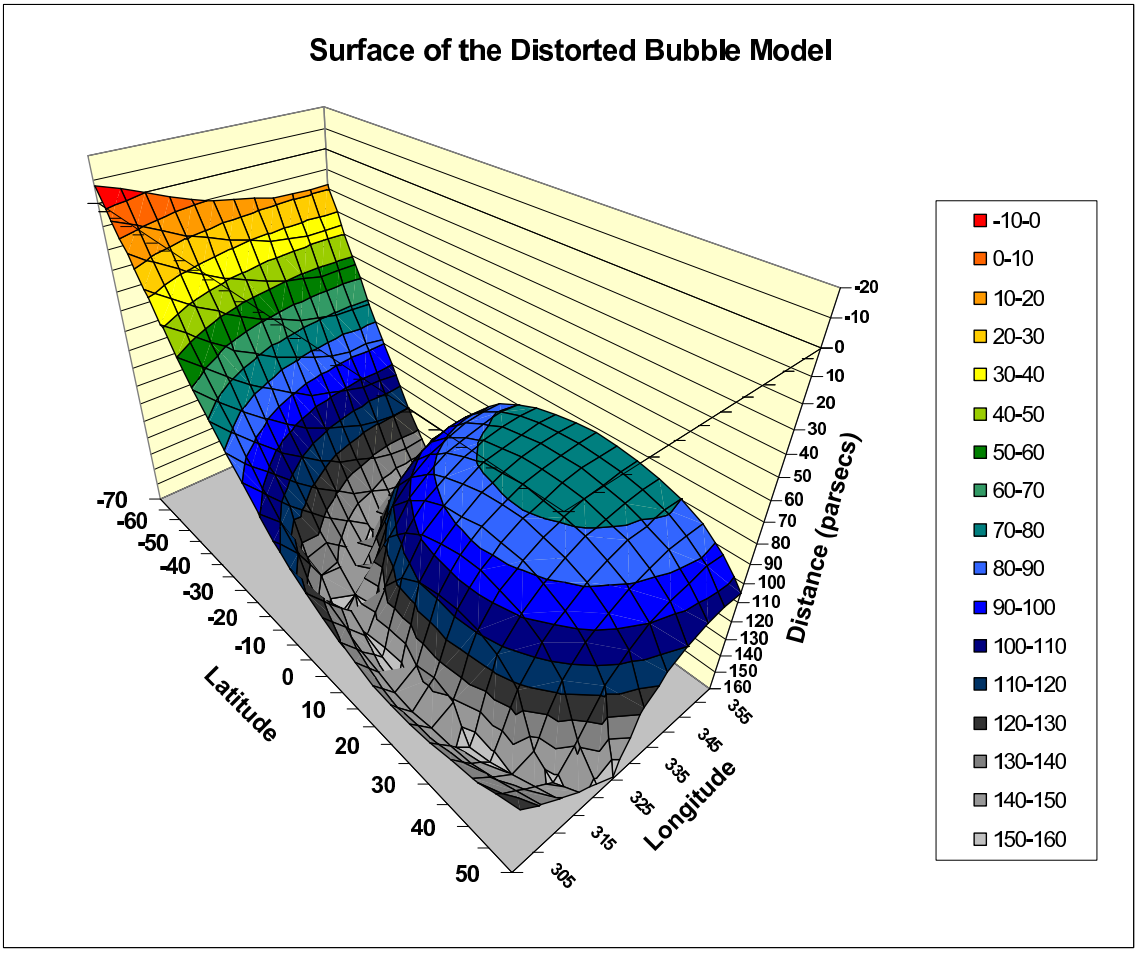

Figure 6.5: A three-dimensional surface plot of the data shown in Figure 6.4, in which the colours represent the distance to the face of the sphere in parsecs. The 'Mexican hat' profile presented by the supposedly spherical model is plainly visible.

(false) coloured shell totally encloses the inner blue region, but because it is relatively thin, it is only discernable near the edges of the structure. A similar arrangement is proposed for the shell around Loop I.

Loop I is not a planetary nebula, but an active, expanding superbubble, and in the model adopted here, the distance in parsecs from the Sun to the boundary of the LHB is defined as dw, and the distance from the Sun to the outer face of Loop I is given as dlo. The winds from the Sco-Cen association continue to heat and pressurize its interior, an action that ensures the continued flow of the neutral material within the Loop towards its outer boundaries. If the Loop is positioned outside the boundary of the LHB, then the value

of dw should always be lower than dlo. However, when an array of dlo values was calculated and compared with a similar array of dw values, derived using the Hutchinson model (Section 6.2), the LHB boundary and the cool material of the Wall were found to enter into the boundary of Loop 1. This unfortunate intersection is illustrated in Figure 6.6. Since the boundary of the LHB predicted by the Hutchinson model is not shaped to accommodate the hot Loop, it would appear that the overall model is incorrect.

Adjustments had to be made to ensure that the modelled sphere did not cross into the established boundary of the LHB, but before this could take place, the model had to be extended to include the newly-identified cool shell.

6.6 Developing the Model

Hutchinson's model of the LHB boundary is based on a wealth of established and accurate data, including Hipparcos measurements and the polarisation and absorption features of many stellar spectra taken from a number of different sources. Also, because the physical properties of the LHB predicted by the model are in close agreement with other published values (quoted in Hutchinson (1999)), it was assumed to be correct, and left unchanged in this implementation. By contrast, the validity of sphere, representing the Loop interior, was in some doubt. Although its profile had already been corrected, it would certainly have to be extended in order to encompass the cool shell identified in the research presented in Chapters 4 and 5, and also moved to prevent its encroachment on the LHB.

A visual inspection of the RASS $\frac{3}{4}$ keV map confirms that most of the flux in the bright central region can be contained within a circle with an angular radius of 42° (Figure 6.3). The models fitted to the SXRB spectra in Chapter 4 identified this region as the Loop 1 interior, and it therefore follows that the measurements reported in Willingale et al. (2003) made in relation to the Loop refer only to this region, and do not include the shell at all.

The projected boundary of the interior, seen in Figure 6.3, convincingly contains the bright X-ray regions in the vicinity of Loop 1, and so was kept unchanged.

A second sphere now had to be added to the model in order to accommodate the

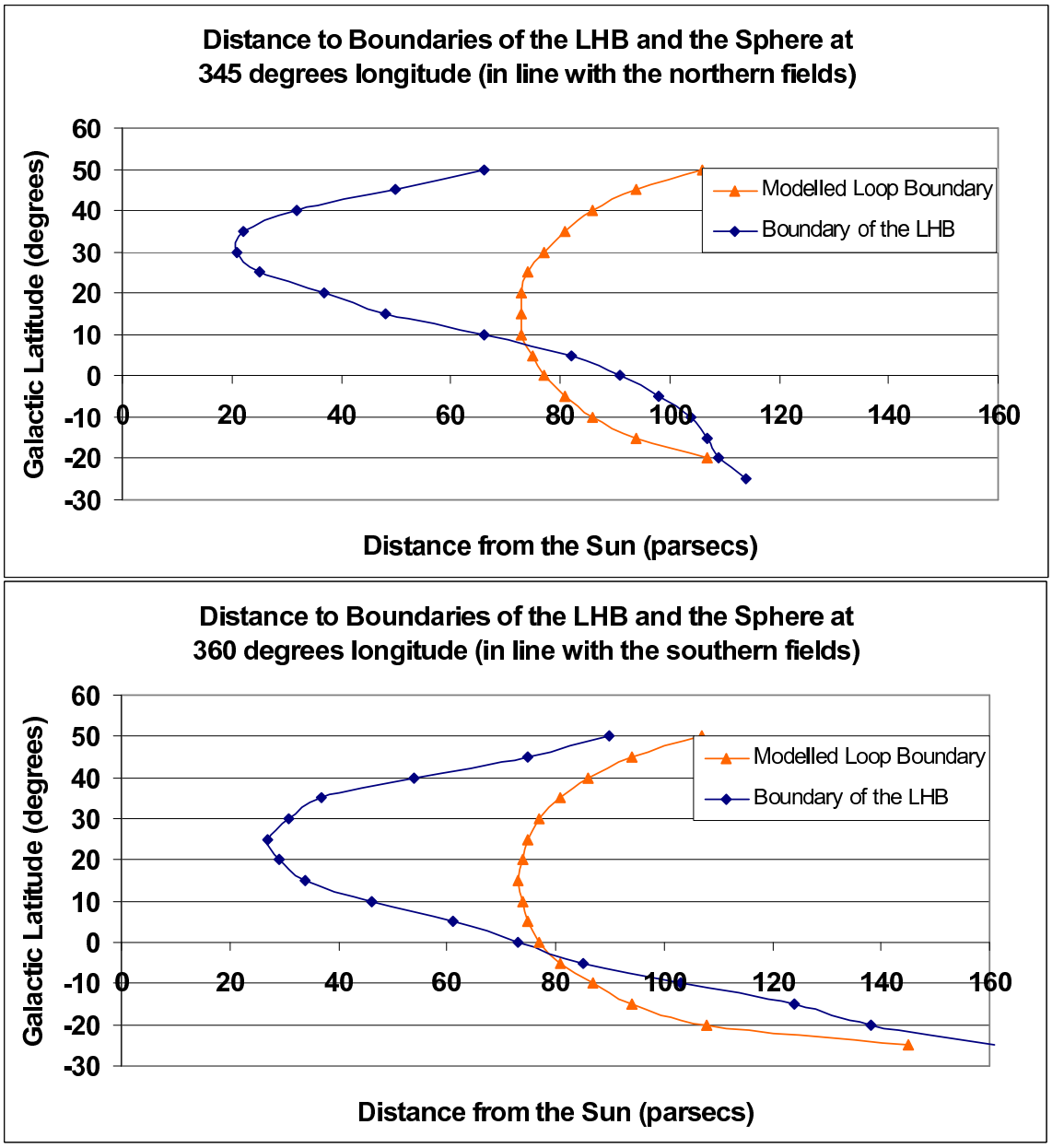

Figure 6.6: The profiles presented by the LHB and the front faces of the Loop when the spherical construct is placed 210 pc from the Sun. The first graph shows a longitudinal slice through 345° in line with the Northern Bulge fields, the second is taken at 360° in line with the Southern fields. Note the incursion of the Loop into the LHB which occurs below 10° latitude in both cases.

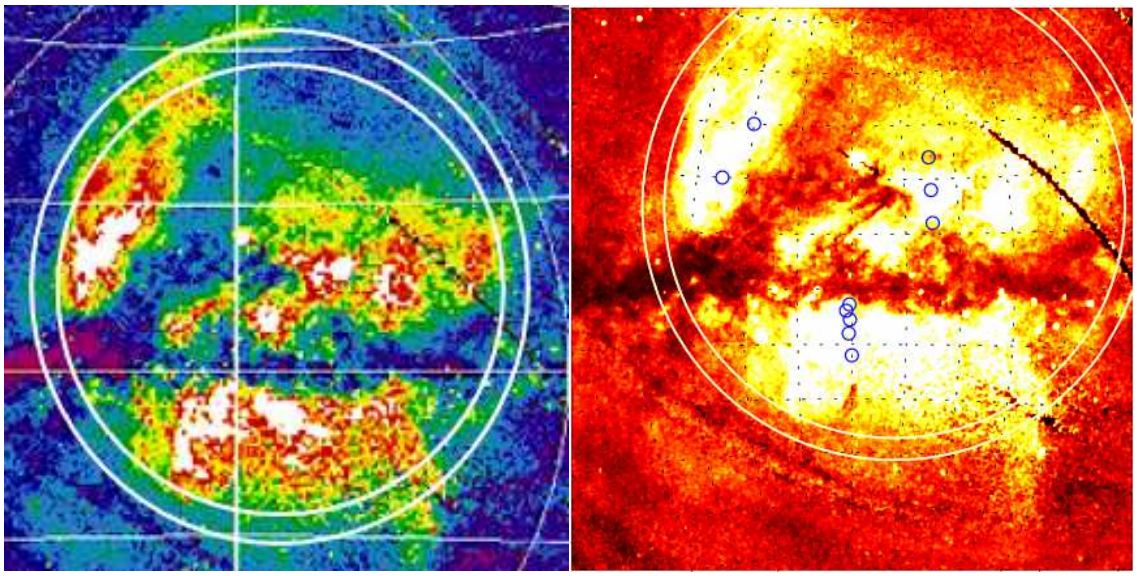

Figure 6.7: The boundaries of both the original 42° radius sphere centred at (352°, 15°), and the larger 46° radius sphere representing the outer edge of the cool shell, superposed on the central region of the $\frac{3}{4}$ keV RASS map. Two versions of the same image are shown, in different colour-ways. An arc of hot material at the top of the shell is more prominent in the left image, whereas the Galactic Plane is clearer in the right image. The small circles in the right-hand image indicate the positions of the Loop I fields.

cool shell which is assumed to entirely surround the hot interior of Loop I to an approximately even depth. Provided that the theoretical model of SNR development described in Section 4.7.4 and shown in Tielens (2005)[1], holds for the Loop, which has certainly been produced by multiple supernova events (∼40, Egger (1998)), then the 42° radius of the interior boundary can be said to represent only eleven-twelfths of the total radius of the SNR. The total radius, to the outer edge of the concentric X-ray emissive shell, must therefore be approximately 46°, giving the shell a uniform thickness of ∼ 4°.

Looking at this new two-sphere arrangement (Figure 6.7), the bright region in the centre of the RASS map suddenly makes more sense. Although the original 42° radius circle used in Willingale et al. (2003) worked well, some flux broke through its boundary. This is particularly noticeable at the Southern limb, and just above the NPS, where a bright arc can be seen to stretch northwards, away from the hot interior. A third, smaller patch overlaps the boundary on the right-hand side. In Willingale et al. (2003), the stray flux

[1] In that volume: page 441, equation 12.70

could not be adequately explained, and so was ignored; the introduction of the shell component, however, offers a new insight into these regions.

The shell has not been clearly imaged before, and is not immediately apparent in the RASS data: at 0.1 keV, it falls mostly outside the energy range included in the $\frac{3}{4}$ keV map, and is swamped in the $\frac{1}{4}$ keV map by the similar signal from the LHB. However, when the second circle, representing the shell, is added to the model, it neatly encloses the excess flux emerging from the Loop interior. Not only does this confirm that that proposed dimensions of the shell are compatible with the observed X-ray flux distribution in the RASS, but it also strongly indicates that the three bright patches of stray flux are associated with the shell, and are possibly regions which have been recently energised though contact with shocked or wind-blown material from the interior.

6.7 The Location of Loop I

While the extension of the sphere to include the shell boundary is undoubtedly beneficial, allowing both the hot interior and the cool shell to be modelled separately, it also exacerbates the overlap issue by increasing the physical size of the remnant, and so forcing more of the Loop's structure to cross the LHB boundary. Because the boundaries described by the interior and shell models fully enclose the Loop I flux imaged in the RASS $\frac{3}{4}$ keV map, its angular size and central co-ordinates are not in doubt. Therefore, to prevent the Loop from entering the LHB, the concentric spheres had to be pushed further back, towards the Galactic Centre.

Initially, Willingale et al. (2003) placed the bubble 210 pc from the Sun on the basis of two arguments. First, that the distance to the nearest part of the sphere should be greater than the minimum distance to the LHB boundary; second, that the north-west limb of the sphere should be 100 pc from the Sun as per the measurement of Bingham (1967), described above in Section 6.3. The first argument would have held true if the LHB were spherical, but this is not the case. The LHB is an irregularly shaped cavity with an hourglass profile, 'nipped in' at the waist and extending into two bulbous arms. The Northern arm extends mainly towards the North Galactic Pole, but the Southern arm stretches diagonally downward, towards Loop I and the Southern Pole. The intersection

between the two structures in the original model occurs in this Southern region, a fact that partly explains why the problem was not detected before, as the Willingale et al. (2003) paper was focussed on the NPS fields in the upper northwest quadrant of the Loop. Nevertheless, it is clear that the sphere representing the hot interior of the Loop should have been placed not beyond the minimum distance to the LHB boundary, but beyond the maximum distance to the boundary within the projected area of the Loop interior.

With regard to the second point, Bingham himself acknowledged that his measurement was an underestimate of the true distance to the NPS. With this in mind, the sphere was pushed back to the upper limit of Bingham's estimate, so that the NPS was 120 pc distant. This placed the centre of the spheres 290 pc from the Sun, some 80 pc greater than the distance used by Willingale et al. (2003).

The distances to the front faces of the shell (dlo_{shell}) and the interior ($dlo_{interior}$) were then calculated for an array of co-ordinates using the method described in Appendix D. These have been plotted in an array, and colour coded to indicate the shape presented by the boundary surface. The results of this procedure are shown in Figure 6.8.

6.8 Consequences of the New Position

When combined, the values from Hutchinson (1999) and the distances shown in Figure 6.8 can be plotted to show the boundary positions of the LHB, shell and interior in profile. As before, this has been done twice, for longitudes 345° and 360°, aligning with the Northern Bulge and Southern fields respectively, and this is shown in Figure 6.9.

As can be seen in Figure 6.6, the sphere representing the hot interior of the Loop entered the LHB when it was placed at its original distance of 210 pc. By moving the sphere back to 290 pc this incursion has been mitigated, but it is still extremely close: while the interior boundary touches the modelled edge of the LHB but does not cross it, in accordance with the tenants of the displacement model, the shell does enter the LHB. Although it would have been possible to place the sphere anywhere along the line of sight, and so push it far beyond the LHB, it would be unreasonable to do so: if the sphere were moved so far back that the shell lay entirely outside the LHB, then the actual volume of

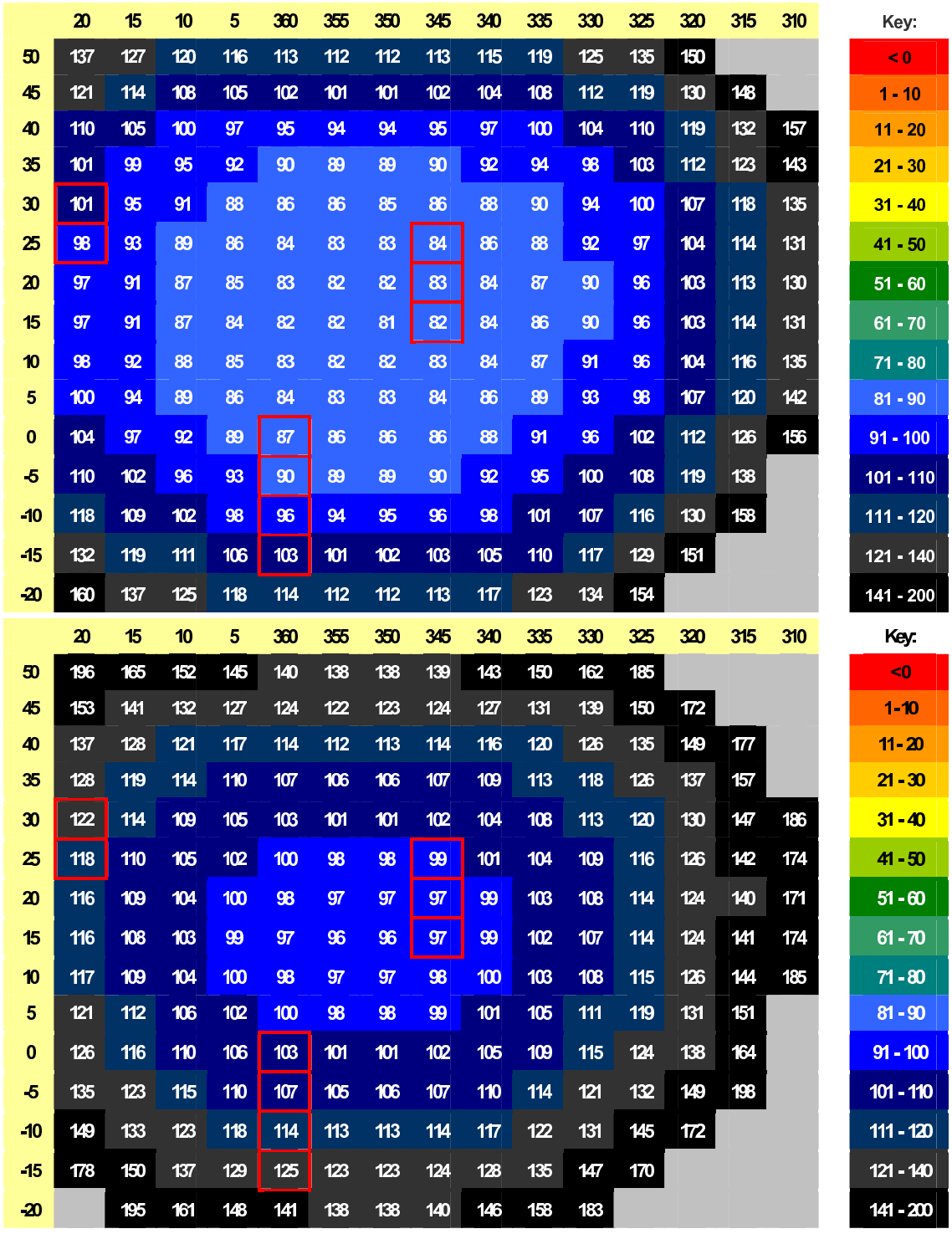

Figure 6.8: The distance in parsecs to the front faces of the shell (top image) and the Loop I interior (lower image). The locations of the Loop I fields are outlined in red. The spherical profile of the corrected model is now apparent.

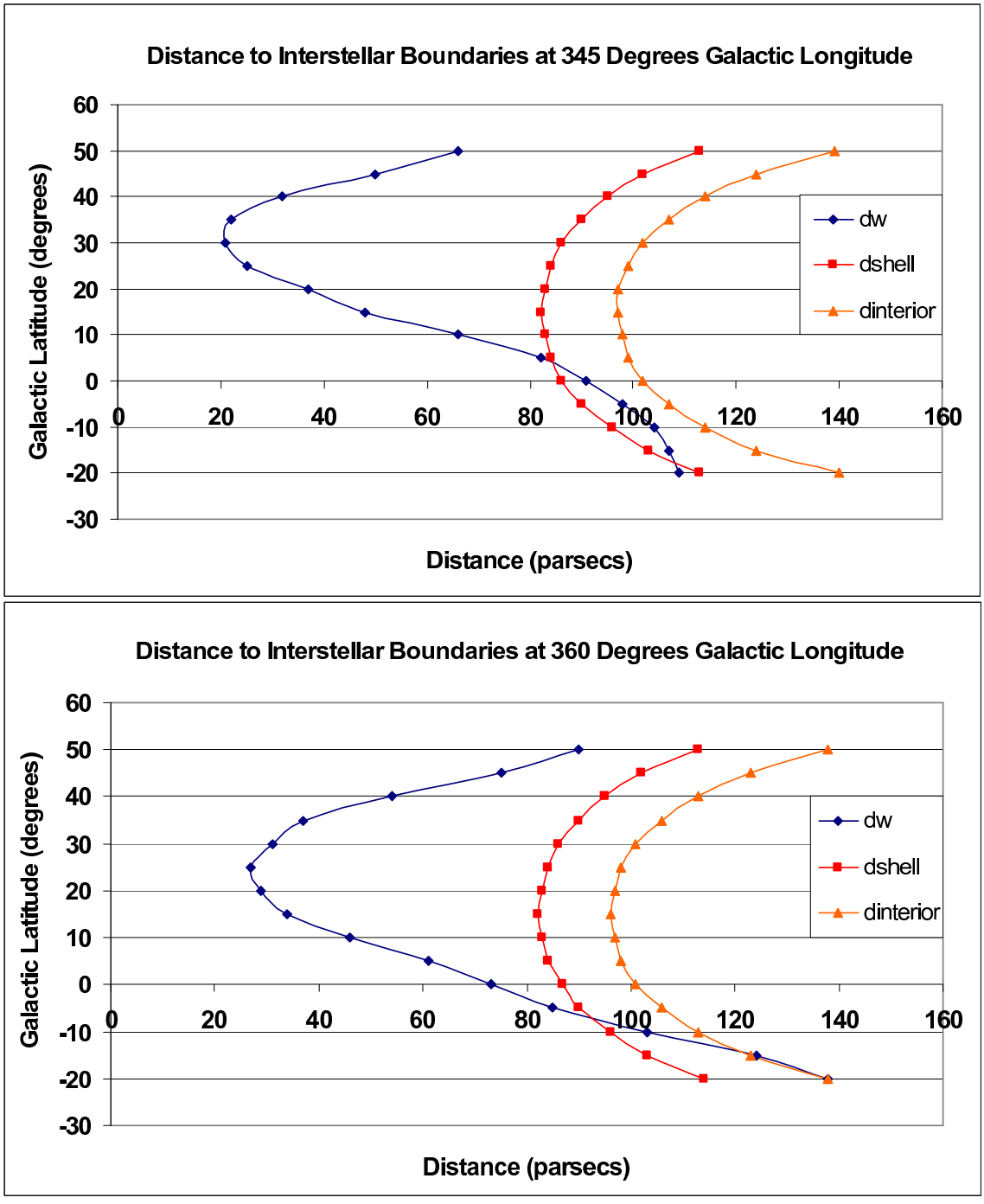

Figure 6.9: The profiles presented by the LHB and the front faces of the Loop's shell and interior when the spherical construct is placed 290 pc from the Sun. The first graph shows a longitudinal slice through 345° in line with the Northern Bulge fields, the second is taken at 360°, in line with the Southern fields. Note the overlap of the shell and LHB.

the Loop would have to be extraordinarily large. Instead, the sphere has been placed at the maximum limit allowed by Bingham's measurement which, to date, is the most reliable estimate of the distance to the NPS.

The fact remains, however, that in this arrangement the shell must partly merge with the LHB. Such a situation is feasible: the shell and the LHB boundary are of a similar composition and temperature, and so, from a thermodynamic perspective, there is little to prevent their constituent plasmas from mixing freely. It is also possible that the Hutchinson model cannot distinguish between the material in the shell and the LHB, both of which have been modelled as 0.1 keV thermal sources. Significantly, the Hutchinson model depends on absorption contours, and defines the boundary of the LHB to be present when a particular column depth has been reached, but because the absorption increases rapidly in proximity to the Wall, the accuracy of the model may be slightly compromised in its vicinity; a region which coincides with the boundary overlap.

As a result of the intersection between the shell and the LHB, the Wall, which was previously described in Hands (2003) and Willingale et al. (2003) as the region of cool, absorbing material lying between the LHB and Loop 1, must now be redefined. A glance at Figure 6.9 highlights the motivation for this. Using the old definition, the depth of the Wall is calculated by subtracting the distance to the LHB boundary from the distance to the front of the Loop. While this is adequate in the north, where there is a clear separation between the LHB and Loop 1, it is insufficient in the Southern fields. In this region, the intersection of the Shell and the LHB produces the 'negative' Wall thicknesses illustrated in Figure 6.10.

When fitting the spectra, both the Loop interior and the shell were subjected to the same level of absorption, representing the foreground HI column lying between the Sun and the front face of the shell. As there is very little absorbing material in the LHB, the fitted absorption was assumed to lie in the Wall, the diffuse gas outside the LHB which gradually increases in opacity as its column depth increases towards the Loop.

The Wall is known to be a dense region of absorbing HI gas, but the X-ray emissive shell could also be absorptive: it is at the leading edge of an enormous supernova remnant, and so should incorporate the debris swept up by its expansion. By contrast, the interior is hot, rarefied, and like the LHB, should contain very little absorbing material. Hence the

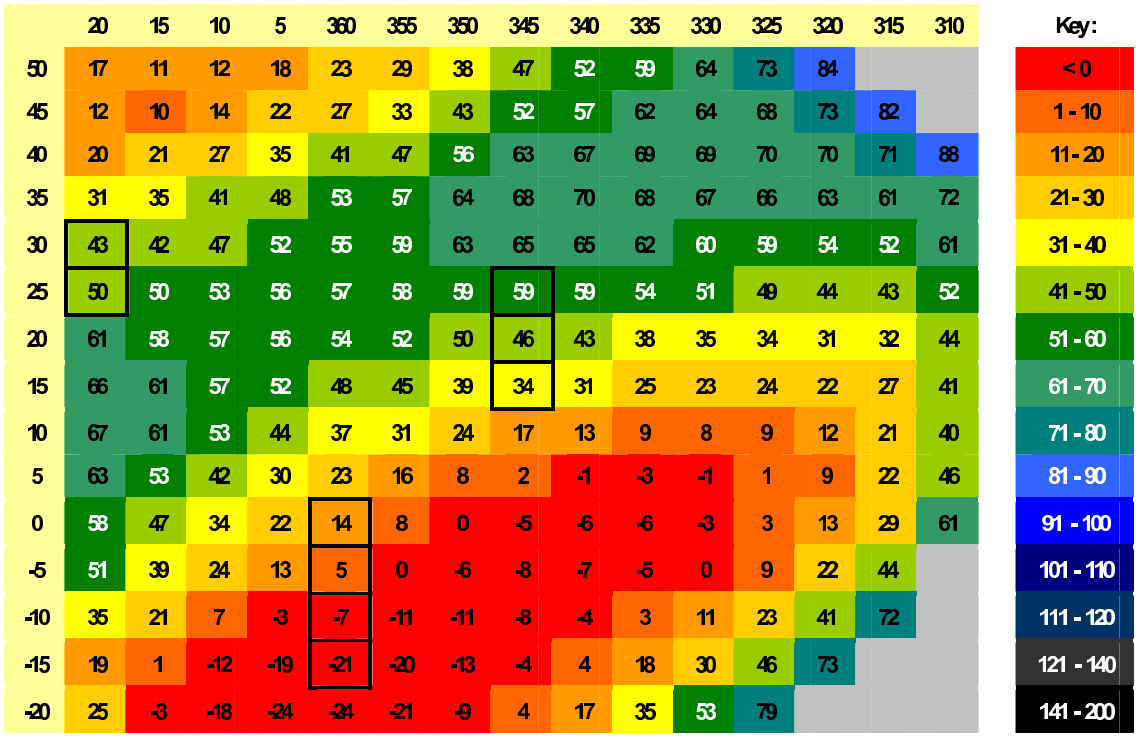

	20	15	10	5	360	355	350	345	340	335	330	325	320	315	310
50	17	11	12	18	23	29	38	47	52	59	64	73	84		
45	12	10	14	22	27	33	43	52	57	62	64	68	73	82	
40	20	21	27	35	41	47	56	63	67	69	69	70	70	71	88
35	31	35	41	48	53	57	64	68	70	68	67	66	63	61	72
30	43	42	47	52	55	59	63	65	65	62	60	59	54	52	61
25	50	50	53	56	57	58	59	59	59	54	51	49	44	43	52
20	61	58	57	56	54	52	50	46	43	38	35	34	31	32	44
15	66	61	57	52	48	45	39	34	31	25	23	24	22	27	41
10	67	61	53	44	37	31	24	17	13	9	8	9	12	21	40
5	63	53	42	30	23	16	8	2	-1	-3	-1	1	9	22	46
0	58	47	34	22	14	8	0	-5	-6	-6	-3	3	13	29	61
-5	51	39	24	13	5	0	-6	-8	-7	-5	0	9	22	44	
-10	35	21	7	-3	-7	-11	-11	-8	-4	3	11	23	41	72	
-15	19	1	-12	-19	-21	-20	-13	-4	4	18	30	46	73		
-20	25	-3	-18	-24	-24	-21	-9	4	17	35	53	79			

Key:
< 0
1 - 10
11 - 20
21 - 30
31 - 40
41 - 50
51 - 60
61 - 70
71 - 80
81 - 90
91 - 100
101 - 110
111 - 120
121 - 140
141 - 200

Figure 6.10: A coloured array of Galactic co-ordinates in the Loop I direction, showing the column depth of the Wall in parsecs calculated using $dlo_{shell} - dw$, a method which excludes the shell from the Wall depth. The negative depth values, coloured red, result from the intersection of the Shell with the LHB boundary. The positions of the Loop I fields are outlined in black.

fitted absorption must refer to material present in both the shell and the Wall. On this basis, both structures should be included in the calculation of the depth of the foreground absorbing column. From this perspective, the depth of the Wall should be calculated by subtracting the distance to the LHB boundary (dw) from the distance to the front of the Loop's interior ($dlo_{interior}$). An array showing the Wall thicknesses derived through this method is shown in Figure 6.11. The column depth values found by this method will be used below in the analysis of the Wall's physical properties.

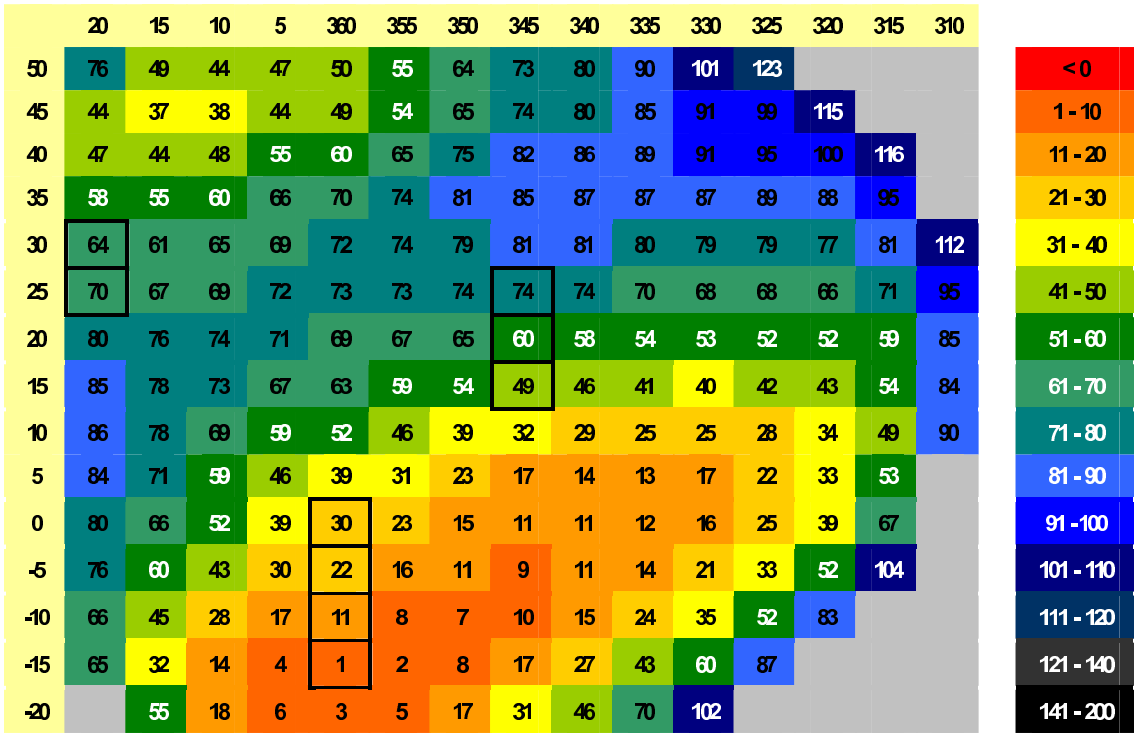

Figure 6.11: A coloured array showing the column depth of the Wall in parsecs, calculated using $dlo_{interior} - dw$, and so including the shell depth. Using this method, the negative column depths are eliminated. The positions of the Loop I fields are outlined in black.

6.9 The Physical Properties of the LISM

Now that the Wall has been defined, and the spherical model positioned, the values of dw, dlo and dhi can be calculated for the Loop I fields. These distances, calculated using the Hutchinson model and the method shown in Appendix D, are presented in Table 6.1.

By using these distances in conjunction with values derived from the best fit parameters presented in Appendix B, the physical properties of the LISM can be determined using the formulae described in Appendix E. These results are presented in Tables 6.2 and 6.3.

Table 6.1: Distances in parsecs to the LHB boundary dw, and to the near (dlo) and distant (dhi) faces of the shell and interior for the Loop I fields.

Field	dw	dlo_{shell}	$dlo_{interior}$	$dhi_{interior}$	dhi_{shell}
X1	59.94	82.36	97.18	477.94	492.76
X2	42.19	82.33	97.15	478.08	492.90
X3	28.11	83.60	98.76	470.28	485.45
N4	41.78	104.50	126.92	365.94	388.37
N5	58.32	100.79	121.65	381.80	402.66
B1	78.99	88.65	105.29	441.14	457.77
B2	82.63	89.76	106.73	435.17	452.15
B3	91.28	90.90	108.24	429.10	446.43
B4	97.56	93.45	111.62	416.09	434.26
B5	110.44	98.20	118.07	393.38	413.25

6.10 Interpreting the Results of the Analysis

There is always a risk that an analysis may be prejudiced by the numerous assumptions required to produce the results. The fact remains, however, that the final values shown in Tables 6.2 and 6.3 could not have been obtained without the best-fit parameters from the spectra (presented in Appendix B) and, if these had been in conflict with the geometric model discussed above, then the derived numbers would have made little physical sense. Fortunately, however, the calculated properties of the LISM do seem consistent with the proposed topography, and have allowed a number of inferences to be drawn.

The results will be interpreted with respect to Galactic latitude as in previous chapters, and also, now that the boundary of the shell and interior have been defined, with respect to the great circle distance (GCD) from the projected sky co-ordinates of the centre of Loop I.

The great circle is defined as the section of a sphere that contains the diameter of that sphere, or in the context of this research, the projected boundary of Loop I. The shortest path between two points on the surface of a sphere has a length equivalent to a segment of the great circle. This distance, measured along the surface of the sphere, not through its interior, is the GCD.

Table 6.2: Final Analysis Values for the Northern Fields

Structure	Property	X1	X2	X3	N4	N5
LHB	Emission Measure (cm^{-6} pc)	5.95×10^{-3}	5.14×10^{-3}	5.57×10^{-3}	3.70×10^{-3}	2.99×10^{-3}
	Electron Density (cm^{-3})	1.10×10^{-2}	1.21×10^{-2}	1.55×10^{-2}	1.03×10^{-2}	7.88×10^{-3}
	Pressure/k_B (cm^{-3} K)	$2.33 \times 10^{+4}$	$2.57 \times 10^{+4}$	$3.28 \times 10^{+4}$	$2.19 \times 10^{+4}$	$1.67 \times 10^{+4}$
Wall	Density (atoms cm^{-3})	$1.12 \times 10^{+21}$	$4.64 \times 10^{+20}$	$4.47 \times 10^{+20}$	$2.31 \times 10^{+20}$	$1.32 \times 10^{+20}$
Loop I	Emission Measure (cm^{-6} pc)	9.03×10^{-2}	9.93×10^{-2}	3.42×10^{-2}	1.36×10^{-1}	7.84×10^{-2}
	Electron Density (cm^{-3})	1.69×10^{-2}	1.78×10^{-2}	1.05×10^{-2}	2.63×10^{-2}	1.91×10^{-2}
	Pressure/k_B (cm^{-3} K)	$1.08 \times 10^{+5}$	$1.13 \times 10^{+5}$	$6.70 \times 10^{+4}$	$1.67 \times 10^{+5}$	$1.21 \times 10^{+5}$
Loop I	Mean Electron Density (cm^{-3})			1.81×10^{-2}		
	Mean Temperature (K)			$3.48 \times 10^{+6}$		
	Total Volume (cm^{-3})			$9.00 \times 10^{+62}$		
	Total Energy (J)			$2.15 \times 10^{+45}$		
	Energy from Pressure (J)			$2.15 \times 10^{+45}$		
Shell	Emission Measure (cm^{-6} pc)	4.13×10^{-2}	5.90×10^{-2}	1.32×10^{-2}	5.79×10^{-2}	5.68×10^{-2}
	Electron Density (cm^{-3})	5.81×10^{-2}	6.94×10^{-2}	3.24×10^{-2}	5.59×10^{-2}	5.74×10^{-2}
	Pressure/k_B (cm^{-3} K)	$1.23 \times 10^{+5}$	$1.47 \times 10^{+5}$	$6.86 \times 10^{+4}$	$1.18 \times 10^{+5}$	$1.22 \times 10^{+5}$
Galactic Latitude (degrees)		12.00	18.00	24.00	20.00	30.00
Great Circle Distance (degrees)		7.44	7.35	11.15	31.81	29.77

Table 6.3: Final Analysis Values for the Southern Fields. Units of flux for the non-thermal component of the GPR are photons keV^{-1} cm^{-2} s^{-1} sr^{-1} at 1 keV.

Structure	Property	B1	B2	B3	B4	B5
LHB	Emission Measure (cm^{-6} pc)	6.78×10^{-3}	5.20×10^{-3}	4.54×10^{-3}	6.03×10^{-3}	2.50×10^{-3}
	Electron Density (cm^{-3})	1.02×10^{-2}	8.73×10^{-3}	7.76×10^{-3}	8.65×10^{-3}	5.23×10^{-3}
	Pressure/k_B (cm^{-3} K)	$2.16 \times 10^{+4}$	$1.85 \times 10^{+4}$	$1.64 \times 10^{+4}$	$1.83 \times 10^{+4}$	$1.11 \times 10^{+4}$
Wall	Density (atom cm^{-3})	$1.98 \times 10^{+21}$	$1.01 \times 10^{+21}$	$1.76 \times 10^{+21}$	$1.83 \times 10^{+21}$	$1.25 \times 10^{+21}$
Loop I	Emission Measure (cm^{-6} pc)	8.81×10^{-2}	8.74×10^{-2}	8.83×10^{-2}	8.87×10^{-2}	8.78×10^{-2}
	Electron Density (cm^{-3})	1.78×10^{-2}	1.79×10^{-2}	1.82×10^{-2}	1.88×10^{-2}	1.96×10^{-2}
	Pressure/k_B (cm^{-3} K)	$1.13 \times 10^{+5}$	$1.14 \times 10^{+5}$	$1.16 \times 10^{+5}$	$1.19 \times 10^{+5}$	$1.25 \times 10^{+5}$
Loop I	Mean Electron Density (cm^{-3})			1.85×10^{-2}		
	Mean Temperature (K)			$3.48 \times 10^{+6}$		
	Total Volume (cm^{-3})			$9.00 \times 10^{+62}$		
	Total Energy (J)			$2.19 \times 10^{+45}$		
	Energy from Pressure (J)			$2.19 \times 10^{+45}$		
Shell	Emission Measure (cm^{-6} pc)	4.57×10^{-2}	4.54×10^{-2}	4.58×10^{-2}	4.61×10^{-2}	4.56×10^{-2}
	Electron Density (cm^{-3})	5.77×10^{-2}	5.69×10^{-2}	5.66×10^{-2}	5.54×10^{-2}	5.27×10^{-2}
	Pressure/k_B (cm^{-3} K)	$1.22 \times 10^{+5}$	$1.21 \times 10^{+5}$	$1.20 \times 10^{+5}$	$1.17 \times 10^{+5}$	$1.12 \times 10^{+5}$
GPR (Thermal)	Emission Measure (cm^{-6} pc)	2.60×10^{-2}	1.81×10^{-2}	4.86×10^{-3}	1.48×10^{-3}	4.94×10^{-4}
GPR (Non-Thermal)	Flux (units above)	86.20	54.05	36.86	19.40	19.40
Galactic Latitude (degrees)		−2.71	−3.87	−5.49	−8.00	−12.00
Great Circle Distance (degrees)		19.59	20.89	22.12	24.52	28.14

Table 6.4: Order of the Points by Latitude and Great Circle Distance

Latitude	−12.00	−8.00	−5.49	−3.87	−2.71	12.00	18.00	20.00	24.00	30.00
Field	B5	B4	B3	B2	B1	X1	X2	N4	X3	N5
GCD	7.35	7.44	11.15	19.59	20.89	22.12	24.52	28.14	29.77	31.81
Field	X2	X1	X3	B1	B2	B3	B4	B5	N5	N4

The GCD from the centre of the modelled sphere to each of the Loop I fields was calculated using the Q software package (Willingale 2004), which compared the co-ordinates of the two points and calculated the angular distance between them, giving the answer in degrees. This value allows the properties of the Loop to be compared by radius. The fields N5 and B5, for example, are located in very different parts of the sky, but lie at similar distances from the projected centre co-ordinate of the Loop. Examination of their physical characteristics with respect to the GCD could reveal if radial symmetry exists within the Loop and this, if found, would strongly support the notion that the bright bulges either side of the Plane do in fact form one contiguous structure, and are not two separate entities.

For reference, the order in which the fields appear in the graphs that follow are shown in Table 6.4.

6.11 Discussion

6.11.1 The Indentation and Southern Interaction Region

As shown in Figure 6.12, the electron density and pressure of the LHB are higher in the Northern Bulge than they are in the Southern and NPS fields, and significantly, this localised peak in values coincides with the region of the LHB that the Hutchinson model shows to be indented.

There are two possible mechanisms which could have generated the characteristic double-lobed shape of the LHB: either a bi-polar explosion, or the deformation of a pre-existing remnant caused by pressure from an outside force. In the first scenario, the

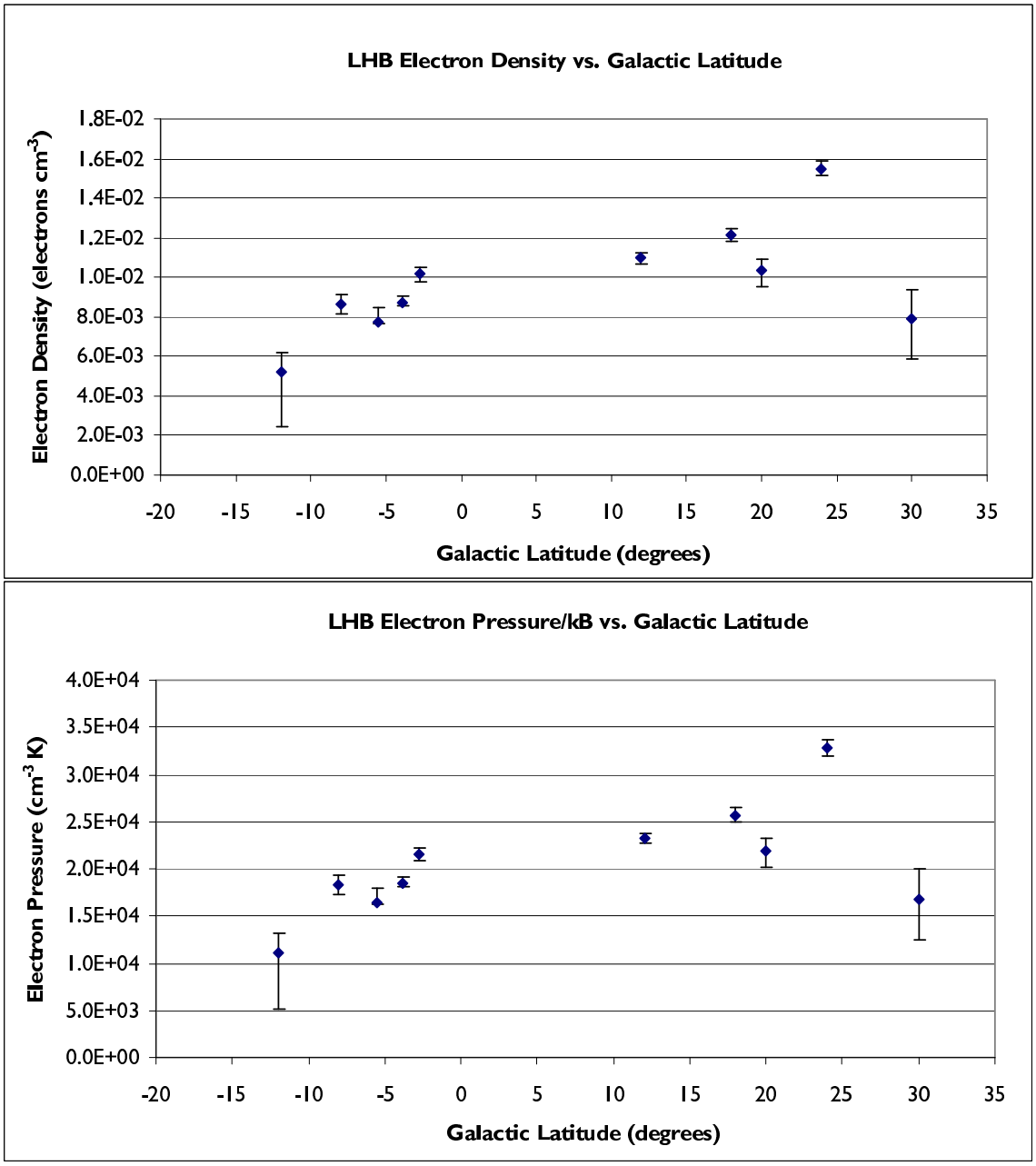

Figure 6.12: Electron density and pressure in the LHB, versus Galactic latitude.

pressure of the plasma in the indented region would be relatively low, as the momentum of such an explosion would cause the plasma to rush away from a central, constricted region. The second process, however, would generate a higher pressure near the deformed region, as a result of the inward-acting compressive force.

Figure 6.12 also shows that the electron density of the LHB plasma is similar in the Southern and NPS fields, but higher in the Northern Bulge fields, where it increases steadily from X1 to X3: a region (between 12° and 25° latitude) coincident with both the waist of the LHB and the Wall.

The material in the Wall is much cooler than that in the LHB; it is molecular and absorbent, not X-ray emissive or dissociated and, unsurprisingly, the results show that it is many times denser than the LHB. Although the displacement model dictates that cold material should not impinge upon hot plasma, the analysis indicates that this is occurring in the indented region. The clue to why this is possible lies in the nature of the LHB: it is an old, hourglass-shaped SNR, with a boundary wall that appears to be open near the Poles (Hutchinson 1999). It would be logical to surmise that its ends breached following their emergence from the HI disk (Section 2.9.2). Once the boundary had been compromised, material would have started to flow out of the LHB interior, and into the surrounding space. The effects of this process are still apparent in the LHB: as the results of the analysis (Tables 6.2 and 6.3) show, the pressure in the LHB is on average $\sim$5.5 times lower than that within Loop 1. Clearly, the LHB has started to depressurize, making it less resilient to the effects of outside pressure.

The Wall is sandwiched between the LHB and Loop 1. If the Loop were static, or not present at all, then the cool Wall would stay outside the warmer LHB, despite the reduced strength of its boundary. However, unlike the LHB, the Loop's boundary is still intact; in the Northern fields the average energy of the interior was found to be 2.15×10^{45} J, all of which could be attributed to pressure (Table 6.2). The Loop's continual expansion displaces and heats the Wall material, and because the pressure it exerts on the Wall is greater than that from the LHB, the resultant force pushes the Wall material into the LHB, deforming its boundary and creating the indent.

The compressive forces acting upon the Wall would be expected to increase its density, and the results do show this to be the case. This is clearly visible in Figure 6.13 illustrates

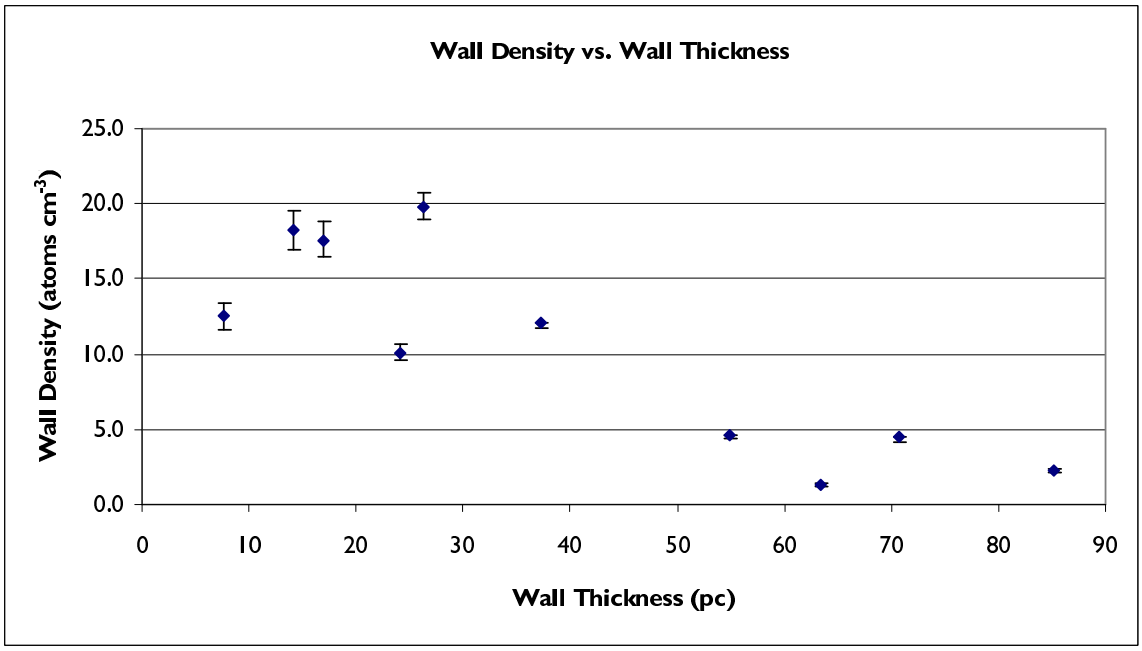

Figure 6.13: Variation of the Wall density by Wall Thickness.

the extent to which the Wall's density increases as it is squeezed between the LHB and the Loop.

During the analysis, the Shell thickness was included in the depth of the Wall (Section 6.8), in order to accommodate the interaction in the Southern fields. The question is therefore: how much of the Wall's density measured in the Southern fields may be ascribed to the Shell? A comparison of Figures 6.14 and 6.15 shows that the density of the Shell material is far lower than that of the Wall, even in the Southern fields where the parameters were held down to average values during the fit. It follows, therefore, that the high density observed in the Southern fields must be a generated by the Wall itself, with very little contribution from the Shell.

It is no coincidence that the highest Wall density should occur in the Southern fields where, in the geometric model, the Shell, Wall and LHB intersect. In this region, the Shell and LHB are pushed close together. This puts pressure on the Wall material, compressing it into a thin layer, with a density of $\sim$ 20 atoms cm^{-3}.

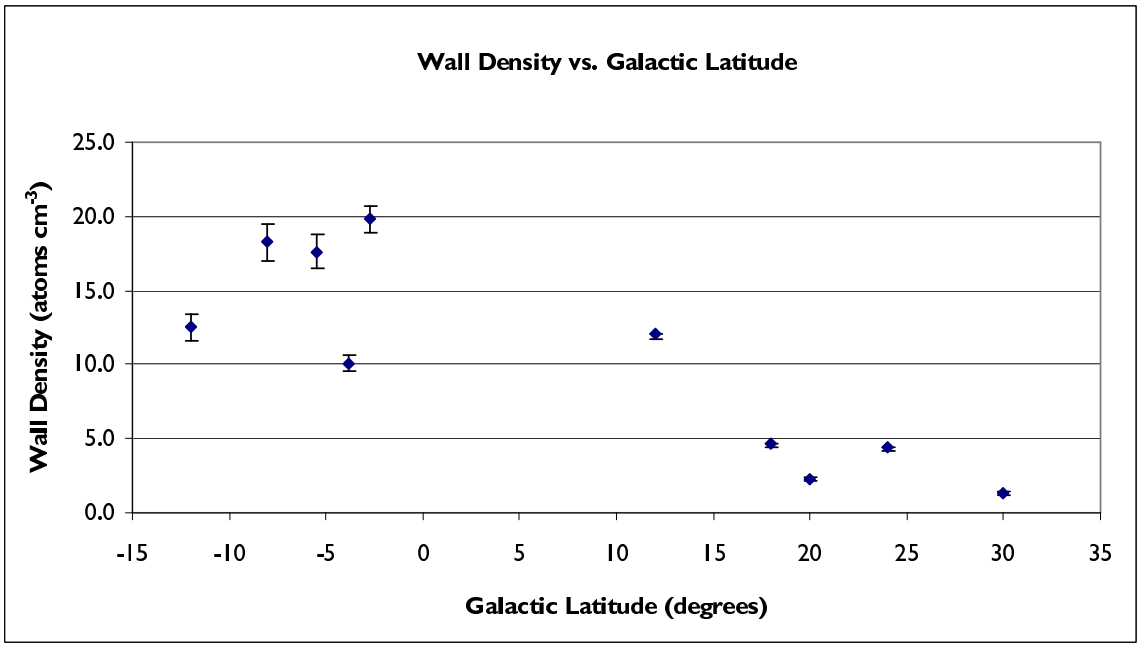

Figure 6.14: Variation of the Wall density by Galactic latitude.

6.11.2 The Shell and Interior of Loop I

Egger & Aschenbach (1995) were the first to show that Loop I could be modelled consistently as a superbubble, produced by the collective energy input of stellar winds and exploding stars. Their model, a sphere of radius of $\sim$160 pc, was found to have a temperature of 4.6×10^6 K and required a mean energy input of $\sim 7 \times 10^{37}$ erg s^{-1} to maintain an assumed expansion velocity of 20 km s^{-1}. Their research was followed in 2002 by Berghöfer & Breitschwerdt, who suggested that to reach its observed angular size, the Loop must have been powered by at least forty separate supernovae, all originating within the Sco-Cen association. The expansion of Loop I looks set to continue, as it contains several active star-forming regions, together with another forty potential supernova candidates (Egger 1998).

Here, the Loop has been modelled by two concentric spheres, with radii of 42° and 46°, representing the Loop interior and the Shell respectively. These have been placed at a distance of 290 pc, making the actual radius of the modelled Loop interior 194 pc, and giving it a volume of 9×10^{62} cm^3. The distance from the centre of the sphere to the outer edge of the Shell is 209 pc, giving the Shell a thickness of 15 pc. These dimensions

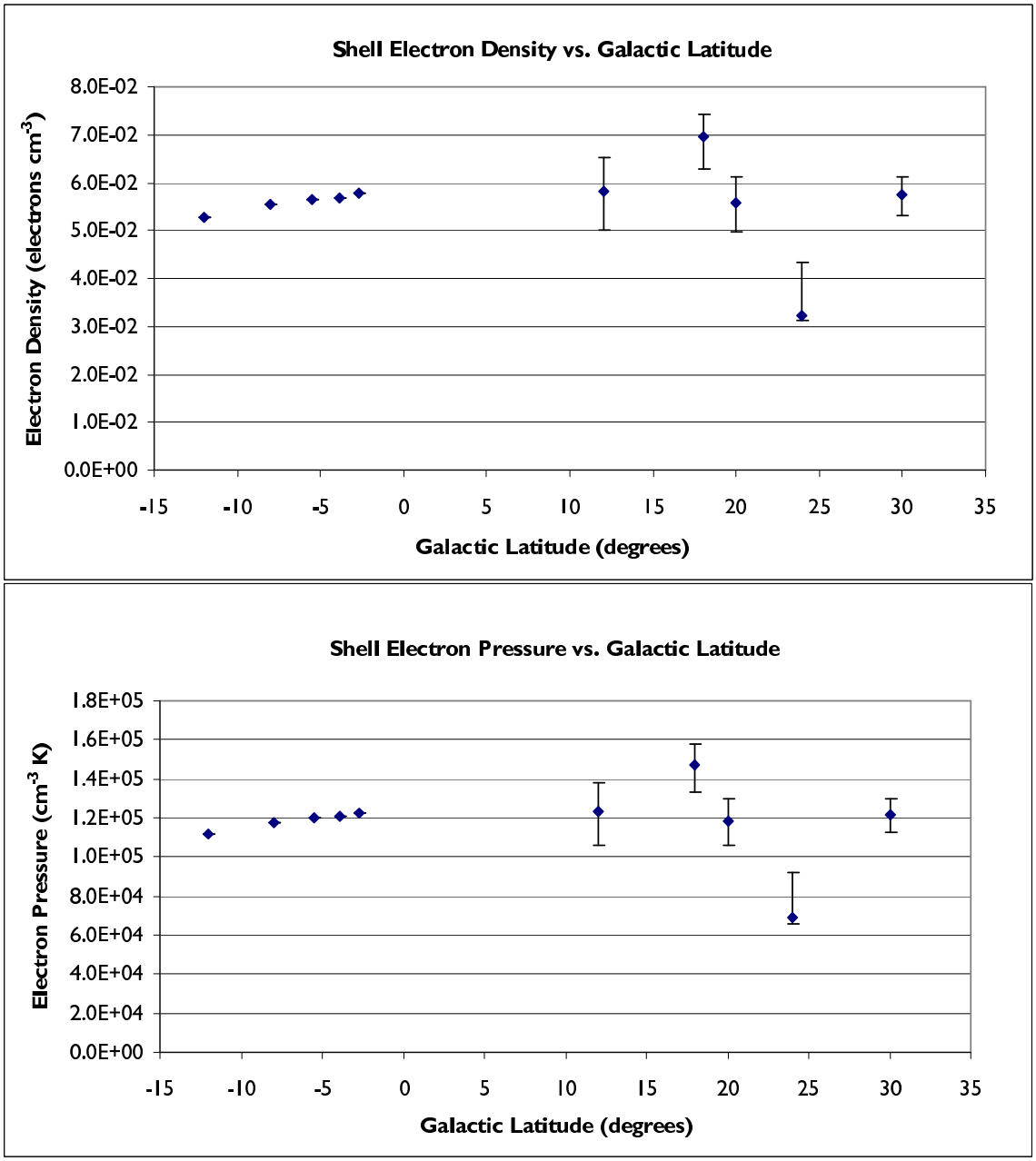

Figure 6.15: Electron density and pressure in the Shell, versus Galactic latitude.

were used in conjunction with the best-fit parameters to produce the results presented in Tables 6.2 and 6.3.

While fitting the spectra in the Southern fields, the normalisations of both the Shell and the Loop were held at average values, in order to prevent them rising to unreasonable values under the influence of the GPR, which was itself fitted with two other components. Although this allowed the fields to be fitted in a credible manner, it has restricted the free fitted data to only five points in Figures 6.16 and 6.17. In these plots, which are plotted against the great circle distance, the points representing the frozen Southern fields have no error bars. Of the remaining points, the three on the left are the Northern Bulge fields, and the two on the right are in the NPS.

In Chapter 4, it was noted that the properties of the Shell and interior of Loop I showed similar trends, suggesting that they are the different aspects of one structure. This observation still holds, and even if the Southern fields are discounted, it can also be seen that the emission measure, pressure and density of the interior plasma gradually increase as the Shell is approached, reaching their maximum values in the NPS fields. This is in line with the model of SNR evolution outlined in Section 4.7.4, in which the plasma in a remnant continues to expand until it hits the denser boundary material. Upon encountering such resistance, the density of the interior plasma would increase as seen, and it should also heat up. Since the plasma temperatures of the Loop and Shell were frozen in the final fits, any variation in temperature will not be seen in the results presented here. However, the higher brightness of the NPS relative to the Loop interior seen in the RASS maps strongly suggests that such heating does occur at the interface between the interior and the Shell.

6.11.3 The Galactic Plane

While fitting the spectra from four of the Southern fields, the normalisations of the Loop, LHB, Shell, and the contribution from the XRB, were found to increase rapidly to unphysical values as the Plane was approached (this was detailed in Chapter 4). The effects of this artificial enhancement were mitigated by freezing the normalisations of the components to expected values, based on the fitted parameters from the unaffected fields in the North. While this reduced the diagnostic power of the parameters, preventing

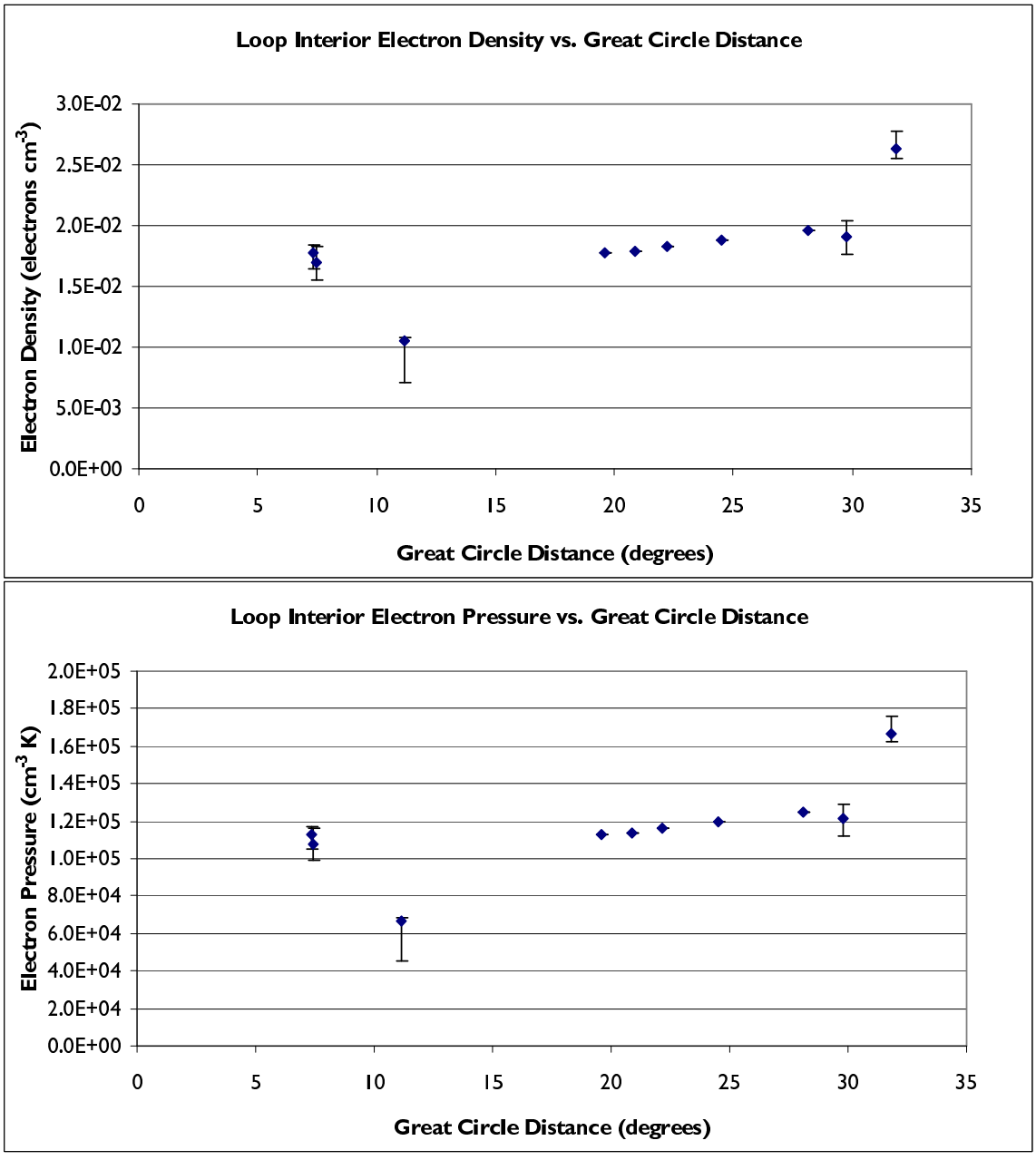

Figure 6.16: Electron density and pressure within the Loop, versus great circle distance.

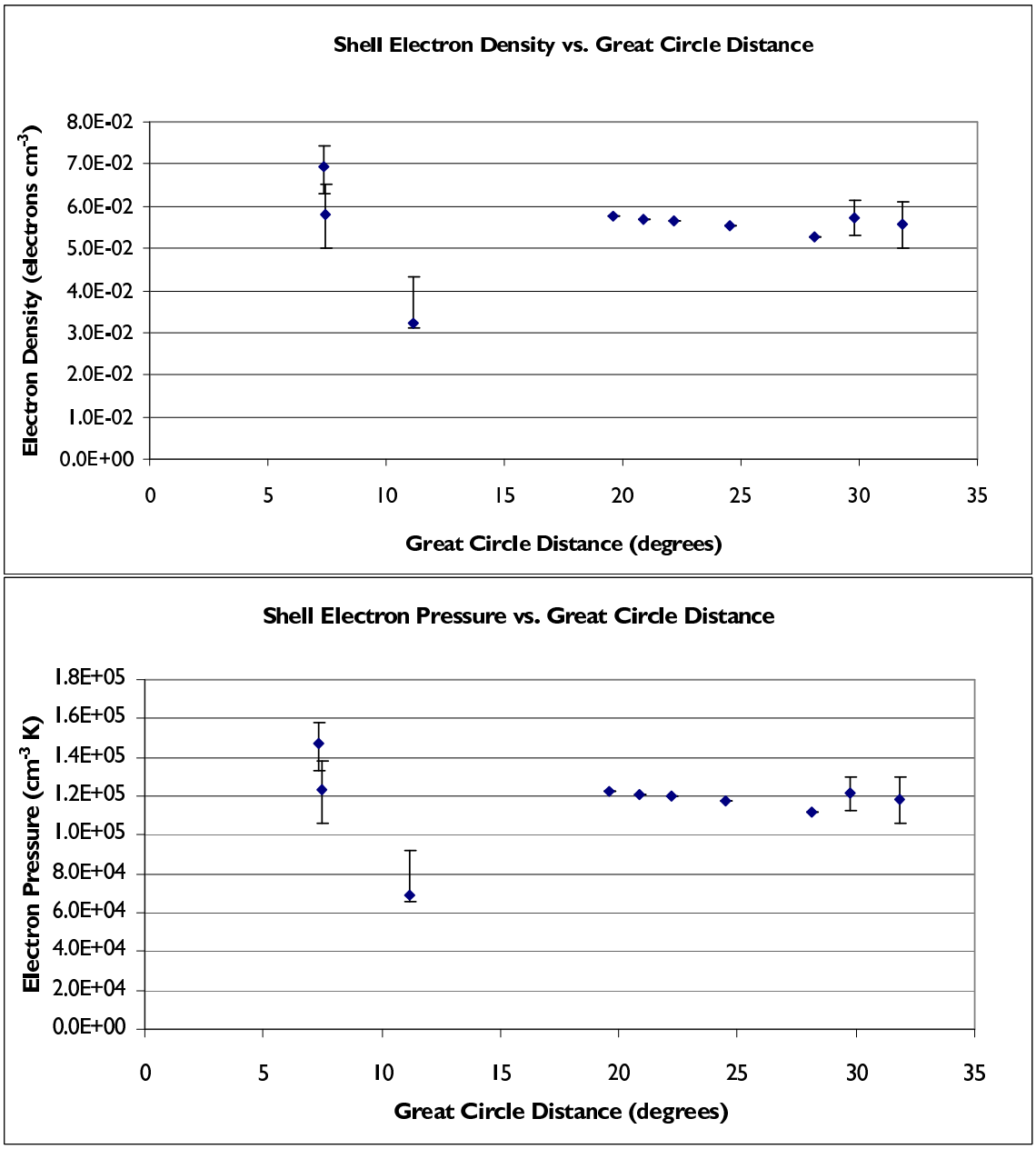

Figure 6.17: Electron density and pressure in the Shell, versus great circle distance.

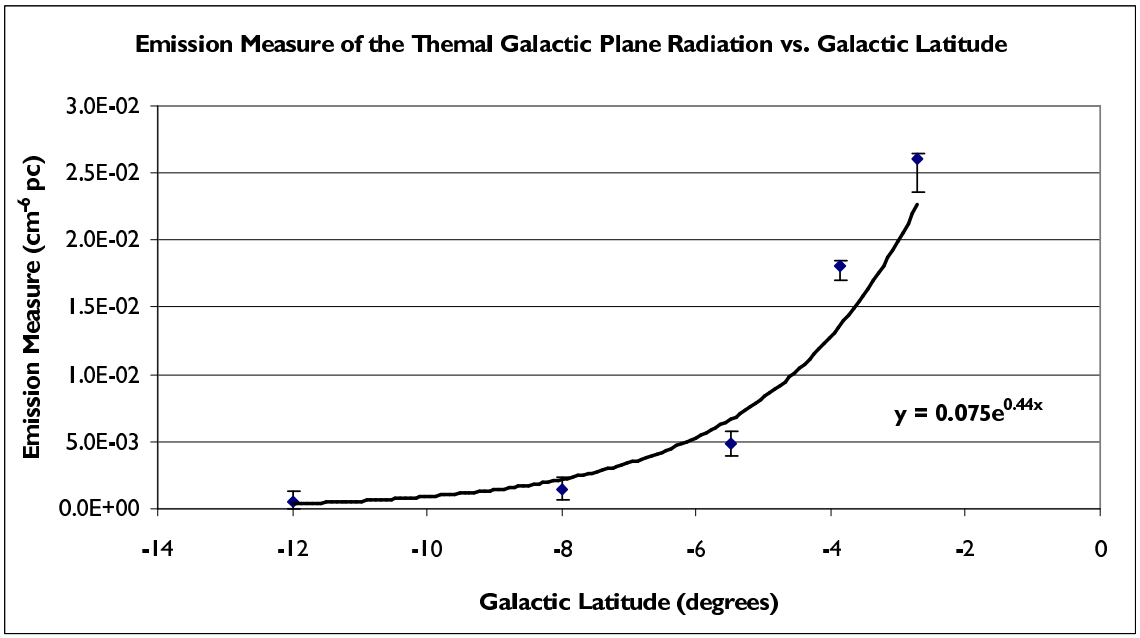

Figure 6.18: Contribution from the thermal GPR (modelled using MEKAL) , versus Galactic Latitude

conclusions from being drawn from the results, it also isolated a hard excess present only within 6° of the Plane. This was eventually fitted by two components, a MEKAL at 1 keV and a power law with a photon index of 2.5, both of which were set behind the full Galactic column. While the thermal source can be connected with the diffuse part of the Galactic Plane Radiation, the non-thermal source has not been previously identified in the literature, and could possibly originate at the Galactic Centre.

As the Figures 6.18 and 6.19 illustrate, both the thermal and non-thermal components rise as the Plane is approached. While the sample size (five data points) is too small to draw firm conclusions, an exponential trend is evident in the data. Included in the Figures are lines of best fit, which show the strength of both components increasing exponentially as the Plane is approached. The further elucidation of these sources will be left as a challenge for researchers who continue this work.

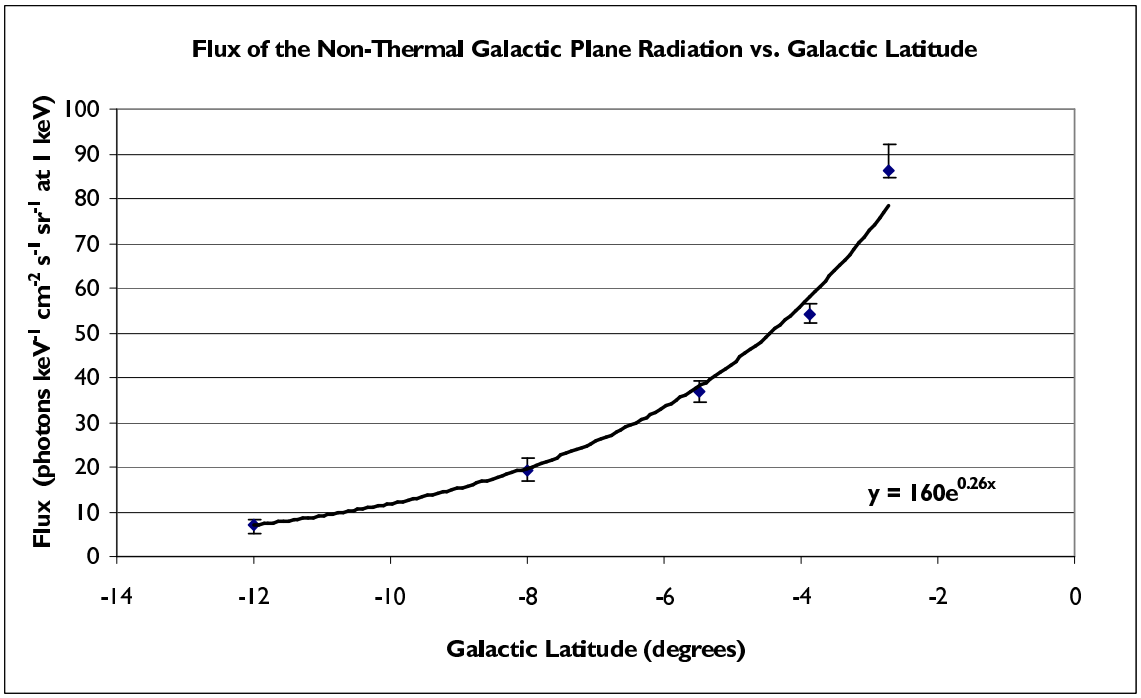

Figure 6.19: Contribution from the Non-Thermal GPR (modelled using a power-law), versus Galactic Latitude

6.12 Summary

In this chapter, a two-part model was created in order to replicate the LISM. The first part, a model of the LHB's boundary wall created by Hutchinson (1999), was based on the level of absorption acting on thousands of X-ray active stars. The second was a geometric arrangement, comprising two concentric spheres, one to define the interior volume, and the other to represent the cool outer shell. The Shell structure is new, and was proposed on the basis of the fits and arguments laid out in Chapter 4. The spheres were centred at (352°, 15°), 290 pc along the line of sight, placing the NPS 120 pc from the Sun, in agreement with distance measurements made by Bingham (1967).

The dimensions of the model were used in conjunction with the best-fit parameters (Appendix B) to determine the physical properties of the LISM, but also revealed a previously unseen interaction that occurs below the Plane between the Shell and the LHB, in which plasma from the two structures seems to mix freely together.

The cause of the indentation in the LHB was also explored. As the results show, the open-ended LHB has started to depressurize, while the Loop continues to expand. It has been deduced that the expanding Loop is pushing the Wall into the LHB, which has deformed under the stress. The density of both the Wall and LHB rise near the indentation, supporting this idea.

The properties of the Shell and interior of Loop I were found to show similar trends, rising and falling together; a fact that strongly indicates that they are indeed different aspects of one structure. The properties of the Northern NPS fields are very similar to those in the Southern B5 field, which lies at approximately the same great circle distance. There is not enough data here to say for certain, but the symmetry in the properties of these fields suggests that the two bright bulges either side of the Galactic Plane are part of one contiguous structure – Loop I – and are not two separate entities. The density and pressure of the Loop's interior also rise as the Shell is approached, as would be expected from a large SNR.

Finally, the MEKAL and the extra power law used to accommodate excess hard flux observed in the Southern fields have offered a glimpse at the Galactic Plane Radiation, and possibly, the signal from the Galactic Centre.

7

Conclusion

The objectives, stated at the beginning of this thesis, were to model the spectrum SXRB, and through this analysis, to investigate the topology, chemical composition and heating mechanisms present within the LISM. Not only has this been done, but several discoveries have been made along the way. Here, the methods and findings reported in the thesis will be summarised and put in the context of earlier research work, and suggestions for the use and further extension of this work will be proposed.

7.1 In the Beginning

The identification of the DXRB by Riccardo Giacconi in 1962 was, in many ways, ahead of its time. The announcement of its discovery triggered much interest in the astronomy community, but early attempts to research the signal further were limited by the technology available. While uncollimated photon detectors could indicate the direction to strong X-ray sources, they did not have sufficient angular resolution to pinpoint their locations, let alone produce detailed spectra. The opacity of the Earth's atmosphere was also a major problem. Extraterrestrial X-rays can be detected only above the ozone layer, which is approximately 54 km from the Earth's surface. To acquire data, detectors had to be carried on-board converted V2 rockets and activated only in a $\sim$ 30 second window of opportunity at the peak of the craft's trajectory. The limited quality and quantity of X-ray data arrested the progress in this field for several decades.

7.2 Existing Knowledge & Uncertainties

In the 1990s, X-ray focussing Wolter mirrors and collimated proportional counters were installed on the ROSAT space observatory. Using this facility, Snowden et al. (1995) produced the RASS maps, shown in Figures 2.5, 2.7, and 2.4, which gave the first visual indication of structure in Giaconni's DXRB. Their raw data was also analysed by spectroscopists, who were able to split the composite DXRB signal into several distinct components.

Most of Giaconni's original signal was attributed to the extragalactic background, the XRB. In the RASS 1.5 keV map, this appears as a hard, diffuse, non-thermal isotropic background signal, superposed with discrete point sources, now known to be distant quasars.

The softer X-ray component of the DXRB, the SXRB, was eventually recognised as the emission from the hot plasma phases of the ISM. Through modelling the SXRB spectrum, researchers were able to decompose it into a number of characteristic signals, each originating from within a separate interstellar plasma structure, and subjected to absorption by the cooler, neutral material that is the ambient medium of the Galaxy.

Of the emissive structures, the closest is the LHB, identified by Cox & Reynolds (1987). The LHB entirely surrounds the Solar System, making it visible in every direction from the Earth. Essentially, it is a hole in the local neutral material filled with a soft, thermally emissive X-ray plasma at 0.1 keV. Its irregular, double-lobed shape and apparently open ends were the cause of much speculation, and while the presence of the cavity could be explained by the displacement model (Section 2.4.4), two other theories competed to explain the source of the hot plasma. Bochkarev (1987) imagined the LHB to be an inter-arm region of the Galaxy, whereas Cox & Anderson (1982) modelled the LHB as an old SNR, which had cooled and been subsequently reheated by a more recent explosion.

The closest structure to the LHB seen when looking towards the Galactic Centre, Loop I, was first observed as a series of radio ridges by Quigley & Haslam (1965), but is now recognised to be a young, hot SNR. In the RASS maps, the Loop appears as three patches of soft emission, and although the consensus opinion holds that it is a single structure, there was little solid evidence to suggest that the bright regions were actually linked.

The close proximity of the LHB to the Loop raised the possibility that the two structures might be interacting. This scenario was mathematically modelled by Yoshioka & Ikeuchi (1990), but not directly observed. Egger & Aschenbach (1995) went further, and proposed that the Wall, a region of absorbing material positioned between the LHB and Loop 1, had been produced through the compression of the ambient ISM by the expansion of the two superbubbles.

Finally, the Galactic Halo, proposed in 1956 by Lyman Spitzer to account for the high velocity clouds observed by Münch and Zirin. The Halo was supposed to lie just beyond the HI disk of the Milky Way. In Willingale et al. (2003) it was modelled as a 0.1 keV thermal plasma, positioned not quite behind the full HI column, and reported to be visible in the Galactic Centre direction.

7.3 Data Reduction

We now have access to more sophisticated instruments, including the XMM-Newton Observatory, which is equipped with Wolter mirrors and photosensitive CCD cameras. These sharply focus the incident X-ray photons, and produce bright images in which point sources can be clearly resolved; attributes which made XMM ideal for this research project.

Twenty archived XMM observations were used in this research, each selected on the basis that all three detectors had been used in full frame mode, with either the thin or medium filter, over a long exposure time. Ten of the fields, named the 'Oxygen' fields, are spread across the sky in the Anti-centre direction. The other ten are grouped within the projected boundary of Loop 1: two in the North Polar Spur, three within the Northern Bulge, and five below the Galactic Plane, near the southern limb of the Loop.

Chapter 3 detailed how a series of scripts were developed and used to produce DXRB spectra from these fields, the co-ordinates of which are shown in Table 3.2 and plotted in Figure 3.2.

7.4 Modelling and Interpreting the Spectra

In Chapter 4, the reduced spectra were fitted with a series of different XSPEC models carefully formulated to represent both the characteristic emissions from the X-ray emissive structures present in the LISM and the absorption acting upon them. The best-fit parameters, presented in Appendix B, confirmed some established ideas, such as the ubiquity of the LHB and the XRB, and also provided new insights into the soft X-ray background.

- The LHB
  The LHB, fitted at 0.1 keV, appears to be brighter in Northern Bulge fields than in the NPS fields; a feature which may result from the compression of the LHB plasma by the encroaching Wall in this region. The LHB is also more prominent in the Anti-centre direction, where it is far more extensive.

- The Shell
  In 2003, a soft excess observed by Willingale et al. in the northern Loop I region was modelled using an absorbed APEC component fixed at 0.1 keV, and interpreted as the signal from a cool Galactic Halo. In theory, such a structure should be easily observed in the Anti-centre direction and away from the Galactic Plane, where there is less absorption and far fewer emissive structures. However, its trace was not seen in the Oxygen field spectra. An absorbed 0.1 keV signal was seen in the Loop fields, but as the Model E series of fits (Section 4.7.6) demonstrate, the high levels of emission and absorption in the Galactic Centre direction prevent the detection of a soft X-ray source lying beyond the Loop. Logically, the 0.1 keV signal had to originate in the foreground. Since the emission measure of the Loop's interior varied in the same way as this component, the two appeared to be linked; hence, the cool component was reinterpreted as the emission from a previously unidentified supershell surrounding Loop I. In the final model, this shell is still represented by an absorbed APEC at 0.1 keV, but the absorption has been made equal to the absorption acting on the Loop's interior, putting both structures at the same distance from the Earth.

- The Loop
  The emission measure of the Loop's interior was found to be $\sim$ 4 times higher in

the NPS than in the Northern Bulge fields, indicating that the plasma near the limb of the bubble is being heated, and perhaps compressed, as it impacts the outer shell. As in Willingale et al. (2003), the plasma of the interior was found to be chemically depleted in oxygen, magnesium, neon and iron.

- The XRB

  A hard component, partly discernable in all twenty spectra, was identified as the contribution from the XRB (Section 2.3.1), and in time honoured fashion, it was modelled using an absorbed power law. However, while the normalization of the XRB is known to be isotropic, the normalization of this component was seen to vary considerably across the sky (Table 4.12). It was free fitted only in the Oxygen and Northern fields, where its level was generally found to be lower than expected, while in the Southern fields, its normalisation was frozen to prevent it from being artificially enhanced by the emission found near the Plane.

  The non-uniformity of this component's contribution is difficult to explain; however, since the energy range of the spectra used in this work is only between 0.1 keV–4.0 keV, it is unlikely that total flux of the XRB has been observed in any of the fields. This may be why in so many of the fields, the level of flux from the XRB was found to be much lower than expected. However, as the Southern fields demonstrated, it is difficult to separate the contributions from hard sources. In some of the fields, the XRB contribution appeared higher than expected, and in these cases, hard contributions from particles, such as soft protons, left behind during the data reduction process may be responsible.

  Although this work can not claim to have characterised the XRB, fitting its signal, together with other rogue hard components from the particle background, served to mask its contribution. This, in turn, has made is possible to extract, fit and characterise the signal from the softer components of the SXRB.

- GPR

  Two additional components, a thermal MEKAL at 1 keV and a non-thermal power law with a photon index of 2.5, were required to fit the spectra from the Southern fields within 6° of the Galactic Plane. Both of these were set behind the full Galactic column. While the thermal source can be tentatively linked to the diffuse part of the Galactic Plane Radiation, the non-thermal source has not been identified previously in literature, but could possibly originate at the Galactic Centre. The strength of

both components was seen to rise exponentially as the Plane was approached.

- The Halo
  Finally, the emission from the Galactic Halo was detected in all ten Oxygen fields. Through fitting four variations of Model B, it was found that the Halo fits best at full Galactic absorption, ruling out the possibility that it is a local source. The Halo plasma was found to resemble that of the Loop interior, with a $0.18 - 0.32$ keV temperature range, and some chemical depletion. The similarity of the Halo plasma to that in the Loop I interior, which itself is the product of many supernovae (Egger 1998), is intriguing, and strongly supports the theory that the Halo was generated through the outflow of material from SNRs, the so-called 'fountain' hypothesis of Halo creation.

7.5 Oxygen

Chapter 5 concentrated on two of the most important emission lines present in the thermal SXRB spectrum: O VII and O VIII, which lie in the energy intervals $0.46 - 0.62$ keV and $0.62 - 0.72$ keV respectively. Not only are these lines considered tracers of plasma at 0.1 keV and 0.3 keV, but their photons also play an important role in the thermal balance of the ISM (Section 5.1).

A new technique, described in Section 5.4, was used to split the flux of the best-fit model in each field into its component parts. This allowed the apparent flux of each plasma component to be measured, and the contribution of each structure to the overall observed oxygen flux to be determined.

The results of this process revealed that the O VII flux observed in the Loop I fields comes mainly from the cool shell and the interior of the Loop, and only $\sim$10% from the LHB. In the Oxygen fields, where the flux is far lower than in the Loop I fields, most of the flux originates in the LHB, in addition to a variable contribution from the Galactic Halo.

The breakdown of the O VIII fluxes is far simpler than that of the O VII. $\sim$90% of the O VIII flux in the Loop I fields comes from the interior of Loop I, with the remainder

produced by the cool shell. It is likely that the O VIII flux in the shell is generated at its inside boundary, which is being constantly heated by the Loop's interior. By the same token, the NPS can be interpreted as a bright, recently reheated region at the interface between the shell and the interior of the Loop. In the Oxygen fields, some of the O VIII flux comes from the LHB, but most of it, $\sim$ 45%, originates in the Halo.

The method also allowed the effects of absorption to be cancelled, enabling the absolute (at source) fluxes of the structures to be calculated. The absolute flux of the LHB was found to be almost constant across all fields, although it was slightly brighter in the Oxygen fields, probably because of the greater extent of the LHB in that direction. The Halo was found to be brighter in O VII than O VIII, but patchy, and so suggestive of a young structure. Taken together with the results obtained in Chapter 4, which showed that the temperature and chemical abundances in the Halo and Loop interior are very similar, this lends strong support to the fountain hypothesis, in which the Halo is thought to have been formed by SNRs which have risen out of the Galactic Plane and burst, expelling their hot interior plasma.

Furthermore, the levels of O VII line flux are similar in the fields closest to the shell, in B4, B5 and the NPS fields, and higher than the level seen in the Northern Bulge fields at the centre of the Loop, supporting the hypothesis that a shell surrounds Loop 1.

7.6 The Third Dimension

Following the methods described in Willingale et al. (2003), the best-fit parameters were projected onto a two-part geometric model, designed to replicate the physical dimensions and orientation of the structures in the LISM. The first part of the model, a representation of the LHB's boundary wall created by Hutchinson, was left in its original form, but the second part, a sphere representing the Loop, has been considerably altered in this implementation.

The values published in Willingale et al. (2003) were calculated using a single sphere centred at (352°, 15°) with an angular radius of 42°, positioned 210 pc from the Sun. In this analysis, the model has been extended to include two concentric spheres, one with a radius of 42° (corresponding to an actual radius of 194 pc) to define the interior volume

of the Loop, and the other, of radius 46° (208 pc), to represent the cool shell, identified in Chapter 4. This was in accordance with the SNR model (Section 6.6), which specifies that the thickness of a remnant's shell should be approximately equal to one-twelfth of the radius of its interior. When superposed on an image of the central region of the Galaxy (Figure 6.7), the projected boundary of the modelled shell encloses the stray flux which had not been accommodated by the smaller, single sphere model of Willingale et al..

The sphere was also moved back along the line of sight to a distance of 290 pc from the Sun in order to prevent the intersection of the LHB and the Loop interior. This placed the NPS at 120 pc from the Sun in agreement with distance measurements made by Bingham (1967), and also had a profound effect on the geometric model, trebling the volume of the sphere to 9×10^{62} cm^3, and making the pressures and densities incomparable to those published in Willingale et al.. Additionally, with the spheres in this position, the shell overlaps and interacts with the boundary of the LHB: a previously unknown interaction.

Since both the shell and the LHB are 0.1 keV thermal plasmas, there is little to impede their interaction. In the Southern fields, the leading edge of the shell pushes into the boundary of the partially deflated LHB. The interaction seems to have compressed the material on either side of the interface, increasing the local density, pressure, and emission measures of the plasma observed in this region (Section 6.11.1).

7.7 A New Vision of the LISM

By linking the research findings and models presented in this thesis with the disparate theories cited in the literature, it has been possible to describe a coherent, consistent vision of the X-ray emissive ISM. In the Anti-centre, the observed signal can be split into contributions from the LHB, the Galactic Halo and the distant XRB, as shown in Figure 7.2. In contrast, the flux observed in the Galactic Centre direction is far more complex, derived from the series of emissive structures depicted in Figure 7.1.

While it is tempting to imagine the emissive structures as static and unchanging, the analysis shows that this is not the case: particularly in the Galactic Centre direction, where the flux from the LHB and Loop I dominate the spectrum. In this direction, it

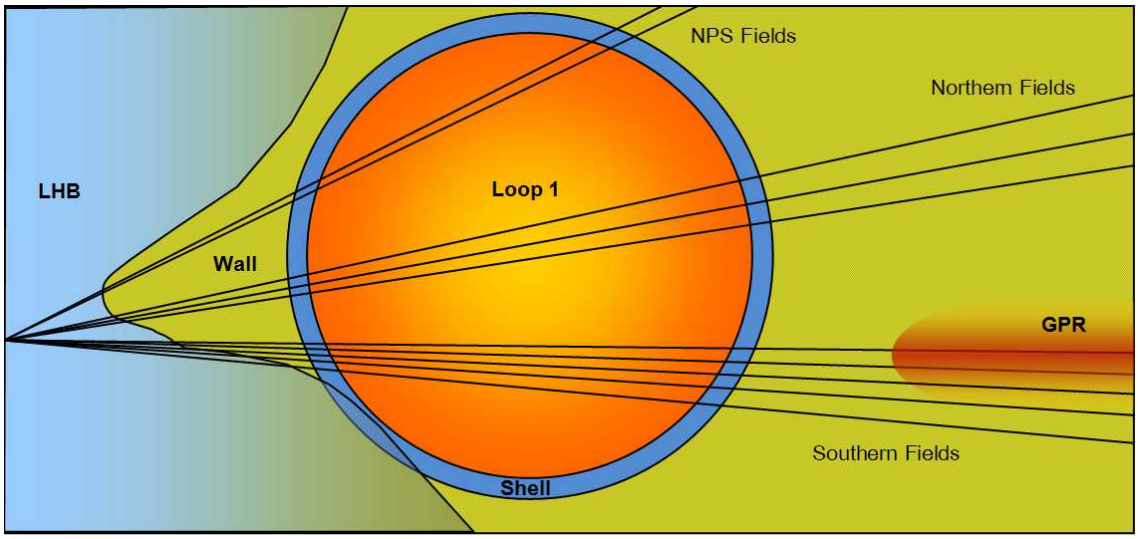

Figure 7.1: Cartoon illustrating the arrangement of the emissive structures lying along the line of sight from the Sun (on the left) towards the Galactic Centre direction. Note the intersection region, where the LHB and the shell overlap. Approximate lines of sight to the Loop I fields are also shown. (Diagram is not to scale.)

is not sufficient to study the structures in isolation: to understand the SXRB signal, one must also consider how they interact.

7.8 The Galactic Centre Direction

All lines of sight from the Earth pass through the LHB, an old irregularly-shaped SNR which envelops the Solar System. Its isotropic 0.1 keV signal covers the sky visible from the Earth, and indeed, it was detected in all twenty fields. Although it is at the ideal temperature to produce O VII, the low density plasma in the LHB generates only $\sim$10% of the O VII flux observed in the Galactic Centre direction. This value is slightly higher in the Oxygen fields, an effect attributed to the greater extent of the LHB in the Anti-centre direction.

Both the $\frac{1}{4}$ keV RASS map and the Hutchinson model suggest that the LHB is open-ended. If this is true, then the LHB could be considered to be between the second and third stages of development (Section 4.7.4). At this point in its evolution, a remnant would have

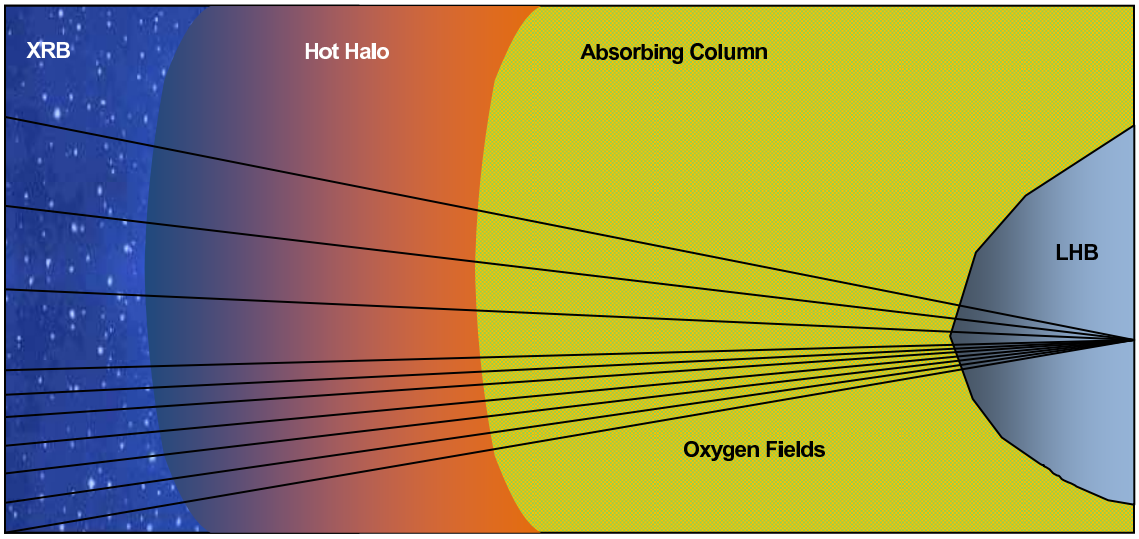

Figure 7.2: Cartoon illustrating the arrangement of the emissive structures lying along the line of sight from the Sun (on the right) towards the anti-centre. Approximate lines of sight to the Oxygen fields are also shown. (Diagram is not to scale.)

expanded out of the HI layer of the Galaxy and breached, releasing its contents into the upper layers of the ISM. This action would cause the remnant's interior to depressurize, weakening its outer boundary until, eventually, it fades into obscurity. Estimates produced using the best-fit parameters and the geometric model (Table 6.2) show that the pressure within the LHB is indeed $\sim$5.5 times lower than that of the enclosed plasma within Loop I indicating that, in the LHB, the outflow process has already begun.

Beyond the boundary of the LHB lies the Wall, a dense, cool layer of absorbing dust and neutral gas which marks the interface between the LHB and its nearest neighbour, Loop I.

Loop I is still expanding, powered by the energy input of the stellar winds from the Sco-Cen association. The outward pressure exerted by the Loop's shock fronts is transferred to the structures adjacent to it. On the near side, this compresses the Wall, and pushes it into the older, depressurised LHB. Pressure measurements in this region (Section 6.11.1) indicate that the weakened boundary of the LHB has deformed under the strain, producing the large indentation illustrated in Figure 7.1 that gives the LHB its familiar hourglass profile. Three-dimensional modelling has also indicated that the shell and LHB interact below the Galactic Plane, compressing the Wall and increasing the

density of the ISM.

Two additional components had to be used in the interaction region discovered in the Southern fields within $\sim 6^{\circ}$ of the Galactic Plane, to accommodate a source thought to be the GPR and also a non-thermal signal that may originate at the Galactic Centre. Although only five data points were obtained for each of these components, when plotted as against latitude, the strength of both appear to rise exponentially as the Plane is approached.

The hot, rarefied interior fitted best at 0.3 keV: the optimum temperature for the generation of O VIII photons. As the flux-splitting analysis showed (Section 5.4.2), $\sim$90% of the absolute O VIII flux observed in the Galactic Centre direction originates within this plasma volume. The VAPEC code used to fit the interior also revealed chemical depletion in oxygen, magnesium, neon and iron, although it is important to note that because these abundances are strongly sensitive to data quality, the best-fit values reported in Appendix B have a large margin of error. The similarity of the field parameters and the oxygen profiles measured in the NPS fields and those of the Southern B5 field, which lies at approximately the same great circle distance, has eased the long-standing debate regarding the Loop: because they are so alike, the two bright bulges either side of the Galactic Plane appear to be part of one contiguous plasma structure, and not two separate entities.

7.9 The Anti-centre Direction

The DXRB spectrum observed from the Anti-centre is far simpler than that observed in the Galactic Centre direction. As Figure 7.2 shows, the only contributors to the total flux are the LHB, the XRB and the Galactic Halo.

The signal from the hot Galactic Halo has been identified here for the first time, and has been observed only in the Oxygen fields. This is because the Halo is set behind the full Galactic column, which entirely absorbs its soft X-radiation in the Galactic Centre direction.

The plasma of the Halo was found to be remarkably similar to that within the Loop, with a $0.16 - 0.32$ keV temperature range (averaging at 0.25 keV), and some chemical depletion.

While it is the primary source of O VIII flux in the Anti-centre, the sky-coverage of the Halo is patchy, and so suggestive of a young, inhomogeneous, unsettled source which has not yet reached equilibrium. Both its likeness to the Loop and the uneven distribution of the Halo plasma are intriguing, and strongly supportive of the theory that the Halo has been generated through the outflow of material from breached SNRs, such as the LHB.

7.10 Final Thoughts and Future Prospects

To better determine the degree to which the interaction contributes to the SXRB spectra, regions inside the boundary of the Loop I, and within $\sim 6^{\circ}$ North of the Plane could be compared with the Southern fields. Such fields would lie outside the interaction region but, assuming that their effects are symmetric about the Plane, would still reside within the area of influence of the GPR and the non-thermal component. Hence, the only differences between them should be produced by the interaction.

Studies of areas within $\sim 6^{\circ}$ of the Plane and beyond the boundary of Loop I would also be useful, as these would allow the GPR and non-thermal component to be observed in relative isolation.

The Galactic Halo is also fit for future study. In this research, its signal was detected in all of the Oxygen fields, but with huge variation in the emission measure. It remains to be seen whether the GPR can be detected in the Anti-centre direction, and how the properties of the Halo vary across the sky. Such investigations will be difficult: the low background flux in the Anti-centre direction means that the derived DXRB spectra are of relatively low quality. The extent of the Halo is also unknown, hindering the calculation of its pressure and density. To continue the investigation of the Halo, it will be necessary to obtain better quality data, possibly by combining several archived XMM data sets to increase the counts present in the derived spectra.

It would also be interesting to analyse the SXRB in fields located within the shell, but beyond the interior, of Loop I. If the proposed shell truly is present then its signal should dominate over the emission from the interior plasma in these fields, and the level of O VII flux observed should greatly exceed the O VIII.

This research will be of use even where the SXRB is not itself the topic of research. Already, it has been used by Vaughan et al. (2006) to determine the distance to a dust halo produced by a gamma ray burst. The next generation of X-ray observatories will certainly be able to produce images with higher angular resolution than either XMM or Chandra. When these come online, the background signal will become even more prominent in X-ray spectra, but if the DXRB is modelled accurately using the techniques presented here, it can effectively be masked out, allowing point sources to be observed with even greater clarity.

Many results are presented in this thesis. Some, such as the properties of the 0.1 keV LHB and 0.3 keV Loop, strengthen earlier work, while others, including the discovery of a super shell around Loop 1, the identification of a hot $\sim$0.25 keV Galactic Halo, and the inferred presence of an intersection between the LHB and Loop 1, challenge existing preconceptions and mark real progress in this field. Although questions still remain unanswered, it is hoped that the work presented here will contribute towards our understanding of the evolution of SNRs, and of the X-ray background of the Milky Way.

A

List of Abbreviations

AGN Active Galactic Nuclei.
APEC Astrophysical Plasma Emission Code.
ARF Auxiliary Response File, used with XMM data.
CCD Charge Coupled Device, the imaging surface of a digital camera.
DoF Degrees of Freedom.
EPIC European Photon and Imaging Camera.
ESA The European Space Agency.
GPR Galactic Plane Radiation.
GTI Good Time Interval, the time period in which usable data is obtained.
HI Neutral atomic hydrogen.
ISM Interstellar Medium.
LHB Local Hot Bubble.
LISM The Local Interstellar Medium.
LTE Long Term Enhancement.
MOS Metal Oxide Camera, part of the EPIC.
N_H Column density of neutral atomic hydrogen.
NPS North Polar Spur.
ODF Observation Data File, containing raw data from XMM.
pn A p-n junction camera, part of the EPIC.
PSF Point Spread Function of a telescope, measured in arcseconds.

PSPC	Position Sensitive Proportional Counter, ROSAT's main x-ray detector.
Q	A programming language based on FORTRAN, created by Dr. R. Willingale.
RASS	The ROSAT All-Sky Survey.
RMF	Response Matrix File, used with XMM data.
ROSAT	The Röntgensatellit X-ray observatory.
SAS	Science Analysis Software, a suite of tools used to process XMM data.
SOC	Science Operations Centre, the organisation that oversees the operation of XMM.
SSC	Survey Science Centre, produces pipeline processed XMM data from ODFs.
SNe	Supernovae.
SNR	Supernova Remnant.
SWCX	Solar Wind Charge Exchange.
SXRB	The Soft X-ray Background (of the Milky Way).
UV	Ultraviolet electromagnetic radiation.
VAPEC	Variable Astrophysical Plasma Emission Code.
XMM	The X-ray Multiple Mirror observatory, also called XMM-Newton.
XRB	The Extragalactic X-ray Background.

B

Best-fit Parameters with Associated 90% Confidence Intervals

The model parameters are listed in the tables that follow, together with the maximum and minimum values they can hold based on a 90% confidence interval. Frozen parameter values, which do not have associated uncertainties, are indicated by a dash (—).

Key to the table headings:

LHB Norm	Normalisation of the Local Hot Bubble	APEC	cm^{-5}
Wall N_H	Neutral hydrogen column density of the Wall	WABS	atoms cm^{-2}
Loop I Norm	Normalisation of the Loop I interior	VAPEC	cm^{-5}
Loop I kT	Plasma temperature of the Loop I interior	VAPEC	keV
Abundances	Elemental abundances within Loop I	VAPEC	Relative to Solar
Shell Norm	Normalisation of the cool shell around Loop I	APEC	cm^{-5}
Halo Norm	Normalisation of the Galactic Halo	APEC	cm^{-5}
Halo kT	Plasma temperature of the Galactic Halo	APEC	keV
GPR Norm	Normalisation of the Galactic Plane Radiation	MEKAL	cm^{-5}
XRB Norm	Normalisation of the XRB Contribution	POWER	photons cm^{-2} s^{-1} keV^{-1}
EX. Powerlaw Norm	Normalisation of the extra power law fitted near the Plane	POWER	photons cm^{-2} s^{-1} keV^{-1}

Table B.1: Best-fit Parameter Values and 90% Confidence Intervals for the Northern Fields (X1, X2, X3, N4 & N5)

Field	X1	X1 min	X1 max	X2	X2 min	X2 max
LHB Norm	7.44×10^{-4}	7.09×10^{-4}	7.79×10^{-4}	6.47×10^{-4}	6.09×10^{-4}	6.83×10^{-4}
Wall N_H	1.74×10^{21}	1.69×10^{21}	1.74×10^{21}	9.85×10^{20}	9.30×10^{20}	9.85×10^{20}
Loop I Norm	1.13×10^{-2}	9.52×10^{-3}	1.31×10^{-2}	1.25×10^{-2}	1.08×10^{-2}	1.35×10^{-2}
Abundances:						
O	0.22	0.19	0.27	0.30	0.27	0.35
Ne/Mg/Fe	0.33	0.28	0.41	0.37	0.32	0.43
Shell Norm	5.17×10^{-3}	3.85×10^{-3}	6.51×10^{-3}	7.43×10^{-3}	6.08×10^{-3}	8.25×10^{-3}
XRB Norm	2.78×10^{-4}	2.44×10^{-4}	3.12×10^{-4}	2.11×10^{-4}	1.72×10^{-4}	2.38×10^{-4}

Field	X3	X3 min	X3 max	N4	N4 min	N4 max
LHB Norm	7.03×10^{-4}	6.70×10^{-4}	7.41×10^{-4}	4.37×10^{-4}	3.71×10^{-4}	4.89×10^{-4}
Wall N_H	1.22×10^{21}	1.13×10^{21}	1.22×10^{21}	7.58×10^{20}	7.14×10^{20}	7.96×10^{20}
Loop I Norm	4.31×10^{-3}	1.99×10^{-3}	4.51×10^{-3}	1.61×10^{-2}	1.58×10^{-2}	1.80×10^{-2}
Abundances:						
O	0.35	0.29	0.62	0.24	0.22	0.27
Ne/Mg/Fe	0.47	0.44	0.62	0.35	0.33	0.37
Shell Norm	1.66×10^{-3}	1.54×10^{-3}	2.97×10^{-3}	6.85×10^{-3}	5.46×10^{-3}	8.20×10^{-3}
XRB Norm	3.49×10^{-4}	3.17×10^{-4}	3.83×10^{-4}	2.88×10^{-4}	2.55×10^{-4}	3.15×10^{-4}

Field	N5	N5 min	N5 max
LHB Norm	3.66×10^{-4}	2.04×10^{-4}	5.21×10^{-4}
Wall N_H	3.22×10^{20}	2.93×10^{20}	3.53×10^{20}
Loop I Norm	9.59×10^{-3}	8.21×10^{-3}	1.09×10^{-2}
Abundances:			
O	0.35	0.31	0.42
Ne/Mg/Fe	0.36	0.31	0.43
Shell Norm	6.94×10^{-3}	5.91×10^{-3}	7.91×10^{-3}
XRB Norm	2.88×10^{-4}	1.39×10^{-4}	2.95×10^{-4}

Table B.2: Best-fit Parameter Values and 90% Confidence Intervals for the Southern Fields (B1, B2, B3, B4 & B5)

Field	B1	B1 min	B1 max	B2	B2 min	B2 max
LHB Norm	8.32×10^{-4}	7.71×10^{-4}	8.79×10^{-4}	6.43×10^{-4}	6.15×10^{-4}	6.95×10^{-4}
Wall N_H	2.01×10^{21}	1.92×10^{21}	2.10×10^{21}	9.40×10^{20}	8.94×10^{20}	9.87×10^{20}
Loop I Norm	1.08×10^{-2}	–	–	1.08×10^{-2}	–	–
Abundances:						
O	0.38	0.35	0.41	0.33	0.32	0.36
Ne/Mg/Fe	0.62	0.58	0.66	0.60	0.59	0.63
Shell Norm	5.61×10^{-3}	–	–	5.61×10^{-3}	–	–
GPR Norm	3.19×10^{-3}	2.89×10^{-3}	3.25×10^{-3}	2.24×10^{-3}	2.11×10^{-3}	2.29×10^{-3}
Ex. Power Norm	4.29×10^{-3}	4.21×10^{-3}	4.58×10^{-3}	2.71×10^{-3}	2.61×10^{-3}	2.84×10^{-3}
XRB Norm	2.83×10^{-4}	–	–	2.83×10^{-4}	–	–

Field	B3	B3 min	B3 max	B4	B4 min	B4 max
LHB Norm	5.56×10^{-4}	5.37×10^{-4}	6.62×10^{-4}	7.35×10^{-4}	6.52×10^{-4}	8.16×10^{-4}
Wall N_H	1.15×10^{21}	1.08×10^{21}	1.23×10^{21}	9.92×10^{20}	9.21×10^{20}	1.06×10^{21}
Loop I Norm	1.08×10^{-2}	–	–	1.08×10^{-2}	–	–
Abundances:						
O	0.28	0.26	0.31	0.28	0.25	0.31
Ne/Mg/Fe	0.41	0.39	0.43	0.38	0.36	0.40
Shell Norm	5.61×10^{-3}	–	–	5.61×10^{-3}	–	–
GPR Norm	5.95×10^{-4}	4.74×10^{-4}	7.09×10^{-4}	1.08×10^{-4}	7.58×10^{-5}	2.83×10^{-4}
Ex. Power Norm	1.83×10^{-3}	1.71×10^{-3}	1.95×10^{-3}	9.59×10^{-4}	8.31×10^{-4}	1.08×10^{-3}
XRB Norm	2.83×10^{-4}	–	–	2.83×10^{-4}	–	–

Field	B5	B5 min	B5 max
LHB Norm	3.07×10^{-4}	6.61×10^{-5}	4.28×10^{-4}
Wall N_H	3.69×10^{20}	3.41×10^{20}	3.93×10^{20}
Loop I Norm	1.08×10^{-2}	–	–
Abundances:			
O	0.37	0.34	0.38
Ne/Mg/Fe	0.34	0.33	0.36
Shell Norm	5.61×10^{-3}	–	–
GPR Norm	6.08×10^{-5}	0.00	1.63×10^{-4}
Ex. Power Norm	3.60×10^{-4}	2.59×10^{-4}	4.20×10^{-4}
XRB Norm	2.83×10^{-4}	–	–

Table B.3: Best-fit Parameter Values and 90% Confidence Intervals for the Oxygen Fields

Field	O1	O1 min	O1 max	O2	O2 min	O2 max
LHB Norm	5.08×10^{-4}	3.51×10^{-4}	5.13×10^{-4}	1.03×10^{-3}	1.29×10^{-3}	1.31×10^{-3}
Halo Norm	2.70×10^{-3}	2.30×10^{-3}	3.95×10^{-3}	6.43×10^{-4}	6.43×10^{-4}	6.51×10^{-4}
Halo kT	0.22	0.18	0.23	0.27	0.26	0.28
XRB Norm	3.15×10^{-4}	2.97×10^{-4}	3.49×10^{-4}	3.63×10^{-4}	3.63×10^{-4}	3.77×10^{-4}

Field	O3	O3 min	O3 max	O4	O4 min	O4 max
LHB Norm	1.64×10^{-3}	1.60×10^{-3}	1.69×10^{-3}	8.49×10^{-4}	8.14×10^{-4}	8.84×10^{-4}
Halo Norm	3.04×10^{-3}	3.04×10^{-3}	3.58×10^{-3}	1.80×10^{-3}	1.34×10^{-3}	2.30×10^{-3}
Halo kT	0.21	0.15	0.22	0.31	0.28	0.36
XRB Norm	1.51×10^{-4}	1.08×10^{-4}	1.51×10^{-4}	2.36×10^{-4}	1.87×10^{-4}	2.86×10^{-4}

Field	O5	O5 min	O5 max	O6	O6 min	O6 max
LHB Norm	1.31×10^{-3}	1.27×10^{-3}	1.35×10^{-3}	1.04×10^{-3}	9.99×10^{-4}	1.07×10^{-3}
Halo Norm	2.01×10^{-4}	9.58×10^{-5}	3.07×10^{-4}	4.38×10^{-4}	4.37×10^{-4}	4.46×10^{-4}
Halo kT	0.28	0.23	0.36	0.23	0.22	0.24
XRB Norm	6.75×10^{-4}	6.20×10^{-4}	7.28×10^{-4}	4.00×10^{-4}	4.00×10^{-4}	4.13×10^{-4}

Field	O7	O7 min	O7 max	O8	O8 min	O8 max
LHB Norm	1.48×10^{-3}	1.46×10^{-3}	1.51×10^{-3}	9.03×10^{-4}	8.74×10^{-4}	9.09×10^{-4}
Halo Norm	3.94×10^{-4}	3.93×10^{-4}	4.01×10^{-4}	1.20×10^{-3}	1.11×10^{-3}	1.18×10^{-3}
Halo kT	0.27	0.26	0.28	0.25	0.20	0.32
XRB Norm	2.64×10^{-4}	2.63×10^{-4}	2.73×10^{-4}	4.79×10^{-4}	4.78×10^{-4}	4.79×10^{-4}

Field	O9	O9 min	O9 max	O10	O10 min	O10 max
LHB Norm	8.60×10^{-4}	8.45×10^{-4}	8.93×10^{-4}	7.49×10^{-4}	7.33×10^{-4}	7.57×10^{-4}
Halo Norm	3.39×10^{-3}	3.39×10^{-3}	3.59×10^{-3}	9.07×10^{-3}	9.07×10^{-3}	1.08×10^{-2}
Halo kT	0.25	0.24	0.26	0.25	0.23	0.26
XRB Norm	2.52×10^{-4}	2.52×10^{-4}	2.59×10^{-4}	2.63×10^{-4}	2.63×10^{-4}	2.82×10^{-4}

C

Calculating the Plasma Emission Measure

C.1 Thermal Models

The best-fit model parameters directly describe the model, not the actual emissive plasma. However, through simple calculations, the fitted parameters can be used to derive real physical properties. One of these, the emission measure of a plasma, is defined as the product of the electron number density n_e and the proton density n_H integrated across the emissive volume, with units cm^{-3}.

The normalisation (N) of the thermal APEC, VAPEC, and MEKAL models is quoted by K. Arnaud (2007) as:

$$N = \frac{10^{-14}}{4\pi[D(1+z)]^2} \int n_e n_H \, dV$$

where D is the angular diameter distance to the source (cm), n_e and n_H are the electron and H densities (cm^{-3}), z is the redshift of the source, and dV is an element of volume of the emissive plasma.

Since most of the signal from the X-ray background originates within the Milky Way, the redshift was set to zero when fitting the data.

Observations of the SXRB concern several structures along the line of sight, and so it is helpful to consider the emissive volume dV as a column of emission, with length dl (in cm) and cross-sectional area $D^2\Omega$, where Ω is measured in steradians, as shown in Figure C.1.

One square arcminute is equal to: $(1')^2 = \left(\frac{1}{60} \times \frac{2\pi}{360}\right)^2$, or 8.46×10^{-8} steradians.

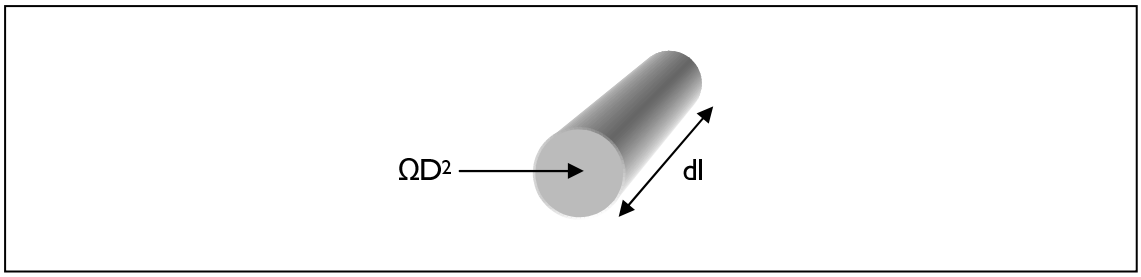

Figure C.1: An Emissive Column of Plasma

The field of view (FOV) is usually given in arcminutes, so substituting for dV in the normalisation and converting Ω to arcminutes produces:

$$N = \frac{10^{-14} \times 8.46 \times 10^{-8}}{4\pi[D(1+z)]^2} \int n_e n_H \, dl \; \Omega \; D^2$$

The emission measure is usually given with dl in parsecs, where 1 parsec = 3.086×10^{18} cm. Hence the normalisation equation can be rewritten as:

$$N = \frac{10^{-14} \times 8.5 \times 10^{-8} \times 3.086 \times 10^{18}}{4\pi} \times \left(\frac{EM}{D^2}\right) \times \text{FOV} = 2.09 \times 10^{-4} \times \left(\frac{EM}{D^2}\right) \times \text{FOV}$$

Where $\left(\frac{EM}{D^2}\right) = \int n_e n_H \, dl \; cm^{-6}$ pc

By rearranging this equation, the emission measures of the interstellar thermal structures can be calculated:

$$\left(\frac{EM}{D^2}\right) = \frac{\text{Best-fit Normalisation}}{2.09 \times 10^{-4} \times \text{FOV}}.$$

The actual field of view (FOV) used in the calculations is equivalent to the average usable area of the MOS detectors, a value determined during the data reduction process immediately following the removal of point sources from the data. The MOS detector was chosen in preference to the pn because, unlike pn, MOS data was available for all of the observations. To maintain consistency during both fitting and analysis, the pn data was scaled relative to the MOS data.

Table C.1: Fixed-Flux Normalisation Values used for the XRB in the A-Series

Field	FOV (Ω) arcmins^2	XRB Normalisation photons keV^{-1} cm^{-2} s^{-1}
O1	561.8	4.29×10^{-4}
O2	571.6	4.36×10^{-4}
O3	594.7	4.54×10^{-4}
O4	609.5	4.65×10^{-4}
O5	601.4	4.59×10^{-4}
O6	562.5	4.29×10^{-4}
O7	547.2	4.18×10^{-4}
O8	591.6	4.51×10^{-4}
O9	536.1	4.09×10^{-4}
O10	570.5	4.35×10^{-4}

C.2 Non-Thermal Models

The power law used to fit the XRB is the only non-thermal code to appear in the final models. It has the form:

$A(E) = kE^{-\alpha}$

where A(E) is the flux of the model at a given photon energy E, k is the model normalisation, and α is the photon index.

Hands (2003) fitted his models using a power law normalisation equivalent to a constant flux of 9 photons keV^{-1} cm^{-2} s^{-1} sr^{-1} at 1 keV, from a measurement made by Lumb et al. (2002).

This same flux value was used in the A-series of fits. Appropriate normalisation values (show in Table C.1) for each field were calculated using the following equation:

$k = 9 \times \text{FOV}.$

D

Geometry of the Loop I Model

Before the properties of the LISM could be derived from the best-fit parameter values, the physical dimensions of the LHB and the Loop had to be defined. The Hutchinson (1999) model was used to calculate the extent of the LHB, but to determine the distances along the line of sight from the Earth to the boundaries of the shell and interior of Loop I, an additional model was required.

To this end, a simple geometric model was created comprising two concentric spheres, positioned 290 pc from the Earth, and centred at (352°, 15°). The first sphere has an angular radius of 42°, which encloses most of the soft X-ray emission from the Loop's hot interior. The second sphere, with an angular radius of 46°, models the outer boundary of the proposed cool shell.

To calculate the distance to the front face (dlo) and far side (dhi) of each sphere, the following method was employed, using the arrangement shown in Figure D.1.

For the triangle shown in Figure D.2, the cosine rule is formulated as:
$a^2 = b^2 + c^2 - 2bc \cos A$

Substituting for the dimensions of triangle ECP (Figure D.1), where r is the radius of the sphere (in parsecs) and ϕ is the angle between the lines EC and EP, produces two equations:

$r^2 = d^2 + dlo^2 - 2d\ dlo \cos \phi$ (1)
$r^2 = d^2 + dhi^2 - 2d\ dhi \cos \phi$ (2)

The distances dlo and dhi are the roots of these quadratics.

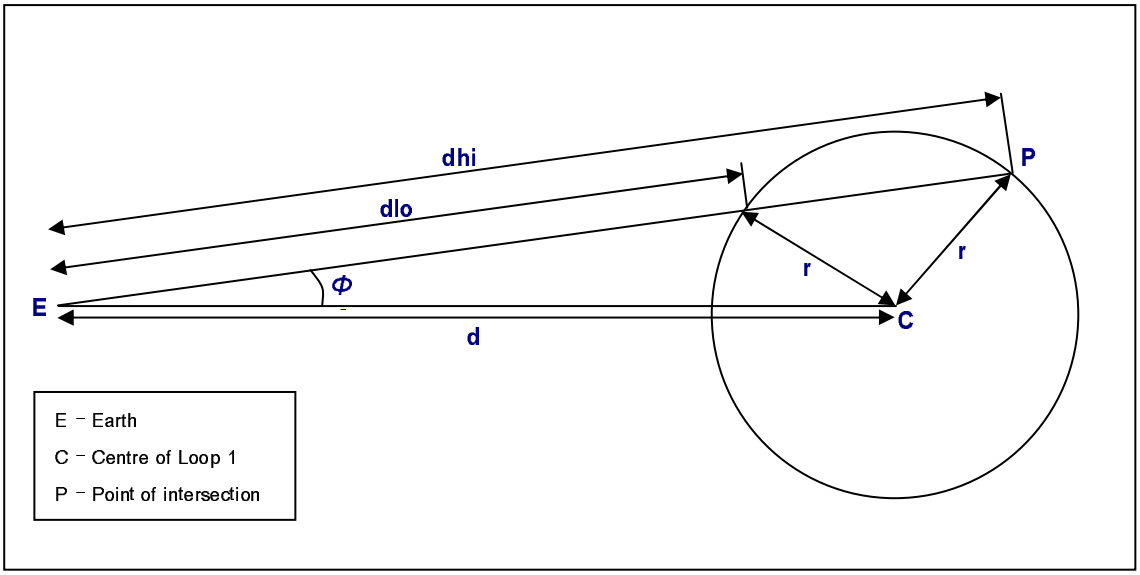

Figure D.1: The geometric arrangement used to measure dlo and dhi for the two spheres that model Loop 1.

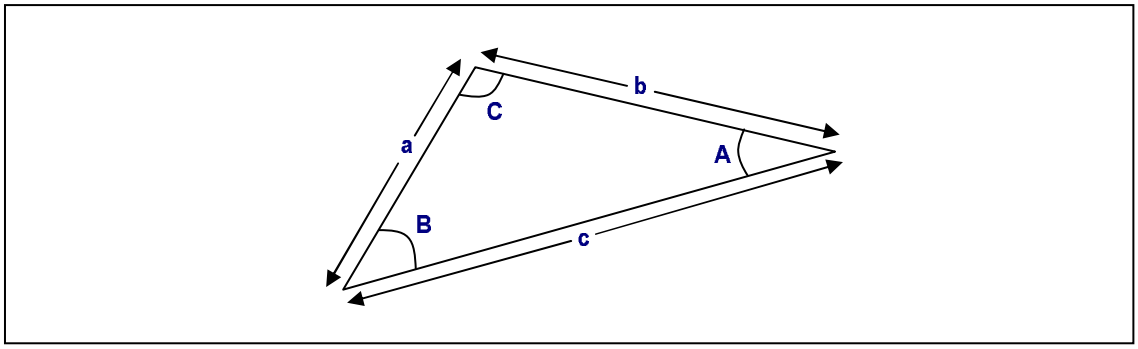

Figure D.2: A triangle, with labelled angles and sides.

To obtain cos ϕ the Galactic (polar) co-ordinates of each observation must be converted into Cartesian co-ordinates to produce a unit vector, designated the 'field vector' F. The unit vector pointing along the line EC, toward the centre of Loop I, is also formulated, this being the 'bubble vector', G.

Then: $\cos\phi = \frac{F \cdot G}{|F| \cdot |G|} = F_x \cdot G_x + F_y \cdot G_y + F_z \cdot G_z$

Now, equation (1) can be solved using the known values for r and d.

The dimensions found using this method were employed to determine the physical properties of the plasma contained within the LHB and Wall, and the shell and interior of Loop I. The calculated values of dw, dlo, and dhi are presented in Table 6.1.

E

Calculating the Properties of the LISM

First, the volumes of the Loop's interior and its shell were calculated, using the assumption that both structures are perfectly spherical. The following equations were then used with these values, the distances in Table 6.1, and the best-fit parameters presented in Appendix B to calculate the physical properties of the structures in the LISM.

E.1 Electron Density

The emission measure EM of a homogeneous plasma, with electron density n_e and emitting volume V is given by:

$$EM = \int n_e^2 \, dV$$

The cross-sectional area of the emitting volume, the field of view of the observation in square arcminutes, is accounted for when calculating the emission measure of the plasma from the normalisation of the fitted plasma codes, so only the length of emitting volume L needs to be included at this stage:

$$\left(\frac{EM}{D^2}\right) = n_e^2 L$$

$$n_e^2 = \frac{\left(\frac{EM}{D^2}\right)}{L}$$

$$n_e = \sqrt{\frac{\left(\frac{EM}{D^2}\right)}{L}}$$

which is the electron density of the plasma in cm^{-3}.

For partially ionised plasma, such as the ISM, the electron density must be weighted. To do this, a factor of 1.21 (Willingale et al. 2003) was included in the formula to calculate the electron density of each structure:

$$n_e = \sqrt{\frac{\left(\frac{EM}{D^2}\right) \times 1.21}{L}}.$$

E.2 Plasma Pressure

Assuming that the ISM is a perfect gas in thermal equilibrium, we can use the Ideal Gas Equation:

$$PV = nkT$$

where P is the pressure and V the volume of a gas containing n atoms at temperature T, and k is Boltzmann's constant.

The electron number density is equal to the number of atoms in the plasma divided by the emitting volume, as follows:

$$n_e = \frac{n}{V}.$$

Rearranging the ideal gas equation and substituting for n_e yields:

$$P = n_e kT$$

and dividing by k converts the temperature to energy, allowing the pressure to be calculated as:

$$\frac{P}{k} = n_e T.$$

Like the electron density calculation above, this must be weighted to account for the ionic composition of the ISM. This is achieved by including the ionisation ratio $n_e = 1.21 n_i$:

$$\frac{n_i + n_A}{n_i} = 1 + \frac{1}{1.21}.$$

Thus the total pressure can be calculated for each structure using the formula:

$$\frac{P}{k} = n_e T \left(1 + \frac{1}{1.21}\right).$$

E.3 Energy of the Loop I Plasma

Finally, the energy E of the Loop interior and shell were calculated. This was done by multiplying the kinetic energy of each particle by the number of particles in each structure, calculated by multiplying the electron density n_e and by volume of the structure.

From kinetic theory, the average translational kinetic energy of a gas molecule at temperature T is given by:

$$\text{Individual } E = \frac{3}{2}kT.$$

Multiplying this by the electron density and the emitting volume, both calculated above, gives the formula used to calculate the total energy in the Loop's plasma:

$$\text{Total } E = \frac{3}{2}kTn_eV.$$

Bibliography

Anders, E. & Ebihara, M. (1982), 'Solar-System Abundances of the Elements', *Geochim. Cosmochim. Acta* **46**, 2363–2380.

Anders, E. & Grevesse, N. (1989), 'Abundances of the Elements—Meteoritic and Solar', *Geochim. Cosmochim. Acta* **53**, 197–214.

Angelini, L. (2007), *Calculate the Total Galactic HI Column Density*, HEASARC.
URL: *http://heasarc.gsfc.nasa.gov/cgi-bin/Tools/w3nh/w3nh.pl*

Anonymous (January 5th, 1896*a*), *Die Presse, Vienna* .

Anonymous (January 7th, 1896*b*), *London Standard* .

Anonymous (March 3rd, 1896*c*), *Science* **3**, 436.

Arnaud, K. A. (1996), Astronomical Data Analysis Software and Systems V, *in* 'ASP Conference Series', Vol. 101, p. 17.

Aschenbach, B. et al. (1985), 'ROSAT PSPC—Scientific Data Processing Requirement Document', *MPE Internal Report 44* .

Barcons, X. & Fabian, A. (2002), *The X-Ray Background*, first edn, Cambridge University Press.

Behr, A. (1959), 'The Interstellar Polarisation of Star Light in the Neighborhood of the Sun', *Veroeffentlichungen der Universitaets-Sternwarte zu Goettingen* **7**, 200.1–200.2.

Bellm, E. C. & Vaillancourt, J. E. (2005), 'Origins of the $\frac{1}{4}$ keV Soft X-ray Background', *ApJ* **622**, 959–964.

Berghöfer, T. W. & Breitschwerdt, D. (2002), 'The Origin of the Young Stellar Population in the Solar Neighborhood – A Link to the Formation of the Local Bubble?', *A&A* **390**, 299–306.

Berkhuijsen, E. M., Haslam, C. G. T. & Salter, C. J. (1971), 'Are the Galactic Loops Supernova Remnants?', *A&A* **14**, 252–262.

Bertiau, F. C. (1958), 'Absolute Magnitudes of Stars in the Scorpio-Centaurus Association', *ApJ* **128**, 533.

Bignami, G. F. & Caraveo, P. A. (1992), 'Geminga—New Period Old Gamma-Rays', *Nature* **357**, 287.

Bingham, R. G. (1967), 'Magnetic Fields in the Galactic Spurs', *MNRAS* **137**, 157.

Blaauw, A. (1961), 'On the Origin of the O- and B-type Stars with High Velocities, and some Related Problems', *Bull. Astron. Inst. Netherlands* **15**, 265.

Bochkarev, N. G. (1987), 'Local Interstellar Medium', *Astrophys. Space. Sci.* **138**, 229–302.

Bowyer, C. S., Field, G. B. & Mack, J. E. (1968), 'Detection of an Anisotropic Soft X-ray Background Flux', *Nature* **217**, 32.

Bregman, J. N. (1982), 'A Corona Around the Milky Way', *Nature* **298**, 10.

Bregman, J. N. & Houck, J. C. (1997), 'The Hot Gas Surrounding the Edge-on Galaxy NGC 891', *ApJ* **485**, 159.

Briel, U. G. et al. (1996), 'ROSAT Users Handbook'.
URL: *http://heasarc.gsfc.nasa.gov/docs/rosat/ruh/handbook/handbook.html*

Brown, R. H., Davies, R. D. & Hazard, C. (1960), 'A Curious Feature of the Radio Sky', *Observatory* **80**, 191–198.

Bunner, A. N. et al. (1969), 'Soft X-ray Background Flux', *Nature* **223**, 1222.

Bunner, A. N. et al. (1972), 'Soft X-rays from the Vicinity of the North Polar Spur', *ApJ* **172**, L67.

Burke, B. F. & Graham-Smith, F. (2002), *An Introduction to Radio Astronomy*, second edn, Cambridge University Press.

Burrows, D. N. (1989), 'Observational Constraints on an Embedded Cloud Model for the Soft X-ray Diffuse Background', *ApJ* **340**, 775–785.

Burrows, D. N. & Mendenhall, J. A. (1991), 'Soft X-ray Shadowing by the Draco Cloud', *Nature* **351**, 629–631.

Burrows, D. N. et al. (1991), The CUBIC Experiment, *in* 'The X-ray Background: Proceedings of the International Workshop in Laredo, Spain', pp. 277–281.

Burstein, P. et al. (1977), 'Three-band Observations of the Soft X-ray Background and Some Implications of Thermal Emission Models', *ApJ* **213**, 405–407.

Burton, W. B. (1988), *Galactic and Extragalactic Radio Astronomy*, Springer-Verlag (New York), pp. 295–358.

Caillault, J. P. et al. (1986), 'X-ray Selected M Dwarfs and the Diffuse X-ray Background', *ApJ* **304**, 318–325.

Caraveo, P. A. et al. (1996), 'Parallax Observations with the Hubble Space Telescope Yield the Distance to Geminga', *ApJ* **461**, L91.

Centurion, M. & Vladilo, G. (1991), 'The Local Interstellar Medium Toward the Center of Loop I', *ApJ* **372**, 494–504.

Chen, L. W. et al. (1997), 'ASCA and ROSAT Observations of the QSF3 Field: the X-ray Background in the 0.1-7 keV Band', *MNRAS* **285**, 449–471.

Cox, D. P. (1997), Modelling the Local Bubble, *in* 'The Local Bubble and Beyond, Proceedings of the IAU Colloquium No. 166', pp. 121–131.

Cox, D. P. (1998), *The Local Bubble and Beyond*, Berlin Springer.

Cox, D. P. & Anderson, P. R. (1982), 'Extended Adiabatic Blast Waves and a Model of the Soft X-ray Background', *ApJ* **253**, 268–289.

Cox, D. P. & Reynolds, R. J. (1987), 'The Local Interstellar Medium', *ARA&A* **25**, 303–344.

Cox, D. P. & Smith, B. W. (1974), 'Large-scale Effects of Supernova Remnants on the Galaxy: Generation and Maintenance of a Hot Network of Tunnels', *ApJL* **189**, L105–L108.

Cravens, T. E. (2000), 'Heliospheric X-ray Emission Associated with Charge Transfer of the Solar Wind with Interstellar Neutrals', *ApJL* **532**, L153–L156.

Dahlem, M. et al. (1999), *XMM Users' Handbook*, XMM SOC Team.
URL: *http://www.mssl.ucl.ac.uk/www_xmm/ukos/onlines/uhb/xmm_uhb.html*

Davidsen, A. et al. (1972), 'Observations of the Soft X-ray Background', *ApJ* **177**, 629–642.

de Geus, E. J. et al. (1989), 'Physical Parameters of Stars in the Scorpio-Centaurus OB Association', *A&A* **216**, 44–61.

Dickey, J. M. & Lockman, F. J. (1990), 'HI in the Galaxy', *ARA&A* **28**, 215–261.

Dickey, J. M. et al. (1977), 'Temperature Distribution of Neutral Hydrogen at High Galactic Latitudes', *ApJL* **211**, L77.

Ebisawa, K. et al. (2003), 'X-ray Emission from the Galactic Plane', *Chin. J. Astron. Astrophys.* **Suppl.**, 281–286.

Egger, R. J. (1998), Interaction of the Local Bubble with its Environment, *in* 'The Local Bubble and Beyond, Proceedings of the IAU Colloquium No. 166', p. 287.

Egger, R. J. & Aschenbach, B. (1995), 'Interaction of the Loop I Supershell with the Local Hot Bubble', *A&A* **294**, L25–L28.

Ehle, M. et al. (2003), *XMM-Newton Users' Handbook*, ESA.
URL: *http://xmm.esac.esa.int/external/xmm_user_support/documentation/uhb_2.1/*

Ewen, H. I. & Purcell, E. M. (1951), 'Observation of a Line in the Galactic Radio Spectrum', *Nature* **168**, 356–358.

Fireman, E. L. (1974), 'Interstellar Absorption of X-rays', *ApJ* **187**, 57–60.

Friedman, H., Lichtman, S. W. & Byram, E. T. (1951), 'Photon Counter Measurements of Solar X-rays and Extreme Ultraviolet Light', *Phys. Rev.* **83**, 1025–1030.

Frisch, P. C. (1996), 'LISM Structure–Fragmented Superbubble Shell?', *Space Sci. Rev.* **78**, 213–222.

Frisch, P. C. & York, D. G. (1983), 'Synthesis Maps of Ultraviolet Observations of Neutral Interstellar Gas', *ApJ* **271**, L59.

Fujimoto, R. et al. (2007), 'Evidence for Solar-Wind Charge-Exchange X-ray Emission from the Earth's Magnetosheath', *Publ. Astron. Soc. Jpn.* **59**, 133–140.

Garmire, G. & Nousek, J. A. (1980), 'A New Component of Diffuse X-ray Emission', *BAAS* **12**, 853.

Garmire, G. P. & Nugent, J. J. (1981), 'Possible Detection of a Galactic Wind', *BAAS* **13**, 786.

Garmire, G. P. et al. (1992), 'The Soft X-ray Diffuse Background Observed with the HEAO 1 Low-Energy Detectors', *ApJ* **399**, 694–703.

Gehrels, N. & Chen, W. (1993), 'The Geminga Supernova as a Possible Cause of the Local Interstellar Bubble', *Nature* **361**, 706–707.

Giacconi, R., Gursky, H., Paolini, F. R. & Rossi, B. B. (1962), 'Evidence for X-ray Sources outside the Solar System', *Phys. Rev. Lett.* **9**, 439–443.

Giacconi, R., Gursky, H., Waters, J. R., Clark, G. & Rossi, B. B. (1964), 'Two Sources of Cosmic X-rays in Scorpius and Sagittarius', *Nature* **204**, 981–982.

Giacconi, R. et al. (1971), 'Uhuru Mission Overview', *ApJ* **165**, L27.

Gleason, K. L. (2006), 'Stratospheric Ozone: Monitoring and Research in NOAA'. **URL:** *http://www.ozonelayer.noaa.gov/science/basics.htm*

Griesen, E. W. (1973), 'Aperture Synthesis of Interstellar Neutral Hydrogen in Absorption. I. The Perseus Arm Feature of Cassiopeia a', *ApJ* **184**, 363.

Hands, A. D. P. (2003), Diffuse and Discrete Sources of Galactic X-ray Emission, PhD thesis, The University of Leicester.

Hayakawa, S. (1973), X- and Gamma- Ray Astronomy, *in* 'Proceedings of the IAU Symposium No. 55', pp. 235–249.

Hayakawa, S. et al. (1977), 'X-ray Features of the North Polar Spur', *ApJL* **213**, L109.

Helfand, D. J. & Caillault, J. P. (1982), 'An Unbiased Survey of Field Star X-ray Emission', *ApJ* **253**, 760–767.

Henry, R. C. et al. (1968), 'Possible Detection of a Dense Intergalactic Plasma', *ApJL* **153**, L11–L18.

Hickox, R. C. & Markevitch, M. (2006), 'Absolute Measurement of the Unresolved Cosmic X-Ray Background in the 0.5-8 keV Band with Chandra', *ApJ* **645**, 95–114.

Hutchinson, I. B. (1999), An Investigation of the Diffuse Gas in the Interstellar Medium, PhD thesis, The University of Leicester.

Inoue, H. et al. (1979), 'Evidence of O Vii Emission Line in Diffuse Soft X-rays from the nH Minimum Region in Hercules', *ApJL* **227**, L85–L88.

Jakobsen, P. & Kahn, S. M. (1986), 'On the Interpretation of the Soft X-ray Background—The Effects of an Embedded Cloud Geometry', *ApJ* **309**, 682–693.

Jansky, K. (1933), 'Radio Waves from Outside the Solar System', *Nature* **132**, 66.

K. Arnaud, B. Dorman, C. G. (2007), *The Xspec Manual*, HEASARC.
URL: *http://heasarc.gsfc.nasa.gov/docs/xanadu/xspec/manual/manual.html*

Knie, K. et al. (1999), 'Indication for Supernova Produced ^{60}Fe Activity on Earth', *Phys. Rev. Lett.* **83**, 1.

Koutroumpa, D., Lallement, R., Kharchenko, V. & Dalgarno, A. (2009), 'The Solar Wind Charge-eXchange Contribution to the Local Soft X-ray Background', *Space Sci. Rev.* **143**, 217–230.

Krasnopolsky, V. A., Greenwood, J. B. & Stancil, P. C. (2004), 'X-ray and Extreme Ultraviolet Emissions from Comets', *Space Sci. Rev.* **113**, 3–4.

Kraushaar, W. L. (2000), *X-ray Astronomy*, Oxford: Pergamon, pp. 293–308.

Kuntz, K. D. & Snowden, S. L. (2000), 'Deconstructing the Spectrum of the Diffuse X-ray Background', *ApJ* **543**, 195–215.

Kuntz, K. D. & Snowden, S. L. (2008), 'The X-ray Components Towards l=111 Degrees: The Local Hot Bubble and Beyond', *ApJ* **674**, 209–219.

Kuntz, K. D. et al. (2000), 'X-ray Constraints on the Warm-Hot Intergalactic Medium', *ApJ* **548**, L119–L122.

Lallement, R. et al. (2004), 'The Heliospheric Soft X-ray Emission Pattern during the ROSAT Survey: Inferences on Local Bubble Hot Gas', *A&A* **418**, 143–150.

Large, M. I., Quigley, M. J. S. & Haslam, C. G. T. (1966), 'A Radio Study of the North Polar Spur II, A Survey at Low Declinations', *MNRAS* **131**, 335.

Levine, A. et al. (1977), 'Ultrasoft X-rays from the Southern Galactic Hemisphere', *ApJ* **211**, 215–222.

Liedahl, D. A., Osterheld, A. L. & Goldstein, W. H. (1995), 'New Calculations of Fe L-shell X-ray Spectra in High-Temperature Plasmas', *ApJL* **438**, L115–L118.

Lisse, C. M. et al. (1996), 'Discovery of X-ray and Extreme Ultraviolet Emission from Comet C/Hyakutake 1996 B2', *Science* **274**, 205–209.

Lockman, F. J. et al. (1986), 'The Structure of Galactic HI in Directions of Low Total Column Density', *ApJ* **302**, 432–49.

Long, K. S. et al. (1976), 'Soft X-rays from the Large Magellanic Cloud—Implications on the Origin of the Diffuse X-ray Background', *ApJ* **206**, 411–417.

Luca, A. D. & Molendi, S. (2004), 'The 2-8 keV Cosmic X-Ray Background Spectrum Observed with XMM-Newton', *A&A* **419**, 837–848.

Lumb, D. (2002), *The Epic Background Files XMM-SOC-CAL-TN-0016: Issue 2.0*, ESA.
URL: *xmm.esac.esa.int/docs/documents/CAL-TN-0016-2-0.ps.gz*

Lumb, D. H., Warwick, R. S., Page, M. & Luca, A. D. (2002), 'X-Ray Background Measurements with XMM-Newton EPIC', *A&A* **389**, 93–105.

Lumb, D. et al. (2002), 'X-ray Background Measurements with XMM-Newton EPIC', *A&A* **389**, 93–105.

Marshall, F. J. (1981), 'Map of the Soft X-ray Sky from SAS-3 Observations', *BAAS* **13**, 788.

Marshall, F. J. & Clark, G. W. (1984), 'SAS 3 Survey of the Soft X-ray Background', *ApJ* **287**, 633–652.

Mathewson, D. S. (1966), 'Magnetic Fields in the Local Spiral Arm', *ApJ* **153**, L47.

McCammon, D. & Sanders, W. T. (1990), 'The Soft X-ray Background and its Origins', *ARA&A* **28**, 657–688.

McCammon, D. et al. (1976), 'Neutral Hydrogen in the Direction of the Small Magellanic Cloud and the Limits of an Extragalactic Soft X-ray Flux', *ApJ* **209**, 46.

McCammon, D. et al. (1983), 'The Soft X-ray Diffuse Background', *ApJ* **269**, 107–135.

McCray, R. & Kafatos, M. (1987), 'Supershells and Propagating Star Formation', *ApJ* **317**, 190–196.

McKee, C. F. & Ostriker, J. P. (1977), 'A Theory of the Interstellar Medium – Three Components Regulated by Supernova Explosions in an Inhomogeneous Substrate', *ApJ* **218**, 148.

Mewe, R., Gronenschild, E. H. B. M. & van den Oord, G. H. J. (1985), 'Calculated X-radiation from Optically Thin Plasmas. V', *A&AS* **62**, 197–254.

Mewe, R., Lemen, J. R. & van den Oord, G. H. J. (1986), 'Calculated X-radiation from Optically Thin Plasmas. VI', *A&AS* **65**, 511–536.

Miyaji, T. et al. (1998), 'The Cosmic X-ray Background Spectrum Observed with ROSAT and ASCA', *A&A* **334**, L13–L16.

Morrison, R. & McCammon, D. (1983), 'Interstellar Photoelectric Absorption Cross Sections, 0.03-10 keV', *ApJ* **270**, 119–122.

Münch, G. & Zirin, H. (1961), 'Interstellar Matter at Large Distances from the Galactic Plane', *ApJ* **133**, 11.

Norman, C. A. & Ikeuchi, S. (1989), 'The Disk-Halo Interaction—Superbubbles and the Structure of the Interstellar Medium', *ApJ* **345**, 372–383.

Nousek, J. A. et al. (1981), 'The Gemini-Monoceros X-ray Enhancement—A Giant X-ray Ring', *ApJ* **248**, 152–160.

Penzias, A. A. & Wilson, R. W. (1965), 'A Measurement of Excess Antenna Temperature at 4080 Mc per s', *ApJ* **142**, 419–421.

Pfeffermann, E. et al. (1987), 'The Focal Plane Instrumentation of the ROSAT Telescope', *Proceedings of the International Society for Optical Engineering* **733**, 519–532.

Pizzolato, F. (2001), 'On the Long Term Behaviour of the MOS Instruments' Quiescent Background'.
URL: *http://www.mi.iasf.cnr.it/fabio/public/background.ps*

Pounds, K. (2007), 'University of Leicester, Private Communication'.

Quigley, M. J. S. & Haslam, C. G. T. (1965), 'Structure of the Radio Continuum Background at High Galactic Latitudes', *Nature* **208**, 741.

Raymond, J. C. & Smith, B. W. (1977), 'Soft X-ray Spectrum of a Hot Plasma', *ApJS* **35**, 419–439.

Read, A. M. & Ponman, T. J. (2003), 'The XMM-Newton Background: Production of Background Maps and Event Files', *A&A* **409**, 395–410.

Revnivtsev, M., Sazonov, S., Churazov, E., Forman, W., Vikhlinin, A. & Sunyaev, R. (2009), 'Discrete Sources as the Origin of the Galactic X-ray Ridge Emission', *Nature* **458**, 1142–1144.

Robertson, I. P., Cravens, T. E. & Snowden, S. L. (2001), 'Temporal and Spatial Variations of Heliospheric X-ray Emissions Associated with Charge Transfer of the Solar Wind with Interstellar Neutrals, Abstract sh21a-11, 2001', *American Geophysical Union* .

Röntgen, W. K. (1896), 'On a New Kind of Rays translated by Arthur Stanton', *Nature* **53**, 274.

Rosner, R. et al. (1981), 'The Stellar Contribution to the Galactic Soft X-ray Background', *ApJL* **249**, L5–L9.

Rougoor, G. W. (1966), 'The Galactic Spurs as a Single Feature', *ApJ* **144**, 852.

Sabol, E. J. (2007), *X-Ray Background Tool*, HEASARC.
URL: *http://heasarc.gsfc.nasa.gov/cgi-bin/Tools/xraybg/xraybg.pl*

Sanders, W. T. (2001), 'Spectra of the 1/4 keV X-ray Diffuse Background from the Diffuse X-ray Spectrometer Experiment', *ApJ* **554**, 694–709.

Sanders, W. T. et al. (1977), 'Soft Diffuse X-rays in the Southern Galactic Hemisphere', *ApJ* **217**, L87–L91.

SAS Development Team (2006), *XMM-Newton Science Analysis Software*, VILSPA.
URL: *http://xmm.vilspa.esa.es/sas/*

Savage, B. D. & de Boer, K. S. (1981), 'Ultraviolet Absorption by Interstellar Gas at Large Distances from the Galactic Plane', *ApJ* **243**, 460.

Schedel, A. (1995), 'An Unprecedented Sensation – Public Reaction to the Discovery of X-rays', *Phys. Educ.* **30**, 342–347.

Sfeir, D. M. (1999), 'Mapping the Contours of the Local Bubble: Preliminary Results', *A&A* **346**, 785–797.

Shapiro, P. R. & Field, G. B. (1976), 'Consequences of a New Hot Component of the Interstellar Medium', *ApJ* **205**, 762–765.

Shelton, R. L. (2009), 'Revising the Local Bubble Model due to Solar Wind Charge Exchange X-ray Emission', *Space Sci. Rev.* **143**, 1–4.

Sidher, S. D. et al. (1996), 'Soft X-ray Observations of the Galactic Halo and the Interstellar Medium', *A&A* **305**, 308–315.

Smith, K. et al. (2001), 'Collisional Plasma Models with APEC/APED: Emission-Line Diagnostics of Hydrogen-like and Helium-like Ions', *ApJ* **556**, L91–L95.

Smith, R. K. & Cox, D. P. (2001), 'Multiple Supernova Remnant Models of the Local Bubble and the Soft X-ray Background', *ApJS* **134**, 283–309.

Snowden, S. L. (1986), Neutral Hydrogen and the Spatial Structure of the Diffuse Soft X-ray Background, PhD thesis, The University of Wisconsin, Madison.

Snowden, S. L. (2000), *The Century of Space Science*, Kluwer Academic Publishers, chapter 1: The Interstellar Medium (Disk plus Halo) The Hot Part (X-ray and EUV), pp. 1–28.

Snowden, S. L. et al. (1990*a*), 'A Color Gradient in the Soft X-ray Diffuse Background', *ApJ* **364**, 118–122.

Snowden, S. L. et al. (1990*b*), 'A Model for the Distribution of Material Generating the Soft X-ray Background', *ApJ* **354**, 211–219.

Snowden, S. L. et al. (1994), 'Soft X-ray and HI Surveys of the Low nH Region in Ursa Major', *ApJ* **430**, 601–609.

Snowden, S. L. et al. (1995), 'First Maps of the Soft X-ray Diffuse Background from the ROSAT XRT/PSPC All Sky Survey', *ApJ* **454**, 643–653.

Snowden, S. L. et al. (1997), 'ROSAT Survey Diffuse X-ray Background Maps II', *ApJ* **485**, 125–135.

Snowden, S. L. et al. (1998), 'Progress on Establishing the Spatial Distribution of Material Responsible for the 1/4 keV Soft X-ray Diffuse Background Local and Halo Components', *ApJ* **493**, 715–729.

Snowden, S. L. et al. (2000), 'A Catalog of Soft X-ray Shadows and More Contemplation of the 1/4 keV Background', *A&AS* **128**, 171–212.

Snowden, S. L. et al. (2004), 'XMM-Newton Observations of Solar Wind Charge Exchange Emission', *ApJ* **610**, 1182–1190.

Sofue, Y. et al. (1974), 'Radio Spurs and Spiral Structure of the Galaxy, II. On the Supernova Remnant Hypothesis for Spurs', *Publ. Astron. Soc. Jpn.* **26**, 399.

Spitzer, L. (1956), 'On a Possible Interstellar Galactic Corona', *ApJ* **124**, 20.

Strüder, L. et al. (2001), 'The European Photon Imaging Camera on XMM-Newton: The pn-CCD Camera', *A&A* **365**, L18.

Tanaka, Y. & Bleeker, J. A. M. (1977), 'The Diffuse Soft X-ray Sky—Astrophysics Related to Cosmic Soft X-rays in the Energy Range 0.1-2.0 keV', *Space Sci. Rev.* **20**, 815–888.

Tielens, A. G. G. M. (2005), *The Physics and Chemistry of the Interstellar Medium*, Cambridge University Press.

Trümper, J. (1983), 'The ROSAT Mission', *Adv. Space Res.* **2(4)**, 241–249.

Turner, M. J. L. et al. (2001), 'The European Photon Imaging Camera on XMM-Newton: The MOS Cameras', *A&A* **365**, L27.

Vaughan, S. et al. (2006), 'The Dust-scattered X-Ray Halo around Swift GRB 050724', *ApJ* **639**, 323–330.

VILSPA (2006), 'XMM-Newton Science Operations Centre'.
URL: *http://xmm.vilspa.esa.es*

Wall, L. (2007), *Perl Documentation*, Perl.
URL: *www.perl.com/pub/q/documentation*

Wang, Q. D. (1998), The Hot Galactic Corona and the Soft X-ray Background, *in* 'The Local Bubble and Beyond, Proceedings of the IAU Colloquium No. 166', pp. 503–512.

Wargelin, B. J. et al. (2004), 'Chandra Observations of the Dark Moon and Geocoronal Solar Wind Charge Transfer', *ApJ* **607**, 596–610.

Weaver, R. et al. (1977), 'Interstellar Bubbles II – Structure and Evolution', *ApJ* **218**, 377–395.

Welsh, B. Y. et al. (1998), 'A New Determination of the Local Distribution of Interstellar NaI', *A&A* **333**, 101.

Welsh, B. Y. et al. (1999), 'EUV Mapping of the Local Interstellar Medium: the Local Chimney Revealed?', *A&A* **352**, 308–316.

Williamson, F. O. et al. (1974), 'Observation of Features in the Soft X-ray Background Flux', *ApJL* **193**, L133–L137.

Willingale, R. (2004), *The Q Reference Manual*, The University of Leicester.
URL: *http://www.star.le.ac.uk/~rw/q_v6/q_manual.html*

Willingale, R. et al. (2003), 'The X-ray Spectrum of the North Polar Spur', *MNRAS* **343**, 995–1001.

Woerden, H. V. et al. (2004), *High Velocity Clouds*, first edn, Kluwer Academic Publishers.

Wolter, H. (1952), 'Wolter Mirror Systems', *Ann. Phys. (N.Y.)* **10**, 94.

Worrall, D. M. et al. (1982), 'HEAO 1 Measurements of the Galactic Ridge', *ApJ* **255**, 111–121.

XMM Science Operations Centre (2006), 'XMM-Newton Science Archive'.
URL: *http://xmm.vilspa.esa.es/xsa/*

Yates, K. W. (1968), 'An Interpretation of the Distribution of Metre Wavelength Radio Emission', *Aust. J. Phys.* **21**, 167.

Yoshioka, S. & Ikeuchi, S. (1990), 'Collision of Cosmological Shock Waves Produced by Explosions and Formation of Large-scale Structures', *ApJ* **360**, 352–369.

Zwicky, F. (1964), 'Basic Results of the International Search for Supernovae', *Ann. Phys. (N.Y.)* **27**, 300.